UNIVERSITEIT VAN PRETORIA
UNIVERSITY OF PRETORIA
YUNIBESITHI YA PRETORIA

EXPERIMENTAL INVESTIGATION OF THE IMPACT OF NON-UNIFORM HEAT FLUX ON BOILING IN A HORIZONTAL CIRCULAR TEST SECTION

by

HANNALIE SCHEEPERS

Report submitted in Partial Fulfilment of the Requirements for the Degree of Master of Engineering (Mechanical)

in the

Department of Mechanical and Aeronautical Engineering

Faculty of Engineering, Built Environment, and Information Technology

UNIVERSITY OF PRETORIA

July 2021

Abstract

EXPERIMENTAL INVESTIGATION OF THE IMPACT OF NON-UNIFORM HEAT FLUX ON BOILING IN A HORIZONTAL CIRCULAR TEST SECTION

Author: H. Scheepers

Supervisor: Prof. J. Dirker

Co-Supervisor: Prof. J.P. Meyer

Department: Mechanical and Aeronautical Engineering

Degree: Master of Engineering (Mechanical Engineering)

The adverse effect of greenhouse gas build-up on the climate has created the need for alternative renewable energy sources to receive significant attention in recent years. Even though some of these energy sources have been utilized on a small scale for centuries, it is only relatively recently that they have been implemented for industrial use. This includes concentrated solar power (CSP) in which solar heat energy is transferred to a fluid to ultimately power a Rankine-based thermodynamic cycle. In the more traditional approach of this technology, an intermediate heat transfer fluid is sent through a solar collector field and then used to heat the thermodynamic working fluid in the power cycle via a heat exchanger to produce a superheated vapour to drive a steam turbine. Alternatively, instead of using an intermediate heat transfer fluid, the working fluid (in this case water) can be sent directly through the solar collector field in a process known as direct steam generation (DSG).

DSG offers a significant opportunity to convert solar thermal energy into mechanical power more efficiently. It is already implemented in CSP plants in several countries, including Spain, China, the United States, India, and South Africa to produce electricity. Depending on the thermal operational limits of the cycle and the temperature of the solar collector field, different working fluids ranging from water to organic fluids such as refrigerants can be used. In addition, a few solar reflector lay-outs exist which is used to reflect and concentrate solar irradiation onto the collector tubes carrying the working fluid. These include parabolic troughs, heliostat fields, and Fresnel lay-outs. Irrespective of the collector or reflector architecture, non-uniform heating profiles are prevalent around the circumference of the collector tubes in which the fluid is heated. This non-uniformity in the heat flux boundary condition can significantly alter the heat transfer performance of the internal fluid as it changes phase from liquid to vapour. Because little research has been done on the thermal operation of flow boiling processes in macro-scale tubes under non-uniform heating conditions, this study is particularly focused on the impact of different uniform and non-uniform heat flux thermal boundary conditions on the heat transfer coefficient (HTC).

Presented here are the results from the steady state flow boiling of R245FA in a laboratory scale horizontal stainless-steel test tube with an inner diameter of 8.5 mm and a length of 900 mm at a saturation temperature of 35 °C and 40 °C. Experiments were conducted at mass fluxes ranging between 200 and 300 kg/m²s at inlet vapour qualities from 0.2 to 0.7 under uniform, and non-uniform imposed heat flux cases that are expected to exist in horizontal parabolic trough solar collectors. Nine (9) different heat flux distributions were investigated. Local and average HTC's were determined based on wall temperature measurements taken along the length and around the circumference of the test

section. Through the choice of the fluid being linked to the possible usage of DSG technology in organic Rankine cycles, the qualitative trends and observed performance variations can be used to predict the same for a working fluid such as water.

It was found that the non-uniformity of the heat flux greatly alters the HTC's of the fluid undergoing boiling but has no effect on the pressure drop characteristics of the fluid undergoing boiling. Heating only on the sides of the tube yielded HTC's that were 46 % lower than achieved under uniform heating. Heating only from the top proved to be more effective in heat transmission to the fluid than heating only from the bottom (as is the case on PTC solar fields), by only a slight margin, and both these cases yielded HTC's that were 30 % lower than the uniform heating case. Applying a bell curve heat flux distribution over the tube walls yielded overall HTC's that differed from the uniform case by a maximum of 5 %, even as the peak heat flux position changes around the circumference of the tube.

A further study may be done to quantify the degree to which the non-uniformity of the heat flux influences the local HTC's, and to develop correlations that may aid in predicting these cases. An integration with flow pattern mapping may also be done to solidify the understanding of the phenomenon governing these observations.

Keywords: Flow boiling, non-uniform heat flux, annular flow, circular horizontal tube, heat transfer coefficients, pressure drop

Publications resulting from this investigation:

A conference paper based on this study has been published in the conference proceedings of the 15th International Conference on Heat Transfer, Fluid Mechanics and Thermodynamics (HEFAT).

H Scheepers, J Dirker, JP Meyer. "Influence of heat flux distribution on flow boiling heat transfer in a horizontal tube"

A journal article based on this study has been submitted to the International Journal of Heat and Mass Transfer for review.

J Dirker*, H Scheepers, JP Meyer. "The effect of circumferentially non-uniform heat flux on flow boiling heat transfer in a horizontal tube"

Acknowledgements

Thank You to my Father in Heaven for tasking me with this absolutely wonderful adventure and siding me with such amazing people to help me and guide me in the best possible way to complete this task. Thank you to my lovely husband, Lorenzo Vergotine, for all the sacrifices you have done to allow me more time to work on this piece, and for your words of truth in encouragement to persevere. Thank you to my family for your full support, reminders of perspective and excitement in my journey. And thank you Prof Dirker for your insight and wonderful guidance, and for siding with me to ensure this project is of utmost value.

Contents

List of Figures

List of Tables

Nomenclature

A	Area	[m^2]
c	Thermocouple calibration offset	[°C]
C	Thermal resistance calibration offset	[°Cm²/W]
$C1$	Conduction heat transfer coefficient	[°C/m]
C_p	Specific heat capacity	[J/kg.K]
C_{dc}	Duty cycle	[-]
D	Diameter	[m]
F	Enhancement factor	(dimensionless)
g	Gravity	[kg/s²]
G	Mass flux	[kg/m^2.s]
h	Enthalpy	[J/kg]
I	Electric current	[A]
k	Thermal conductivity	[W/m.K]
L	Length of the test section	[m]
m	Thermocouple calibration gradient	[-]
$\dot{m}$	Mass flow rate	[kg/s]
M	Thermal resistance calibration gradient	[-]
Nu	Nusselt number	$Nu = \frac{\alpha L}{k}$ (dimensionless)
P	Electric power	[W]
p_{n}	Distance between thermocouples on a station	[m]
Pr	Prandtl number	$\mathrm{Pr} = \frac{\nu}{\alpha}$ (dimensionless)
$\dot{Q}$	Heat transfer rate	[W]
q''	Heat flux	[W/ m^2]
r	Radius	[m]
R	Electrical resistance	[Ω]
Re	Reynolds number	$Re = \frac{\rho V D}{\mu}$ (dimensionless)
S	Suppression factor	(dimensionless)
$S_{\overline{x}}$	Standard deviation	[-]
t	Thickness of an object	[m]
t_δ	T-type distribution	[-]
T	Temperature	[°C]
$\overline{T}$	Average temperature	[°C]
v	Volume of fluid	
V	Electric potential difference	[V]
$\overline{\boldsymbol{V}}$	Mean velocity	[m/s]
x	Vapour quality	[-]
X	Variable placeholder	[-]
y	Radial position of a thermocouple	[m]
z	Axial length of control volume	[m]

Greek Letters

α	Heat transfer coefficient	[W/m^2.K]
μ	Dynamic viscosity	[Pa.s]
ν	Kinematic viscosity	[m^2.s]
ρ	Density	[kg/m^3]
θ	Circumferential variable	[°]

Subscripts

avg	Average
B	Bulk fluid property
c	Cross section
cal	Calibrated
cb	Convection boiling
CCW	Counter-clockwise
CW	Clockwise
cond	Conduction
conv	Convection
eff	Effective
eq	Equivalent
fg	Saturated liquid to saturated vapour
f	Saturated liquid state
g	Saturated vapour state
h	Heated
ht	Heat transfer
HW	Heating wire
ins	Insulation
i	Inner/inlet
in	Inlet
liq	Subcooled liquid phase
loss	Loss to ambient
m	Station number index
mid	The middle of an object
n	Segment number index
nb	Nucleate boiling
o	Outer/outlet
out	Outlet
Ω	Related to the heating element resistors
p	Pressure
P	Power
PH	Preheater
PP	Peak to peak value
PS	Power supply
rad	Radial
RMS	Root mean squared

s	Surface
sat	Saturation
sp	Single phase
sp,fo	Single phase forced
SS	Stainless-steel
tan	Tangential
TC	Thermocouple
tp	Two-phase
TS	Test section
uncal	Uncalibrated
Uniform	Related to a uniform distribution
W	Wall

Abbreviations

CSP	Concentrated solar power
DSG	Direct steam generation
HTC	Heat transfer coefficient
LFC	Linear Fresnel collector
PTC	Parabolic trough collector
PWM	Pulse width modulation
RMS	Root mean squared
RTD	Resistance temperature detector

1 Introduction

1.1 Background

Energy is a basic requirement for all life on earth. In this modern age, we have grown reliant on a certain amount of energy in the form of electricity for residential and commercial purposes. One of the most common methods of production of electricity is by utilising thermodynamic cycles which are generally powered by heat obtained from the incineration of fossil fuels such as coal, oil, and natural gas. Unfortunately, the use of such fuels is detrimental to the environment because of the associated greenhouse gas emissions and the long-term adverse effect it has on global climate change. Therefore, alternative thermal energy sources are required to support a more sustainable energy future.

The research and development into alternative renewable energy sources for power generation has increased in recent years. Some of the natural resources that have been successfully used in power generation include solar energy, wind energy, nuclear energy, hydroelectric energy and geothermal energy (Altenergy, 2018). The modern technologies that harness these renewable sources include solar power plants, wind turbines, nuclear –, hydroelectric –, and geyser power plants. Solar energy is utilized in two distinctly different ways: direct electricity generation making use of photo voltaic cells, and the utilisation of the concentrated thermal solar power in thermodynamic cycles. The latter is of interest in this investigation.

Even though using the sun's energy to aid in human industry is not a new concept, the commercial application of solar power for power generation is a relatively new field, which only gained traction a few decades ago (Boretti *et al.*, 2017). The first operational CSP plant was built in Sant'Ilario, Italy in 1968. The layout of the plant was like that of the modern power tower plants, with a central receiver surrounded by a field of heliostat reflectors. In 1982, feasibility tests were done by the United States of America Department of Energy. Thereafter, the CSP industry developed to include technologies like parabolic trough (PTC) solar reflectors and Fresnel reflectors, that was supplied of its heat by fewer reflectors per tube, than what was seen on the power tower plants. Currently, DSG is implemented on solar power tower plants, and in PTC fields, due to the temperature ranges possible and application of the technology.

The development in technologies for sustainably harnessing energy from the sun has reached a point where many industries now have solar panels for heating a process flow and electricity generation for large corporations or closed communities. Many countries like India, China, Spain, the United States of America, and South Africa now have commercial solar power fields which make use of these technologies to produce electricity, or on a smaller scale, to generate a heated substance for a different use, such as pasteurization of cheese, heating of oil for frying processes, etc.

Figure 1 indicates two possible simplified layouts of a CSP plant that utilizes a solar collector field with for instance PTCs. Figure 1a shows a representation of a simplified Rankine or Inorganic Rankine cycle operating with a heat transfer fluid that is heated in the solar collector field. In the recent past, it had become common for the heat transfer fluid to be a molten salt or organic oil, capable of reaching very high temperatures without changing physical phase – maintaining its state as a liquid in the tubes (Boretti *et al.*, 2017). This heat transfer fluid is used in a heat exchanger to create superheated steam, or high-pressure air – the working fluid – which would be used to turn a Rankine steam turbine to generate electricity. As can be seen from the figure, a heat exchanger is the only thermal point of contact between the heat transfer fluid and the working fluid. The exergy losses introduced through the heat exchangers have made it improbable to obtain better efficiencies for the system (Boretti *et al.*, 2017).

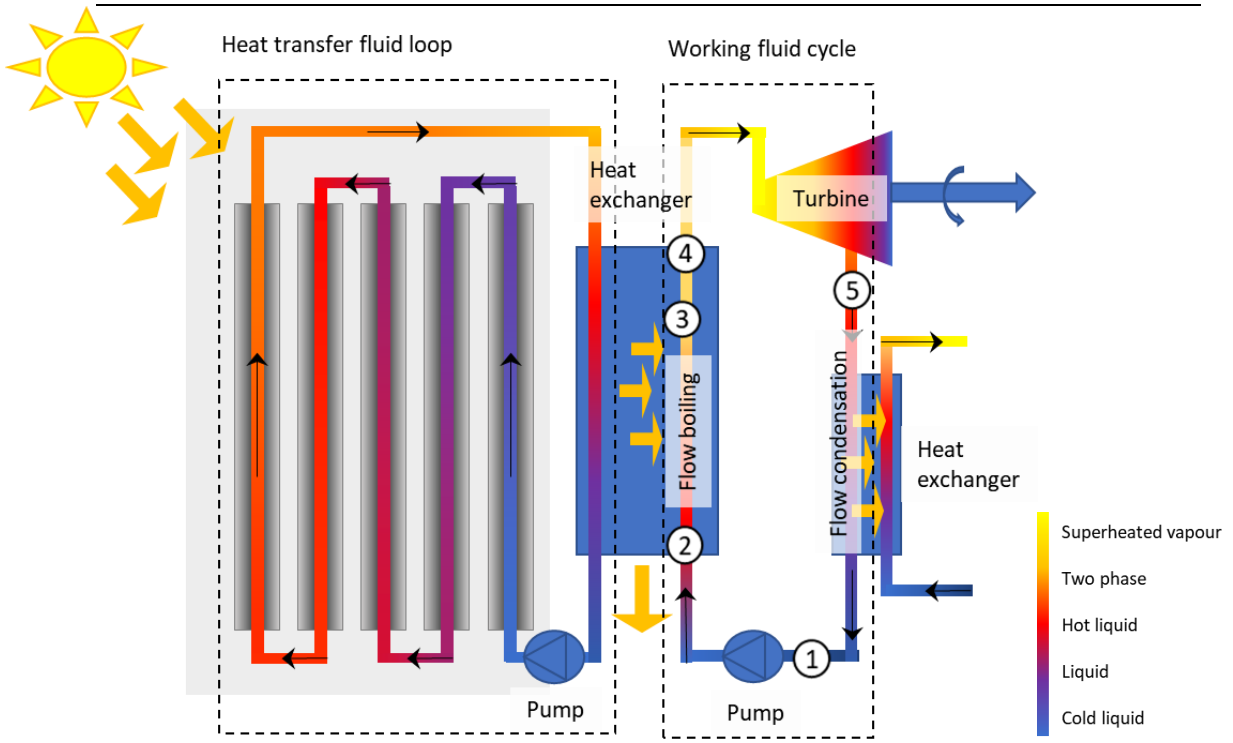

(a)

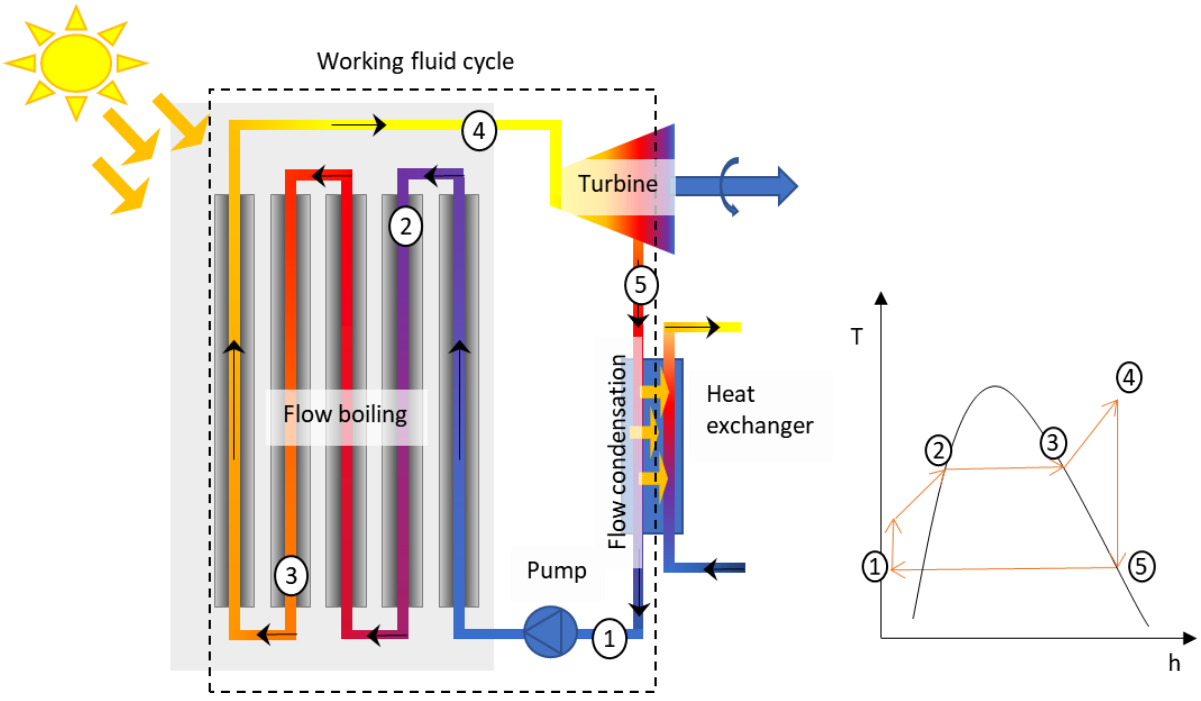

(b)

Figure 1: Diagrams of a simplified CSP plant layout for the heating of (a) a molten salt/organic oil heat transfer fluid, and (b) the working fluid via DSG

An alternative is being researched, where the fluid heated on the solar field is the same fluid used in the Rankine power generation cycle. Water as a working fluid would be ideal when the solar collector temperatures are high (> 400 °C), while organic fluids such as refrigerants are suitable for lower solar

collector field temperatures (100 – 300 °C) (Rycroft, 2016). When looking at Figure 1b, a representation of a simplified DSG system operating with a single fluid acting as the heat transfer fluid and working fluid can be seen. The need for a heat exchanger is eliminated, as the heat transfer fluid and working fluid are one and the same.

Both cases require superheated vapour at the inlet to the turbine, and a condenser to return the working fluid to a liquid state before it enters a pump. In Figure 1a, the heat exchanger is responsible to enable flow boiling and produce a superheated vapour in the working fluid, while in Figure 1b, the flow boiling process occurs in the solar collector field.

The generation of steam on the solar field inherently holds many obstacles, the greatest and most obvious of these being the introduction of two-phase flow in the system. Compared to diabatic operation in the liquid (preheating) and vapour (superheating) flows, the two-phase flow region has more intricacies associated with it. According to Sardeshpande and Ranade (2013), several characteristics need to be considered. These include the flow rate, the impact of the liquid and vapour flow patterns, the change of the local saturated vapour mass fraction, pressure drops and the critical heat flux.

The flow patterns introduced in a two-phase flow during boiling have significant impacts on the heat transfer and pressure drop characteristics of the fluid. These flow patterns are influenced by gravitational forces, due to the density difference in liquid and vapour states, as well as shear forces and surface tension force effects. The orientation of the tube, influencing the direction of flow of the working fluid is therefore of importance. On many CSP plants, solar power towers are used, which mostly make use of vertical channels for boiling of the working fluid. In contrast to this, the flow in PTC channels is generally horizontal. In a horizontal channel, being heated from the bottom, bubbles may form and rise to the top of the tube. Inherently, the direction of the buoyancy force on the vapour phase is perpendicular to the direction of flow: the bubble formation and bubble flow are vertical, while the bulk fluid flow direction is horizontal. Research on two-phase flow was done mainly on vertical flow boiling in conventional tube sizes, with the horizontal channels being in the micro- and mini-channel ranges (Kandlikar, 2002, Saisorn *et al.*, 2013, Kandlikar and Steinke, 2003). The characteristics of two-phase flow in such small channels are inherently different to what would be seen in conventional channels (Kandlikar, 2002, Sardeshpande and Ranade, 2013).

Figure 2 displays the ray reflection mechanism often seen in PTC and Fresnel concentrators. When considering this figure, it can be seen that the sun's rays are concentrated to the lower half of the tube, significantly more than what is concentrated at the top half of the tube. In the ideal scenario, the heat is concentrated with high intensity onto a small tube wall region, while other circumferential regions of the tube will receive significantly lower heat intensities (Hachicha *et al.*, 2018). The heat flux distributions that were considered in most investigations are seldom close to realistic, with the heat fluxes imposed on the surface of the tube often being uniform circumferentially and axially. Not many investigations have been done on the effect that a non-uniform heat flux boundary may have on the flow in the tube (Wang *et al.*, 2017).

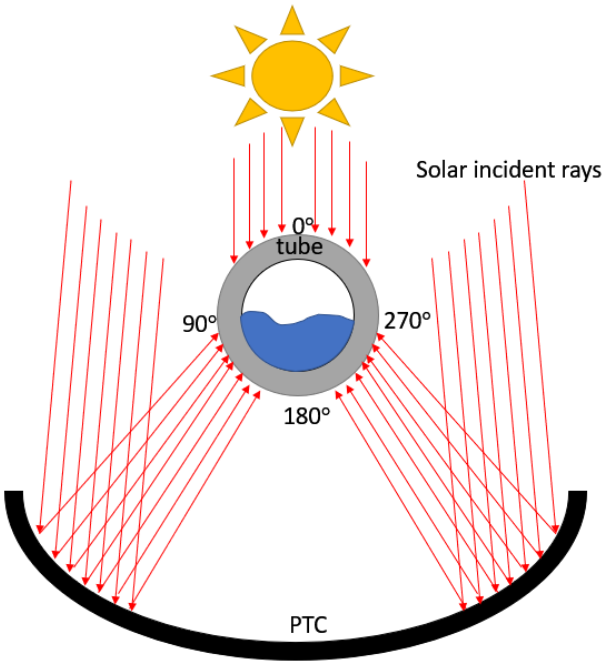

Figure 2: Heat flux imposed on absorber tubes of parabolic trough collector and Fresnel concentrator fields

In addition to the prevalence of non-uniform heat flux, the earth's rotation in conjunction to solar tracking in which the reflector orientation is adjusted to follow the relative azimuth position of the sun during the day, add an additional layer of complexity. Besides the motion of the concentration point on the tube wall, focal and tracking discrepancies can result in a wide range of different and dynamic heat flux distributions around the tube at different times of the day. The non-uniformity and transient nature of the heat flux applied onto the tube wall of a PTC on a solar field requires significant insight into the heat transfer and pressure drop performance of the fluid to accurately model and design the systems for optimal efficiency. However, the literature that is widely available on the thermal performance and hydrodynamic behaviour of fluids undergoing flow boiling focus on uniform heat flux conditions. Some investigations (Dirker *et al.*, 2018, Chang *et al.*, 2014) have been done on the effect of non-uniform heat flux distributions on flow in a horizontal tube undergoing preheating in the liquid phase. It was found that under certain conditions, particularly when buoyancy driven flows are present, a significant difference in the HTC's was established, between non-uniform and uniform heat flux distributions conditions. This is a noteworthy discovery because the heat flux location and relative intensity has a direct impact on the thermal performance of a solar collector tube which must be taken into consideration during the thermal design of the collector system. Very little similar investigations have been done on the two-phase or flow boiling regimes.

1.2 Problem Statement

The effect of a circumferential non-uniform heat flux distribution on flow boiling heat transfer performance in a horizontal tube is not well documented. Little to no experimental investigations have been conducted to explicitly determine the impact on the local and global HTC's around the circumference and length of a non-uniformly heated tube. It is unclear if a correlation can be drawn between the type of heat flux distribution and the thermal performance of such a tube, or whether the current state of flow boiling literature is suitable to describe its steady state operation.

1.3 Objectives

The main objectives of this study were to:

- design and construct a test section, which had the capability to induce both circumferentially non-uniform and uniform heat flux distributions onto a horizontal tube. The test section was implemented into an existing facility and specific operating conditions were established and maintained.
- collect specific data points to make it possible to determine the quantities of interest (that included HTC's), such that sensible conclusions could be drawn on the differences introduced by the application of non-uniform and uniform heat flux boundary conditions.
- analyse the data and compare it to existing information, to establish a correlation between non-uniform heat flux boundary conditions and the HTC of the fluid.

1.4 Limitations/Delineations

DSG makes use of water as working fluid in steam Rankine cycles and organic fluids in Organic Rankine cycles. When this technology is utilised in the industrial milieu, the temperatures and pressures exceed the safe working conditions required for laboratory investigations. Thus, a refrigerant, R245FA, was used as a modelling fluid, which had comparative heat transfer and pressure drop properties at lower saturation temperatures and pressures. The qualitative characteristics of the fluid under laboratory conditions could be extended to be applicable to the working fluid used in the industry.

The heating conditions on the tube could be adjusted dynamically.

1.5 Document Structure

A literature study follows in Chapter 2, with reference to topics of interest in this study. Special attention is given to the effect of non-uniform heat fluxes on HTC's on the backdrop of channel size and tube orientation, operating flow regimes and flow patterns, critical heat flux and pressure drop over a heated length.

The experimental setup is described in Chapter 3. The facility is covered, and the test section design is established in more detail. In Chapter 4 the procedure followed during experimentation is set out. This includes the calibration methods, the results of the heat flux control circuit validation and the test matrix.

The data analysis and data reduction methods are set out in Chapter 5.

Chapter 6 contains the results of the validation of the setup and the experiments. These are discussed in detail, paying attention to the HTC's seen in non-uniform heat flux boundary cases and how these compare to the HTC's seen in uniform heating cases.

Chapter 7 contains conclusions and recommendations as well as a summary of the investigation.

Several appendices follow, for the reader interested in more detailed descriptions and results of topics mentioned throughout the study.

2 Literature Study

This chapter focuses on establishing understanding of the applications of this investigation, specifically CSP and DSG. Thereafter, the properties influencing the heat transfer and pressure drop characteristics of a fluid undergoing flow boiling subject to non-uniform heating will be considered, including channel orientation and size, flow patterns, heat flux distributions and the role of pressure in a heated section.

2.1 CSP and DSG

CSP technology has been developed over the last 30 years to become more efficient in the transfer of energy and more accessible commercially and for smaller industries (Clifford, 2017). Commercially solar power towers have been tested and implemented in many countries, such as the United States of America, Spain, France, and South Africa to be a supplementary source of electricity generation. More widely, however, has been the implementation of PTCs (Boretti *et al.*, 2017, Gunther *et al.*, 2012) in the generation of power, and process flow heating, in countries like Sweden, India, Oman and Thailand.

Table 1 notes the DSG projects currently operational in some capacity on CSP plants. The country in which the projects are running are noted, along with the technology being used in the solar field. The tube orientation is noted where the information is available. The status of the plant and project type are also indicated. This information can be used to assess the importance of study in the field of PTCs on CSP, using DSG, or at least on the study of heat transfer of a fluid flowing in a horizontal tube. The size of the plant in terms of the gross turbine efficiency and the solar field net capacity are also noted. Table 1 is limited in its scope to include only power plant projects where DSG is used in the process of generating electricity.

Table 2 notes DSG projects currently underway in smaller industrial applications. These are not limited to electricity generation, but to the use of water as a working fluid in a temperature range where boiling is a definite physical state change occurring in the normal operation of the system. The table only includes projects that make use of technologies where the tubes are positioned horizontally, and solar rays are directed onto the tubes to heat the working fluid. The project names are noted, along with the country in which the project is running. The larger industry, that the project can be classified into, is stated, to accentuate the diversity of DSG in PTC and linear Fresnel collector (LFC) applications. A more detailed description of the application is also mentioned, along with the temperature range the working fluid operates in.

Table 1: DSG in industrial CSP plants (NREL, 2018)

Power plant project name	Country	Receiver technology	Status	Project type	Electricity generation [MWh/yr]	Heat transfer fluid	Gross turbine capacity [MW]	Field net capacity [MW]	Tube orientation
Kimberlina Solar Thermal Power Plant	United States	LFC	Currently Non-Operational	Demonstration		Water	5	5	Horizontal
Planta Solar 10	Spain	Power Tower	Operational	Commercial plant	23 400	Water	11	11	Vertical
Planta Solar 20	Spain	Power Tower	Operational	Commercial plant	48 000	Water	20	20	Vertical
Puerto Errado 1 Thermosolar Power Plant	Spain	LFC	Operational	Prototype	2 000	Water	1.4		Horizontal
Ivanpah Solar Electric Generating System	United States	Power Tower	Operational	Commercial	1 079 232	Water	392	377	Vertical
Sierra SunTower	United States	Power Tower	Currently Non-Operational		2.629	Water	5	5	Vertical
Thai Solar Energy 1	Thailand	PTC	Operational	Commercial	8 000	Water/ Steam	5	5	Horizontal
Dahan Power Plant	China	Power Tower	Operational	Demonstration & experimentation	1 950	Water/ Steam	1	1	Vertical
Khi Solar One	South Africa	Power Tower	Operational	Commercial	180 000	Water/ Steam	50	50	Vertical
Lake Cargelligo	Australia	Power Tower	Currently Non-Operational	Demonstration		Water/ Steam	3	3	Horizontal
ACME Solar Tower	India	Power Tower	Operational			Water/ Steam	2.5	2.5	Vertical
eLLO Solar Thermal Project	France	LFC	Under Construction	Commercial	20 200	Water	9	9	Horizontal
eCare Solar Thermal Project	Morocco	LFC		Demonstration	1 600	Water	1	0	Horizontal
Liddell Power Station	Australia	LFC	Currently Non-Operational	Commercial	13 550	Water/ Steam	3	3	Horizontal
Greenway CSP Mersin Tower Plant	Turkey	Power Tower	Operational	Demonstration		Water	1.4	1	Vertical
Huanghe Qinghai Delingha 135 MW DSG Tower CSP Project	China	Power Tower	Currently Non-Operational		628 448	Water/ Steam	135	135	Vertical
Sundrop CSP Project	Australia	Power Tower	Operational		1 700	Water/ Steam	1.5	1.5	Vertical
Shangyi 50MW DSG Tower CSP project	China	Power Tower	Under Development			Water/ Steam	50	50	Vertical
Zhangbei 50MW DSG Fresnel CSP project	China	LFC	Currently Non-Operational			Water/ Steam	50	50	Horizontal
Zhangjiakou 50MW CSG Fresnel project	China	LFC	Under Development			Water/ Steam	50	50	Horizontal
Dadri ISCC Plant	India	LFC	Under Construction	Demonstration	14 000	Water	14		Horizontal

Table 2: DSG in smaller industrial applications (SHIPPlants, 2018)

Project name	Country	Industry	Receiver technology	Application	Temperature range of operation
Agrana Fruit	Mexico	Manufacturing of food products	PTC	Boiler preheating: Heating of make-up water	25 – 118 °C
Alanod Solar	Germany	Manufacturing of fabricated metal products, except machinery and equipment	PTC	Production of saturated steam for heating of the supply line	143 °C, 4bar
Bomans Lackering	Sweden	Manufacturing of computer, electronic and optical products	PTC	Hot water for chemical baths that provide gold plating for radio cabinets/surface treatment	heat at 160 °C
Cremo SA	Switzerland	Manufacturing of dairy products	PTC	Milk processing, coffee cream production/sterilization	170°C for high temperature process, 125°C for low temperature process
El NASR Pharmaceutical Chemicals	Egypt	Manufacturing of basic pharmaceutical products and pharmaceutical preparations	PTC	Production of process steam for a pharmaceutical company	173 °C
Emmi AG, Fromagerie Tête de Moine	Switzerland	Manufacturing of dairy products	PTC	Steam for different dairy processes/ Heating of supply heat storage	140 - 180°C
Frito Lay	United States	Manufacturing of food products	PTC	Steam for heating the oil to fry potato chips	243 °C
Grupo Mosa la Luz SA de CV	Mexico	Manufacturing of food products	PTC	Boiler preheating, cooking, Heating of make-up water	55 - 110 °C
Honeywell Technology Solutions	India	Manufacturing	PTC	Space cooling of production hall	165 °C, 17 bar
Iberotel Sarigerme Park	Turkey	Hospitality	PTC	Steam for hotel laundry, hot water, and kitchen uses/cleaning	150 – 180 °C
Matatlan Dairy	Mexico	Manufacturing of dairy products	PTC	Heating of process heat storage	18,5 to 80-100 °C
Meiser Textil	Germany	Manufacturing of textiles	PTC	Proof of concept	max 140 °C
PSG Hospital Laundry	India	Human health and social work activities	PTC	Drying and sterilization in laundry	150 °C & 3 bar
SKF Technologies Mysore	India	Manufacturing of fabricated metal products, except machinery and equipment	PTC	Heating water for circulation through the treatment tanks in the phosphating plant, surface treatment	Pressurized water at 130 °C is passed through coils of tanks of phosphating process where 95 °C is needed
SURPRISE SHIP for sewage sludge drying	United States	Water supply; sewerage; waste management and remediation activities	PTC	Drying sewage sludge	90-100°C
Siddharth Surgical	India	Manufacturing of textiles	PTC	Cleaning and bleaching	110 °C
Bergamo	Italy	Manufacturing of machinery and equipment	Fresnel collector	Refrigeration	195 °C
FIFA world cup solar cooled demonstration stadium	Qatar	Construction	Fresnel collector	Cooling of demonstration stadium for FIFA/Heating of supply heat storage	180°C Heat supply for absorption chiller that cools the stadium
JTI (Jordan)	Jordan	Manufacturing of tobacco products	Fresnel collector	Cooling and Process Heat	190 °C-225 °C

Nuova Sarda Industria Casearia	Italy	Manufacturing of dairy products	Fresnel collector	Heating of supply line	Steam at 200 °C and 12 bar, directly fed into steam system of cheese production without storage
RAM Pharma	Jordan	Manufacturing of basic pharmaceutical products and pharmaceutical preparations	Fresnel collector	Pharmaceutical production process	160-165°C, 204°C
Solar Process Heat for Car Paintshop	Germany	Manufacturing of motor vehicles, trailers, and semi-trailers	Fresnel collector	Drying of paint coat in automobile industry	200/220°C
Solar cooling for data center	South Africa	Information and communication	Fresnel collector	Cooling of data center for a telecommunication company	180 °C
Solar cooling for stainless steel pipe industry	Germany	Manufacturing of fabricated metal products, except machinery and equipment	Fresnel collector	Cooling process of stainless-steel pipes and office building	200 °C
Solar refrigeration in the food industry	Germany	Manufacturing of food	Fresnel collector	Refrigeration of cold storage room	200 °C
Tamil Nadu - Textile Industry	India	Manufacturing of textiles	Fresnel collector	Heating of supply line	100-135 °C
Test facility at the QSTP	Qatar	Professional, scientific, and technical activities	Fresnel collector	Heating of process medium	180 °C
University of Sevilla	Spain	Education	Fresnel collector	Refrigeration	165°C
Winery Grombalia	Tunisia	Manufacturing of beverages	Fresnel collector	Solar cooling by feeding an ammonia-water absorption chiller	110-160°C

PTCs are fundamentally similar to solar power towers, in that the rays from the sun are concentrated to a central focal point containing a fluid which is heated (Zarza *et al.*, 2004). The difference in these technologies, however, are in the temperature ranges over which each of the technologies work. Solar power towers have fields of reflectors concentrated at a single focal point containing mostly vertical tubes, while PTCs are a single horizontal tube, as the focal point of a single parabolic trough reflector (Zarza *et al.*, 2004). It follows that the temperatures achieved in a solar power tower heating fluid can range upwards of 600 °C (Clifford, 2017), where a PTC can reach between 80-400 °C (Zarza *et al.*, 2004). This makes parabolic technology ideal for use in feedwater heating, or even DSG for power generation.

2.2 Fluid dynamics

The flow of heat through a fluid undergoing boiling is of great importance in the determination of effectiveness of the heating system. In the power generation cycle, the HTC gives an indication of the effectiveness of usable heat transferred to the fluid, which may be extracted from the fluid at a later stage.

During flow boiling, it is assumed that heat transfer is done by a combination of nucleate and convective boiling. Heat transferred to the fluid causes the density of the fluid to change, creating a buoyancy effect. When the fluid is heated more, the fluid will evaporate. The movement of the fluid due to density changes brought on by the transfer of heat to the fluid can be categorized as convective boiling. Nucleate boiling occurs when the fluid evaporates. Greco (2008) stated that at high heat fluxes and evaporating pressures nucleate boiling mechanism predominantly influences the heat transfer, while at low heat fluxes and evaporating pressures convective boiling mechanism has the predominant effect.

The HTC of a fluid, determined by:

$$\alpha = \frac{q_{\mathrm{f}}^{"}}{T_{\mathrm{W}} - T_{\mathrm{B}}} \tag{1}$$

is influenced by the tube geometry and inclination, the mass flux of the fluid, quality of the fluid, the heat flux boundary condition to the fluid and evaporating pressures in the system. The effect these conditions have on the HTC is discussed next.

2.2.1 Dimensionless numbers

The effects that mass flux, geometry and fluid properties have on the characteristics of the flow can be captured in dimensionless form. The inclusion of these influences makes it possible to study trends and compare experimental data over a wide range of experimental setups.

The dimensionless Nusselt number is a measure of the ratio between the heat transfer of a fluid in liquid state by conduction alone and the heat transfer by convection (Shires, 2011). It is defined as:

$$Nu = \frac{\alpha D}{k} \tag{2}$$

It considers the fluid properties as it is heated as well as the characteristic length of the flow passage geometry. This quantity is widely used to report on the heat transfer characteristics of single-phase flows.

A momentum and geometry relation makes it possible to determine flow regime. This can be done by means of the Reynolds number which is defined as:

$$Re = \frac{\rho \overline{\boldsymbol{V}} D_{\mathrm{i}}}{\mu} \tag{3}$$

Fully developed flow in a circular tube with a Reynolds number of lower than approximately 2100 is in the laminar regime, while a Reynolds number higher than approximately 4000 is associated with the turbulent regime. A Reynolds number between approximately 2100 and 4000 is referred to as the transitional flow regime (Sydney, 2005).

The Prandtl number is the ratio of momentum diffusivity to thermal diffusivity:

$$\mathrm{Pr} = \frac{\nu}{\alpha} \tag{4}$$

It is often used in combination with the Reynolds number to calculate correlations for the prediction of the Nusselt number where too little information is available on the temperature and pressure of the fluid to determine the conductive and convective heat transfer characteristics.

Vapour quality, mass flux and heat flux can be used directly as parameters for comparison, making sure to take details about channel geometry and heat flux distribution into account. Two-phase HTC's are reported directly, as the required characteristics to non-dimensionalise this quantity to a Nusselt number are commonly unknown entities.

2.2.2 Existing correlations and predictions

Many correlations have been suggested to predict the heat transfer characteristics of fluids as it is heated under certain conditions. A rudimentary knowledge of these correlations can lead to a better understanding of the characteristics that is seen in a two-phase region, though significant alteration of these correlations is required for an accurate prediction of two-phase conditions. Most of the correlations redundantly included here are to indicate the foundation on which predictions of the HTC's are made.

Dittus and Boelter (1930) proposed a correlation that has been utilized widely in the determination of the Nusselt number for a fluid. The conditions of this correlation, however, excludes some cases that are seen often. This correlation is only appropriate for constant wall temperature, constant wall heat flux and turbulent flow of a single-phase fluid. The correlation proposed by Sieder and Tate (1936) endeavoured to capture a wider range of cases, by expanding the Prandtl number range. Since then, many have created other correlations, lending from these and other researchers, to capture more accurately and more widely, the Nusselt numbers and HTC's of many different flow conditions and cases. Some of these correlations are reported in Table 3. Most of these correlations are for circumferentially uniform heat flux cases. The correlations for flow boiling suggested by Chen (1966), improved upon by Liu and Winterton (1991) and fine-tuned for application to non-uniform flow boiling of R245FA by Wang *et al.* (2019) are of special importance in this study. The correlation presented by Wang *et al.* (2019) is critically important in this study as it is the only correlation presented to date that considers the effects of non-uniformity in the heat flux, and coincidentally was developed on experimental R245FA results.

The correlation suggested by Chen (1966) endeavoured to capture the HTC associated with a two-phase flow region (α_{tp}), by superimposing the contributions of nucleate boiling (α_{nb}) and the single phase equivalent HTC (α_{sp}). The correlation suggested by Wang *et al.* (2019) built upon this idea and included the possibility of a convective boiling contribution (α_{cb}) accounting for the liquid state of the fluid undergoing flow boiling.

Table 3: HTC correlations widely used

Author and year	Correlation	Conditions
(Dittus and Boelter, 1930)	$Nu = 0.023 \times Re^{0.8} \times \mathrm{Pr}^{n}$ $n = \begin{Bmatrix} 0.4\ for\ heating \\ 0.3\ for\ cooling \end{Bmatrix}$	$0.7 \leq \mathrm{Pr} \leq 160$ $Re \geq 10000$ $\frac{L}{D} \geq 10$
(Sieder and Tate, 1936)	$Nu = 0.27 \times Re^{0.8} \times \mathrm{Pr}^{0.3334} \left(\frac{\mu}{\mu_W}\right)^{0.14}$	$0.7 \leq \mathrm{Pr} \leq 16700$ $Re \geq 10000$ $\frac{L}{D} \geq 10$
(Whitaker, 1972)	$Nu = 0.015 \times Re^{0.83} \times \mathrm{Pr}^{0.42} \times \left(\frac{\mu}{\mu_W}\right)^{0.14}$	$2300 \leq Re \leq 1 * 10^5$ $0.48 \leq \mathrm{Pr} \leq 592$ $0.44 \leq \frac{\mu}{\mu_W} \leq 2.5$
(Chen, 1966)	$\alpha_{\mathrm{tp}} = S\alpha_{\mathrm{nb}} + F\alpha_{\mathrm{sp}}$ $X_{\mathrm{tt}} = \left(\frac{1-x_{\mathrm{eq}}}{x_{\mathrm{eq}}}\right)\left(\frac{\rho_{\mathrm{g}}}{\rho_{\mathrm{f}}}\right)^{0.5}\left(\frac{\mu_{\mathrm{f}}}{\mu_{\mathrm{g}}}\right)^{0.1}$ $\frac{1}{X_{\mathrm{tt}}} > 0.1 : F = 2.35\left(\frac{1}{X_{\mathrm{tt}}} + 0.213\right)^{0.736}$ $\frac{1}{X_{\mathrm{tt}}} < 0.1 : F = 1$ $\alpha_{\mathrm{sp}} = 0.023 \times Re_{\mathrm{f}}^{0.8} \times \mathrm{Pr}_{\mathrm{f}}^{0.4} \times \left(\frac{k_{\mathrm{f}}}{D_{\mathrm{h}}}\right)$	This correlation is widely used in literature and considered as a benchmark for boiling HTC prediction (Sardeshpande and Ranade, 2013).

	$S = \frac{1}{\left(1 + 2.53 \times 10^{-6} Re_{\mathrm{f}}^{1.17}\right)}$ $\alpha_{\mathrm{nb}} = 0.00122 \left(\frac{k_{\mathrm{f}}^{0.79} C_{pf}^{0.45} \rho_{\mathrm{f}}^{0.49}}{\sigma^{0.5} \mu_{\mathrm{f}}^{0.29} h_{\mathrm{fg}}^{0.24} \rho_{\mathrm{g}}^{0.24}}\right) \Delta T_{\mathrm{sat}}^{0.24} \Delta P_{\mathrm{sat}}^{0.75}$	
(Liu and Winterton, 1991)	$\alpha_{\mathrm{tp}} = \left[(S\alpha_{\mathrm{nb}})^2 + \left(F\alpha_{\mathrm{sp,fo}}\right)^2\right]^{\frac{1}{2}}$	A general correlation for flow boiling in tubes
(Wang *et al.*, 2019)	$\alpha_{\mathrm{tp}} = F\alpha_{\mathrm{cb}} + S\alpha_{\mathrm{nb}}$ $S = \left(A + B \times F^C \times Re_l^L\right)^M$ $\alpha_{\mathrm{cb}} = 0.023\, Re_{\mathrm{l}}^{0.8} \mathrm{Pr}_{\mathrm{l}}^{0.4} \frac{\lambda}{d}$ $\alpha_{\mathrm{nb}} = 55 \mathrm{Pr}^{0.12} (-\log_{10} P_{\mathrm{r}})^{-0.55} M^{-0.5} q^{0.67}$ $F = 1 + 2.4 \times 10^4 Bo^{1.16} + 1.37 \left(\frac{1}{X_{\mathrm{tt}}}\right)^{0.86}$ $Fr < 0.05 F = F \times Fr^{0.1-2Fr}, S = S \times Fr^{0.5}$ $Bo = \frac{q}{G h_{\mathrm{r}}}, Fr = \frac{G^2}{\rho_{\mathrm{l}}^2 g D}$	$Re \in [6.41 \times 10^4, 4.76 \times 10^5]$ $\mathrm{Pr} \in [28.19, 35.83]$ For R245FA under circumferentially non-uniform heating

2.3 Tube geometry and inclination

2.3.1 Channel size

The channel size has an influence on the development of the flow as it undergoes boiling. The flow boiling characteristics are different in different channel sizes. This may be due to the relative heat transfer area around a volume of fluid. When compared to larger diameter channels, smaller diameter channels have larger wall surface area for heat transfer per volume of liquid. The convective and nucleate boiling characteristics of the flow are therefore different in the different channel sizes.

The influence of the tube diameter (D) on the effective heat transfer ($\dot{Q}_{\mathrm{eff}}$) to or from a body of fluid over a tube length (L) can be derived by considering the ratio of the volume of fluid (v_{f}), to the heat transfer surface area (A_{ht}):

$$\dot{Q}_{\mathrm{eff}} \propto \frac{A_{\mathrm{ht}}}{v_{\mathrm{f}}} \tag{5}$$

where

$$A_{\mathrm{ht}} = \pi D_{\mathrm{i}} L \tag{6}$$

$$v_{\mathrm{f}} = \frac{\pi D_{\mathrm{i}}^2}{4} L \tag{7}$$

Simplifying Equation (*5*), it is evident that the heat transfer quantity is inversely proportionate to the tube diameter:

$$\dot{Q}_{\mathrm{eff}} \propto \frac{4}{D_{\mathrm{i}}} \tag{8}$$

Therefore, as the diameter of the tube increases, the effective heat transfer into the fluid reduces. A larger heat rate is required on a larger tube diameter to establish the same boiling characteristics as seen on a small tube diameter. This phenomenon makes it critical to establish the limits at which the tube diameter influences the physical mechanisms of heat transfer during flow boiling.

A general criterion in the categorization of channel sizes for use in engineering applications was proposed by Kandlikar (2002). According to this criterion, channels with hydraulic diameters between 10 µm and 200 µm are classified as micro-channels, while channels with hydraulic diameter between 200 µm and 3 mm are classified as a mini-channels, and channels with hydraulic diameters larger than 3 mm are classified as conventional channels.

The channel size utilized in solar power plants that make use of parabolic trough technologies fall within the conventional channel category. The flow development and characteristics will therefore need to be tested in a conventional channel. Any correlation or experiment done on mini- or micro-channels should not be considered in this investigation.

2.3.2 Channel orientation

The five major forces influencing flow boiling phenomena (surface tension, inertia, gravity, viscous forces and evaporation momentum forces (Kandlikar, 2010)) are affected by the orientation and flow direction of the fluid. The effect of gravity in the heat transfer characteristics of a fluid is significant, especially as the flow undergoes boiling. It is therefore critical that the orientation used in the investigation be considered when correlations and predictions are made.

The effect that orientation of the channel has on the HTC of a fluid was investigated by Saisorn *et al.* (2013) and Kharangate *et al.* (2016). The results were that the HTC of a fluid flowing upward or downward in a vertical channel is larger than that of flow in a horizontal channel at low mass fluxes. At higher mass fluxes the HTC's seem to be equal for all orientations. An investigation done by Kundu *et al.* (2014a) was done on a copper tube, undergoing uniform heat flux. At low vapour quality, the effect of inclination on the HTC is significant, with the highest HTC obtained with a vertical inclination.

2.4 Flow patterns

Flow patterns are general representations of the liquid/vapour distributions within a tube during flow boiling. From experimental observations different flow patterns are prevalent depending on the mass flux and vapour quality (saturated vapour mass fraction) combination in a particular region in the tube. The saturation (boiling) temperature also has an impact on the flow patterns. Because there is an increase in the local vapour quality along the length of a diabatic flow boiling tube, different local flow patterns may exist between the inlet and the outlet of the tube.

Experimentation done in the two-phase region should always take the flow pattern into consideration when drawing conclusions. The dispersion of molecules influences the division of energy in a volume of fluid, and the heat transfer of the volume of fluid is different in each flow pattern. A region that consists of more vapour may inherently be expected to have a lower HTC than a liquid region.

Bennett *et al.* (1965-1966) defined flow patterns observed in the two-phase boiling in a vertical upward flow channel. These patterns have since been seen and reported on widely. The presence of the same flow patterns has been noted in the horizontal flow boiling cases, with some alterations and additions due to the interaction of gravity. The most observed flow patterns in horizontal channels are shown in Figure 3.

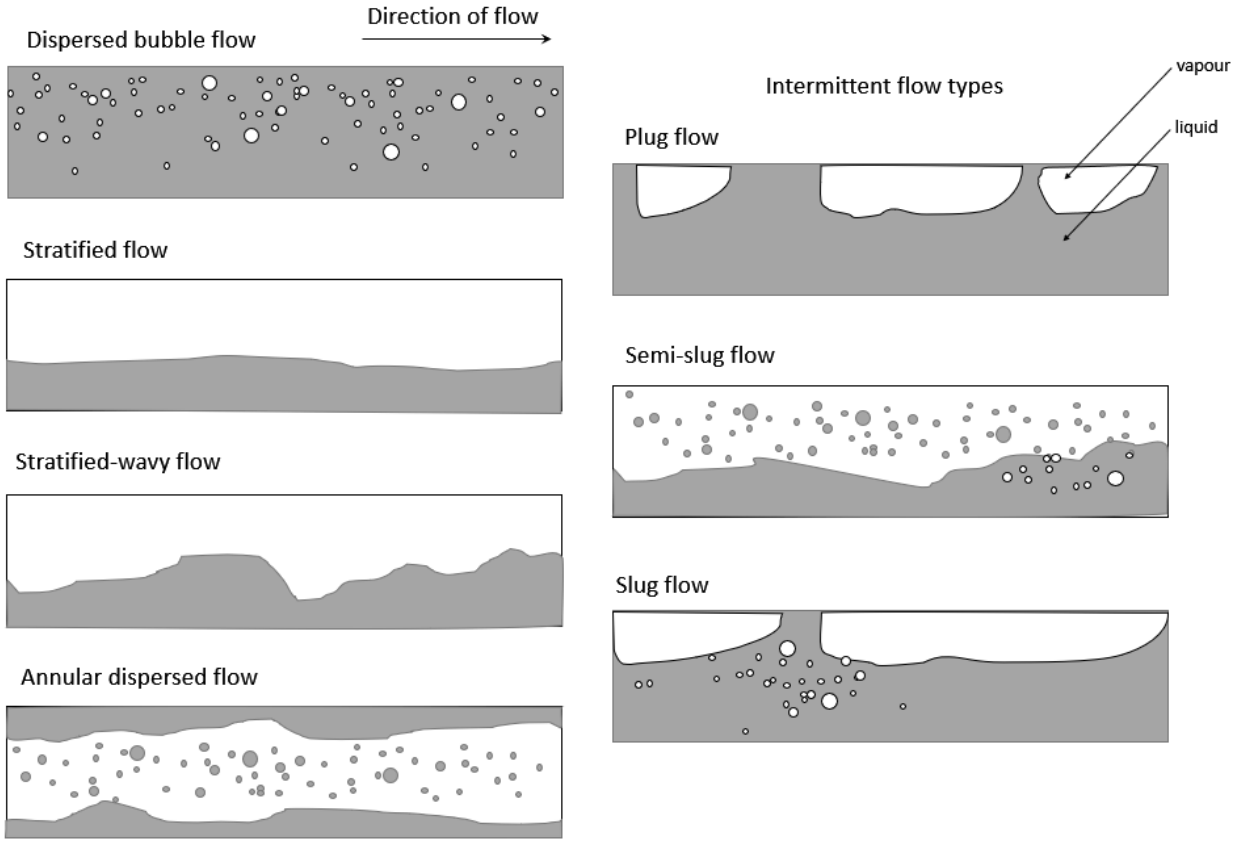

Figure 3: Flow patterns in horizontal flow boiling adapted from Hewitt (2008)

Flow boiling in a horizontal tube has the flow direction perpendicular to the upward movement of the heated fluid. As the fluid enters a heating section bubbles appear if the local wall temperature is above the saturation temperature. If the fluid is close to or at saturation conditions, these bubbles ascend to the top of the fluid and dispersed bubble flow might be observed. A further increase in the number of bubbles as the fluid is heated will lead to the bubbles at the top of the flow merging. When the coalesced vapour volumes are comparable in size to the channel diameter, they are referred to as plugs, and the flow pattern is referred to a plug flow. If these plugs merge to create a very clear distinction between fluid and gas in the tube, a stratified flow pattern is obtained with vapour at the top, and liquid at the bottom. As the liquid is heated further, the secondary flow created in the liquid results in stratified wavy flow, where the boundary layer between liquid and gas is moving. With a further increase of heat in the fluid, bubbles form still, creating a churning of the fluid, which results in liquid droplets in the gas phase, and bubbles in the liquid phase. The presence of waves in the flow can lead to the formation of slugs which flow through the tube at a high velocity (Hewitt, 2008). As the amount of vapour in the tube increases, a liquid film may appear on the tube wall around the vapour. The vapour moves at a higher velocity than the liquid and results in flow pattern known as annular flow. With an increase of heat transfer to the fluid, this liquid film thins out, leaving areas on the tube wall susceptible to dry-out (Sardeshpande and Ranade, 2013). It has been reported that dry-out in R245FA occurs at a vapour quality of 0.75 - 0.85, for a flow with mass flux G = 100 kg/m^{2}s and a uniform heat flux of q'' = 12 kW/m^2 at saturation temperatures between 55 °C and 95 °C (Guo *et al.*, 2020).

As mentioned, each flow patterns corresponds to a range of mass fluxes and vapour qualities of the fluid. Many investigations into flow pattern mapping has been done, by among others, Elatar and Siddiqui (2014), Grauso *et al.* (2013), Spedding *et al.* (2003) and Khaledi *et al.* (2014). The flow pattern map of R245FA determined experimentally by Liu *et al.* (2020) is shown in Figure 4.

From the map it can be seen that plug flow (black) is prevalent only when the vapour quality is close to zero, and at the upper limits of the vapour quality spectrum dry-out (green) occurs. At low mass fluxes, the flow pattern is stratified-wavy (blue) predominantly. At mass fluxes between 100 and 200 kg/m²s the lower half of the vapour quality spectrum yields flow patterns that correspond to the intermittent flow pattern (red), and the upper half of the vapour quality spectrum yields flows that are wavy-annular (blue – green) and annular (pink).

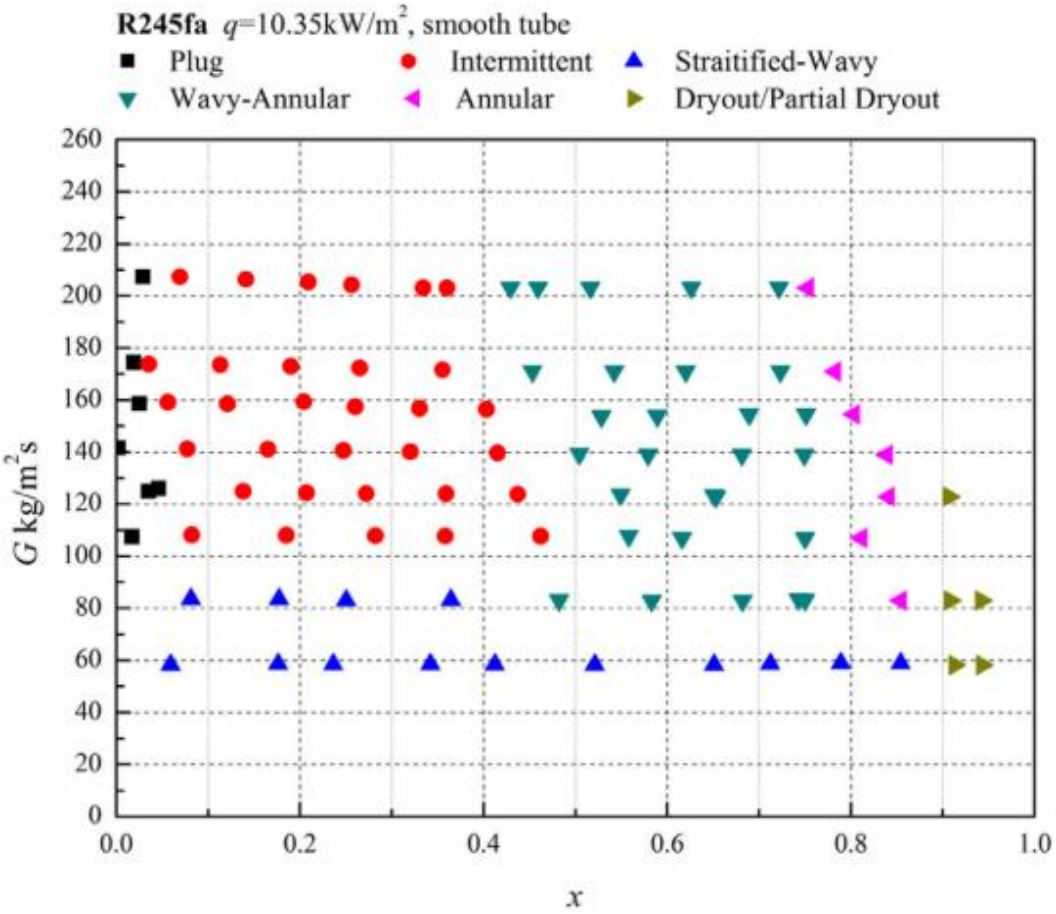

Figure 4: A flow pattern map for R245FA experimentally determined by Liu et al. (2020) for low mass fluxes

An increase in mass flux results in an increase of HTC (Greco, 2008, Kundu *et al.*, 2014b). It is stated by Greco (2008) that this is due to an increase of velocity which enhances convective boiling. At lower vapour qualities nucleate boiling is dominant, and the HTC's are very similar for different mass fluxes.

Developments have been made in the prediction of HTC in a fluid undergoing flow boiling, using the flow pattern maps and the HTC results obtained from multiple investigations. Flow pattern-based heat transfer models are setup in such a way that the HTC of the volume is determined by the superimposition of the heat transfer of the wetted and non-wetted part of the tube. The non-wetted part contribution is described through the incorporation of the dry angle, θ_{dry}, which contains the effects of the void fraction and flow pattern. The wetted part contribution is determined as a superposition of the effects of nucleate and convective boiling on the HTC in which the film thickness is encapsulated (Weise *et al.*, 2020).

From the contributions of each of these terms, a logical physical reasoning can be done to determine the cause of the results seen in experiments. For instance, a flow that consists of a low mass flux and high heat flux will be dominated by nucleate boiling, which stands to reason that the critical heat flux capacity of the flow would be low, as the contribution of the convective boiling term is negligible. In

contrast, in annular and intermittent flow regimes, the convective boiling terms dominate, and experimentally no premature dry-out was seen in the analysis done by (Weise *et al.*, 2020). When the dry angle is zero, meaning the tube wall is fully wetted, the HTC seen at high vapour qualities was lower than the HTC seen at the lower vapour qualities. This suggests that regardless of the convective contribution, the inclusion of nucleate boiling will increase the likelihood of dry-out occurring. High vapour qualities increase the nucleate contribution to the HTC's. For flow patterns where the convective contribution dominates, dry-out may be effectively avoided, and the trend expected in the HTC is such that as the vapour quality increases, the HTC also increases. Again, this is only true when nucleate boiling does not constitute a considerable contribution to the HTC, which is the case at lower vapour qualities.

2.5 Heat Flux Distributions

There have recently been many investigations into the different heat flux distributions that are achieved by different technologies. The horizontal tube CSP technologies used most widely are PTC types. There have not been many experimental investigations into the non-uniform heat flux distributions that are achieved on a solar field using PTC, mainly due to the accuracy accepted in the numerical methods used. All of the works considered in this section, therefore are numerical investigations. Some computational fluid dynamic (CFD) investigations on the heat flux distributions achieved by this technology have been published (Cheng *et al.*, 2010, Okafor *et al.*, 2014). Many of these investigations have made use of CFD, including direct modelling Monte Carlo methods and raytracing to attempt to capture most realistically what could be achieved on a solar field (Wang *et al.*, 2017, Tang *et al.*, 2017, Okafor *et al.*, 2017, Mwesigye *et al.*, 2014). The numerical study by Hachicha *et al.* (2018) on DSG mentions the heat flux distribution shown in Figure 5. This distribution has also been noted by Cheng *et al.* (2010), Li *et al.* (2016), Mwesigye *et al.* (2014) and Tang *et al.* (2017). The concentrator information and specifics on the setup are presented in Table 4.

Table 4: Summary of heat flux distribution seen on an LS-3 concentrator

Description	Value	Unit
Parabolic Trough Collector	LS-3 concentrator	
Concentration ratio	82	-
Aperture size	5.76	m
Absorber tube outer diameter	0.07	m
Absorber tube inner diameter	0.05	m
Overall length	50	m
Base-line solar incidence level	1	kW/m²
Peak optical efficiency	77	%

Consider Figure 5 that contains a schematic cross section view of a circular solar heat collector tube. The circumferential angular position is defined with 0° coinciding with the top of the tube and follows a clockwise notation with 180° representing the bottom and 360° representing the top again. Also included in Figure 5 is an example heat flux distribution around the circumference that uses this angular coordinate system to indicate which circumferential locations experiences the highest and lowest local heat flux quantities. It can be seen from this distribution, which has been reported by Hachicha *et al.* (2018) for an LS-3 concentrator of aperture 5.76 m and an absorber tube of outer diameter of 0.07 m that a large variation in the heat flux is present and ranges in this case between 1 000 W/m² and 47 000 W/m². The regions with the highest heat flux coincide with lower half of the collector tube. This is because the solar radiation is reflected and concentrated by the curved mirror from below. The local drop in the heat flux directly at the bottom of the tube coincides with the shadow of the collector tube on the reflective surface.

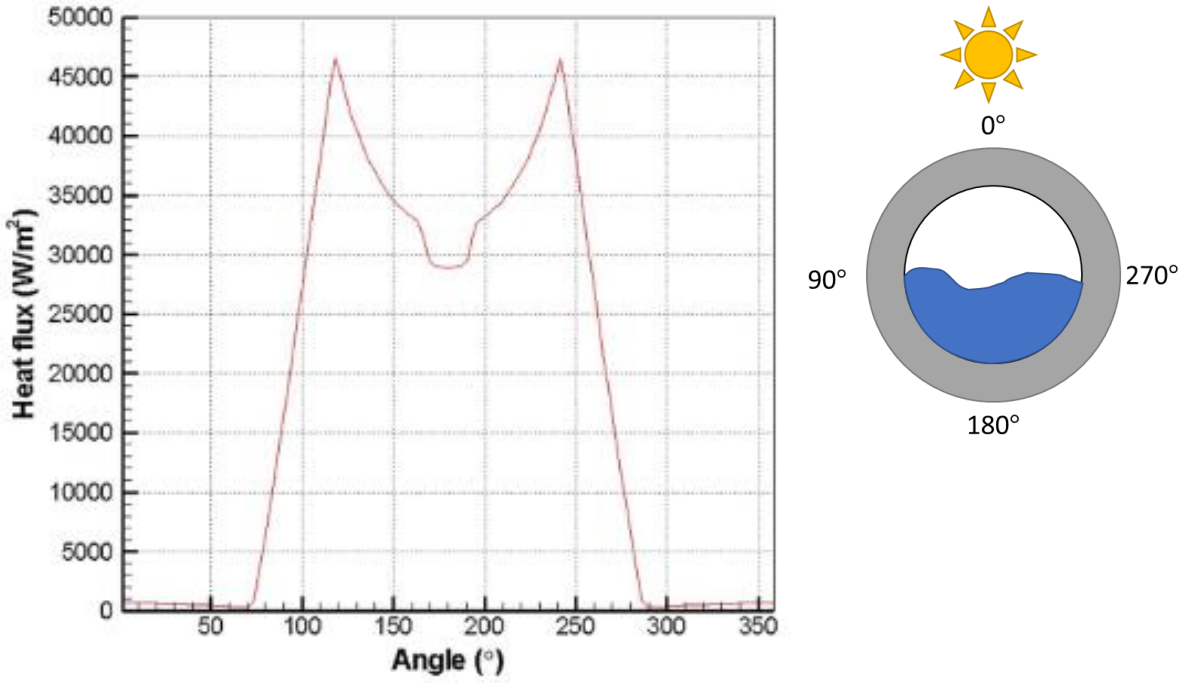

Figure 5: Heat flux distribution determined by Hachicha et al. (2018) appearing on parabolic trough solar collector tubes

The distribution that is affected on the absorber tube of a PTC depends highly on the time of day, the geometric parameters and focal mismatch problems that may occur on the solar field. Figure 6 shows the efficiency that is achieved throughout the course of a day (Chaudhary *et al.*, 2018). From this figure it can be seen that the peak efficiency of 70 % of heat transfer is achieved at between 13:00 and 14:00 for this specific day. At the beginning and at the end of the day, the efficiency of the system is much lower, reaching a low limit of 20 %. The incident energy that is supplied onto the reflector varies between 100 W/m² at the beginning and end of the day and 700 W/m² at midday.

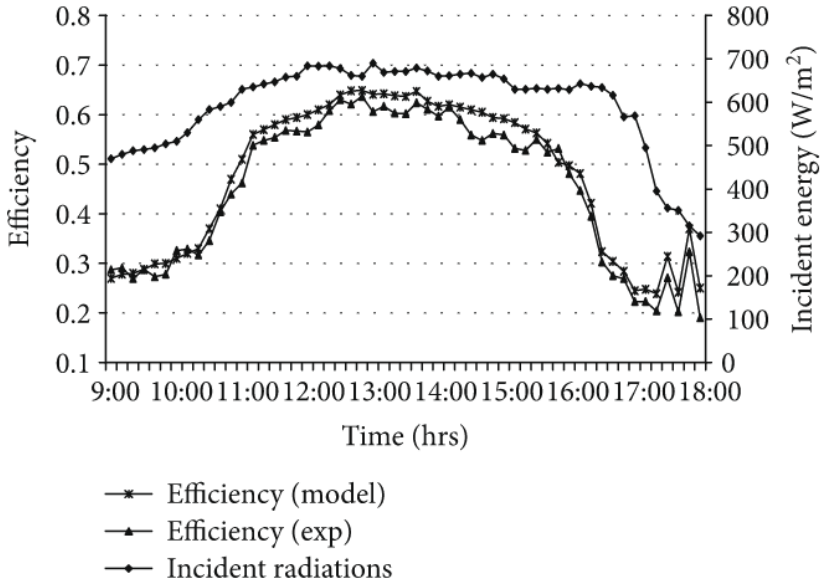

Figure 6: Effect that the time of day has on the efficiency of a PTC reported by Chaudhary et al. (2018)

In order to better represent the impact of the reflector geometry and to put into context the reported heat flux distribution of the literature reported here, a series of ray-trace simulations were conducted as part of the current study. Figure 7 shows a SolTrace investigation done on a PTC with an aperture of 5.7 m. The focal lengths and rim angles vary between two limiting cases of 0° and 90°. As the rim

angle increases, the heat distribution is more effectively spread over the bottom half of the tube. Figure 8 displays a similar SolTrace investigation on four distinct existing PTC geometries. The Sky Trough has a larger aperture than the LS-3 and ENEA PTC's and the heat flux that is applied onto the tube is more than what is seen on the latter. The details of these cases are displayed in Table 5. An increase in the aperture of a PTC causes an increase in the heat flux that is effectively focused onto the tube. Playing around with the geometric parameters of the PTC different heat flux distributions can be affected, however, the limiting case is such that the heat flux is concentrated at the bottom of the absorbed tube.

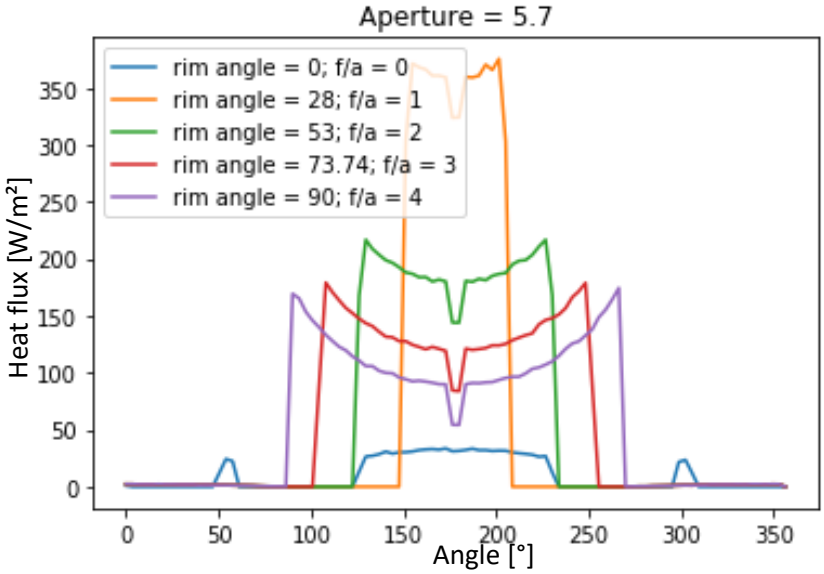

Figure 7: Effect of geometric alterations of PTC on the heat flux distribution on an absorber tube wall

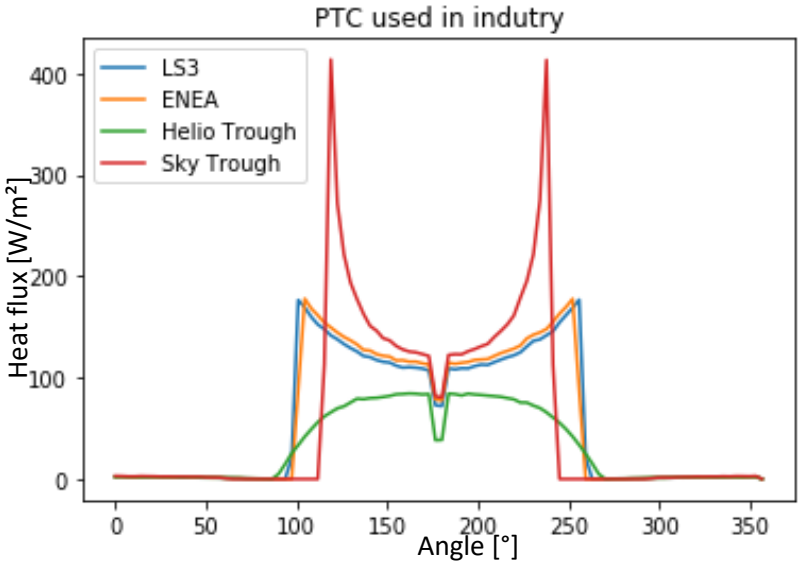

Figure 8: Heat flux distribution around an absorber tube when different PTC geometries are used

Table 5: Geometric data on different PTC reflectors used for heat flux distribution determination

Description	LS-3	ENEA	Helio Trough	Sky Trough
Aperture [m]	5.76	5.76	6.77	6
Module length [m]	12	12.5	19.1	14
Rim angle [°]	80	77	89.5	82.5
Focal length [m]	1.71	1.8	1.71	1.71
Absorber tube diameter [m]	0.07	0.07	0.09	0.08

The key to an effective heat flux concentration of solar rays onto an absorber tube, lies in the ability of the PTC to accurately capture the solar rays. This is done through solar tracking. When there are errors in the tracking, the effective heat flux applied onto the absorber tube is directly impacted. Presented in Figure 9 is two cases in which the power distribution (heat flux distribution) is changed due to tracking errors. As can be seen in Figure 9a, the heat flux distribution magnitude is affected by longitudinal angle (meaning the length of the tube) tracking errors, while in Figure 9b transverse angle (meaning the width of the tube) tracking errors changes the distribution profile. It can be seen that the power flux is reduced when the tube does not line up in the north-south orientation as the sun moves east to west (Figure 9a), and when the PTC is not positioned at an angle to capture as much as possible of the sun's rays (Figure 9b). The angle of the sun to the PTC reflector greatly impacts the distribution of the power flux on the tube. Investigating the HTC implications of this may be useful.

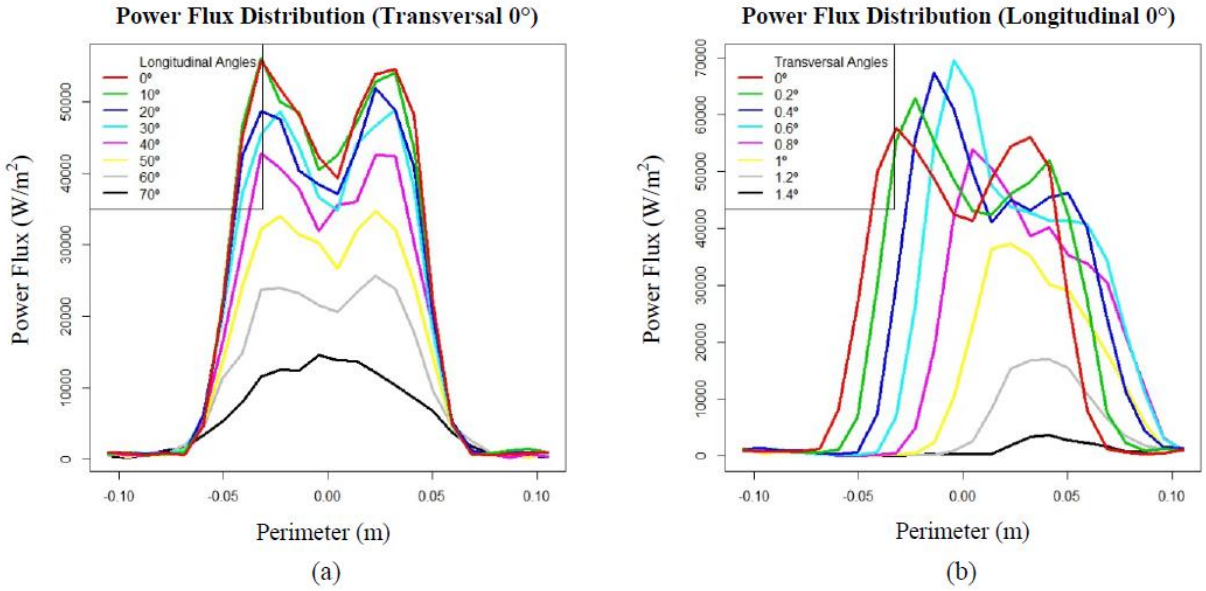

Figure 9: View of the heat flux distribution seen at (a) different longitudinal angles and (b) different transversal angles. (Sallaberry et al., 2018)

2.6 Effect of non-uniform heat flux on the fluid

A non-uniform heat flux on a single-phase fluid can induce natural convection within the absorber tube, which causes vortices to appear in the cross section. This secondary flow caused by a non-uniform heat flux boundary condition has been captured in numerical simulations done by Li *et al.* (2016) and an experimental investigation done by Lin and Lin (1996b), and can be seen in Figure 10 and Figure 11. When looking at Figure 10, the secondary flow patterns can be seen in the streamlines and arrows that form two vortices in the tube. Similarly, in Figure 11 the vortices that are developed in the channel can be seen by the arrows. In both these figures, the highest velocity flow is at the point where the vortex midpoints are adjacent to one another and the tube wall. From this it can be deduced that where the heat flux is higher, a density difference is established in the fluid, causing the fluid to churn in the vertical direction, though the bulk fluid flow is horizontal. This then constitutes a secondary flow pattern. This has the potential to greatly impact the heat transfer in the fluid (Wang *et al.*, 2017).

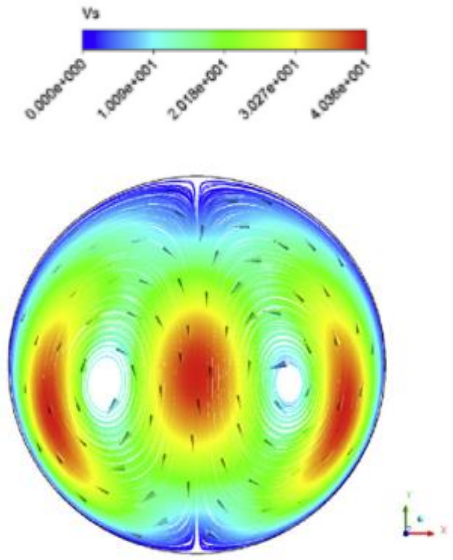

Figure 10: Secondary flow pattern caused by a non-uniform heat flux with a higher heat flux at the bottom of the tube (Li et al., 2016)

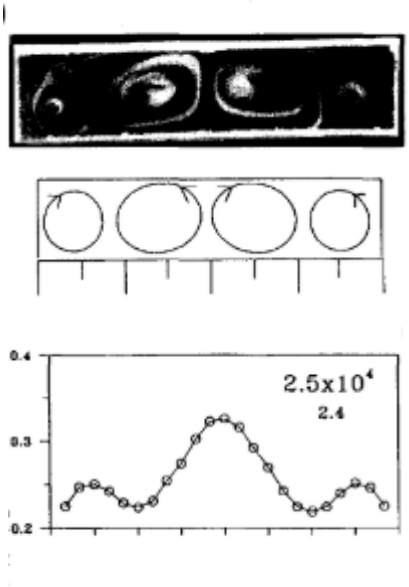

Figure 11: Secondary flows created by non-uniform heat flux boundary condition at the bottom of a rectangular tube (Lin and Lin, 1996a)

From the numerical studies done by Li *et al*. (2015, 2016) on non-uniform heating of a horizontal single-phase flow it was found that the Nusselt number of the fluid was higher than the uniform case when the heat flux applied on the tube was a maximum at the bottom. This was true for the turbulent regime and fully developed laminar flow. In the laminar flow case, a secondary flow pattern was seen, as indicated in Figure 10. It is mentioned that an attempt to quantify the flow through a non-uniformly heated tube by an approximation of forced convection would not achieve the same results.

Experimental investigations into the effect that non-uniform heat flux boundary would have on the heat transfer of a fluid flowing through a tube have been done on a wide range of cases. These include multiple vertical tubes under non-uniform heating (Hao *et al.*, 2016), horizontal rectangular tubes (Lin and Lin, 1996b), horizontal trapezoidal channels (Remley *et al.*, 2001) and horizontal smooth tubes (Dirker *et al.*, 2018, Wang *et al.*, 2019). In each of these investigations, the characteristics of the flow under non-uniform heat flux boundary condition were very different from the characteristics achieved when a uniform heat flux boundary condition was imposed. The HTC's expected, as predicted by aforementioned correlations created on uniformly heated sections, were systematically erroneous. This gives rise to the idea that non-uniform heat flux applied to the boundary of a flow may reliably alter the HTC of the flow.

An increase in heat flux results in an increase of the HTC in the vapour quality region where nucleate boiling dominates, when the flow is in the mass flux region of between 100 – 400 kg/m^{2}s (Greco, 2008, Kundu *et al.*, 2014b, Manavela Chiapero *et al.*, 2014, Wang *et al.*, 2019). According to Greco (2008), at higher qualities (qualities >30%) the effect of the heat flux on the HTC is negligible, however a contrary result was seen by Wang *et al.* (2019). In this most recent non-uniform heat flux flow boiling experimental study, the HTC was consistently higher with high heat fluxes, until dry-out occurred. The difference may lie in the uniformity of the heating boundary.

The most recent experimental study done by Wang *et al.* (2019) on non-uniform heat flux flow boiling, could be of great significance to the current work. A study was done on the effect of circumferentially non-uniform heat flux on the flow patterns and overall heat transfer coefficient of R245FA as it undergoes flow boiling at saturation temperatures of 40 °C and 60 °C and mass fluxes between

193 kg/m²s and 386 kg/m²s. The suggested application for this study was DSG in PTC utilising organic working fluids.

The experimental setup was such that a stainless-steel tube, with a 10 mm diameter, would be heated by four heating segments utilising the Joule effect. The non-uniformity of the heat flux was established by heating with the bottom two heating segments only. Further details on the experimental setup are elaborated upon in Section 6.2.

The effect of the non-uniform heat flux on the flow patterns of the fluid was found to be considerable. If the heat addition to the fluid was the same for a uniform and non-unform heat flux distribution, the transition point between intermittent and annular flow patterns altered, with the transition for the non-uniform case being higher than the uniform counterpart. It was also found that nucleation site formation was much easier in the non-uniform cases and the contribution of nucleate boiling to the HTC of the fluid is more prominent than previously assumed.

The HTC for the fluid as it was heated from the bottom was determine, however, not compared to a uniform heat flux counterpart. The influence of mass flux and saturation temperature alterations were investigated to determine if there were any discrepancies introduced by the non-uniformity of the heat flux. It was found that with an increase in mass flux an increase in the HTC is seen, and dry-out is not affected. An increase in the saturation temperature also yielded higher HTC's. A correlation was suggested to predict the HTC for non-uniform heating cases and had a 20 % margin of error in its accuracy for the data sets it was developed on.

The results in this study is used as a validation tool in Section 6.2, and therein is further elaborated on the similarities and differences between this study and that done by Wang *et al.* (2019).

2.7 Pressure Considerations

2.7.1 Saturation pressure

The effect that saturation pressure has on the HTC of a fluid was studied by among others Balachander *et al.* (2011) and Greco (2008). These authors reported similar conclusions. At low saturation pressures the HTC is proportional to the pressure, due to the effects of the vapor density and the mechanism changes of convective and nucleate boiling. At high mass fluxes and relatively high saturation pressures the HTC is inversely proportional to the pressure.

2.7.2 Pressure drop

When flow undergoes a phase change from liquid to vapour, a pressure drop in the flow is inevitable. This can be explained by a velocity increase exhibited by the fluid as it changes phase to the vapour phase.

The total pressure drop of a fluid is due to a variation of potential and kinetic energy of the fluid and captured by three distinctly different quantities: static pressure change, momentum pressure change, and pressure drop due to friction. A detailed review of the literature regarding these quantities and their interplays can be found in the report by Sardeshpande and Ranade (2013). The pressure drop over a section experiencing phase change has been investigated widely as part of flow characterization by, among others, Dirker *et al.* (2014), Ould Didi *et al.* (2002), Manavela Chiapero *et al.* (2014) and Hamersma and Hart (1987). Reported by Ould Didi *et al.* (2002) was a relation of the pressure drop measured on an experimental setup and the correlations proposed by five others. The best correlation for pressure drop prediction was then defined.

The physical phase change that the boiling fluid undergoes, influences the pressure drop over the section in question immensely. As presented in Grauso *et al.* (2013), the pressure drop is influenced by the mass flux, vapour quality, and the saturation temperatures. As the mass flux increases, so too

does the pressure drop. The pressure drop decreases with an increase in saturation temperature. The effect of the mass flux alteration is more significant than that seen due to saturation temperature alteration. The velocity of the fluid therefore has a larger influence on the pressure drop than the state at which boiling occurs.

The pressure drop increases with an increase in vapour quality. The highest pressure drop seen in experiments always precede dry-out. The pressure drop is low when slug flow is prevalent. As the flow develops to intermittent and annular flow the pressure drop increases, however, it cannot be concluded that the pressure drop in the latter is constant over all vapour qualities in this regime. As the vapour quality increases, so too does the pressure drop. The relation between vapour quality increase and pressure drop increase is mostly linear for vapour qualities below 0.6, generally. As the vapour quality increases above 0.6, the pressure drop curve flattens. This flattening is always present in the annular flow regime.

As the flow patterns are related to vapour quality, and the pressure drop seen in investigations always alter with vapour quality changes, the pressure drop range seen in a certain flow pattern can be deduced. It should however be noted that the pressure drop is more closely related to vapour quality changes than to flow patterns, and the inference of pressure drop by flow pattern may turn out to be erroneous.

The frictional pressure drop correlation presented in Lazarek and Black (1982) also concludes that the highest pressure drop is achieved at the vapour quality directly preceding dry-out, and at vapour qualities corresponding to annular flow a flattening of the pressure drop curve occurs.

The detailed consideration of the causes of pressure drop is outside the scope of this investigation. Quantitatively capturing the total pressure drop over the test section is sufficient for comparison with literature.

2.8 Summary

This chapter presented a discussion on the applications in DSG that the investigation on non-uniform heat flux flow boiling may have by considering the industrial applications being utilized in the world. The fluid dynamics that are of importance were mentioned, and the properties that influence these dynamics were discussed. These included geometric considerations (channel size and orientation), flow patterns, heat flux distributions and the role of pressure in the investigation.

Past studies were consulted in the isolation of possible heat transfer correlations that may be used for validation and in a comparative study. Few investigations have been done on non-uniform heat flux boiling of flow in conventional horizontal channels, but all have yielded HTC’s different from predicted values.

3 Experimental Setup

This chapter presents details on the experimental setup that was used in this investigation. This includes the build and operation of the facility, followed by the build and operation of the test section. A circuit for the control of the non-uniform heating required over the test section is also described. This is followed by the experimental operation of the plant, paying attention to measurements taken, work procedure and the test cases that were considered.

3.1 Facility

The facility located in the thermal fluid laboratory at the University of Pretoria was designed, built and validated by Van den Bergh *et al.* (2019). It is represented schematically in Figure 12 in which measurement stations and major components are indicated.

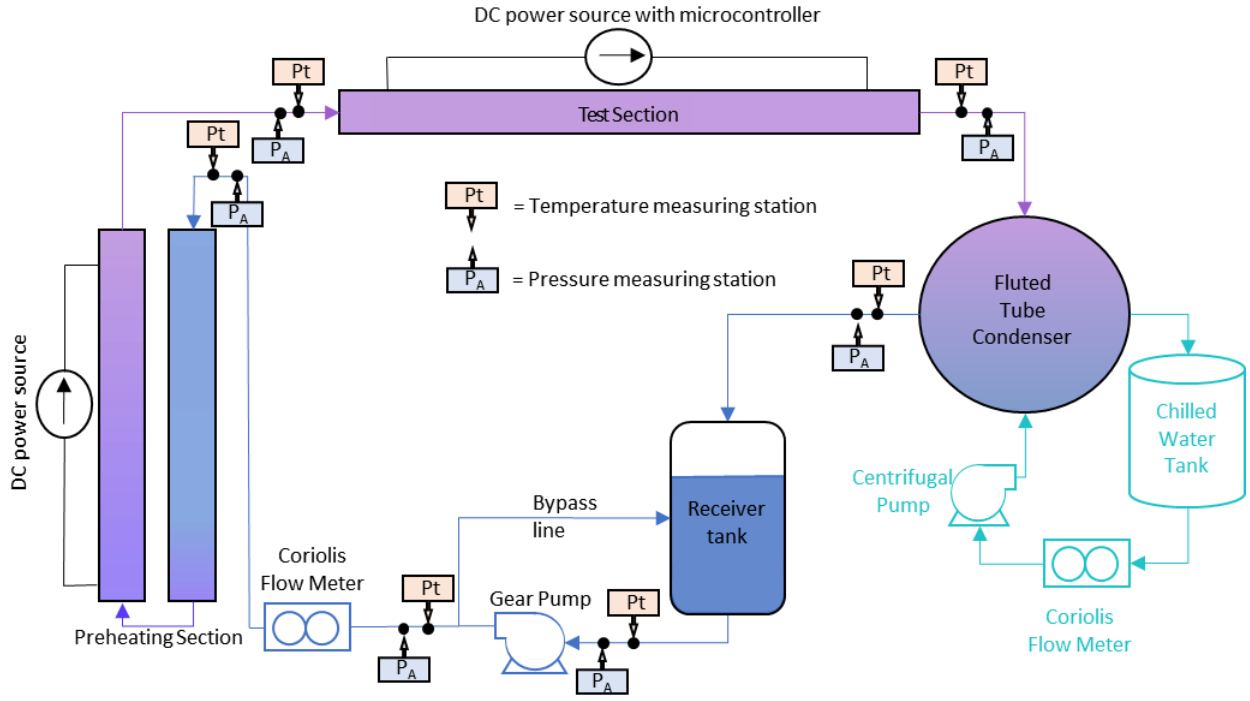

Figure 12: Schematic of test facility, designed and built by Van den Bergh et al. (2019)

The set-up consisted of a closed loop system, with R245FA as the working fluid. The bulk of the fluid was held at a saturated state in an 18-liter GVN™ receiver tank. The tank was elevated to provide a net positive suction head of 3 m to the gear pump, and to ensure that only liquid was supplied to the rest of the flow loop. The fluid passed through a filter drier before entering a Gather P90090 gear pump. This pump was specified to handle a maximum system pressure of 60 bar, a maximum differential pressure of 20 bar and had the capability to produce flow rates between 14.4 l/h and 540 l/h.

A bypass line was present at the outlet of the gear pump and allowed direct fluid return into the receiver tank. The flow through this line was controlled by a needle valve and was used to help regulate flow through the main testing line if needed, particularly for cases which required a flow rate much lower than the rated flow rate range of the gear pump. The flow rate in the test line was measured by a Micromotion™ CMF010 Coriolis mass flow meter with a maximum flow measuring capacity of 0.04 kg/s at an accuracy of 0.1%.

The thermal and pressure conditions of the fluid was adjusted by using preheating sections. For this purpose, two 1.9 m-long sections were employed which consisted of copper tubes with a 12.7 mm outer diameter and an inner diameter of 11 mm. Constantan heating wires with a diameter 0.38 mm and a resistance of 35 Ω each were coiled tightly around these tubes such that they could be powered separately by two Elektro-Automatik™ EA-8360-30 DC power supplies, capable of a maximum output of 3000 W or 360 V and 30 A at a 0.05 % accuracy on the output voltage or current. Insulation, with a thickness of 80 mm and a thermal conductivity of 0.036 W/mK, was wrapped around the preheater section to reduce heat losses to the environment.

The fluid exiting the preheater was channelled through a high-pressure flexible hose to a calming section. The flexible hose was insulated similarly to the preheater and was introduced into the system to establish modularity in the facility set-up, making it possible to lengthen the calming section, introduce sight glasses or have longer test sections, without introducing strain on the existing facility infrastructure. The flexible hose was connected to the calming section with stainless-steel flare fittings from Swagelok™.

Ahead of the test section, an adiabatic straight calming section with a length of 0.5 m and an inner diameter of 8.5 mm was used to dampen the flow pattern interference of the upstream components and bends in the flow path. The length was based on guidelines from literature (Cho and Tae, 2001) to be at least ten times longer than the diameter of the test section (at least 85 mm).

The fluid was passed through the test section where it was electrically heated by an Elektro-Automatik™ EA-8360-15 DC power supply, capable of a maximum output of 1500 W or 360 V and 15 A at a 0.05 % accuracy on the output voltage or current. Similar insulation as mentioned before was wrapped around the test section to reduce heat losses to the environment. More information on the test section construction and operation is contained in Section 3.2.

After the test section the fluid passed through a fluted tube-in-tube condenser by Turbotec™ (BTSCC-72) with a maximum rating of 72 kW which was used to remove heat from the fluid and to return it to the desired liquid state. The condenser was serviced by water at approximately 6 °C that was supplied by a large capacity external chiller system. The water was pumped by an Ebara™ 90 centrifugal pump, with a maximum flow rate capacity of 90 l/min. The mass flow rate of the water was controlled using a three-way valve, which is interfaced with the data acquisition and control system (discussed later). The mass flow rate of the water was measured by a Micromotion™ CMF025 Coriolis flow meter with a maximum measurement capacity of 0.4 kg/s with an accuracy of 0.1%. T-type thermocouples were used to monitor the inlet and outlet temperatures of the water.

The state of the fluid as it moved through the facility was monitored through temperature and pressure measurements taken at six points throughout the system to aid in checking the energy balance over the system. These points are indicated in Figure 12 and marked by “Pt” and “P_A” symbols which are associated with respectively temperature and pressure measuring probe locations. The temperatures at the inlet and outlet of the test section was measured by two Pt100 resistance temperature detectors (RTD’s). At the outlet of the condenser, inlet of the pump, outlet of the pump and inlet of the preheater the temperature was measured by four T-type thermocouples attached to the top, bottom, and sides of the outer wall of the tube at the measurement point, resulting in 16 T-type thermocouples used. The thermocouples were secured with 3M™ Aluminum Foil Tape 425, which could be moved as required, for facility modularity, yet were secure during operation. Pressure values were measured by absolute pressure transducers, calibrated externally through WIKA® (a supplier and calibrator of a wide range of calibration instruments for the measurement of pressure and temperature). The uncertainty associated with the measured pressures ranged between 1.05 % and 1.6 %.

3.2 Test section

The test section and its control circuitry were designed, constructed, and commissioned during this study by the candidate and was developed to apply various circumferential heat flux distributions onto the test tube. A schematic representation of the test section is given in Figure 13. It consisted of a 316/316L stainless-steel tube (thermal conductivity of k_{SS} = 16.5 W/mK) and had a heated length of 900 mm (L_h), an inner diameter of 8.48 mm (D_i), an outer diameter of 12.7 mm (D_o) and a wall thickness of 2.11 mm (t_{SS}). The inner diameter was the same as the inner diameter of the copper tube used in the calming section. Quick release face seal Swagelok™ fittings were used to reduce flow disturbance at the connection point of the stainless-steel tube onto the existing tubing. The fittings resulted in a leak proof connection that can be changed easily, aiding in the modularity of the facility.

The inner diameter was chosen such that the validation conditions of the facility were met with this modular expansion of the test facility operation. Further, the data available for the refrigerant at the time of this study included works on tube diameters similar to the selected size. Finally, the intension of the current study was to establish the relation between the heat flux distribution and the heat transfer performance qualitatively and did not necessitate the tube's inner diameter being comparable to industry applications directly. Further work on this study could be repeated on tube diameters more suited to direct industry application.

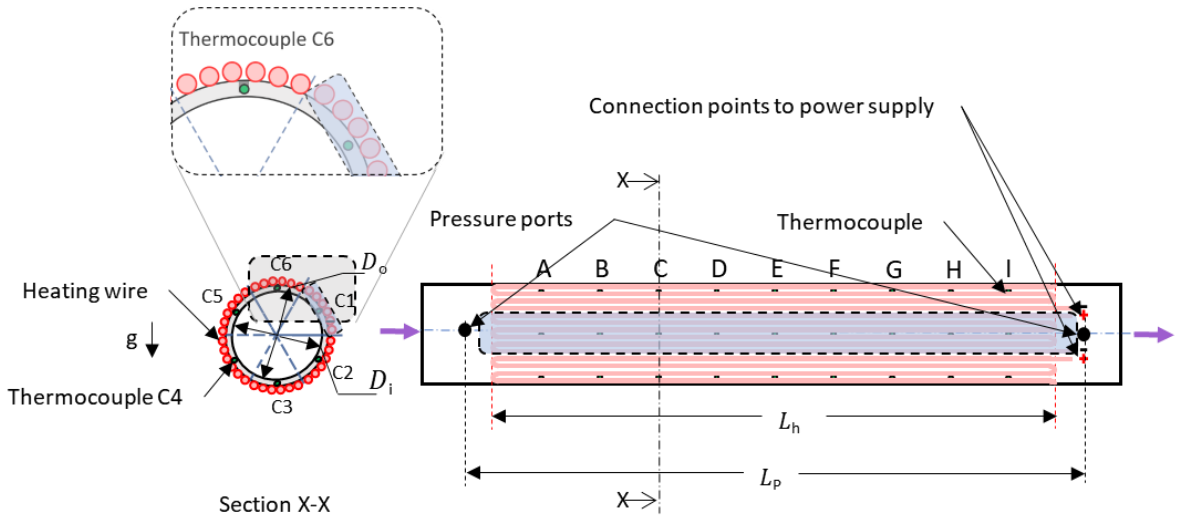

Figure 13: Schematic representation of the test section that was used during investigation

The selection of material for the test section tube was done such that the non-uniformity of the imposed heat flux, which had to be applied on the external surface, could be transferred to the inner wetted surface of the tube. A numerical analysis (documented in detail in Appendix A) of the conduction heat transfer in the tube wall was performed to determine the impact of selecting either stainless steel or copper as possible building materials. The parameters for the investigation are set out in Appendix A. For a typical inner wall flow boiling heat transfer convective boundary condition, the conductivity of the two materials were compared on the basis of the tangential conduction of an imposed radial heat flux. From that analysis it was found that when stainless steel is used with a non-uniform heat flux conditions, only approximately 17 % of the locally imposed radial heat flux on the outer tube wall was conducted tangentially, while for copper about 33 % of the imposed heat flux was conducted tangentially. Based on this, stainless-steel was selected as the tube wall material.

Heating wires (shown with red in Figure 13) were positioned along the length of the test section and were grouped to enable localised heating of longitudinal segments around the circumference of the

tube. The grouping consisted of six heating segments (elements) around the circumference containing six lengths of heating wire per element. For reference purposes the heating elements are numbered clockwise from 1 to 6, with the top segment being the element number 6, and the bottom element number 3. This numbering convention is repeated in the reference to the thermocouple positions. Each element was powered by a parallel leg controlled as described in Section 3.3. The choice of six elements were based on the realisable heating control method, described in Section 3.3, which was based on a microcontroller capable of accommodating 6 output channels. This practical consideration was a dominant factor which influenced the selection of the resolution of heating segments around the tube circumference. More heating element around the circumference would have been preferred but could not be accommodated at this stage of the investigation. The maximum number of wire lengths that could comfortably be accommodated geometrically around the tube was 36. Therefore, the six heating elements consisted of six lengths of heating wire positioned longitudinally onto the stainless-steel tube. One such a grouping is indicated in Figure 13 by the blue shaded region. The six groupings allowed controllable and semi-localised uniform heat flux to be applied by heating an element along the entire length of the test tube. The heating wires were evenly spaced around the circumference and at centre-to-centre 1.1 mm apart. The heating elements were constructed from 0.38 mm diameter constantan wire which was coated with 0.2 mm thick PFA insulation with a thermal conductivity of 0.25 W/mK. The constantan wire had an electric resistance of 4.1 Ω/m and a thermal conductivity of 11.3 W/mK. Each of the heating elements had an electrical resistance (±0.1 Ω) as is summarised in Table 6. The resistance measurements were taken while the elements were not powered, and the fluid flowing through the tube was at ambient conditions, 26.5 °C, 165 kPa.

Table 6: Resistance values for the heating elements around the circumference of the tube

Element number	Resistance	Unit
R_1	21.4 (±0.1)	Ω
R_2	20.8 (±0.1)	Ω
R_3	21.0 (±0.1)	Ω
R_4	20.6 (±0.1)	Ω
R_5	21.0 (±0.1)	Ω
R_6	21.1 (±0.1)	Ω

Thermal contact between the heating elements and the outer surface of the test section was maintained by tightly wrapping Kapton tape around the heating wires. The Kapton tape had a thermal conductivity of approximately 2 W/mK (Benford *et al.*, 1999) and a peak operating temperature of 260 °C. In addition to the Kapton tape, AT10 PVC heavy duty pipe-wrap tape was also applied around the test section along its entire heating length and secured with cable ties positioned 8 mm apart. Insulation, with a thickness of 80 mm and a thermal conductivity of 0.036 W/mK, was wrapped around the test section to reduce heat losses to the environment.

T-type thermocouples were positioned around the circumference of the tube to monitor the tube wall temperature along the length of each heating element. For each heating element a set of 9 thermocouples that were spaced equidistantly at intervals (z_{m}) of 100 mm (±0.05 mm) along the heated length was used. A numbering scheme was adopted to represent the axial location temperature measurement from the inlet to the outlet of the test section using letters A to I as indicated in Figure 13. For instance, measurement location C5 referred to axial location C at the circumferential heating segment number 5.

This resulted in 54 measuring points in total. The thermocouples were positioned in the midway across the tangential width of the heated segments and were embedded into the tube wall. For this purpose, 1.5 mm diameter holes were drilled to a depth of 1mm (±0.05 mm) into the stainless-steel tube with

a vertical milling and drilling machine. An example of an actual thermocouple installation is shown in Figure 14, which is a photograph of heating wires positioned around the stainless-steel tube, with thermocouples attached with thermal adhesive, prior to wrapping with Kapton tape and insulation. The thermocouple which had a measuring tip diameter of 1 mm was placed into each hole and kept in location with an Araldite™ epoxy adhesive (2014-2).

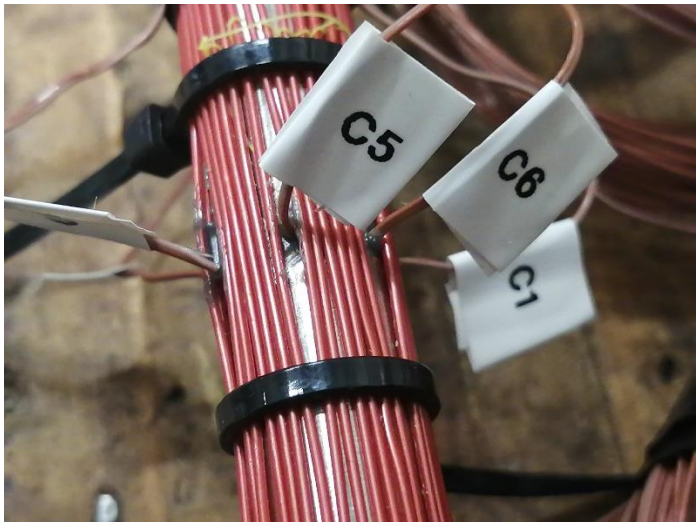

Figure 14: Photograph of heating wires and thermocouple placement around the test section

Two Pt100 RTD's were positioned at the inlet and outlet of the test section, submerged into the fluid. These were used as the reference temperatures to which the test section T-type thermocouples were calibrated (Section 4.1.2) and the source for the calculation of the bulk fluid temperature. The accuracy of the RTD's was 0.06 °C. In addition to the thermocouples on the test section wall, twelve T-type thermocouples were positioned in the insulation around the test section, at a radial distance of 19.5 mm apart, such that the heat loss through the insulation could be determined for each heating segment. Six were positioned closer to the test section tube, and six radially further from the tube. All these thermocouples were placed at the center of a test segment in the axial direction.

Two pressure ports were installed on the stainless-steel tube, before and after the heating section at a distance of 1 m (L_{p}) apart as indicated in Figure 13. The ports were constructed by drilling 0.5 mm holes through the tube wall and then silver soldering 6.5 mm outer diameter, 4 mm inner diameter copper tubes over the holes. The ports were orientated horizontally on the test section. Swagelok™ quick release ferule fittings were used to connect the test tube to a pressure measuring station. The pressure over the test section was measured with two different methods. The first consisted of absolute pressure transducers, placed at the inlet and outlet of the test section. The absolute pressure transducers had accuracies of between 1.05 % and 1.6 %. The difference obtained in this measurement was compared to the second method of pressure measurement. This consisted of a differential pressure transducer capturing the pressure drop over the test section directly during operation. The differential pressure meter that was used was a Validyne™ DP15 with a diaphragm capable of measuring a differential pressure of up to 14 kPa, with an accuracy of 0.5% of the full scale. This diaphragm was connected in a pressure measurement station parallel to the test section.

3.3 Control circuit

The heating of the test section was controlled by a custom-built circuit. Each heating segment around the circumference of the tube was independently controlled by a pulse width modulation (PWM) pin on an Arduino® UNO microcontroller. This reduced losses, ensured that electric overload of the system did not occur, and increased the accuracy of control.

Each heating wire was electrically connected through a series of NPN transistors to a PWM pin on the Arduino Uno. The microcontroller board had 6 PWM pins. The connection was done such that low side switching occurred. This method is beneficial because a high side switch had a lower electric current capability (as there is more resistance in a P-Type transistor) than a low side switch (Lewis, 2019), and a higher current capability was required in this application.

The low side switch (shown in Figure 15) was connected in such a way that the PWM pin of the UNO powered a Darlington TIP120 transistor as a pre-driver to a higher rated power transistor. The current required in the heating segments was too large for a TIP120 (maximum current 1 A) to carry, and the TIP120 provided the required current gain and voltage isolation for the NPN 2N3055 power transistor (Loflin, 2018). The required switching current of the Darlington transistors was 20 to 40 mA, while that of the power transistors were 500 mA. The power transistors were rated to carry electric current up to 15 A at 60 V.

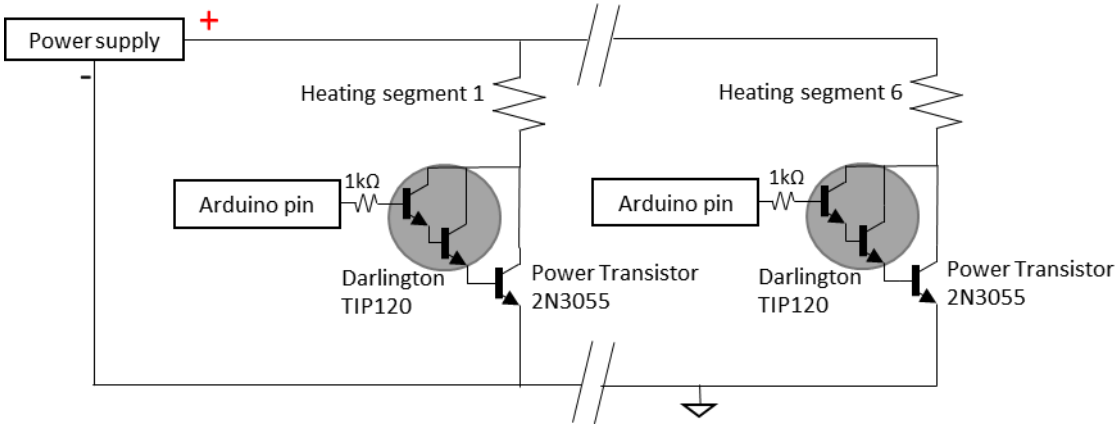

Figure 15: A schematic of the control circuit indicating the parallel connections

Each parallel leg of the control circuit was to function independently from the others. The control exerted through a PWM signal was mainly done by the manipulation of the on-off time for the maximum peak-to-peak output setting, by changing the duty cycle. The duty cycle setting on a PWM pin, coded onto the microcontroller, was the percentage of time that the signal was to be on. When the peak-to-peak output voltage of V_{PP} is set, with a duty cycle of C_{dc}, the effective root mean squared (RMS) voltage (V_{RMS}) can be expressed as follows:

$$V_{\mathrm{RMS}} = \sqrt{C_{\mathrm{dc}} \times V_{\mathrm{PP}}^2} \tag{9}$$

Verification of the control circuitry was done and described in Section 4.3. The expected duty cycle was compared to the actual duty cycles achieved. Due to the nature of the duty cycle calculation, depending on integer division for the counter clocks on the microcontroller, as well as the errors introduced by the measurement frequency of the wave forms generated, the accuracy of the duty cycle imposed could be determined to be 0.5 %. During the verification of the control circuit, each channel's behaviour was considered to establish its operation. The actual square waves and duty cycles that were seen were very close to the expected operation for every heating element, behaving relatively identical. During operation, the total current (I_{tot}) and total voltage supplied over the test section heating elements were directly captured from the power supply output to the LabVIEW data acquisition interface (described in Section 3.4) that was used in this investigation.

The square waves were the main controlling factor for the heating of the test section. Transistors were switched by the duty cycles which were programmed onto the microcontroller. The transistors were mounted onto heat sinks rated to remove at 1.5 °C/W during normal operation. The power transistors

and heat sinks were housed in an aluminium enclosure, represented in Figure 16, made from sheet metal. This enclosure ensures good ventilation around the heat sinks and acted as a redundant heat sink itself. The Darlington transistors were soldered onto a stripboard, with heat sinks positioned and fastened on these transistors (see Figure 17). These transistors along with the microcontroller were positioned in a plastic box and placed in the aluminium box.

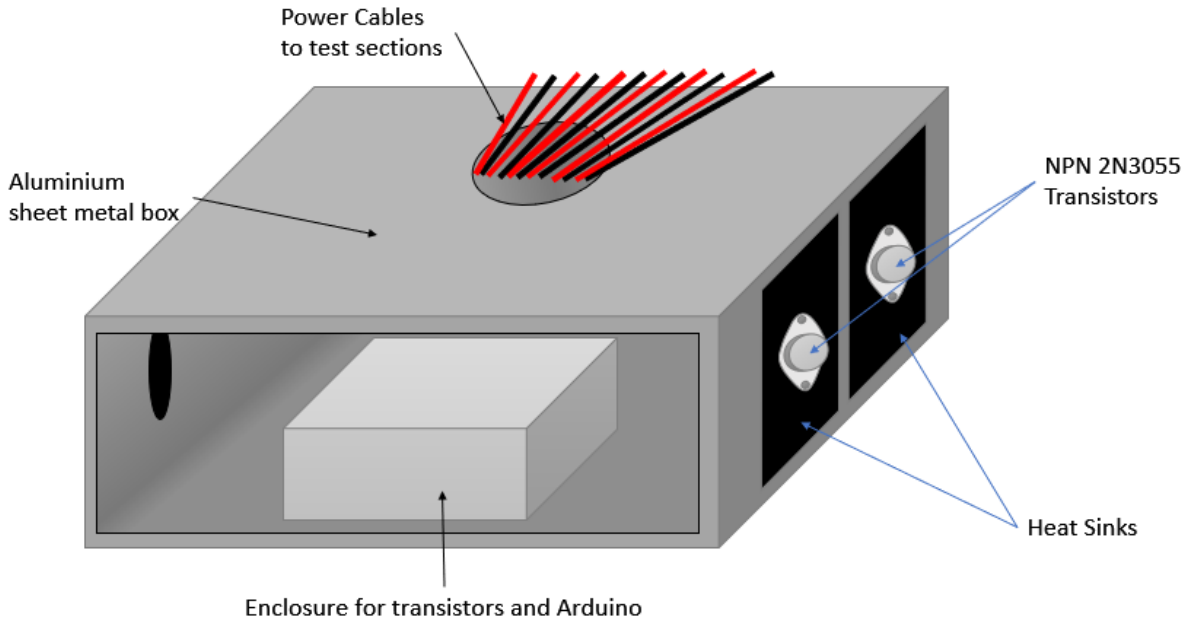

Figure 16: Schematic of aluminium box for mounting of control circuitry

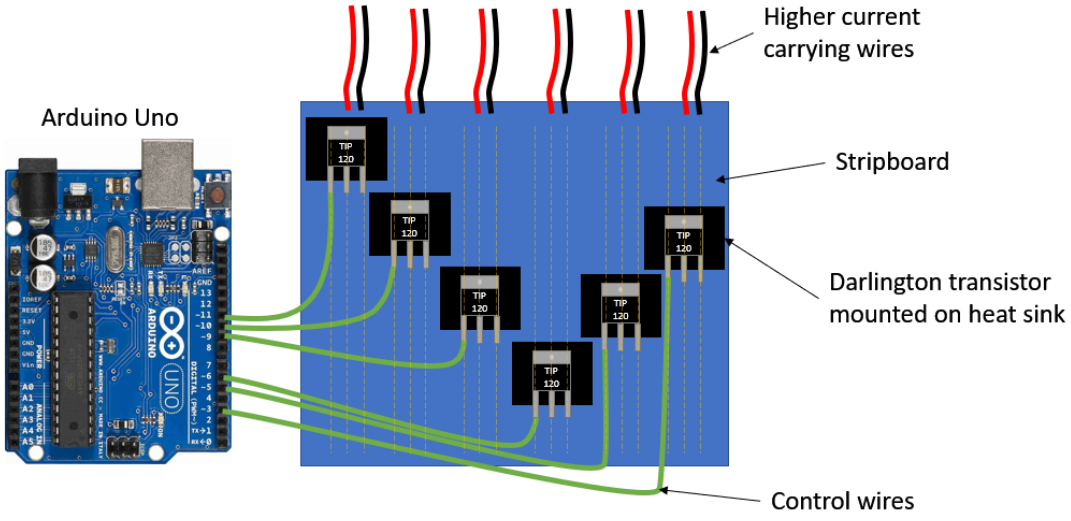

Figure 17: Schematic of stripboard with Darlington transistors and control wiring

3.4 Data logging and acquisition

All measurements were made by a National Instruments data acquisition system and interfaced with a personal computer with LabVIEW software. Each method of measurement had a dedicated input module and data card as are set out in Table 7.

Table 7: Measurement type and associated input module and data cards

Measurement instruments	Input module type	Data card type
T-type thermocouples	SCXI – 1102	SCXI – 1303
Absolute pressure transducers	SCXI – 1122	SCXI – 1322
Pt100 thermocouples	SCXI – 1503	SCXI – 1306
Validyne DP15 sensor	SCXI – 1102	SCXI – 1303
Coriolis mass flow meters	SCXI – 1100	SCXI – 1308

The communication module that was used by the data acquisition unit was a 32-bit USB connection module SCXI – 16000. Data was collected at 10 Hz intervals for 40 second per experimental test point. This resulted in 400 data points per experiment. Figure 18 displays a screenshot taken of the LabVIEW interface that was specifically developed for this study. The interface was condensed in such a way that all required monitoring information could be seen on a single window. Firstly, the test section thermocouples readings were displayed in the centre largest graphic area, when looking at Figure 18. To the left of this graph, the pressure drop measured directly was displayed. Below that was the representation of the mass flux of the refrigerant through the facility, calculated continually from the measured mass flux. At the top ribbon of the screen, the data handling interface was positioned, where the output files were managed, by the number of data points captured, and setting of the frequency at which data was logged. A representation of the facility similar to that illustrated in Figure 12 is integrated onto the screen and positioned in between the graphs mentioned previously. Here, the temperature and pressure measurements were displayed in a way similar to Figure 12. At the lower left corner, the energy balance of the system was displayed, and at the top right of the window the heat loss over the test section was continually calculated. Finally, on the left upper corner, the power supplies were controlled by selecting the wattage output required of each power supply. The power supply control was integrated with the LabVIEW system. Over the test section, continual calculations were run, using the CoolProp (Bell et al., 2014) wrapper for Python, interfaced with LabVIEW, to display the inlet and exit quality over the test section, as well as to determine the state at each measurement point. It could be determined directly from this screen whether two-phase flow was present at any point in the flow loop.

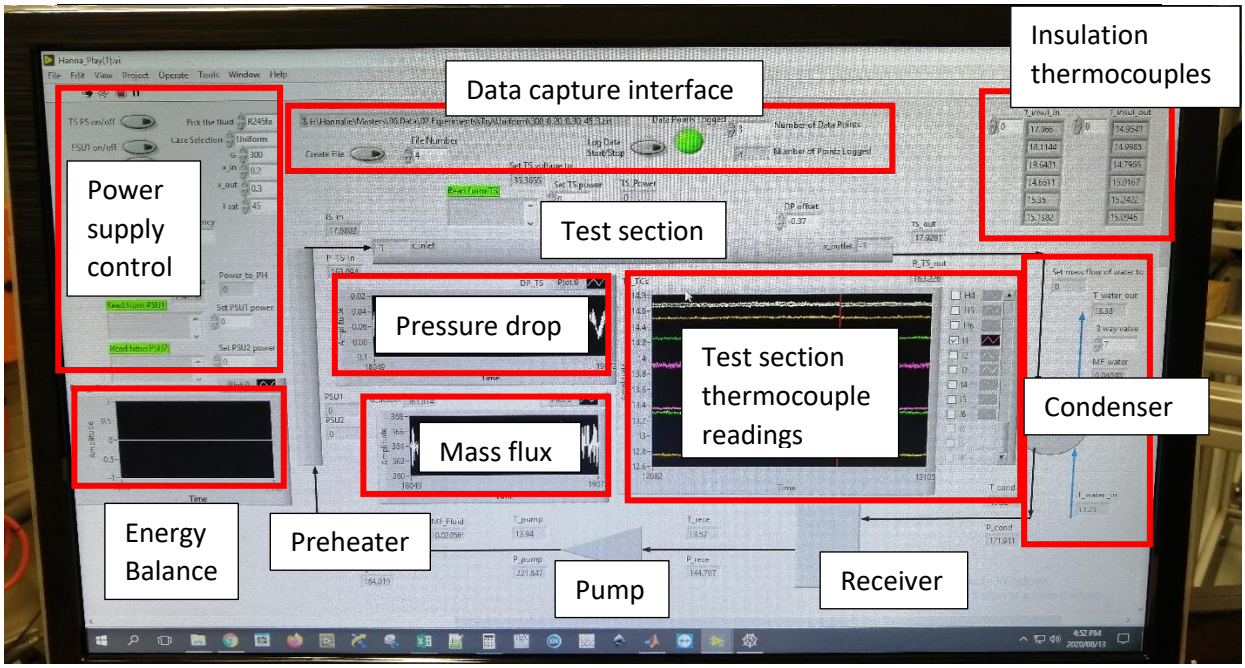

Figure 18: Screenshot of LabVIEW interface developed for this study

3.5 Summary

In this chapter the experimental setup used for the non-uniform heat flux flow boiling investigation was described. It included the build and operation of the facility, followed by the build and operation of the test section. The control circuit for the heating elements were then described, which would establish the non-uniformity in the heat flux applied over the test section tube. Finally, the interface used to control and monitor the plant was displayed and described.

In the following chapter, the experimental procedure follows. This chapter focuses on the calibration of the measurement instruments, the commissioning of the facility, the verification of the control circuit, the selection of the heat flux distributions to be used, and the test matrix and testing procedure.

4 Experimental procedure

In this chapter the calibration of the measurement instruments is described, followed by the commissioning of the facility and the verification of the control circuit. Then the heat flux distributions that were used are presented, followed by the complete test matrix and the experimental procedure. The repeatability of the experiments is addressed at the end of this chapter.

4.1 Calibration

During the testing phase, there were multiple controlling and monitoring considerations to keep track of. The accuracy and precision of the monitoring equipment were required to be as good as possible under the operating circumstances. The absolute pressure transducers, differential pressure transducers, mass flow meters and thermocouples had to be calibrated to increase the accuracy of all the readings taken. The absolute pressure transducers, Coriolis mass flow meters and RTD's were externally calibrated. The two subsections that follow focus mainly on the calibration of the differential pressure transducer and of the calibration of the facility and test section T-type thermocouples.

4.1.1 Differential pressure transducer

The differential pressure transducer was calibrated manually, by establishing the upper and lower limits of operation and zeroing the measurement apparatus. This established a gradient according to which the milli-amperage readings were adjusted to kilopascal readings. The offset of these readings was determined daily, as the diaphragm in the differential pressure transducer would have been deformed by latent pressures of the previous day's operation. The pressure transducer needed to be calibrated *in situ*, as the physical connector points and tightness of the attachments used would alter the calibration of the diaphragm.

4.1.2 T-type thermocouples

Two distinctly different calibration operations were performed depending on whether the thermocouples were on the test section or not. Based on this, the thermocouples were separated into two groups. The first consisted of the 16 T-type thermocouples (discussed in Section 3.1) that were positioned around the facility at the stated measuring stations. The second group contained the 54 T-type thermocouples that were attached to the test section using thermal adhesive into the tube walls, as described in Section 3.2. The facility thermocouples could be calibrated in a thermal bath, however, the test section thermocouples needed to be calibrated *in situ*, as the thermal adhesive would affect the calibration of the thermocouples.

The temperature measurement devices that were used to monitor the facility included two Pt100 RTD's, used at the inlet and outlet of the test section and 16 T-type thermocouples positioned at four measurement stations set out previously in Figure 12. Calibration of these devices was done by submerging the probes into a Lauda Proline thermal bath at set temperatures, and referencing these readings to a Lauda DCS2 DigiCal digital thermometer as reference probe, capable of obtaining an accuracy of 0.01 °C. Seven isothermal set points were selected over the expected operating range of the thermocouples between 15 °C and 45 °C. The temperature range was captured in both heating and cooling cycles. Data capture was done during steady state conditions (once the digital thermometer feedback did not vary by 0.01 °C for 5 minutes) over 40 seconds, which resulted in 400 data point recordings per temperature.

The thermocouples that were installed onto the test section were calibrated *in situ*, during steady state isothermal single-phase flow in the liquid region at high mass flow rate which guaranteed turbulent flow conditions in the test section. The Pt100 RTD's that were calibrated with the facility thermocouples were used as reference probes during this calibration operation. The calibration was

done in such a way that the preheater and condenser of the system established the required temperature of the fluid, and the difference between the readings of the Pt100s at the inlet and outlet of the test section was smaller than 0.01 °C for 8 minutes. Seven set points were used between 15 °C to 45 °C which fell within the expected operating conditions during the main experiments of this study.

A linear correction correlation (Equation (*10*)) was determined for each thermocouple and implemented continuously during experimentation to adjust the uncalibrated thermocouple readings (T_{uncal}) to more accurate readings. Finding the coefficients of the linear curve fit (m, c) was done by substituting the reference probe reading as the calibrated thermocouple value (T_{cal}). The reference probe was a digital thermometer or a Pt100, depending on the case, as described previously.

$$T_{\mathrm{cal}} = m \times T_{\mathrm{uncal}} + c \tag{10}$$

The calibration curves for all the thermocouples used on the facility can be found in Appendix B.

4.2 Facility Commissioning

The commissioning of the facility was done in the same manner as described by Van den Bergh *et al.* (2019). The facility had two valves installed after the preheater and before the condenser, to make it possible to change the test section without losing the bulk of the refrigerant already loaded into the facility.

The newly manufactured test section was inserted into the isolated test section region. The test section along with the pressure sensing station, which had all been connected, was pressurised with nitrogen to ensure that no leaks were present. The section was then depressurised. The facility was then reconnected to this isolated section by opening the valves. Since nitrogen had been used to check for leaks on the test section, there would still be surplus air in the system. This was bled out at the highest points in the system and throughout the facility in corners which could be possible collection points for bubbles. It was done every day for a week after the refrigerant had run through the complete system while no experimentation was done. Monitoring of the thermodynamic state of the system made it possible to note the point at which the facility had pure R245FA throughout. Thereafter testing commenced.

4.3 Control circuit verification

The creation of a custom-built control circuit warrants inquest into whether the appropriate and predicted function is fulfilled by the circuit. This section details this investigation.

A series of duty cycles within the expected operating range for this study was imposed on the circuit and verified with an oscilloscope. The circuit was built with a rheostat set to the expected resistance of the heating wire and used as a proxy load. Multiple duty cycles were imposed, yielding square waves that resulted in predictable effective RMS currents and voltages. The details of this verification, stating the duty cycles and power supply voltage over the load can be found in Appendix C. Figure 19 indicates square wave that was the result of a peak-to-peak voltage of 15 V switched by a PWM programmed to a duty cycle of 68.63 % over the load.

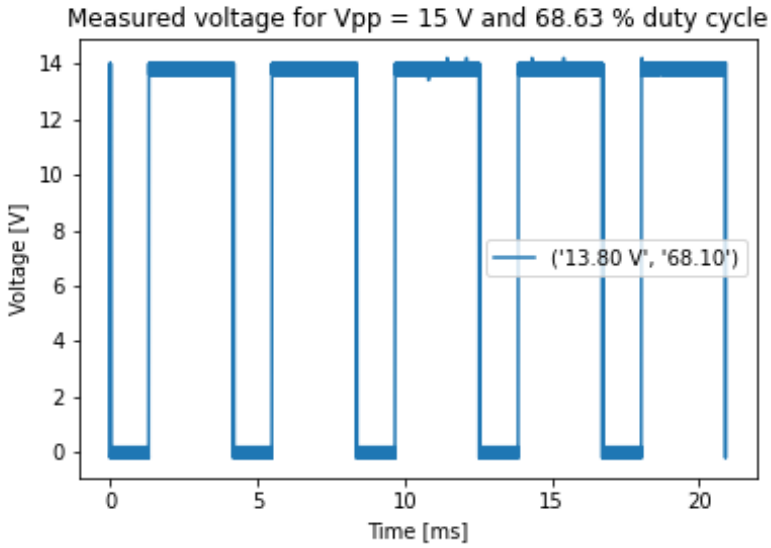

Figure 19: Validation of imposed square wave on heating wire of segment 6, maximum voltage of 15 V, duty cycle of 68.63 %

As can be seen in Figure 19, the applied voltage is not the maximum voltage that is dissipated over the load. This difference in the supplied and resulting voltages are due to losses that occur over the circuitry components during normal operation. The details pertaining to these losses need not be scrutinised for the operation of the circuitry to be quantified successfully in the current application. Seeing a square wave with a duty cycle close to or equal to that which was required, is sufficient.

There is some more useful information that can be collected from this verification, with no impact on the study, other than solidifying understanding and predictability of the system. The discrepancy in the voltage measured over the load and the voltage supplied by the DC power supply during verification was noted and a linear relation was applied to the supplied voltage to determine the effective voltage over the load, as can be seen in Figure 20. This was solely for the operator to make predictive calculations during testing and has no further implications on the study.

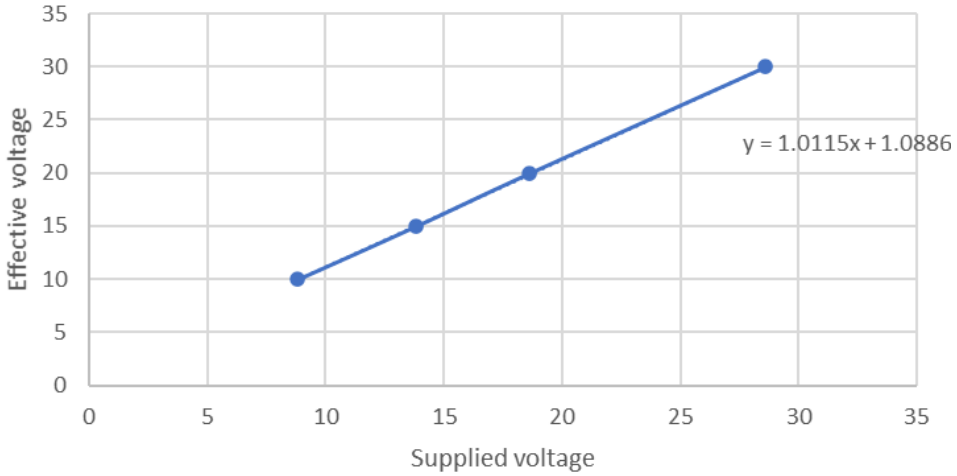

Figure 20: Linear fit between the supplied and effective peak voltage over a heated segment

The relation between the effective power and duty cycle was also found to be linear, as expected, with the gradient of the line depending only on the total power supplied, with an intercept at zero.

The control circuit reacted as expected over the full range of operating conditions and a predictive tool could be implemented in determining experimental conditions required to establish set points

and heat flux distribution cases effectively. Due to the parallel nature of the circuitry, a single power supply could be set, with the duty cycle selection being the point of control for each of the six elements to heat the tube section independently. The controller was effective in the regulation and distribution of the current to the different heating segments.

4.4 Heat flux distribution

The test section was heated in a controlled way by making use of a parallel circuit described in Section 3.3. The duty cycle settings on the Arduino UNO microcontroller, which would switch transistors, as described in Sections 3.3 and 4.3, made it possible to control the power supplied to each of the heating elements. It also aided in the variability of the heat flux distributions that could be studied.

Non-uniformity in the heat flux applied over a tube could have been achieved simply, by only heating the bottom portion of the tube. In this study, however, non-uniformity and the kind of non-uniformity of the heat flux were of interest. This required a few distinctly different heating cases. The applied heat flux details of these cases are laid out in Table 8 and displayed in Figures 21 to 26. In total nine different heat flux distributions were considered.

Table 8: Details on non-uniform heat flux distributions

Case number	**Description**	**Local uniform heat flux applied per heating element (q''_{Ω}) [kW/m^2]**					
		1	**2**	**3**	**4**	**5**	**6**
I	Uniform heating	6.75	6.75	6.75	6.75	6.75	6.75
II	Bottom heating	0	13.5	13.5	13.5	0	0
III	Top heating	13.5	0	0	0	13.5	13.5
IV	Left heating	0	0	0	20.25	20.25	0
V	Right heating	20.25	20.25	0	0	0	0
VI	Peak heating on Segment 3	4.86	8.10	12.15	8.10	4.86	2.43
VII	Peak heating on Segment 6	8.10	4.86	2.43	4.86	8.10	12.15
VIII	Peak heating on Segment 1	12.15	8.10	4.86	2.43	4.86	8.10
IX	Peak heating on Segment 2	8.10	12.15	8.10	4.86	2.43	4.86

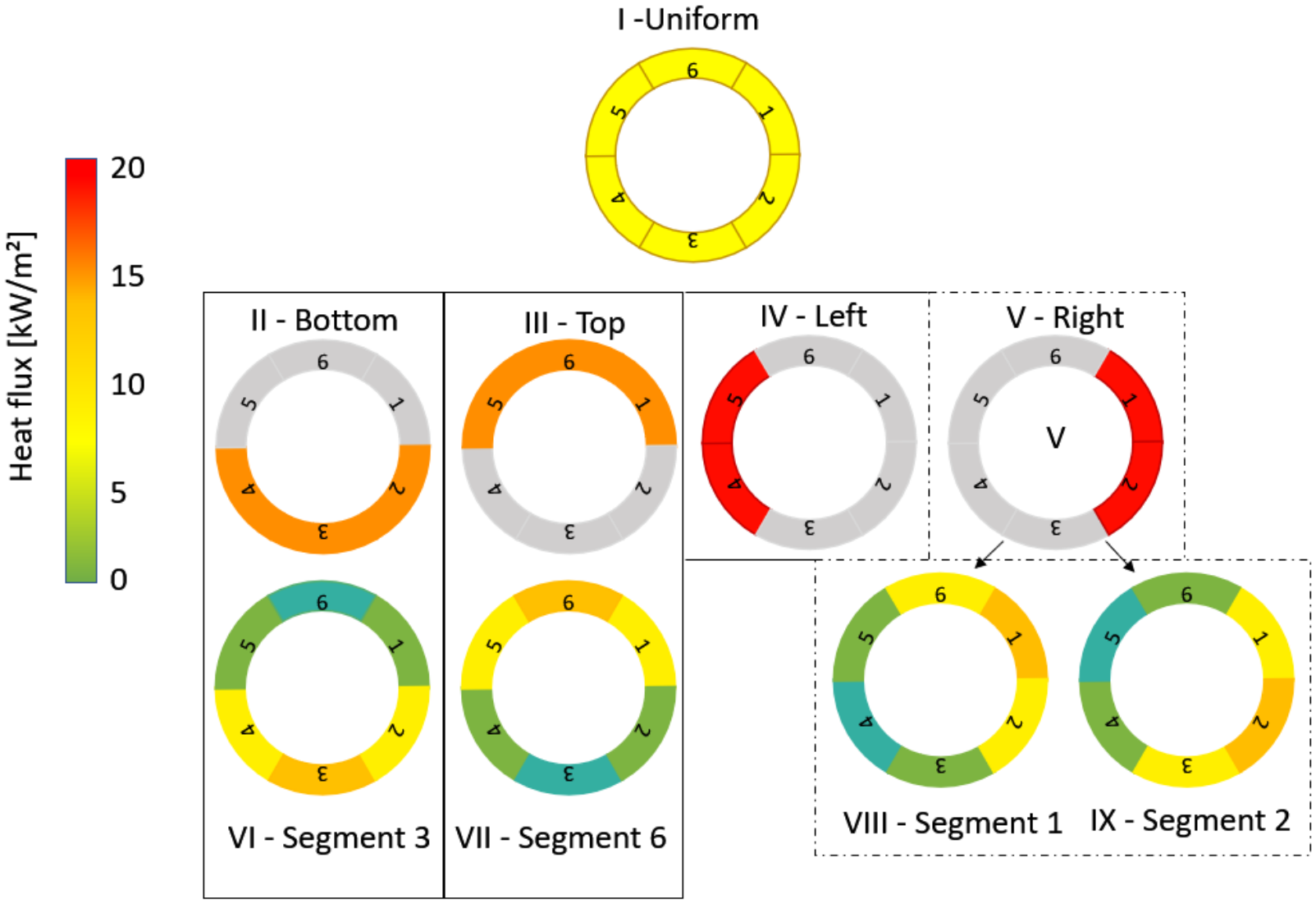

Figure 21: Details on non-uniform heat flux distributions

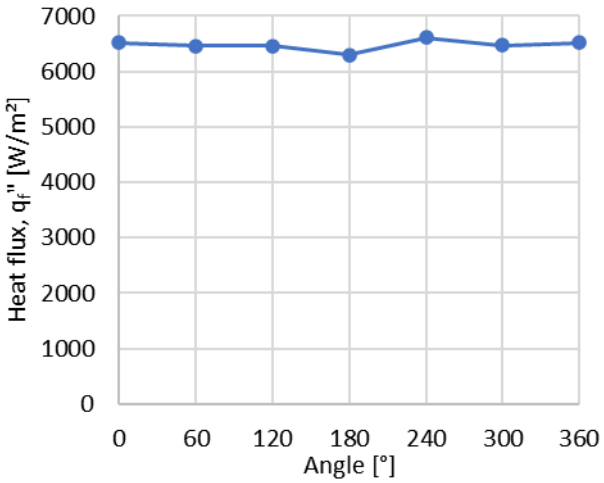

Figure 22: Heating case I – Heat flux supplied uniformly around the circumference of the tube

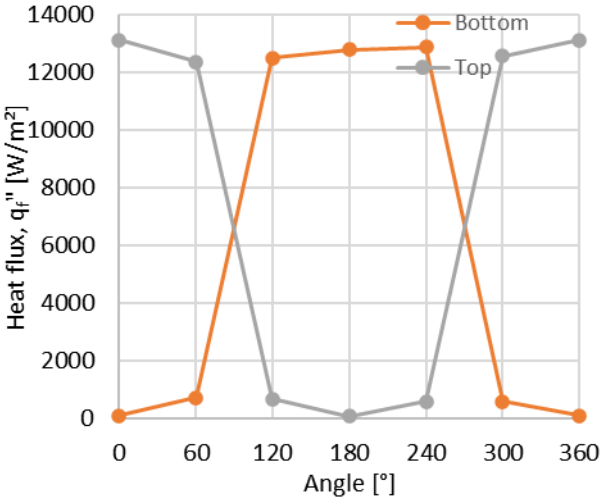

Figure 23: Heating cases II and III – Heat flux applied to the bottom and top segments of the tube

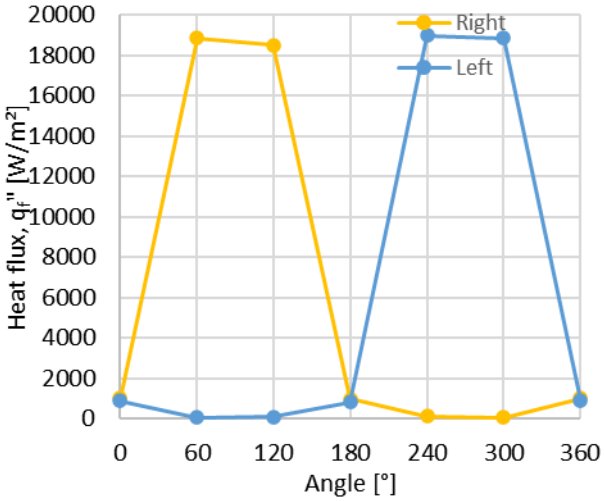

Figure 24: Heating cases IV and V – Heat flux applied to the right and left segments of the tube

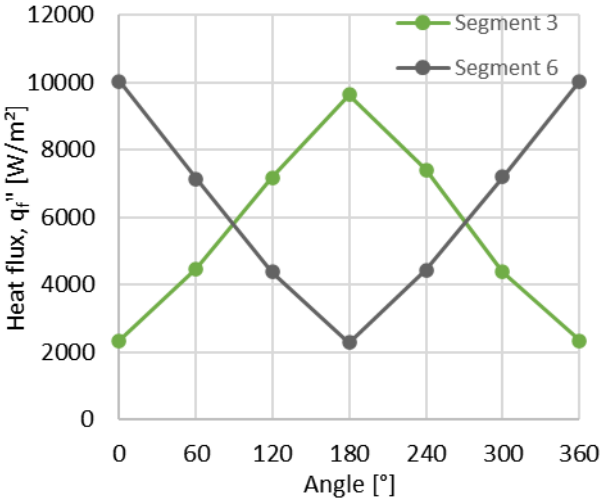

Figure 25: Heating cases VI and VII – Heat flux distributed evenly around the bottom and top segments of the tube

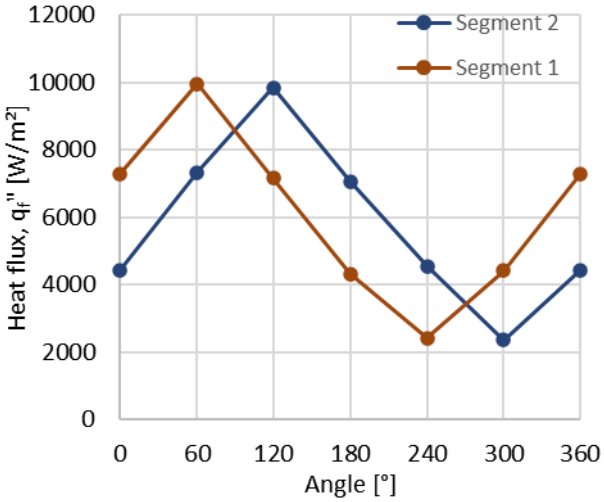

Figure 26: Heating case VIII and IX– Heat flux distributed evenly around the top right and bottom right segments of the tube

The uniform case (case I) was run as a control for comparison to all non-uniform cases. The first four non-uniform distributions (cases II – V, Figures 23 and 24) were to satisfy the quantitative first order investigation of whether heating from these positions on the tube would yield different heat transfer characteristics in the fluid, compared to the other cases in this list.

The last four cases (cases VI – IX, Figures 25 and 26) had a peak segment on the circumference of the tube where the heat flux applied would be significantly greater than the adjacent segments. This would result in the quantification of whether a focused heating would be more beneficial to the heat transfer characteristics in the fluid, compared to a dispersed heat flux distribution.

The heat flux distributions were chosen based on the limitations of the facility used for testing. The maximum current rating of the resistance heating wires was 2 A. The diameter of the tube was also set from the beginning, as the modularity of the facility did not account for alterations in tube diameter, only in tube length. Additionally, having the heat rate into the fluid constant over different heat flux distributions meant that the upper limit current of 2 A restricted the upper heat flux amplitude for all heating cases. In Figure 24 it should be noted that the maximum heat flux is shown. This maximum heat flux was at 20 kW/m², and a total heat rate of 170 W. Distributing 170 W uniformly resulted in a heat flux of 6.67 kW/m², and the non-uniform cases as set out in Figures 23 to 26. Ultimately, the tests done in this investigation did not endeavour to mimic any practical cases. Rather to provide initial evidence to the fundamental influence of non-uniform heat flux distributions.

4.5 Test matrix

Table 9 contains the conditions over which experimental testing was done and covered two mass fluxes (200 and 300 kg/m²s), two saturation temperatures (35 and 40°C), and 10 vapour qualities (ranging from 0.228 to 0.690). The vapour qualities are the average of the inlet and outlet vapour qualities. This resulted in a total of 360 combinations that were included in the test matrix. When looking at the quantities to be used in the investigation, the accepted precision was mentioned in brackets next to the target value. The saturation temperature of 35 °C was a state at the lower end of the facility operating window, and therefore the temperature scatter would have been larger than what was seen at a saturation temperature of 40 °C.

To ease in the housekeeping of all these cases, four clusters were created, governed by the mass flux and saturation temperature required for the tests. The first cluster, 200_35 was tested at a mass flux of 200 kg/m²s and a saturation temperature of 35 °C. The second cluster, 200_40, was tested at the same mass flux but at a saturation temperature of 40 °C. The two other clusters, 300_35 and 300_40, were tested at a mass flux of 300 kg/m²s and saturation temperatures of 35 °C and 40 °C, respectively. Each of these clusters consisted of tests over the full range of vapour qualities as set out in Table 9, and all the heat flux distribution cases mentioned in Table 9.

The mass fluxes were chosen at a range that encapsulated the bulk of the literary information on the flow boiling of R245FA. The saturation temperatures were chosen such that the physical characteristics of the R245FA boiling may be comparable to water at the DSG application temperatures, under which it is subject to boil. The vapour qualities were chosen to ensure annular flow during boiling.

During testing a constant power supply was maintained, regardless of distribution: the experimental total heat rate was set at 170 W. The lengthwise variation in vapour quality for the clusters of tests was between 0.0509 and 0.0775, depending on the mass flux and saturation temperature. This was assumed to be small enough to warrant a two-dimensional heat transfer assumption (tangential and radial) at an average vapour quality between the inlet and outlet.

Table 9: Test matrix

Condition to be established	**Unit**	**Quantity to be used in investigation** **Target value (Accepted precision)**	
Mass flux, G	kg/m^{2}s		200 (± 2.1%) 300 (± 2.1%)
Saturation Temperature, T_{sat}	°C		35 (±4.4 %) 40 (±1.75 %)
Average vapour quality, x_{ave}	-	0.228 (±0.002) 0.276 (±0.002) 0.332 (±0.002) 0.375 (±0.003) 0.440 (±0.005)	0.492 (±0.002) 0.544 (±0.004) 0.590 (±0.005) 0.651 (±0.007) 0.690 (±0.005)
Heat flux distribution cases Preliminary testing: Local heat flux = 6.67 kW/m² Experimental testing: Total heat rate: 170 W		I – Uniform heating II – Bottom heating III – Top heating IV – Left heating V – Right heating	VI – Peak heating at Segment 3 VII – Peak heating at Segment 6 VIII – Peak heating at Segment 1 IX – Peak heating at Segment 2

4.6 Test Procedure

The procedure to be followed during testing is described in Figure 27. There were three operational stages that had to be completed for successful testing. The first was the start-up, in which the facility was switched on and a steady state flow through the facility was established. The second phase was recurring, and the main operation of the facility, where the experimental data was generated and captured. The third phase was the shutdown of the system which had to occur systematically and slowly to avoid thermal and flow shocks on the system.

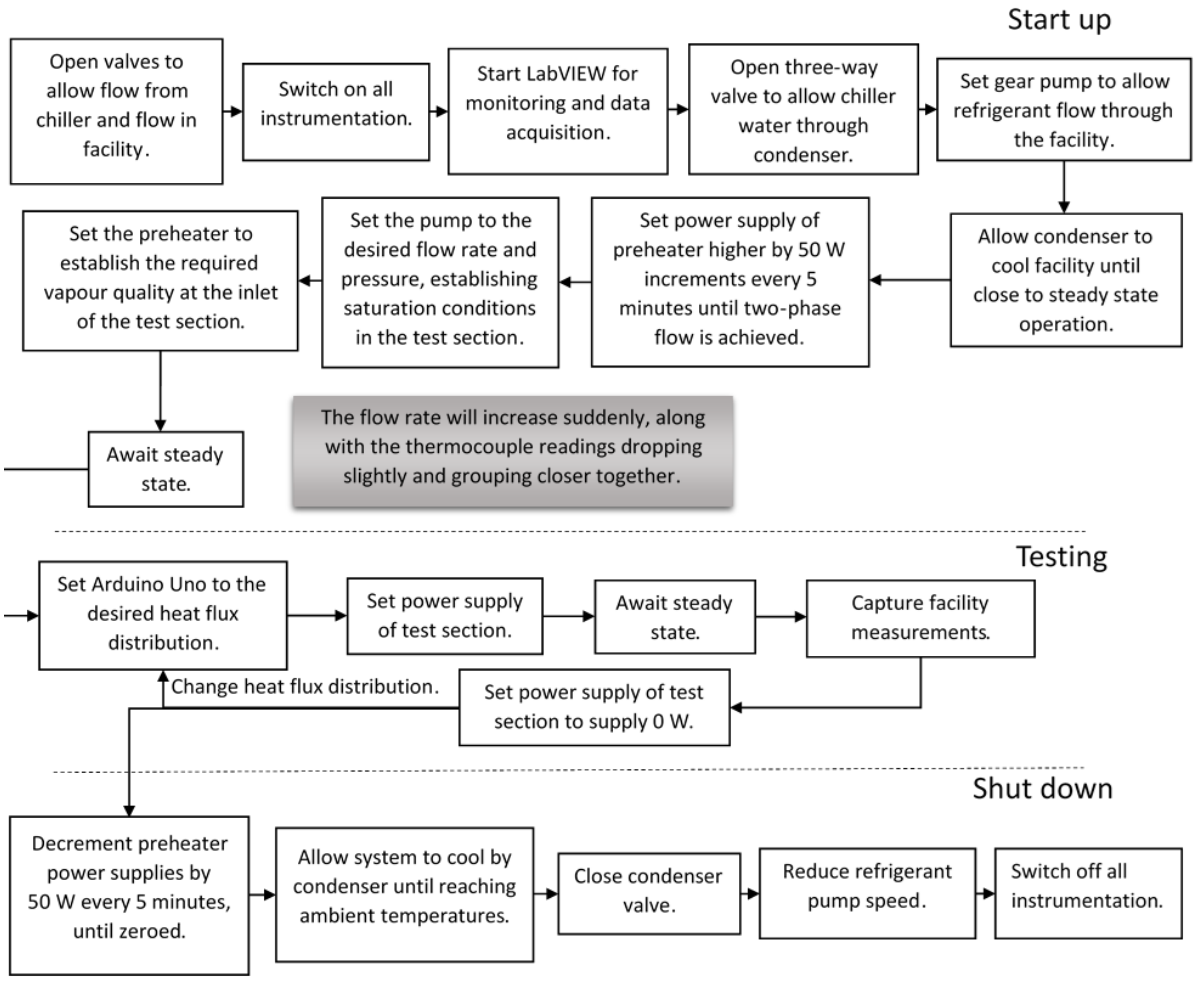

Figure 27: Flow diagram of procedure to be followed during testing

During start-up of the system, it was critical to ensure flow was possible through the facility. This was done by opening all the valves on the system. Thereafter, all pumps, power supplies, mass flow meters and data acquisition units were powered up. Flow was established through the system by supplying a changeable voltage to the refrigerant gear pump and opening the three-way valve controlling the flow of chilled water from the external chiller system through the condenser.

The flow of chilled water through the condenser and refrigerant through the system could run uninterrupted until the refrigerant had cooled significantly, from ambient conditions to close to the chiller supply temperature. This would be the base temperature to which the refrigerant was returned during operation.

When the system had cooled sufficiently, the two power supplies over the preheater were switched on. The power supplied to the preheaters would be increased by 50 W every 5 minutes. This would heat the refrigerant sufficiently fast to ensure the establishment of a set point quickly, without causing dry-out or a shock through the facility. The set point required was determined according to the test matrix. The pressure in the preheater and test section was determined by the pump of the refrigerant, and this pressure established the saturation temperature at which two-phase flow was achieved.

The flow rate of the refrigerant was another parameter that was of critical importance. To establish the flow rate required, under the conditions of the saturation temperature, a bypass valve would be opened or closed as required during setup of the test case. The balance of the flow rate, saturation temperature, heat flux from the preheater and required set point entering the test section required delicate adjustment. The set point was achieved once the flow rate was within 3 % of the total required flow rate and the saturation temperature was within 0.5 °C. The difference between the supplied and absorbed power had to be less than 10 % of the total power supplied into the system for 20 minutes for steady state to be established. This was the energy balance error. The bulk of the energy lost over the facility was focused between the outlet of the condenser and the inlet of the preheater and did not impact the test section experiments.

The test section was then heated according to the non-uniform heat flux case under consideration. The only parameter that was changed during testing at a particular set point was the non-uniform heat flux case that was applied to the test section. This was done by selecting the test case on the Arduino Uno through its interface. In order not to overpower the Arduino microcontroller board, the setting of the non-uniform test case was always done while the power supply was set to a 0 W output. Thereafter the power supply was set to 170 W, translating to an average heat flux over the test section of around 6.6 kW/m^2. This remained constant, regardless of the non-uniform test case applied.

Once the temperature measurements over the test section was within $\pm$ 0.02 °C and the energy balance over the system was below 10 % for 8 minutes, the measurements were recorded. A new set point was established by altering the refrigerant pump voltage, the bypass valve, and the power supply settings for the preheater.

When testing for a particular day was concluded, the test section power supply was zeroed, and the preheater power supplies were decremented by intervals of 50 W. This was to not overwhelm the system with a shock or have the conditions of flow damage the flow meters and valves. Once the preheater power supplies were zeroed, the three-way valve controlling chiller water supply was closed and the gear pump voltage decremented slowly to reduce the flow of the refrigerant through the system in a controlled way. All instrumentation was switched off, and all valves were closed when the gear pump control was zeroed.

4.7 Repeatability

Time constraints limited the number of replicates that was done in this study. It should however be mentioned that repeatability was taken into consideration by the predictability of the facility. During testing the focus was on maintaining as similar an ambient environment as possible when testing the different cases, as it was crucial that an energy balance was achieved and consistently low. This was done in the following way. When testing, the mass flux and saturation temperatures were always the first setpoints invoked. Thereafter, the quality of the fluid was set and finally the heat flux distributions were applied. The heat flux distributions were the changing variable throughout testing, as the heat rates were constant, and a steady state operation could be achieved much faster.

If, in the course of a day, the testing for a specific cluster of cases, having similar mass fluxes, saturation temperatures and vapour qualities, the testing could not be completed, it was usual practice to halt experimentation mid-cluster and continue on the next day. The facility operated at such a high predictability that continuing on where the testing had halted previously never altered the measurement readings on the facility and test section. During testing there was confidence in the facility that alterations within the prediction parameters (Van den Bergh *et al.*, 2019) of the system would yield fully predictable results.

4.8 Summary

This chapter described the methods used for calibration of the differential pressure transducer and the thermocouples used on the facility. The facility validation was described, as well as the commissioning of the test section onto the facility. The control verification was done, to establish whether the newly created control worked in the way it was intended. Thereafter, the heating cases that would be used during testing were laid out, followed by a consolidation of all the testing conditions that would be investigated. The chapter concluded with the procedure to be followed during testing, including the start-up, testing and shut-down procedures and a note on repeatability.

5 Data analysis

The measurements that could be taken on the facility included temperature, pressure, flow rate and power input. Establishing the heat transfer and pressure drop characteristics of the flow as it moves through the system can be done by the incorporation of these measurements, through well-developed equations, into new quantities that define the required states. These equations are set out in this section. The ultimate quantities that will be reported on is the HTC's of the flow at different points on the system, and the pressure drop that is seen over the system. The pressure drop that is seen over the system was measured directly. The HTC's encapsulate the measured temperature, flow rate and power. These values are compared on the basis of the flow characteristics, including the mass flux, vapour quality and saturation temperature.

5.1 Data reduction method

The HTC is an indication of the thermal characteristics of a fluid in a specific state. Local and global thermal characteristics can be determined using this quantity.

Consider Figure 28 that shows a representation of the test section. It is divided into local control volumes along the length and around the circumference according to the location of the wall thermocouples. As mentioned previously, the thermocouples were spaced equidistantly along the length of the tube (direction z) at 9 locations (labelled from A to I, corresponding to index symbols m = A to m = I) beneath each heating section (n = 1 to n = 6).

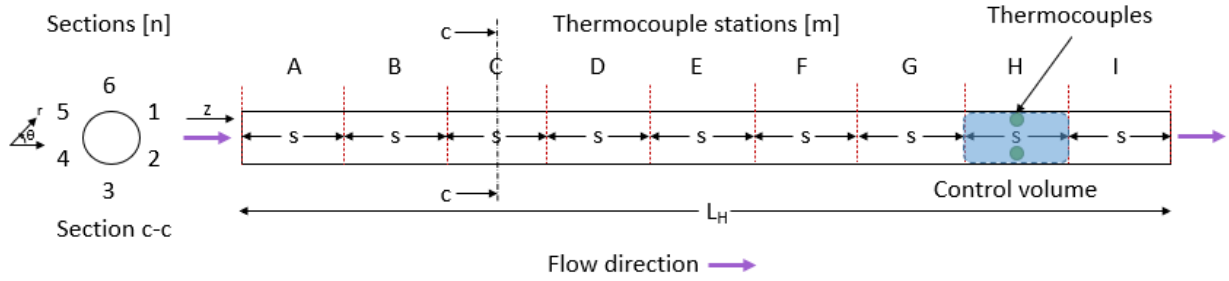

Figure 28: Test section schematic indicating station and segment numbering along with directional coordinates

In order to determine the local HTC (α_n), the local wetted inner wall heat flux value ($q''_{f,n}$) and the local temperature difference between the wetted wall ($T_{W,n}$) and the bulk fluid temperature (T_B) are required:

$$\alpha_n = \frac{q''_{f,n}}{T_{W,n} - T_B} \tag{11}$$

The bulk fluid temperature was obtained as follows:

$$T_B = \frac{1}{2}(T_{in} + T_{out}) \tag{12}$$

The inlet and outlet temperatures (T_{in} and T_{out}) were measured directly with Pt100 RTD's, that were submerged in the flow. Continually during testing the expected saturation temperatures were determined at the measured pressures, while simultaneously, the expected saturation pressures were being determined at the measured temperatures. Utilising CoolProp (Bell *et al.,* 2014) in this way made it possible to definitively conclude whether saturation conditions were in fact present during tests, and isolate the instance that the saturation conditions were no longer present. This ensured that during testing the saturation state could be enforced by continual monitoring and adjustments.

The circumferential local wall temperature was evaluated as the average axial wall temperature along the heated length:

$$T_{\mathrm{W,n}} = \frac{1}{9}\sum_{\mathrm{m=1}}^{9} T_{\mathrm{W(m,n)}} \tag{13}$$

where $T_{\mathrm{W(m,n)}}$ is the local wetted surface temperature at each monitoring location on the tube wall.

The local wetted surface temperature was related to the local thermocouple measurement via a linear heat flux relation which accounted for the radial placement of the thermocouple in the stainless-steel wall and any other interfacial thermal contact resistances:

$$T_{\mathrm{W(m,n)}} = T_{\mathrm{TC(m,n)}} - q''_{\mathrm{o,n}} R_{\mathrm{m,n}} \tag{14}$$

Here $T_{\mathrm{TC(m,n)}}$ is the local thermocouple measurement value after the calibration adjustment was implemented to it, $q''_{\mathrm{o,n}}$ is the heat flux on the outer surface of the tube wall and $R_{\mathrm{m,n}}$ is the effective equivalent thermal resistance between the thermocouple tip and the wetted surface.

The outer surface heat flux for each circumferential segment was based on the applied heating from the heating element ($\dot{Q}_{\Omega,\mathrm{n}}$) and heat transfer to or from the laboratory through the insulation ($\dot{Q}_{\mathrm{ins,n}}$), for that segment:

$$q''_{\mathrm{o,n}} = \frac{\left(\dot{Q}_{\Omega,\mathrm{n}} + \dot{Q}_{\mathrm{ins,n}}\right)}{\frac{\pi D_{\mathrm{o}} L_{\mathrm{h}}}{6}} \tag{15}$$

The heating element heat rate was determined as follows:

$$\dot{Q}_{\Omega,\mathrm{n}} = I_{\mathrm{n}}^2 R_{\mathrm{n}} \tag{16}$$

where I_{n} is the root mean square (RMS) electric current through the particular element, and R_{n} is the electric resistance of the particular heating element. The value of R_{n} was determined during the construction phase of the test section as mentioned in Section 3.2, and I_{n} was calculated according to the applied heat flux condition under consideration. Because all six elements were connected in parallel and powered from the same power supply, but individually controlled, the current distribution to each element had to be determined based on the individual control system settings. Figure 29 shows a simplified circuit of the heating elements, represented as resistors (R_1 to R_6). The current that was supplied to each individual heating element was determined by taking the duty cycle ($C_{\mathrm{dc,n}}$) and the total electric current (I_{tot}), which was measured directly, into account on the parallel current division as follows:

$$I_{\mathrm{n}} = I_{\mathrm{tot}} \frac{\frac{C_{\mathrm{dc,n}}}{R_{\mathrm{n}}}}{\sum_{n=1}^{6} \frac{C_{\mathrm{dc,n}}}{R_{\mathrm{n}}}} \tag{17}$$

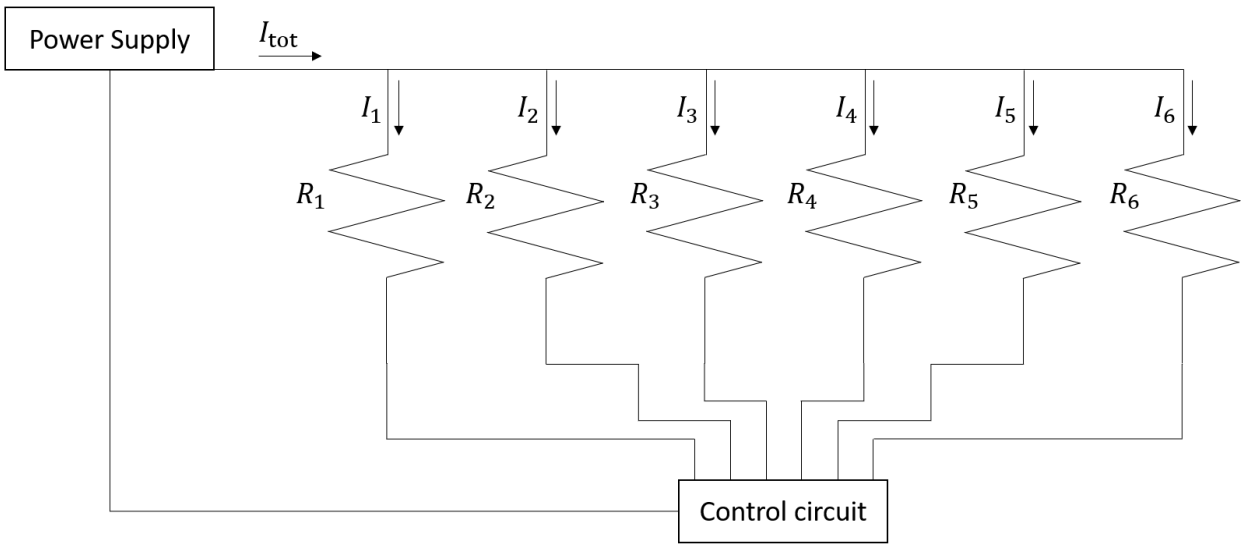

Figure 29: Simplified heating segment circuit

The heat transfer through the insulation for the particular segment was determined as follows:

$$\dot{Q}_{\mathrm{ins,n}} = \frac{k_{\mathrm{ins}} A_{\mathrm{ins,n}} \left(T_{\mathrm{ins,o,n}} - T_{\mathrm{ins,i,n}}\right)}{t_{\mathrm{ins}}} \tag{18}$$

Here k_{ins} is the conductivity of the insulation, $A_{\mathrm{ins,n}}$ is the conduction heat transfer area defined in Equation (*19*), and $T_{\mathrm{ins,o,n}}$ and $T_{\mathrm{ins,i,n}}$ are the temperatures measured directly at an outer and inner position on the insulation and t_{ins} is the thickness of the insulation between the thermocouples.

$A_{\mathrm{ins,n}}$ for a specific segment was expressed as follows:

$$A_{\mathrm{ins,n}} = \frac{\pi D_{\mathrm{mid}} L_{\mathrm{h}}}{6} \tag{19}$$

where D_{mid} is the mid insulation diameter given as follows:

$$D_{\mathrm{mid}} = D_{\mathrm{o}} + t_{\mathrm{ins}} \tag{20}$$

Before the calculation in Equation (*14*) could be executed, the effective equivalent thermal resistance between the thermocouple tip and the wetted surface had to be determined. Consider Figure 30 which gives a schematic cross-sectional view of the test section at some particular axial location m. When looking at Figure 30, it should be noted that the outer dark grey region indicates the insulation over the tube, and the inner light grey region indicates the tube wall. Between these two regions, the cross sections of the heating wires are represented in red as they were laid lengthwise over the test section. As mentioned previously, the tube was split into six circumferential segments, numbered 1 through 6, and each heating element (one per segment) had 6 heating wires placed against the tube outer wall. The green dots indicate the thermocouple positions placed in the tube wall as well as in the insulation around the tube. The enlarged view of segment 6 indicates the approximate relative placement of the heating wires, and wall thermocouple, with a relevant equivalent thermal resistance of $R_{\mathrm{m,n}}$ between the wetted surface and thermocouple tip. For visual convenience, this resistance is represented by an arrow and overlaid onto the view but should not be confused with the radial placement of the tip.

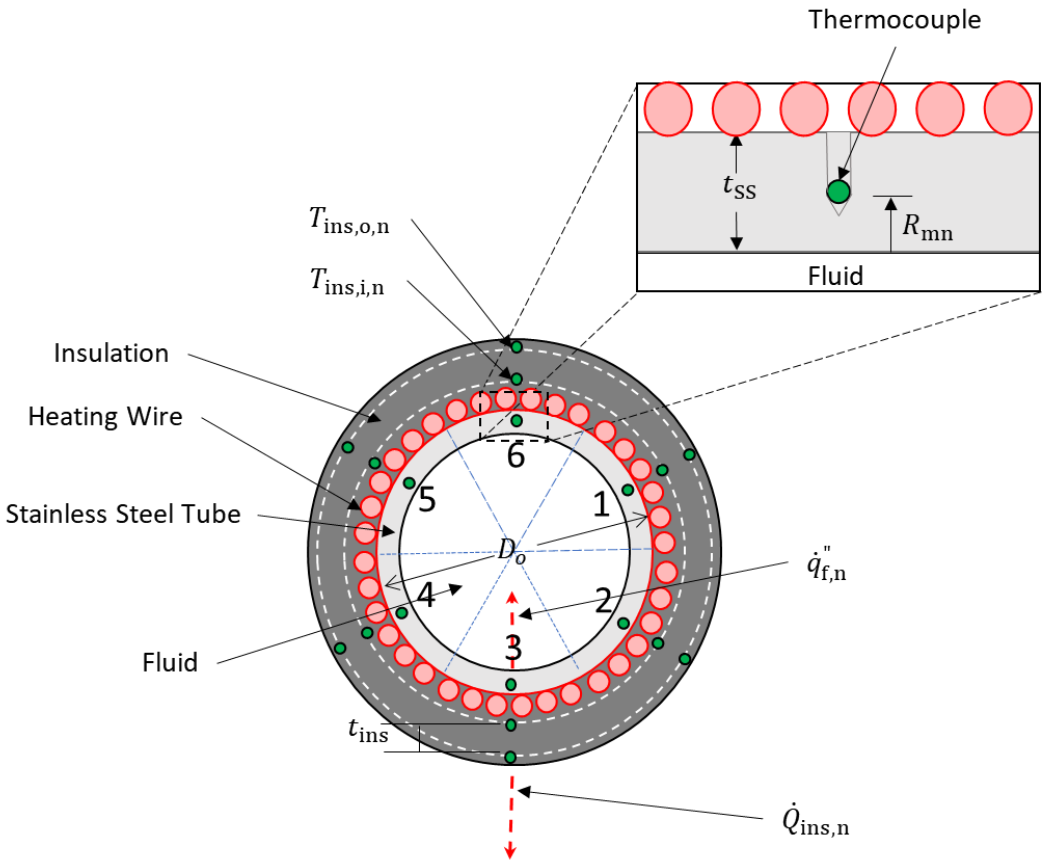

Figure 30: Schematic cross-sectional view of the test section at some particular axial location m

The value of $R_{m,n}$ for each thermocouple was determined prior to the flow boiling experiments by conducting a series of liquid single-phase diabatic steady state uniform heat flux experiments in the highly turbulent flow regime. To produce the uniform heat flux, all six heating elements were powered at the same level, and to ensure a liquid phase, the preheater was not switched on.

For such conditions, the effective equivalent thermal resistance was determined as follows:

$$R_{m,n} = \frac{\left(T_{TC,(m,n)} - T_W\right)}{q''_{uniform}} \tag{21}$$

Here the wetted wall temperature was determined by applying the single phase Gnielinski heat transfer coefficient:

$$T_W = T_B + \frac{q''}{\alpha_{liq}} \tag{22}$$

with:

$$\alpha_{liq} = \frac{k_f Nu}{D_i}. \tag{23}$$

k_f is the liquid thermal coefficient evaluated at the average bulk fluid temperature (which is evaluated according to Equation (12)) using CoolProp (Bell *et al.*, 2014), and Nu is the Nusselt number obtained in terms of the standard Reynolds number (Re) based on the inner diameter, and the Prandtl number (Pr) also evaluated at the average bulk fluid temperature as follows:

$$Nu = \frac{\frac{f}{8}(Re - 1000)\mathrm{Pr}}{1 + 12.7\left(\frac{f}{8}\right)^{\frac{1}{2}}\left(\mathrm{Pr}^{\frac{2}{3}} - 1\right)} \quad (24)$$

$$f = (0.79\ln Re - 1.64)^{-2}$$

For the liquid phase tests, the outer wall uniform heat flux in Equation (*21*) was based on the total power input of all six-heating elements and the total heat transfer through the insulation:

$$q''_{\mathrm{uniform}} = \frac{\sum_{n=1}^{6}\left(\dot{Q}_{\Omega,n} + \dot{Q}_{\mathrm{ins,n}}\right)}{\pi D_{\mathrm{o}} L_{\mathrm{h}}} \quad (25)$$

The liquid phase tests were conducted at four uniform outer wall heat flux levels between 2000 W/m^2 and 7600 W/m^2 and the mass flow rate was set such that fluid remained in the liquid phase. From the collected data the effective equivalent thermal resistance of each thermocouple tip was correlated via a linear equation with the applied heat flux on the outer wall:

$$R_{\mathrm{m,n}} = M_{\mathrm{m,n}}\, q''_{\mathrm{o}} + C_{\mathrm{m,n}} \quad (26)$$

Here $M_{\mathrm{m,n}}$ and $C_{\mathrm{m,n}}$ are the linear regression coefficients that were determined individually for each thermocouple installation. The results from this investigation are presented in Appendix D.

The only variable in Equation (11) that has to be determined is the inner wall heat flux, $q''_{\mathrm{f,n}}$. Having the overall mechanism of heat transfer around the tube wall defined the finer heat flux distribution that develops in the tube wall can be approximated with an iterative numerical and analytical hybrid approach. This was required because even though stainless-steel has a relatively low thermal conductivity, a portion of the applied heat flux on the outer tube wall surface was conducted tangentially in the circumference, particularly in severely non-uniform heat flux case. Therefore, the applied heat flux distribution was not fully transferred to the inner wall.

To model the in-wall heat flux in the radial and tangential directions, the tube wall was divided into four cells in the radial direction and 18 cells in the tangential direction according to a finite difference scheme. The four radial cells are shown in Figure 31, and the 18 tangential cells extend past the image displayed.

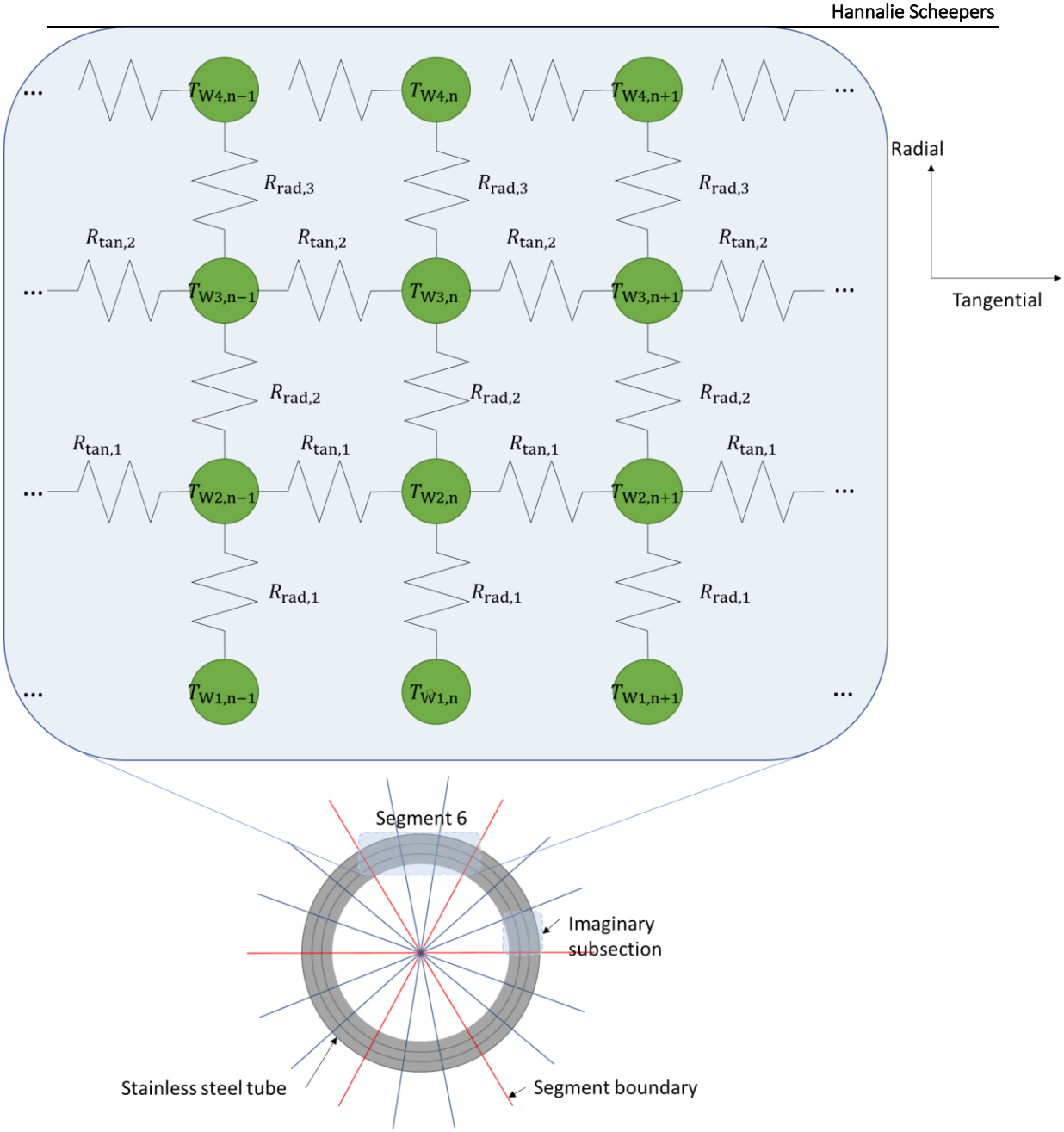

Figure 31: Temperature and thermal resistance network approximation used in the numerical analytical hybrid analysis method

For each wall node the energy balance principle was applied and a set of 72 linear equations (4 x 18, one for each node) was solved simultaneously. The outer wall boundary condition was set to be the same as the applied heat flux values for each segment as determined in Equation (*15*) and a convective thermal boundary was applied on the inner wall, based on the HTC from Equation (*11*). The radial ($R_{\mathrm{rad,n}}$) and tangential ($R_{\mathrm{tan,n}}$) thermal resistances between neighbouring nodes were modelled as follows:

$$R_{\mathrm{path}} = \frac{\Delta x}{k_{\mathrm{SS}} A_{\mathrm{face}}} \tag{27}$$

Where Δx is the linear distance between the neighbouring grid points and A_{face} is the cell face of each finite difference control volume to the relevant neighboring element. Both of these were determined

according to the relative radial or tangential conduction directions, depending on which direction was relevant.

Once the in-wall heat flux fields were calculated the inner wall heat flux values for each segment in Equation (*11*) was updated, and the HTC coefficient was re-evaluated until the HTC coefficient converged.

The calculation of the inlet vapour quality (x_{i}) was done by analysing the preheater before the test section.

$$x_{\mathrm{i}} = \frac{h_{\mathrm{i}} - h_{\mathrm{f}}}{h_{\mathrm{fg}}} \tag{28}$$

By applying the energy balance principle to the preheater, the inlet specific enthalpy (h_{i}) to the test section was determined as follows:

$$h_{\mathrm{i}} = \frac{\dot{Q}_{\mathrm{PH}}}{\dot{m}} + h_{\mathrm{PH}} \tag{29}$$

Here $\dot{Q}_{\mathrm{PH}}$ is the total heat rate applied on the preheaters, measured directly from the power supply, assuming no losses, $\dot{m}$ is the mass flow rate of the refrigerant, measured directly from the mass flow meter and h_{PH} is the inlet enthalpy to the preheater. The inlet specific enthalpy to the preheater was determined continually through CoolProp (Bell *et al.*, 2014), by making use of the temperature and pressure measurements taken at the inlet to the preheater.

The enthalpy of evaporation (h_{fg}) was also determined by CoolProp (Bell *et al.*, 2014) at the average pressure condition, from the absolute pressure transducers, over the test section, along with the inlet temperature measurement of the Pt100 RTD.

5.2 Uncertainty analysis

The uncertainty associated with a measured quantity is affected by random and systematic errors associated with that measurement. An uncertainty analysis was done by including the instrument bias as well as the dispersion of the data points. The uncertainty associated with all quantities of this study was established with a confidence interval of 95 %, and reported in the form:

$$X_{\mathrm{i}} \pm \delta X_{\mathrm{i}} \tag{30}$$

where X_{i} is the value of the measured quantity and δX_{i} is the uncertainty associated with it.

The method of propagation of uncertainty, described in Moffat (1982), was used to determine the uncertainty of all calculated quantities. If the quantity was comprised of a function of n variables, (X_{i}), each with an associated uncertainty, (δX_{i}), then the uncertainty associated with the calculated quantity (δR) is calculated by:

$$\delta R = \sqrt{\sum_{\mathrm{i}=1}^{N} \left(\frac{\partial R}{\partial X_{\mathrm{i}}} (\delta X_{\mathrm{i}}) \right)^2} \tag{31}$$

The dispersion of data points in all measurements were integrated into its uncertainty by the method described in Dunn (2014). The precision of a measurement, leading to the true mean of that measurement could be established by the standard deviation ($S_{\overline{x}}$) and a constant in a two-sided T-type distribution, t_{δ}:

$$\delta R_{\mathrm{p}} = t_{\delta} S_{\overline{x}} \tag{32}$$

The uncertainties associated with the equipment used in the investigation are listed in Table 10.

Table 10: Uncertainties of parameters evaluated by measurements

Parameter	Unit	Range	Uncertainty
Pressure transducer	[kPa]	50 – 2500	± 3.1 kPa
Differential pressure transducer	[kPa]	0 – 14	± 0.5 kPa
T-type thermocouples	[°C]	-200 – 350	± 0.1 °C
Pt100 thermocouples	[°C]	0 – 100	± 0.06 °C
Coriolis mass flow meters	[kg/m^{2}s]	0 – 0.04	0.11 %
	[kg/m^{2}s]	0 – 0.4	0.11 %
Vernier caliper	[mm]	0 – 200	20 µm
Measuring tape	[mm]	0 – 5000	1 mm
Power supplies	[V]	0 – 360	0.2 %
	[A]	0 – 30	0.2 %
	[A]	0 – 15	0.2 %

All thermophysical fluid properties at measured state points were calculated using CoolProp (Bell *et al.*, 2014), and yielded results with uncertainties as indicated in Table 11.

Table 11: Uncertainties of thermophysical fluid properties calculated using CoolProp (Bell et al., 2014)

Parameter	Unit	Range	Uncertainty
Density (ρ)	[kg/m^3]	0 °C – 150 °C	0.04 %
Constant pressure specific heat (C_P)	[J/kgK]	0 °C – 150 °C	0.06 %
Conductive heat transfer coefficient (k)	[W/mK]	0 °C – 150 °C	2 %
Dynamic viscosity (μ)	[Pa·s]	0 °C – 150 °C	1 %

A sample calculation for the uncertainty of a reported HTC is shown in Appendix E.

The condensed results for the uncertainty analysis done on the reported experimental results for on uniform heating case is shown in Table 12 to indicate the effect of uncertainty propagation.

Table 12: Uncertainties of calculated results

Parameter	Unit	Range	Uncertainty	
			min	max
$T_{\mathrm{TC,(m,n)}}$	[°C]	35.34 – 61.06	0.009 °C	0.1 °C
T_{B}	[°C]	34.45 – 40.61	0.07 °C	0.18 °C
T_{W}	[°C]	35.33 – 47.48	0.009 °C	0.37 °C
ΔT	[°C]	0.52 – 8.15	0.07 °C	0.39 °C
$q''_{\mathrm{f,n}}$	[W/m²]	555 – 13294	176	519 W/m²
α_{n} – lengthwise averaged HTC	[W/m²K]	477 – 4360	8 %	18 %
α_{ave} – overall averaged HTC	[W/m²K]	1415 - 3334	4.2 %	17 %
x_{ave}	[-]	0.226 – 0.695	0.4 %	1.3 %

The HTC had an uncertainty that was influenced by the heat flux and temperature difference between the wall and bulk fluid temperatures. The largest contribution to the HTC uncertainty was due to the temperature differences. When the temperature difference was small, the uncertainty associated with the HTC increased.

The bulk fluid temperature had an uncertainty that was better than a singular thermocouple was able to produce, when the statistical dispersion of the data logged was also accounted for. This was the case since two Pt100 RTD's were used in the determination of the bulk fluid temperature and the uncertainties of both these measured quantities were propagated into the reported bulk temperature uncertainty. The thermocouple reading uncertainties were improved by calibration, however, the extrapolation of the thermocouple readings to the expected wall temperature readings increased the uncertainty associated with this quantity.

The uncertainties of the average HTC's (α_{n}) of a heated segment n, ranged from 8 % to 18 %. Where a low heat flux was applied to the tube wall segment, the temperature difference was very small, increasing the uncertainty of the associated local HTC. In Section 6.1 the uncertainty associated with the HTC's reported for this study increased with an increase in vapour quality. This was due to the uncertainty associated with the temperature difference between the inner wall temperature and the bulk fluid temperatures.

As the vapour quality increases, the pressure drop over the test section also increases. This causes a temperature drop over the test section to become larger, as the saturation temperature and pressure are directly proportional. This leads to the determination of the bulk fluid temperature to have a higher uncertainty associated with it, as the uncertainty scales with the difference in inlet and outlet temperatures, which is used directly to determine the bulk fluid temperature per Equation (*12*).

5.3 Summary

The methods used to analyse the data captured during experimentation was set out in this chapter. The equation to find the local HTC was described, followed by a breakdown to determining all attributing factors. It included the local wetted wall heat flux value and difference between the wetted wall and bulk fluid temperatures. The local wetted wall temperature required knowledge of the equivalent thermal resistance of the thermocouples, which was determined through an independent set of tests. Finally, the uncertainty associated with measurements were discussed, as well as the propagation of this uncertainty into the final calculated results.

6 Validation and results

This chapter presents the experimental results obtained from the data handling described in Chapter 5. Firstly, the data reduction method is validated against two sets of independent data. The first is the study on boiling of R245FA done by Van den Bergh *et al.* (2019), under uniform heating, and the second is the study done by Wang *et al.* (2019) on boiling of R245FA under circumferentially non-uniform heating. Thereafter, the results obtained from a preliminary test are presented, being a first order indication of the results that can be expected. The results obtained in this investigation are presented next. The temperatures measured and wetted wall temperatures calculated are discussed, followed by the effective HTC results. Finally, the different heat flux distribution cases are compared, and quantitative conclusions are drawn from the results.

6.1 Validation of data reduction method for the uniform heating case

The validation of the data reduction method was done by comparing the results obtained by Van den Bergh *et al.* (2019). This was done for two-phase flow boiling of R245FA, subject to a uniform heating boundary condition in a similar sized tube. A brief comparison between the testing conditions of the current study and that of Van den Bergh is presented in Table 13.

Table 13: Conditions for validation with uniform heating case

	Validation case (current study)	**Van den Bergh *et al.* (2019)**
Tube inner diameter	8.5 mm	8.5 mm
Tube material	Stainless-steel	Copper
Heat flux case	Uniform heating	Uniform heating
Heat flux applied	6.578 ± 0.05 kW/m²	7.494 ± 0.004 kW/m²
Saturation temperature	34.65 ± 0.33 °C	35.01 ± 0.37 °C
Mass flux	200.47 ± 3.71 kg/m²s	201.06 ± 2.96 kg/m²s

The test section tube used in the study by Van den Bergh et al. (2019) was a copper tube of 800 mm heated length. A nichrome heating wire was wrapped around the tube and powered to produce a uniform heating boundary condition. Four thermocouples were positioned at the top, bottom, and sides of the tube. The measurements were averaged and extrapolated to determine the wetted wall temperature. The HTC's achieved in the two different testing cases are compared in Figure 32. Over the full range of vapour qualities (0.228 – 0.695) the current study achieved HTC's that correspond with that of Van den Bergh et al. (2019) within between 0% and 9 %. The maximum difference was obtained at a vapour quality of 0.695 and peaked at 9 %. Almost exact matches were achieved for vapour qualities less than 0.4. This is indicative of a successful validation.

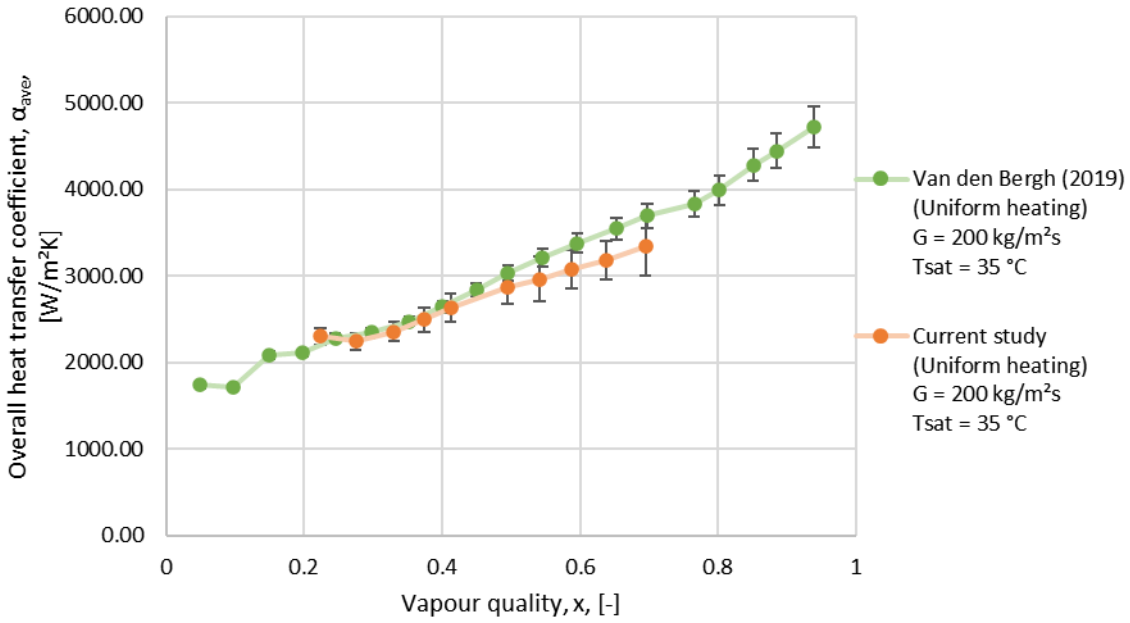

Figure 32: Results for validation with uniform heating case at G = 200 kg/m²s and T_{sat} = 35 °C

6.2 Validation of data reduction method for the non-uniform heating case

A comparison for a non-uniform heating condition was also done against some results from Wang *et al.* (2019). The testing conditions of the two cases are set out in Table 14.

Table 14: Conditions for validation of a non-uniform heating case

	Current study		**Wang *et al.* (2019)**	
Tube inner diameter	8.5 mm		10 mm	
Tube material	Stainless-steel		Stainless-steel	
Heat flux case	Bottom heating		Bottom heating	
Heat flux applied [kW/m²]	6.9 ± 0.3		9.95 ± 1.53 %	
Saturation temperature [°C]	39.75 ± 0.14	39.90 ± 0.34	40 ± 0.05 %	40 ± 0.05 %
Mass flux [kg/m²s]	194.54 ± 3.54	276.29 ± 4.47	192.9 ± 1.38 %	275.6 ± 1.38 %
Number of thermocouples on circumference	6		4	

The test section build used in the investigation by Wang *et al.* (2019) also consisted of a stainless-steel tube, which was heated using the Joule effect on nickel-chromium insulating film electric heaters. The film electric heaters were places such that top, bottom and side heating is possible. The thermocouples used to determine the wall temperatures were placed between two electric heaters, as indicated in Figure 33. During non-uniform testing, the thermocouples measured the temperature of the tube under different conditions. The top thermocouple measured the temperature of the tube not being heated locally; the thermocouple at the bottom measured the temperature of the tube being heated locally; and the thermocouples positioned on the sides of the stainless-steel tube measured the temperatures at the interface between the heated and non-heating sides. These thermocouple readings were then extrapolated and averaged to determine the inner wall temperature of the stainless-steel tube. This wall temperature was used to calculate the HTC.

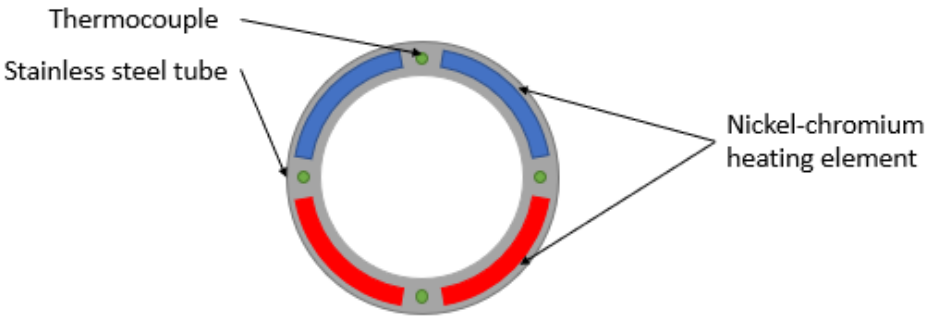

Figure 33: Reproduction of schematic of stainless-steel test section used by Wang et al. (2019)

Due to the construction of the test section and the data reduction method employed by Wang *et al.* (2019), a comparison of the overall average HTC's directly is difficult. The thermocouples in the current study were placed in the centre of each heating segment, ensuring that no temperature measurements were done at the interfaces between heating segments. As such, the comparison of data and data handling methods between this study and that done by Wang *et al.* (2019) inherently differ and yielded distinctly different trends. Figure 34 displays the results in two different non-uniform bottom heating cases at different mass fluxes.

As can be seen from this figure, the differences between the overall average HTC's reported by Wang *et al.* (2019) and the current study was a maximum of 20 %. This may be primarily due to the applied heat flux being lower in the current study. The influence of the heat flux magnitude plays a significant role in the magnitude of the HTC.

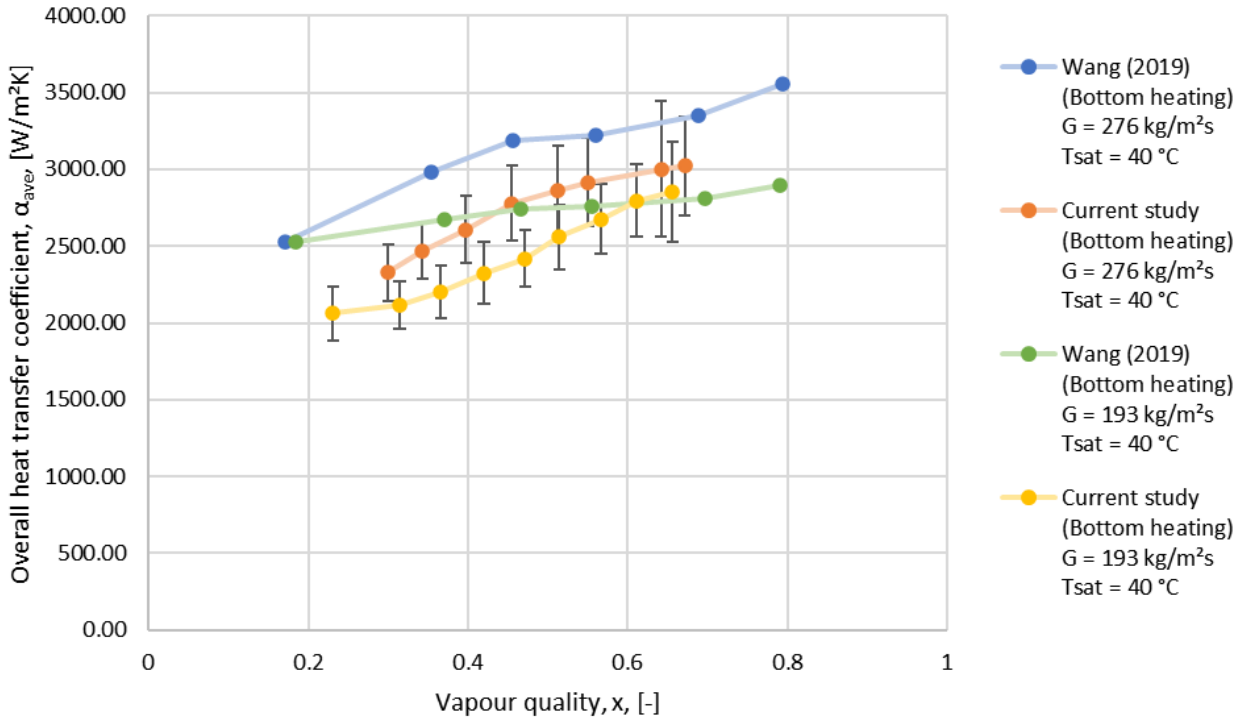

Figure 34: Results for validation against a non-uniform heating case at G = 275.9 kg/m²s and T_{sat} = 40 °C

6.3 The effect of a constant heat flux non-uniformly applied

Preliminary tests were done to determine the results that could be expected in the larger study. The test section was heated with non-uniform heat fluxes such that the heat flux applied was always 6.67 kW/m². This effectively established a foundation from which to extrapolate what might happen

if the total heat rate stayed constant, while the distribution of heat was different. The uniform heating case in the larger study was done with a heat flux per segment of 6.67 kW/m². This was equivalent to 160 W overall heat rate supplied into the tube. The larger study was done in all non-uniform cases, with the heat rate constant at 160 W, with only the distribution being altered. However, for the preliminary tests reported here, the heat flux of 6.67 kW/m² was set, and if a segment would be powered, it would supply 6.67 kW/m², as shown in Figure 35. The heat rates therefore in the preliminary study was different for the different non-uniform heating cases investigated. Uniform heating was done at a heat rate of 160 W, top and bottom heating at 80 W and right and left heating at 53.4 W. The HTC's reported were lengthwise averaged, α_θ.

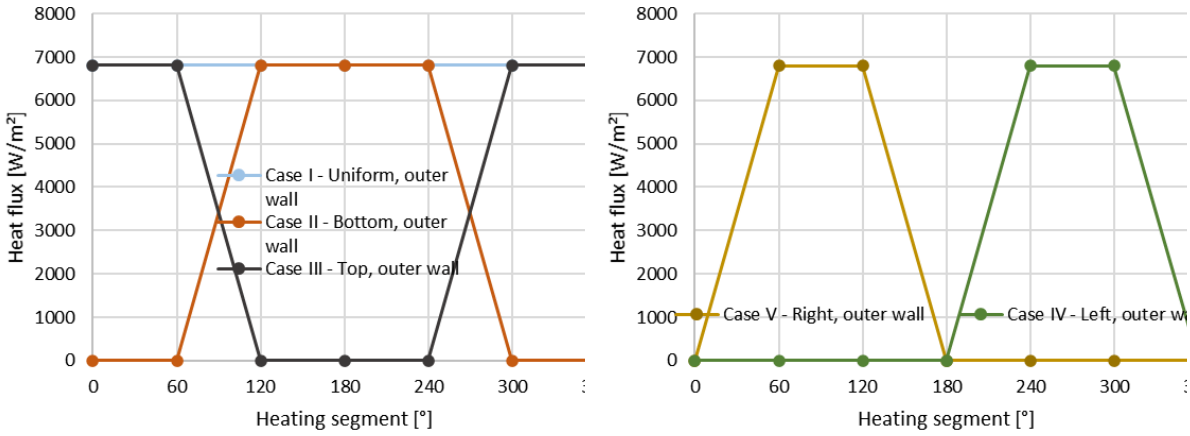

Figure 35: Heat flux applied around the tube for preliminary testing at G = 300 kg/m²s and T_{sat} = 35 °C at a vapour quality of x = 0.45

The tests were run at a mass flux of 300 kg/m²s, and a saturation temperature of 35 °C. Two inlet vapour quality conditions were tested, x = 0.228 and 0.440. The results achieved for both these cases were very similar and only the results for the vapour quality of 0.440 will be presented.

The dispersion of the heat flux in the tube wall was determined with the numerical data handling described in Section 5.1. The heat flux distribution that is in contact with the fluid at the inner tube wall, (shown in Figure 36), is very different from the applied heat flux distribution at the outer wall (Figure 35). Heat was distributed from the segments with a higher heat flux to segments with lower heat fluxes.

The heat flux applied uniformly around the tube dispersed such that the heat flux at the inner wall at the bottom of the tube was lower than the applied heat flux at the adjacent segments. A heat loss accounted for the total heat rate at the outer wall being greater than the total heat rate at the inner wall. The top segment (segment 6) experienced the highest heat flux at the inner wall of the tube. All non-uniform heat flux cases showed a significant alteration of the heat flux distributions due to the tangential wall conduction influence. The highest heat flux peaks were decreased and the segments that were not heated yielded a heating boundary at the inner wall.

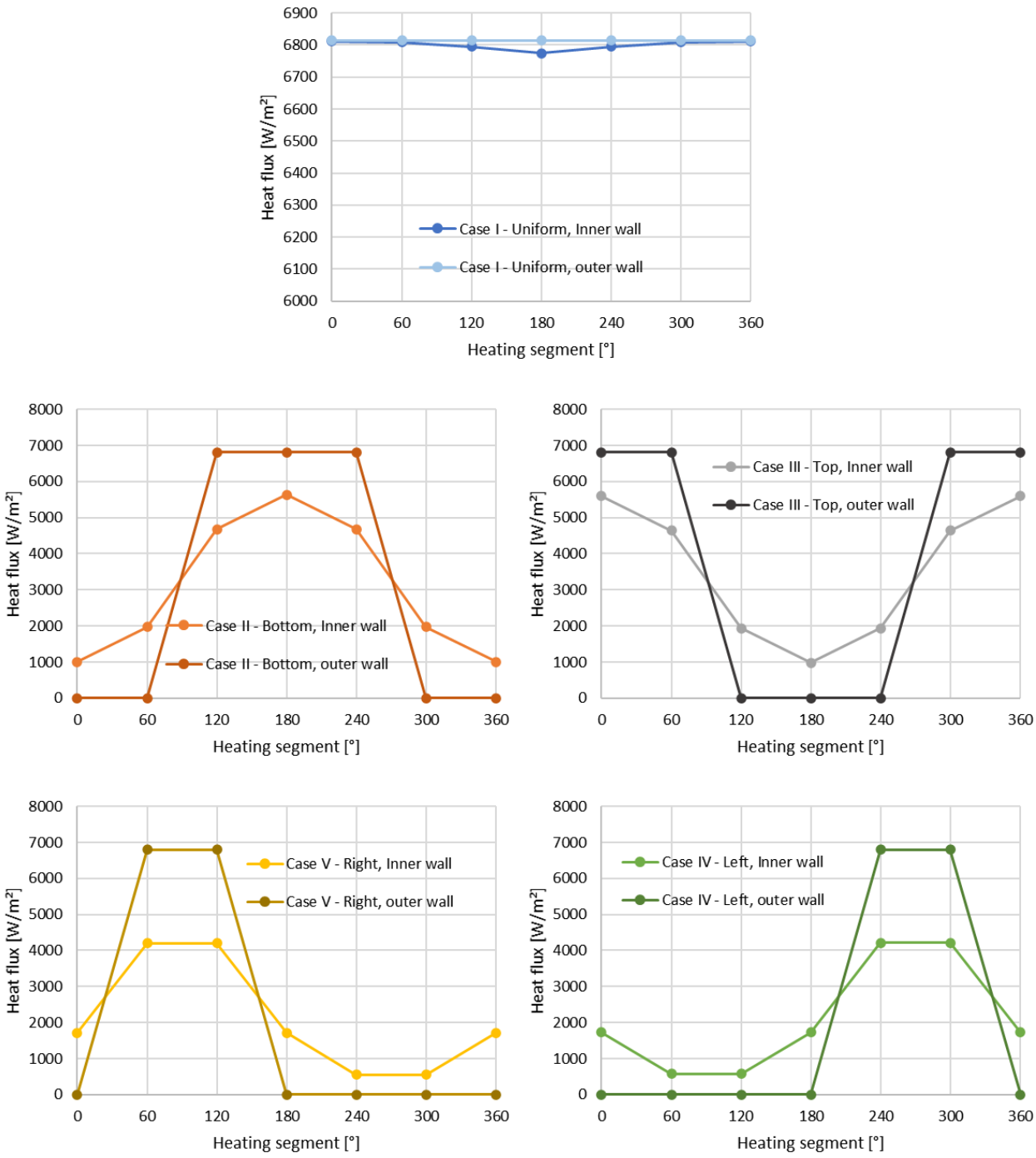

Figure 36: Effect of the heat flux dispersion on the heat flux at the inner wall of the tube

The temperatures measured for all the different heating cases are shown in Figure 37. As was the case in the heat flux plots, the uniform heating results will be presented in blue, the bottom heating case will be presented in orange, the top heating case is grey, the left heating case is green, and the right heating case is yellow.

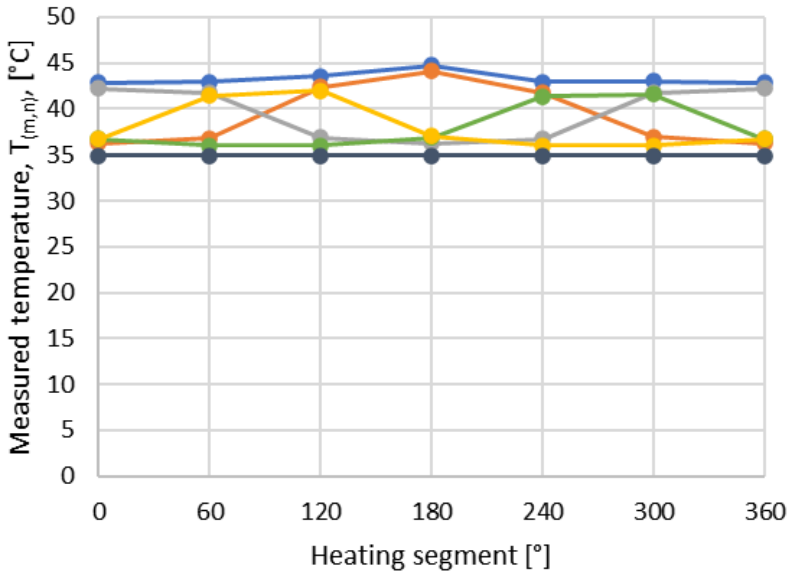

Figure 37: Measured temperatures for all preliminary cases at G = 300 kg/m²s and T_{sat} = 35 °C at a vapour quality of x = 0.45

In case I – Uniform, the lowest segment (segment 3) indicated higher lengthwise averaged measured temperatures than the adjacent segments. This was surprising was the heat flux at the inner wall of the lowest segment was the lowest heat flux due to tangential wall conduction. In the non-uniform cases (case II – V), the heated segments indicated higher temperature reading than the adjacent segments. Where no heat flux was applied, the temperature is only slightly higher than the bulk fluid temperature (indicated with a dark line). The mid-segment of a three-segment heating case (cases II and III) resulted in the mid-segment temperature being comparable to case I results for that specific segment. All cases seemed symmetrical around the tube circumference. Figure 38 displays the overall average measured temperature for the different cases. The uniform case yielded the highest average measured temperature, while case V – Right heating had the lowest measured temperature. Case III also had a higher temperature than case II.

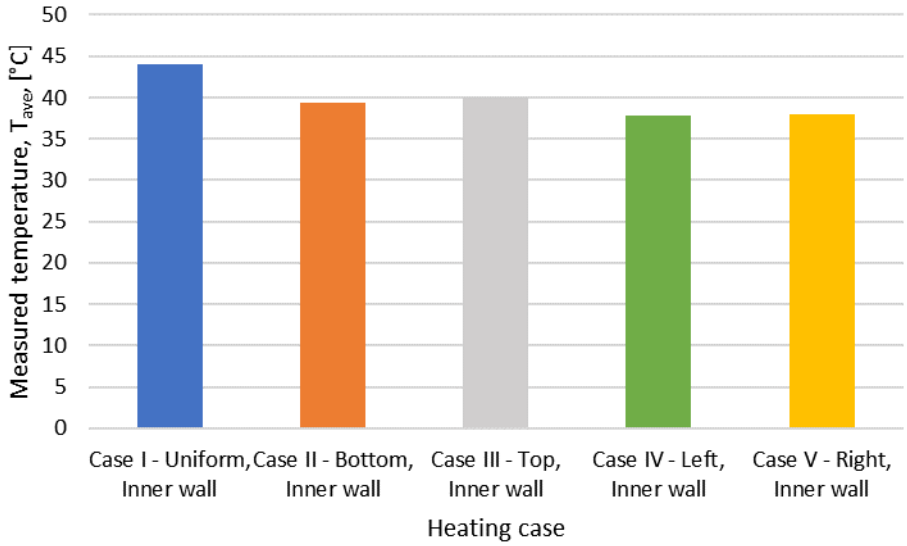

Figure 38: Overall average measured wall temperature for all preliminary cases at G = 300 kg/m²s and T_{sat} = 35 °C at a vapour quality of x = 0.45

Displayed in Figure 39, are the lengthwise averaged wetted wall temperatures calculated for each heat flux distribution case. The wetted wall temperatures for all non-uniform cases were higher than the

bulk fluid temperatures (displayed as a dark line) as expected. Most non-uniform cases displayed a higher wetted wall temperature at the bottom segment, segment 3, than the remaining segments, but top heating had a lower wall temperature at the bottom, due to the lowest heat flux at this segment.

The distribution of the wetted wall temperatures for cases IV and V are interesting, in that although heat was applied to two segments on the sides of the tube, the corresponding wetted wall temperatures were lower than the wall temperatures at the top and bottom segments. The temperature profiles of cases II and III are mirror images and seemed to achieve a good symmetry. Cases IV and V seem to share some characteristics in its distribution, though not as strongly symmetrical as was expected. Where the segments were heated, the wall temperatures were slightly higher than the corresponding segments on the other side of the tube. Though the left-hand side of the tube, specifically segment 5, yielded a wetted wall temperature that was slightly higher than its counterpart, segment 1.

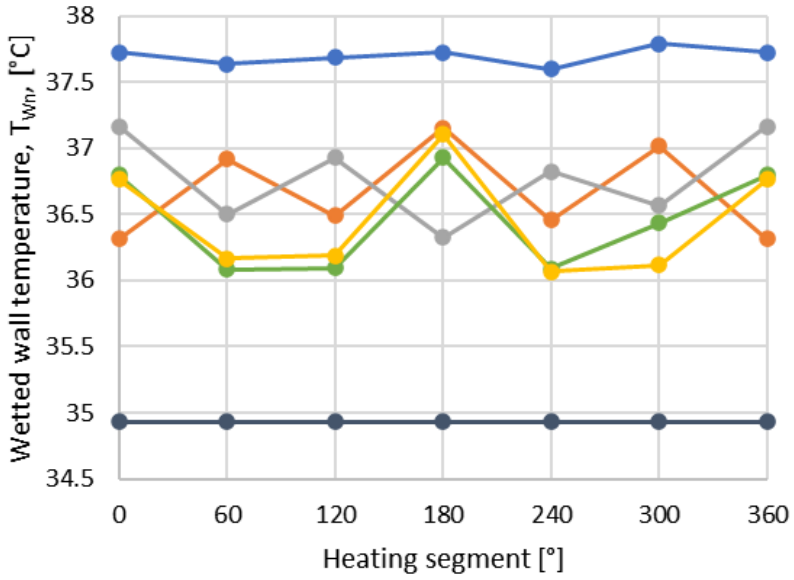

Figure 39: Wetted wall temperatures for all preliminary cases at G = 300 kg/m²s and T_{sat} = 35 °C at a vapour quality of x = 0.45

The total heat rate applied influences the wetted wall temperatures: as the heat rate is lowered, the average wetted wall temperatures also dropped. The overall averaged wetted wall temperatures are displayed in Figure 40. Case I had a higher overall wetted wall temperature than the non-uniform cases. Cases IV and V yielded the lowest overall average wall temperatures, and the overall average wetted wall temperature of case III was lower than case II by 0.25 °C. This gives rise to an expectation that the HTC may be slightly higher for the cases experiencing a lower heat rate application.

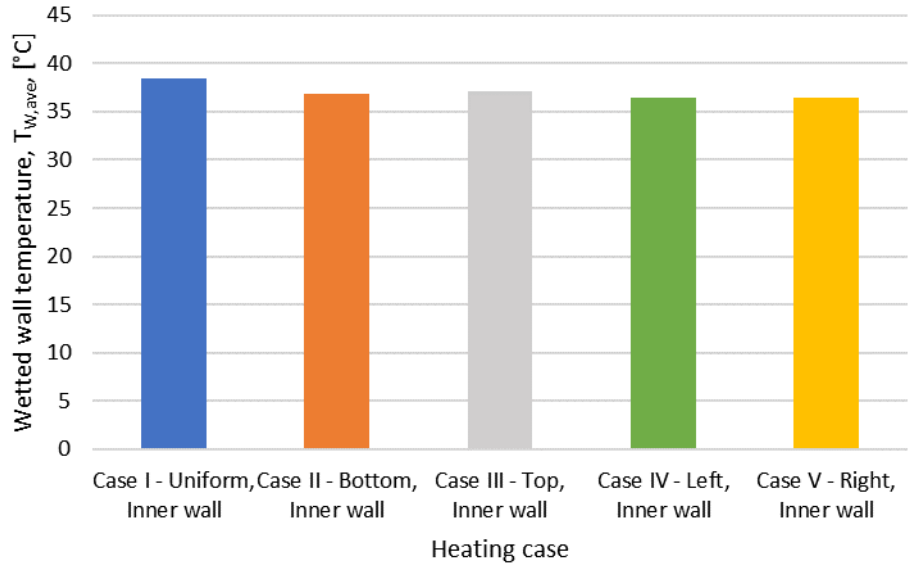

Figure 40: Overall average wetted wall temperature for all preliminary cases at G = 300 kg/m²s and T_{sat} = 35 °C at a vapour quality of x = 0.45

The lengthwise averaged HTC's are displayed in Figure 41. The local lengthwise averaged HTC achieved for case I (blue) are uniform over the circumference, as was expected. Cases II and III (orange, and grey) achieved higher HTC's where the segments were heated. The center segment in each case, being positioned at the bottom and top of the tube, respectively, had an HTC associated with it that was lower than the adjacent heated segments. Where there was no heat applied, a lower HTC resulted. The HTC at the heated segments in cases IV and V (green and yellow), were slightly higher than the HTC's found in case I for those segments. The unheated segments had HTC's comparable to the unheated segments of cases II and III. Where a heat flux of ± 6.7 kW/m² was applied, the lengthwise averaged HTC was between 2.5 and 3.5 kW/m²K.

Case IV (green) displayed a distribution that was not mirrored in case V (yellow). Segment 4, at 240 °, had a higher HTC associated with it than its counterpart in case V, segment 2, at 120 °. The HTC achieved on segment 4 was also not similar to the HTC on segment 5 (300 °), but higher. The wall temperatures reported for this segment were lower than segment 5, which may account for this difference in distribution of HTC. This anomaly may be of significance, or it may disappear in subsequent cases. The uncertainty associated with the HTC's seems to point to a significance in this anomaly. In the larger study, discussed in Section 6.4, this will be further investigated.

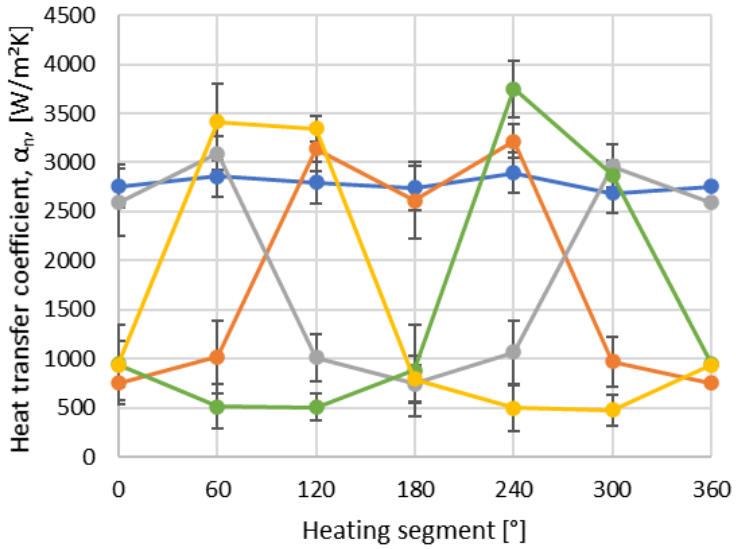

Figure 41: Local lengthwise averaged heat transfer coefficients for all preliminary cases at G = 300 kg/m²s and T_{sat} = 35 °C at a vapour quality of x = 0.45

The local HTC's achieved in case I were lower than the highest local HTC's achieved in cases II – V. The overall average HTC achieved for the cases considered in the preliminary investigation are shown in Figure 42. Cases II – V yielded lower HTC's than what was seen in case I and case III yielded a higher overall average HTC than case II. A comparative is presented in Table 15, where the overall average HTC for each of the non-uniform cases is compared to case I results. The table columns list the average heat transfer coefficient, the associated uncertainty, and an indication of the decrease in the overall HTC when compared to the uniform HTC.

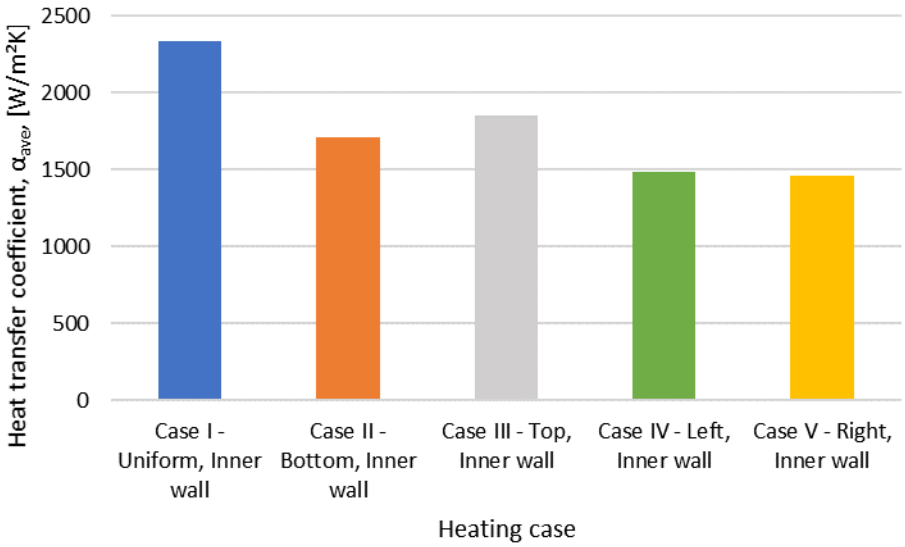

Figure 42: Overall heat transfer coefficient for all preliminary cases at G = 300 kg/m²s and T_{sat} = 35 °C at a vapour quality of x = 0.45

The final results for the 0.228 vapour quality investigation are included in the table to enable comparison in the effect that vapour quality may have on the HTC characteristics. In general, the qualitative tendency was the same, regardless of the vapour quality. However, the quantitative effect of the non-uniformity in heat flux is much larger in the higher vapour quality test cluster.

Case IV and V seemed to achieve only 53 % of the overall HTC found in case I (at a vapour quality of 0.440), which alludes to a very poor heat transfer mechanism. At a lower vapour quality (x = 0.228),

the overall average HTC achieved is a little larger fraction of case I, however, only 63.5 %. Case III yields the highest heat transfer efficiency of the non-uniform cases, at 72 % (x = 0.440) and 79.2 % (x = 0.228). The case most often seen in industry, case II, achieved only 73 % of the uniform HTC at x = 0.228. This means that the HTC of the fluid is not only determined by the heat flux applied locally over an area, but also related to the form of non-uniformity applied, and this is not linearly scalable. It is not necessarily true that having half the heating segments powered, will yield an HTC of half the magnitude of a uniform heating case.

Table 15: Overall average HTC for preliminary tests at G = 300 kg/m²s and T_{sat} = 35 °C

	x = 0.228			**x = 0.440**		
	α_{ave} [W/m²K]	**Uncertainty [W/m²K]**	**% of uniform HTC**	**α_{ave} [W/m²K]**	**Uncertainty [W/m²K]**	**% of uniform HTC**
Case I – Uniform	2335.8	104.1	100.0 %	2783.6	212.7	100.0 %
Case II – Bottom	1706.2	148.8	73.0 %	1782.1	265.7	64.0 %
Case III – Top	1850.1	143.5	79.2 %	2009.0	247.2	72.2 %
Case IV – Left	1482.4	197.3	63.5 %	1488.8	250.4	53.5 %
Case V – Right	1461.6	186.0	62.6 %	1486.9	259.9	53.4 %

6.4 The effect of a constant heat rate non-uniformly applied

The heat flux distributions used in the larger study are reported in the section. The heat rate for all the non-uniform cases was 160 W and was applied to the outer wall of the stainless-steel tube according to the non-uniform distribution chosen. The local heat flux applied onto the outer wall changed toward the inner wall according to the numerical method described in Section 5.1, and similar to what was shown in Section 6.3.

The heat rate staying constant resulted in the local heat flux being higher than 6.67 kW/m² when applied non-uniformly, for cases II – V. Figure 43 displays the heat flux that was applied on the outer wall of the tube for cases I – V. Additionally, the effective heat flux applied at the inner wall for these cases are displayed, along with the resulting temperature difference between the wall temperature and the bulk fluid temperature.

As can be seen in the figure, the uniform distribution does not change from the outer wall to the inner wall. Conduction is significantly present in cases II – V, due to the non-uniformity of the heat flux applied. The segments that were not heated in these cases did have an effective heat flux at the inner wall due to the effects of conduction. This resulted in slight changes in the temperature differences circumferentially. The heat flux distribution at the inner wall was directly responsible for the temperature difference distribution at the inner wall of the tube, for all cases. The temperature differences achieved did not, however, have as large of a gradient between adjacent segments as was seen in the heat flux.

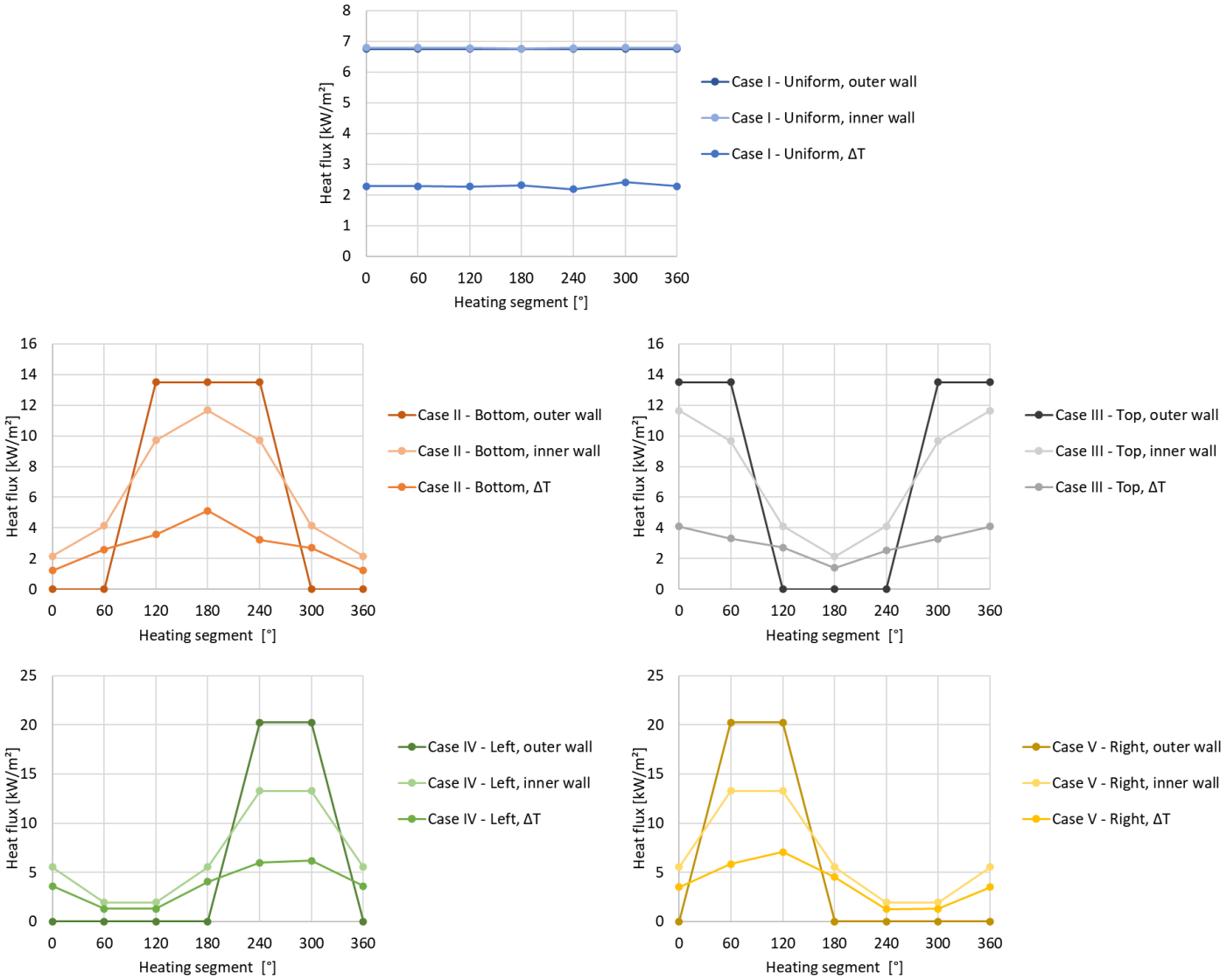

Figure 43: Effect of the heat rate dispersion on the heat flux at the inner wall of the tube and the resultant temperature difference

6.5 Results for all test cases

The results of all the test cases with a mass flux of 200 kg/m²s at a saturation temperature of 35 °C (cluster 200_35) are shown in the following sections. Contour plots of the different heating cases are presented, over the vapour qualities investigated. The vapour qualities under consideration were between 0.226 and 0.695. The measured temperatures are presented, determined as averaged values per segment, along the length of the tube. This is followed by the lengthwise averaged calculated wetted wall temperatures and the lengthwise averaged HTC's. Similar results on the test cases run on the mass flux of 200 kg/m²s at a saturation temperature of 40 °C (cluster 200_40), and the test cases run on the mass flux of 300 kg/m²s at the saturation temperatures of 35 °C (cluster 300_35) and 40 °C (cluster 300_40) can be found in Appendix F.

Figure 44 represents case I – Uniform heating for a mass flux of 200 kg/m²s and saturation temperature of 35 °C. Looking at Figure 44a, the measured temperatures over all vapour qualities investigated, did not yield a large difference circumferentially. A slightly higher temperature was measured at the lowest segment of the tube, segment 3, like what was found in the preliminary investigation, presented in Section 6.3. As the average vapour quality of the fluid increases, the measured temperature decreases, predictive of a higher pressure drop prevalent as the fluid undergoes flow boiling.

Figure 44b presents the lengthwise averaged wetted wall temperatures, extrapolated from the measured temperatures and the equivalent thermal resistances of the thermocouples, described in Section 5.1. This plot indicates that the wetted wall temperature is much closer to the bulk fluid temperatures, indicating the presence and influence of a liquid state in the fluid. This is as designed, that the fluid is in an annular flow pattern, distributing a liquid film on the tube wall around the tube circumference. The higher temperature at segment 3 can still be seen, as well as the temperature drop with the vapour quality increase.

Figure 44c presents the lengthwise averaged HTC's, calculated from the wetted wall temperatures presented in Figure 44b, and the heat flux applied, described in Section 5.1. As was expected from the higher wetted wall temperatures seen in Figure 44b, the HTC's were lower at segment 3. This was also seen in the preliminary investigation, described in Section 6.3. As the vapour quality increased, the HTC's also increased, pointing to a lesser difference in the wetted wall temperature and bulk fluid temperature at higher vapour qualities.

Figures 45 to 52 show the results of all the non-uniform heat flux investigations (cases II – IX) for the mass flux of 200 kg/m²s at a saturation temperature of 35 °C. The cases are presented like the uniform heating case, with the measured temperatures lengthwise averaged, followed by the lengthwise averaged wetted wall temperatures and lengthwise averaged local HTC's.

6.5.1 Case I – Uniform heating

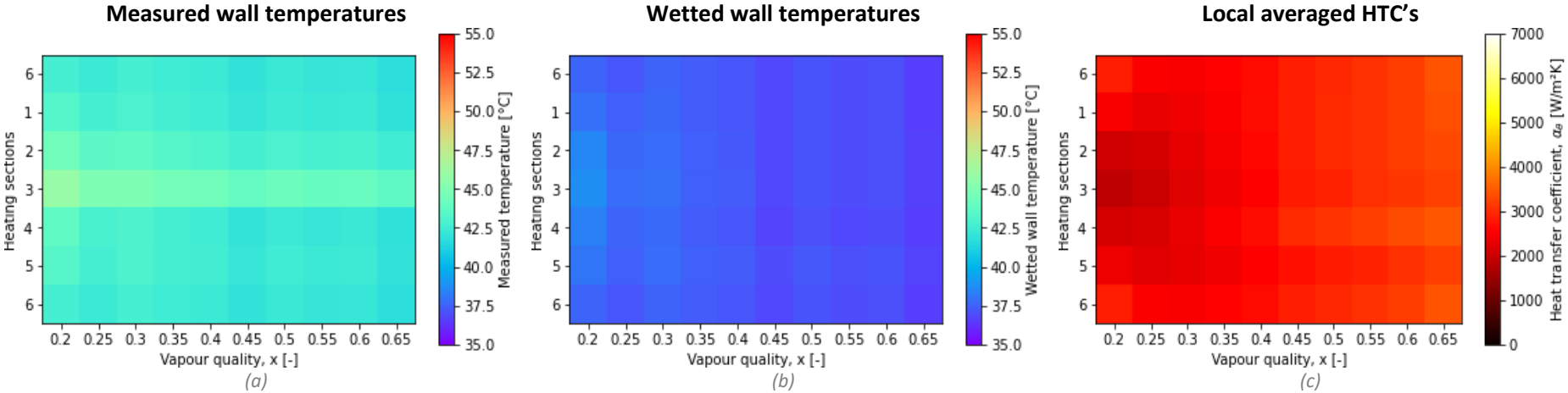

Figure 44: Results for case I - Uniform heating for G = 200 kg/m²s and T_B = 35 °C

6.5.2 Case II – Bottom heating

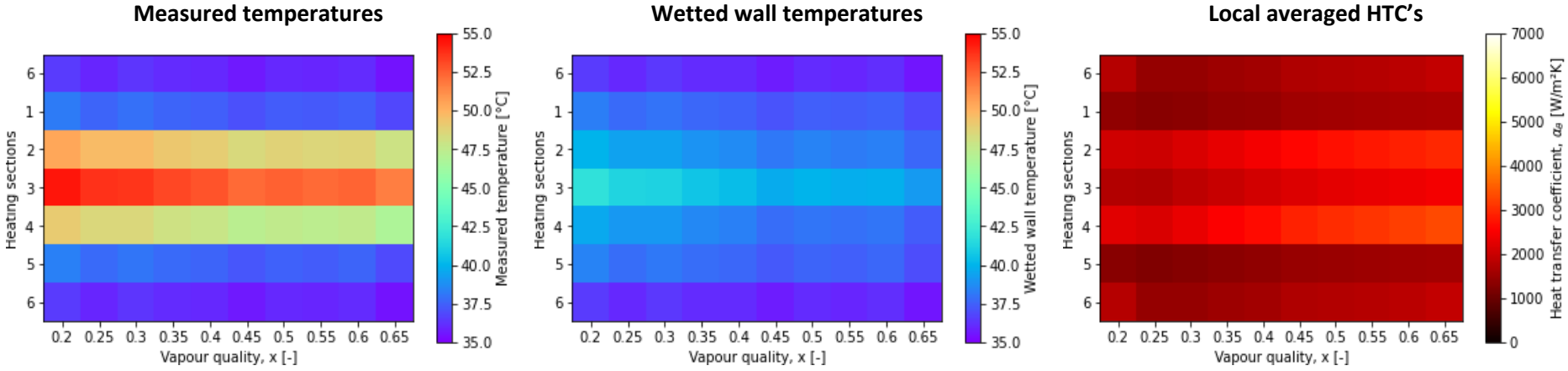

(a) *(b)* *(c)*

Figure 45: Results for case II - Bottom heating for G = 200 kg/m²s and T_B = 35 °C

6.5.3 Case III – Top heating

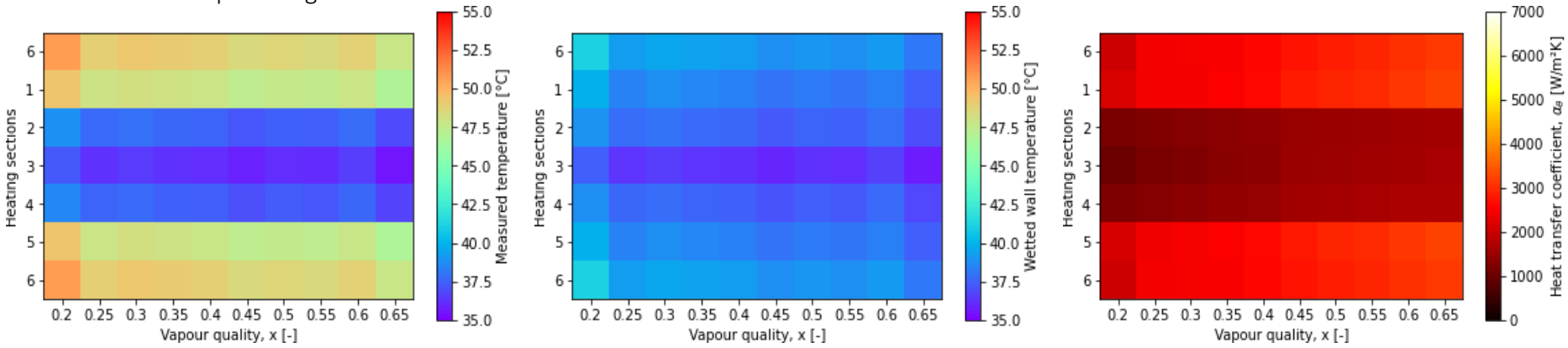

(a) *(b)* *(c)*

Figure 46: Results for case III - Top heating for G = 200 kg/m²s and T_B = 35 °C

6.5.4 Case IV – Left heating

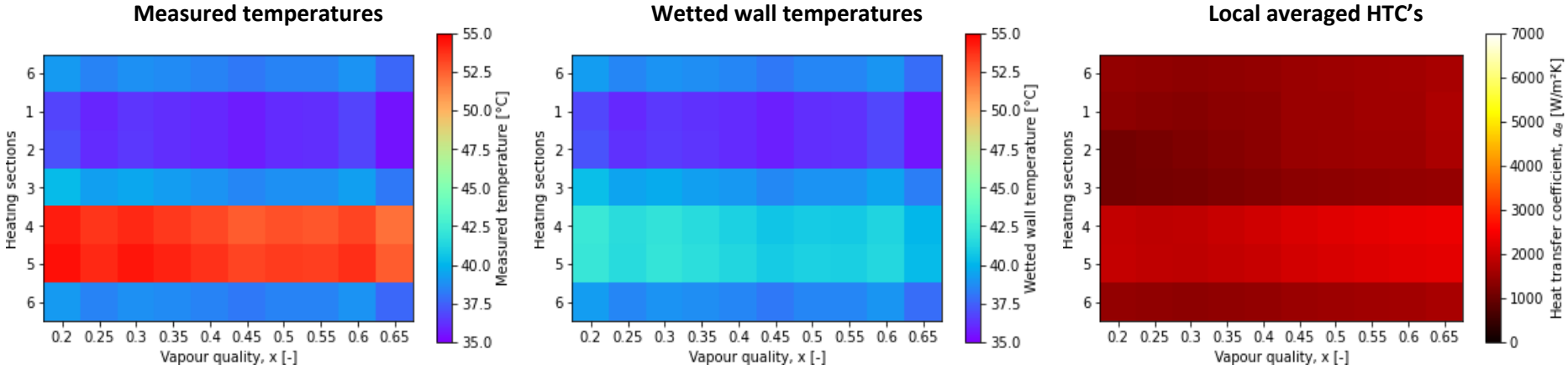

(a) *(b)* *(c)*

Figure 47: Results for case IV - Left heating for G = 200 kg/m²s and T_B = 35 °C

6.5.5 Case V – Right heating

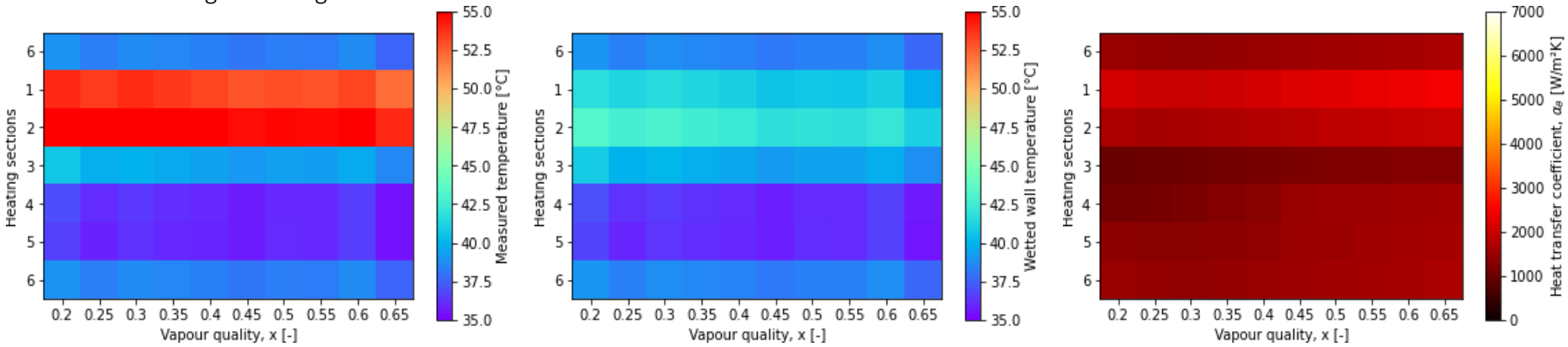

(a) *(b)* *(c)*

Figure 48: Results for case V - Right heating for G = 200 kg/m²s and T_B = 35 °C

6.5.6 Case VI – Segment 3 heating

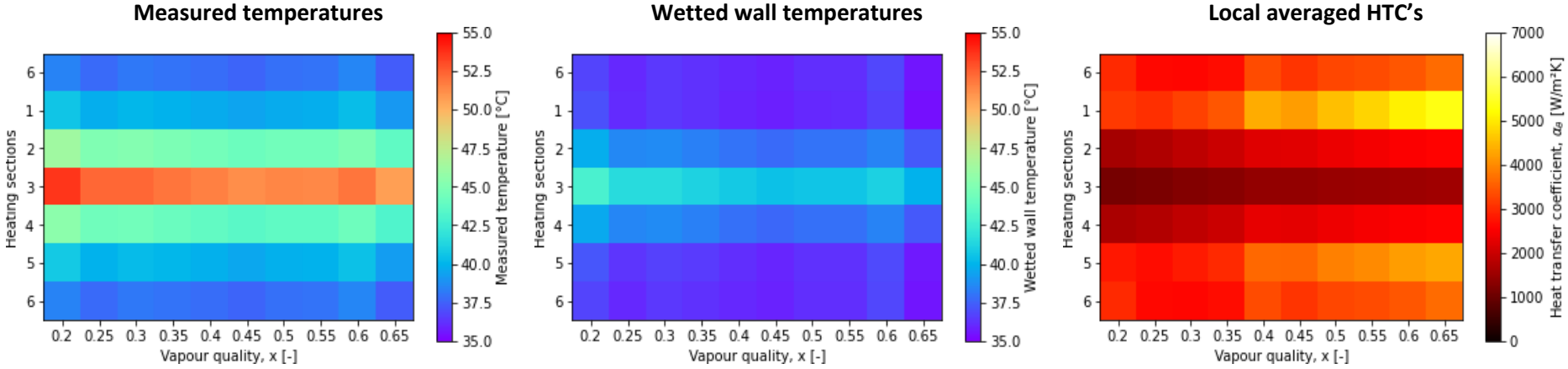

(a) *(b)* *(c)*

Figure 49: Results for case VI – Segment 3 heating for G = 200 kg/m²s and T_B = 35 °C

6.5.7 Case VII – Segment 6 heating

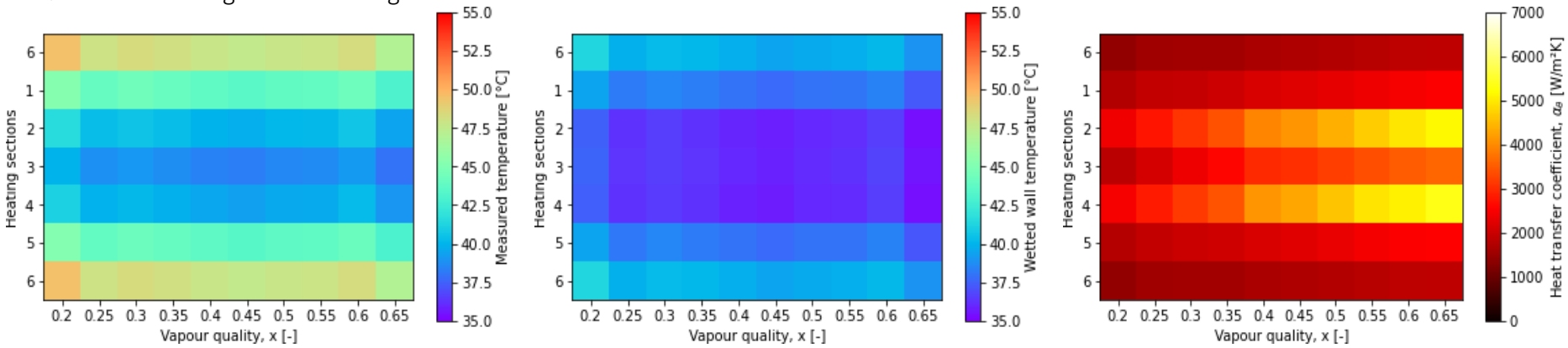

(a) *(b)* *(c)*

Figure 50: Results for case VII – Segment 6 heating for G = 200 kg/m²s and T_B = 35 °C

6.5.8 Case VIII – Segment 1 heating

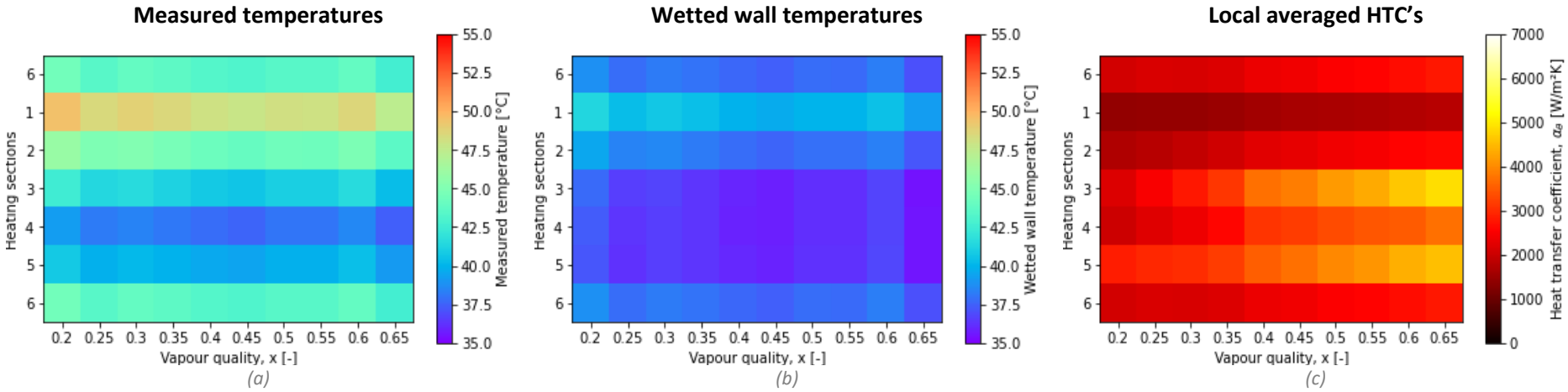

(a) *(b)* *(c)*

Figure 51: Results for case VIII – Segment 1 heating for G = 200 kg/m²s and T_B = 35 °C

6.5.9 Case IX – Segment 2 heating

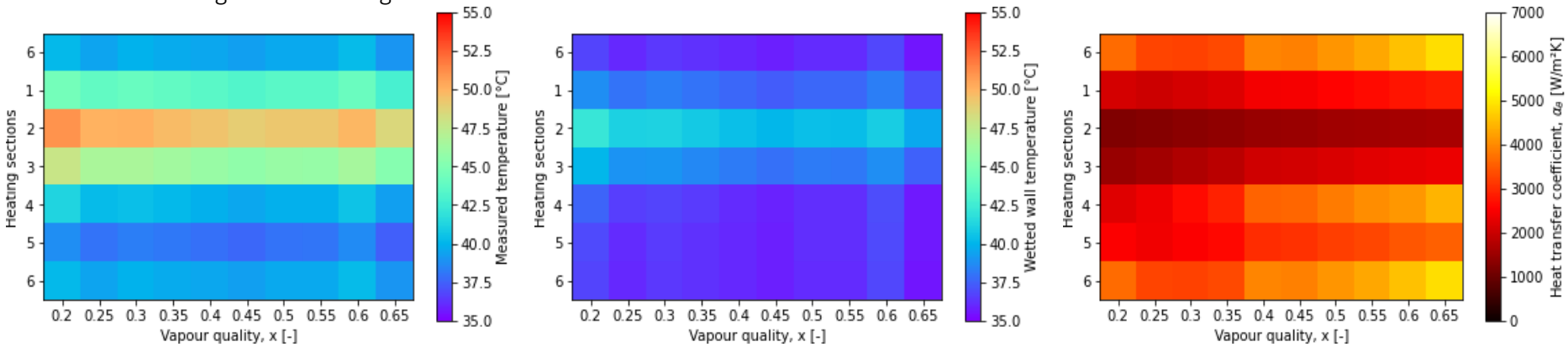

(a) *(b)* *(c)*

Figure 52: Results for case IX – Segment 2 heating for G = 200 kg/m²s and T_B = 35 °C

The case where the tube is heated by the bottom three segments, case II, is shown in Figure 45. The lengthwise averaged measured temperatures indicate that, though the heat flux is applied equally on the three bottom segments, segment 3 has a larger temperature measurement than its adjacent heated segments. The top segment, segment 6, in this case not heated, has a temperature slightly higher than the bulk fluid temperature. The wetted wall temperatures are significantly lower than the measured wall temperatures, still possessing the same distribution, where segment 3 is warmer than the adjacent heated segments. This results in local lengthwise averaged HTC's distributed such that segment 3 has a lower HTC when compared to the adjacent segments, though very slightly lower.

Figure 46 presents the measured and wetted wall temperatures and HTC's for the non-uniform heat flux case where the tube is heated through the top three segments, case III. The measured temperature of segment 6 is not notably higher than the adjacent segments. The wetted wall temperature distribution alters the temperature readings such that segment 6 has a higher temperature, and segment 3 has a lower wetted wall temperature. The resulting HTC's are distributed such that the top segments have about equal HTC's, and the lower segments have about equal HTC's, with the top HTC's being higher.

Figures 47 and 48 present the cases where the heat was applied to the tube through two segments, located at the left and right sides of the tube (cases IV and V), respectively. The measured temperatures in these cases are significantly higher than what was measured in the previously discussed cases. This is due to the high heat flux applied on these segments. The full heat rate of 160 W is to heat the tube through a third of its area. The wetted wall temperatures are higher than the fluid bulk temperature, but much lower than the measured wall temperatures. The HTC's achieved in these cases were a higher value where heating was applied on the tube, and the lowest HTC value at segment 3. Further, as mentioned in the preliminary tests, the HTC discrepancy seen in case IV, is not seen in case IV of this cluster, however, a slight resemblance of the anomaly is seen in case V of this cluster.

For cases II – V described thus far, the segments having HTC's comparable to the local HTC's achieved in case I are only segments 3 and 6 of cases II and III, respectively. The local HTC's achieved for cases IV and V were lower than the local HTC's achieved in case I. This gives the impression that cases IV and V will have poorer heat transfer efficiency, which was also seen in Section 6.3.

Continuing on, the following will be a discussion on the heating cases where the greatest heat flux was focused on a single segment, while the distribution applied over the tube anticipates a bell curve heat flux dispersion and endeavours to enhance its effect. Figures 49 to 52 display the results for the cases where the heat was supplied non-uniformly, but distributed as a bell curve distribution, focused on a single segment. Figure 49 displays the results for the case where the heat is supplied onto the tube through all the heating segments, with the peak heat flux at segment 3. Figure 50 presents the results for the case where segment 6 is subject to the peak heat flux, Figure 51 presents the results for the case where segment 1 is subject to the peak heat flux and Figure 52 displays the results for the case where segment 2 is subject to the peak heat flux.

The temperatures measured in cases VI - IX were highest at the segment where the peak heat flux was applied. The distributions of the temperatures are directly correlated to the heat flux distributions onto the tube. The wetted wall temperatures were lower than the measured temperatures, and higher than the bulk fluid temperature, with a similar distribution than was seen in the measured temperatures. The resulting HTC distributions are slightly less intuitive.

Looking at Figure 49, where the peak heat flux was applied to segment 3, the resulting HTC is the lowest in the complete distribution. The highest HTC's are reported at the segments that are furthest

from this point and adjacent to segment 6. Looking at Figure 50, where the peak heat flux is applied to segment 6, the resulting HTC is the lowest of all the segments. Again, the highest local HTC is achieved at the segments adjacent to the segment that is furthest from the peak heat flux.

Similarly, Figures 51 and 52 display results where the segments with the peak heat flux yield the lowest HTC's. For case VIII, the highest heat flux is applied to a segment adjacent to the top of the tube. The highest HTC in this case, is located adjacent to the furthest segment from the peak heat flux, as was the case in cases VI and VII. Case IX has the highest heat flux applied to a segment adjacent to the bottom of the tube. The highest HTC in this case, again, is adjacent to the furthest segment from the peak heat flux of the tube.

The HTC's achieved in cases VI – IX yielded results that, when averaged, may constitute a uniform heating effect. The segments with higher HTC's are higher than the local HTC's reported for the uniform cases, and those with lower HTC's are lower than the local HTC's reported for the uniform cases. It may be that anticipating the normal distribution dispersion in a tube yields a better overall HTC result.

6.6 The effect of gravity and tube manufacturing

Gravity plays a role in flow boiling characteristics of a fluid, as discussed in Section 2.6. It is, however, not expected to be a governing entity in this investigation, as the flow regime is annular. An annular flow consists of a fluid film covering the tube inner wall all around, ensuring no bubble interactions at the tube wall, when care is taken to steer clear of a critical heat flux boundary condition.

Nevertheless, a gravitational influence was seen in the two non-uniform heating cases where the peak heat flux was applied to the bottom of the tube, cases II and VI. Due to the nature of heat rising, the lowest segment consistently displayed a lower local HTC than was seen in symmetrical top heating cases, cases III and VII. In the investigations that would highlight the effect of gravity, cases VIII and IX, no gravitational interaction was seen. The HTC distributions achieved in these two cases seemed independent of gravitational effects.

Investigation into the effect of the manufacturing of the tube can be done by taking into consideration that a pressure port was attached onto the tube between segments 1 and 2. Case V, heating on the right side of the tube, where segments 1 and 2 would be the heating source, seems to capture the influence of turbulence introduced by a discontinuity in the inner tube wall. This alteration in the HTC distribution was also seen in the other clusters of the investigation, displayed in Appendix F. The segment closer to the top of the tube, that is heated, segment 1, yielded a local HTC that was higher than its adjacent heated segment, segment 2. This anomaly was not seen in the mirror case, case IV. Both the heated segments, segments 4 and 5, yielded a local HTC that was similar, and did not indicate any considerable difference.

6.7 The effect of saturation temperature and mass flux on the local HTC

The characteristic lengthwise averaged heat transfer coefficients for three distinct bottom heating cases are displayed in Figure 53. Looking at the figure, it is clear that the saturation temperature and mass flux do not influence the distribution of the local HTC's achieved. There is, however, a clear influence on the magnitudes of the HTC's.

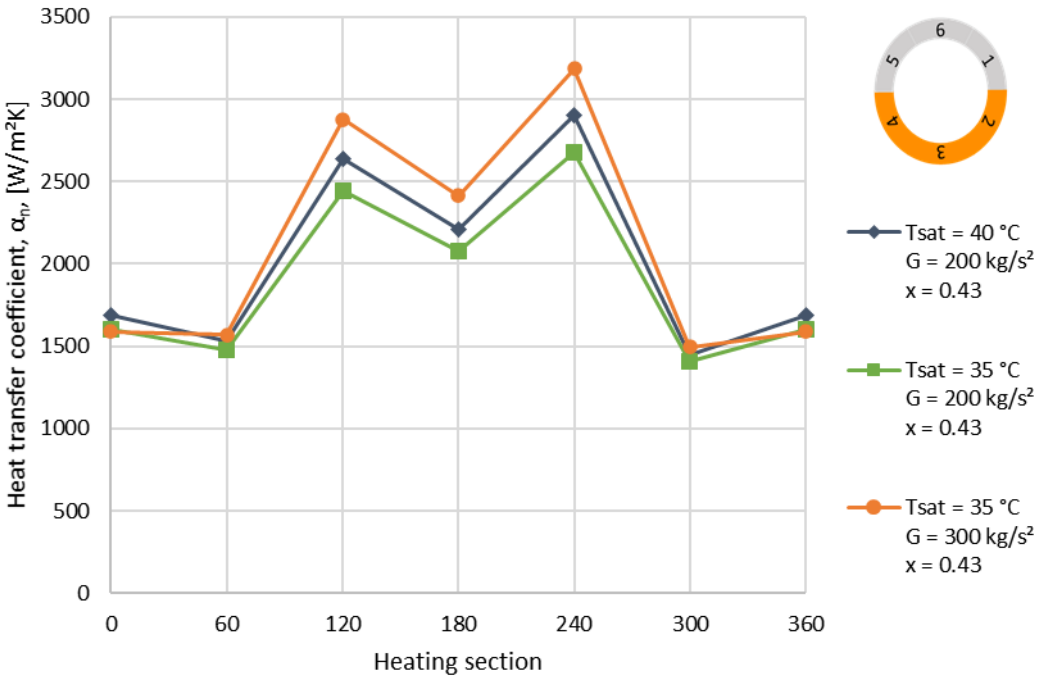

Figure 53: The effect of the saturation temperature on the local HTC of three bottom heating cases

Taking the green case (saturation temperature of 35 °C, mass flux of 200 kg/m²s) as the base case, the effect of the change in saturation temperature and mass flux can be clearly seen. When the saturation temperature is increased to 40 °C, this results in a slight increase in the magnitude of the HTC, and its effect is seen in all the segments independently, though smaller where the heat flux was lower. Changing the mass flux to 300 kg/m²s yields a much larger influence on the local HTC's achieved than was seen with a change in saturation temperature. The local HTC increase is significant where the heat flux applied is larger, and more difficult to discern where lower heat flux levels are applied. It can therefore be concluded that a higher mass flux and saturation temperature will yield a higher local HTC, though the effect of the mass flux change is much larger than the effect of the saturation temperature change.

6.8 The effect of non-uniformity of heat flux on the pressure drop over the heated section

Figure 54 presents the differential pressure measured over the test section during testing. The data for the pressure drop and HTC investigations were collected simultaneously. It should be noted from the figure that the pressure drop measured for all heating cases stayed constant, regardless of the non-uniformity of the heat flux distribution applied on the test section. This is because the pressure drop over the test section is only affected by the total heat rate applied to the test section, which stayed constant, and was only distributed differently.

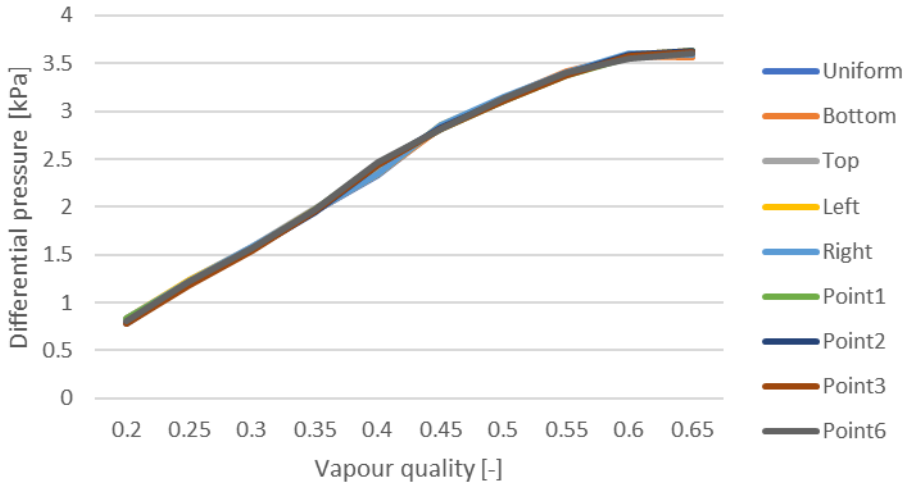

Figure 54: Pressure drop over the test section at different vapour qualities under different heat flux conditions for G = 200 kg/m²s and T_B = 35 °C

As described in Section 6.4, the measured temperatures decreased as the vapour quality increased. This is due to the pressure drop that increases as the vapour quality increases. For a saturated state to prevail, the saturation temperature needs to lower as the pressure in the system decreases. In all test cases the inlet conditions for the test section were held constant. Therefore, a larger pressure drop at a higher vapour quality would require a lower temperature proportionally.

This investigation focused on the circumferential differences in temperature over the test section, and the longitudinal temperature differences were averaged into the different segment temperatures. Effectively, the total average temperature of a segment dropped, due to the increased longitudinal temperature drop initiated by the pressure drop.

6.9 The effect of non-uniformity on the overall averaged HTC

The scrutiny of the non-uniformly heated cases has alluded to a very large influence of non-uniformity of an applied heat flux on the overall average HTC achieved in the annular flow boiling of R245FA. The differences can be seen in Figures 55 to 58.

Consistently, over all clusters, the case V yielded the lowest overall HTC, with case IV trailing closely. Case II yielded overall HTC that were higher than cases IV and V, though throughout, heating from the top proved to be slightly better. Cases VI – IX resulted in overall HTC's that are comparable to, and even in some cases, improve upon the uniform HTC's achieved.

In cases IV and V, two segments contribute to the increase in the overall HTC, while four segments contribute very little to the overall HTC. In cases II and III, three segments contribute to the increase of the overall HTC. However, the local HTC of the heated segments in cases IV and V do not reach the same local HTC that is achieved on the heated segments of cases II and III. This is due to the combination of the local heat flux and the affected local temperature difference. Intuitively, high temperature differences locally would be expected with high local heat fluxes, however, the combination of these quantities into HTCs show that the differences expected may not be what is achieved when a non-uniform heating is applied. Furthermore, the reduction in effectiveness of the local heat flux to realise an expected temperature difference locally, suggests a possibility of an optimal configuration, which in this study may have been overcome, resulting in the reduction of the effective HTC locally, and as a result overall.

Looking finer into the cases VI – IX, the heating on segment 1, case VIII, yielded higher overall HTC than its counterpart, case IX. Similarly, case VII indicated a higher overall HTC result than was obtained

in case VI, though this was not true for clusters 300_35 and 300_40. It may be that the mass flux may have a significant influence on which non-uniform heating case would yield a higher heat transfer efficiency.

Therefore, it can be concluded that, to yield a higher overall HTC it is better to anticipate the bell-shaped distribution of heat around the tube and apply the heat in a bell-shaped distribution around the tube. It is more beneficial to heat with every heating segment around the tube than to heat only certain segments and trust the distribution of heat through the material to cause a beneficial HTC in the fluid. When heating a tube non-uniformly, the optimal result will be achieved when heating the tube from the top. The most efficient heating case may be determined by the influence of the mass flux, however, no conclusive results to this end can be presented, as replicates in this study may be of more value.

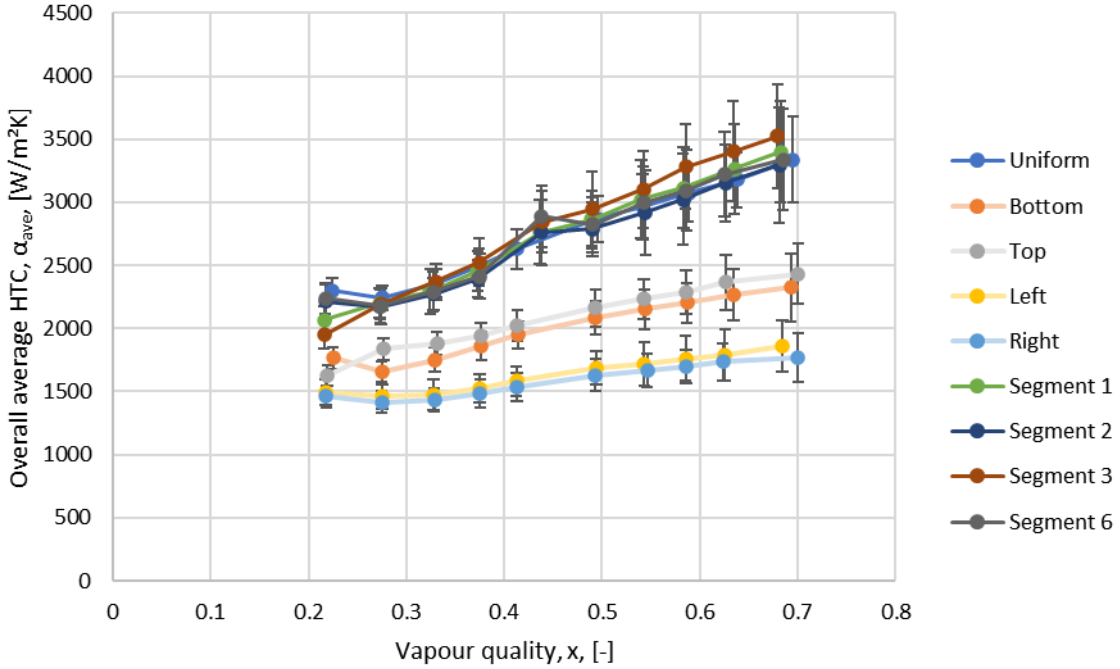

Figure 55: Overall HTC for all uniform and non-uniform cases with T_{sat} = 35 °C and G = 200 kg/m²s

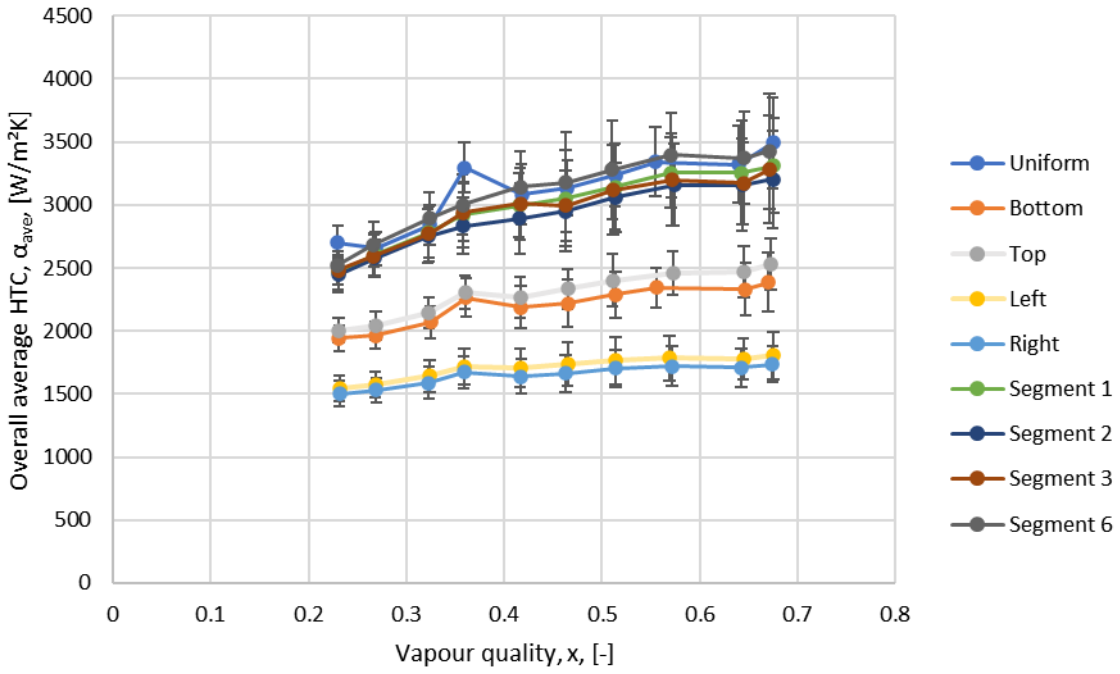

Figure 56: Overall HTC for all uniform and non-uniform cases with T_{sat} = 35 °C and G = 300 kg/m²s

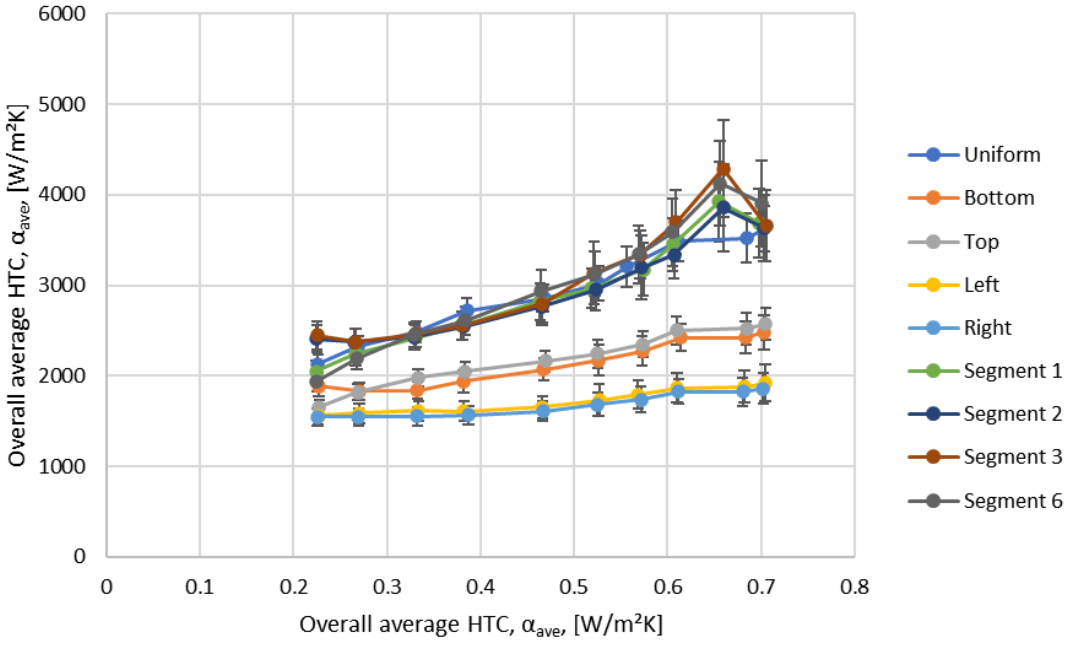

Figure 57: Overall HTC for all uniform and non-uniform cases with T_{sat} = 40 °C and G = 200 kg/m²s

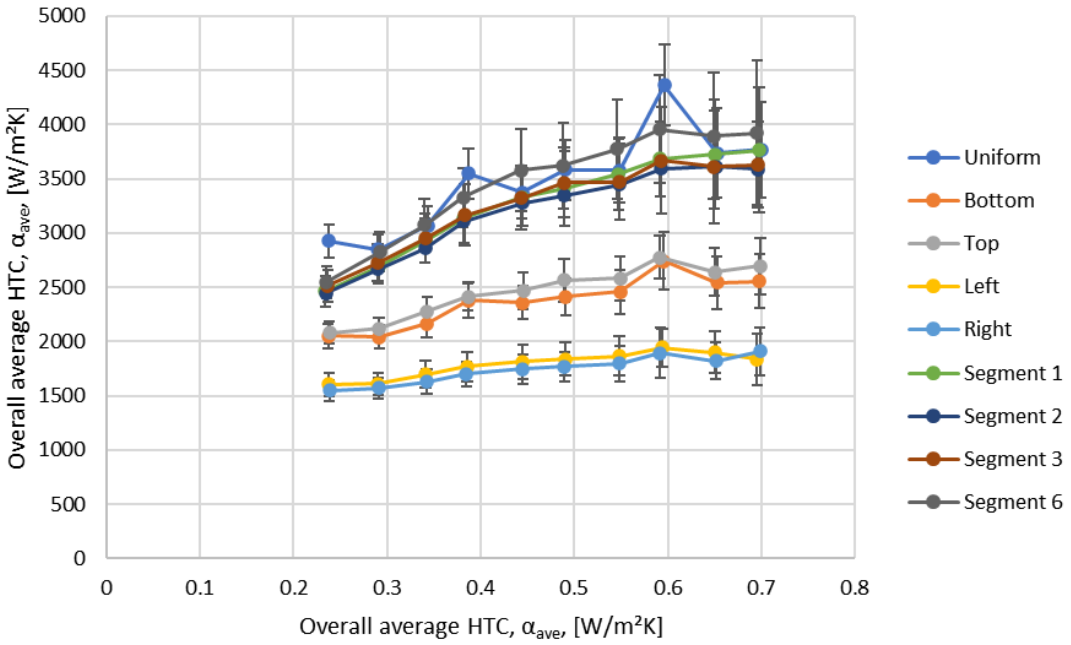

Figure 58: Overall HTC for all uniform and non-uniform cases with T_{sat} = 40 °C and G = 300 kg/m²s

The anomalies seen in these plots could not be avoided, as the facility on which tests occurred, operated at its limiting conditions. A saturation temperature of 40 °C is unstable when it is paired with a mass flux of 300 kg/m²s, and a vapour quality of 0.6. Similarly, at a vapour quality of 0.65, a saturation temperature of 40 °C and a mass flux of 200 kg/m²s resulted in flow anomalies that could not be ironed out during testing. A high mass flux of 300 kg/m²s at the lowest saturation temperature possible on the facility, 35 °C, resulted in multiple unstable conditions, the largest of which occurred at a vapour quality of 0.35.

7 Summary, Recommendations and Conclusion

7.1 Summary

The integration of PTC technology on solar fields as a means of integrating of an alternative energy source to coal incineration, has proven to be a viable solution. The design and prediction of operation of these PTC's have been largely based on the assumption that uniform and non-uniform heat flux distributions do not have significant influences on the overall HTC of the fluid as it boils. Very little has been studied to prove or disprove this assumption. This investigation was done to experimentally study the effect of circumferential non-uniformity of the heat flux on the HTC achieved in the annular flow boiling of R245FA.

The facility used for this investigation was a modular Organic Rankine setup, that made it possible to integrate a non-uniformly heated test section into the facility. A control system was designed to facilitate easy heat flux distribution manipulation over six elements of Nichrome heating wire. The test section had a heated length, (L_{h}), of 0.9 m, an inner diameter, (D_{i}), of 8.5 mm and a wall thickness, (t_{SS}), of 2.11 mm. The flow was heated with a total heat rate of 170 W, distributed in nine (9) distinctly different cases, while undergoing flow boiling in the annular flow pattern ($0.2 \leq x \leq 0.7$).

The experiments were done on four combinations of saturation temperatures of 35 and 40 °C and mass fluxes of 200 and 300 kg/m²s. An increase in saturation temperature and mass flux led to an increase in the HTC, on the overall and local resolution. This was in agreement with what had been seen in other HTC investigations, specifically under uniform heating. The effect of the mass flux was seen to be more substantial.

The goal was to evaluate and compare local and overall averaged HTC's to establish the effect that the heat flux distributions have on the heat transfer properties of the fluid. This was done by temperature measurements taken on the tube outer wall and extrapolating into the tube inner wall, to determine the inner wall temperature. An equivalent thermal resistance was utilised to achieve this extrapolation. An overall pressure drop was also directly measured, to isolate the influence of non-uniformity of the heat flux. It was found that the circumferential distribution of heat flux had no impact on the pressure drop of the fluid as it undergoes boiling.

The uniform distribution HTC results were compared to similar studies, and the results were in agreement. A single non-uniform heating case, heating from the bottom, was considered for validation of the non-uniform method. However, the construction of the test setup seemed to influence the results significantly, and a conclusion of the validity of the method was solely based on the agreements found in the uniform distribution case.

It was found that the non-uniformity in heat flux significantly influence the HTC locally and subsequently overall. The overall HTC achieved when the tube is heated from the sides is markedly lower than a uniform heating case (45.6 % lower). Bottom heating is less effective than top heating, overall, and both these cases are significantly less effective than uniform heating (28 % lower). The non-uniform cases where a bell-shaped heat flux distribution is anticipated, yielded results that are directly comparable with a uniformly heated segment. It was found that focusing the peak heat flux at the bottom, top and sides, yielded remarkably similar results (5 % average difference), with the most effective of the four focused heat flux cases being dependent on the mass flux and saturation temperature combinations.

7.2 Conclusion

Overall HTC and lengthwise averaged HTC were captured for nine (9) different heat flux distribution cases. It was found that, in cases where the heat flux was applied to the top, bottom and sides, the highest HTC locally were found where the heat flux was highest. However, the bell shape distributed heat fluxes yielded the lowest HTC locally where the heat flux was at a peak. This suggests that a peak local heat flux exists that corresponds to a peak HTC.

Heating from the sides yields the lowest overall HTC, and heating at the bottom is less efficient than heating only from the top. Distributing the heat in a bell-shaped distribution around the tube circumference was found to be as effective as the uniform heating case, and in some instances, more effective.

The PTC application with DSG specifically utilises a bottom heating non-uniformity in heat flux distribution. In this study it was determined that for a bottom heating non-uniform case there was a difference of at least 28 % between the HTC achieved under uniform and non-uniform heating distributions. Therefore, approximating the heating characteristics of a non-uniformly heated substance from a uniform analysis may be erroneous.

Non-uniformity in the circumferential distribution of heat to a tube has a significant influence on the heat transfer characteristics of the fluid but does not influence the pressure drops that the fluid undergoes when boiling.

7.3 Recommendations

When a further study is done on the effects of circumferentially non-uniform heat flux on flow boiling of a refrigerant, the following recommendations may prove useful.

The largest contributor to the uncertainty on the HTC was the temperature difference over the tube wall. Improving the temperature measurement at construction will greatly reduce this uncertainty. Channels may be machined into the tube on the outer wall, in which to sink the thermocouple wires. Alternatively, a thermal boundary may be introduced that discourages heat transfer directly to the thermocouple wires.

The stability of the flow was impacted by the operational limitations of the facility. Early on in the investigation alterations may need to be made on the facility to ensure the experimental requirements are met within optimal operational regions. Alterations may be done considering factors including pump operation, tube length implications and heating capabilities. Further work on this study may be repeated on larger tube diameters more suited to direct industry application.

Increasing the resolution on the distribution network may refine the results to a point that quantitative conclusions may be made on the effect of non-uniformity on the HTC of a fluid, and the possibility may arise to establish correlations.

This study suggests that there may be a peak local heat flux combination with a peak HTC, when the heat flux distribution is a bell-shaped curve. An investigation into this anomaly may prove to establish methods of improvements of efficiency in the industry.

8 Bibliography

ALTENERGY. 2018. *Renewable energy* [Online]. Alternative Energy. Available: http://www.altenergy.org/renewables/renewables.html [Accessed 30 Sept 2019].

BALACHANDER, P., RAJA, B. & LAL, D. M. 2011. Investigation on Boiling Heat Transfer Characteristics of R404A in a 7.49-mm Smooth Horizontal Tube. *Experimental Heat Transfer,* 24**,** 355-369.

BELL, I. H., WRONSKI, J., QUOILIN, S. & LEMORT, V. 2014. Pure and Pseudo-pure Fluid Thermophysical Property Evaluation and the Open-Source Thermophysical Property Library CoolProp. *Industrial & Engineering Chemistry Research,* 53**,** 2498-2508.

BENFORD, D. J., POWERS, T. J. & MOSELEY, S. H. 1999. Thermal conductivity of Kapton tape. *Cryogenics,* 39**,** 93-95.

BENNETT, A. W., HEWITT, G. F., KEARSEY, H. A., KEEYS, R. K. F. & LACEY, P. M. C. 1965-1966. Flow visualisation studies of boiling at high pressure. *Proc.Inst.Mech.Eng,* 180.

BORETTI, A., CASTELLETO, S. & AL-ZUBAIDY, S. 2017. Concentrating solar Power Tower: Latest Status Report and Survey of Development Trends.

CHANG, C., LI, X. & ZHANG, Q. Q. 2014. Experimental and Numerical Study of the Heat Transfer Characteristics in Solar Thermal Absorber Tubes with Circumferentially Non-uniform Heat Flux. *Energy Procedia,* 49**,** 305-313.

CHAUDHARY, G. Q., KOUSAR, R., MUZAFFAR, A., AMAR, M., KHURAM PERVEZ, A., SHABAZ KHAN, L., MUHAMMAD RAMEEZ UD, D. & DITTA, A. 2018. Small-Sized Parabolic Trough Collector System for Solar Dehumidification Application: Design, Development, and Potential Assessment. *International Journal of Photoenergy,* 2018**,** 12.

CHEN, J. C. 1966. Correlation for Boiling Heat Transfer to Saturated Fluids in Convective Flow. *Industrial & Engineering Chemistry Process Design and Development,* 5**,** 322-329.

CHENG, Z. D., HE, Y. L., XIAO, J., TAO, Y. B. & XU, R. J. 2010. Three-dimensional numerical study of heat transfer characteristics in the receiver tube of parabolic trough solar collector. *International Communications in Heat and Mass Transfer,* 37**,** 782-787.

CHO, K. & TAE, S. J. 2001. Condensation heat transfer for R-22 and R-407C refrigerant-oil mixtures in a microfin tube with a U-bend. *International Journal of Heat and Mass Transfer,* 44**,** 2043-2051.

CLIFFORD, K. H. 2017. Advances in central receivers for concentrating solar applications. *Solar Energy*.

DIRKER, J., MEYER, J. P. & GARACH, D. V. 2014. Inlet flow effects in micro-channels in the laminar and transitional regimes on single-phase heat transfer coefficients and friction factors. *International Journal of Heat and Mass Transfer,* 77**,** 612-626.

DIRKER, J., MEYER, J. P. & REID, W. J. 2018. Experimental investigation of circumferentially non-uniform heat flux on the heat transfer coefficient in a smooth horizontal tube with buoyancy driven secondary flow. *Experimental Thermal and Fluid Science,* 98**,** 480-496.

DITTUS, F. W. & BOELTER, L. M. K. 1930. Heat transfer in automobile radiators of tubular type. *Univ. California, Berkeley. Publ. Engrg. ,* 2**,** 443–461.

DUNN, P. F. 2014. Measurement and data analysis for engineering and science. Third edition. ed. Boca Raton: CRC Press, Taylor & Francis.

ELATAR, A. & SIDDIQUI, K. 2014. The effect of mixed convection on the structure of channel flow at low Reynolds numbers. *International Journal of Heat and Fluid Flow,* 46**,** 29-42.

GRAUSO, S., MASTRULLO, R., MAURO, A. W., THOME, J. R. & VANOLI, G. P. 2013. Flow pattern map, heat transfer and pressure drops during evaporation of R-1234ze(E) and R134a in a horizontal, circular smooth tube: Experiments and assessment of predictive methods. *International Journal of Refrigeration,* 36**,** 478-491.

GRECO, A. 2008. Convective boiling of pure and mixed refrigerants: An experimental study of the major parameters affecting heat transfer. *International Journal of Heat and Mass Transfer,* 51**,** 896-909.

GUNTHER, M., JOEMANN, M. & CSAMBOR, S. 2012. Advanced CSP Teaching Materials: Chapter 5 Parabolic Trough Technology.

GUO, Q., LI, M. & TIAN, X. 2020. Experimental study on flow boiling heat transfer characteristics of R134a, R245fa and R134a/R245fa mixture at high saturation temperatures. *International Journal of Thermal Sciences,* 150**,** 106195.

HACHICHA, A. A., RODRÍGUEZ, I. & GHENAI, C. 2018. Thermo-hydraulic analysis and numerical simulation of a parabolic trough solar collector for direct steam generation. *Applied Energy,* 214**,** 152-165.

HAMERSMA, P. J. & HART, J. 1987. A pressure drop correlation for gas/liquid pipe flow with a small liquid holdup. *Chemical Engineering Science,* 42**,** 1187-1196.

HAO, Y., WANG, Y. & HU, T. 2016. The flow distribution in the parallel tubes of the cavity receiver under variable heat flux. *Applied Thermal Engineering,* 108**,** 641-649.

HEWITT, G. F. 2008. Multiphase flow in the energy industries. *Journal of Engineering Thermophysics,* 17**,** 12-23.

JABARDO, S., MARIA, J., FILHO, B. & PEDONE, E. 2000. Convective boiling of halocarbon refrigerants flowing in a horizontal copper tube - an experimental study. *Experimental Thermal and Fluid Science,* 23**,** 93-104.

KANDLIKAR, S. G. 2002. Fundamental issues related to flow boiling in mini-channels and micro-channels. *Exp. Therm. Fluid Sci.,* 26 389–407.

KANDLIKAR, S. G. 2010. Scale effects on flow boiling heat transfer in microchannels: a fundamental perspective. *Int. J. Therm. Sci.***,** 1073–1080.

KANDLIKAR, S. G. & STEINKE, M. E. 2003. Predicting Heat Transfer During Flow Boiling in Minichannels and Microchannels. *TRANSACTIONS- AMERICAN SOCIETY OF HEATING REFRIGERATING AND AIR CONDITIONING ENGINEERS,* 109**,** 667-676.

KHALEDI, H. A., SMITH, I. E., UNANDER, T. E. & NOSSEN, J. 2014. Investigation of two-phase flow pattern, liquid holdup and pressure drop in viscous oil–gas flow. *International Journal of Multiphase Flow,* 67**,** 37-51.

KHARANGATE, C. R., O'NEILL, L. E. & MUDAWAR, I. 2016. Effects of two-phase inlet quality, mass velocity, flow orientation, and heating perimeter on flow boiling in a rectangular channel: Part 1 – Two-phase flow and heat transfer results. *International Journal of Heat and Mass Transfer,* 103**,** 1261-1279.

KUNDU, A., KUMAR, R. & GUPTA, A. 2014a. Evaporative heat transfer of R134a and R407C inside a smooth tube with different inclinations. *International Journal of Heat and Mass Transfer,* 76**,** 523-533.

KUNDU, A., KUMAR, R. & GUPTA, A. 2014b. Heat transfer characteristics and flow pattern during two-phase flow boiling of R134a and R407C in a horizontal smooth tube. *Experimental Thermal and Fluid Science,* 57**,** 344-352.

LAZAREK, G. M. & BLACK, S. H. 1982. Evaporative heat transfer, pressure drop and critical heat flux in a small vertical tube with R-113. *International Journal of Heat and Mass Transfer,* 25**,** 945-960.

LEWIS, J. 2019. *Low side vs. High side transistor switch* [Online]. Available: https://www.baldengineer.com/low-side-vs-high-side-transistor-switch.html [Accessed October 22 2019].

LI, Z. Y., HUANG, Z. & TAO, W. Q. 2016. Three-dimensional numerical study on fully-developed mixed laminar convection in parabolic trough solar receiver tube. *Energy,* 113**,** 1288-1303.

LIN, W. L. & LIN, T. F. 1996a. Experimental study of unstable mixed convection of air in a bottom heated horizontal rectangular duct. *International journal of heat and mass transfer.,* 39**,** 1649.

LIN, W. L. & LIN, T. F. 1996b. Experimental study of unstable mixed convection of air in a bottom heated horizontal rectangular duct. *International Journal of Heat and Mass Transfer,* 39**,** 1649-1663.

LIU, J., LIU, J. & XU, X. 2020. Diabatic visualization study of R245fa two phase flow pattern characteristics in horizontal smooth and microfin tube. *International Journal of Heat and Mass Transfer,* 152**,** 119513.

LIU, Z. & WINTERTON, R. H. S. 1991. A general correlation for saturated and subcooled flow boiling in tubes and annuli, based on a nucleate pool boiling equation. *International Journal of Heat and Mass Transfer,* 34**,** 2759-2766.

LOFLIN, L. 2018. *Using Darlington Transistors Driving 2N3055-MJ2955 Power Transistors* [Online]. Available: http://www.bristolwatch.com/ele/tr6.htm [Accessed June 2019].

MANAVELA CHIAPERO, E., FERNANDINO, M. & DORAO, C. A. 2014. Experimental results on boiling heat transfer coefficient, frictional pressure drop and flow patterns for R134a at a saturation temperature of 34 °C. *International Journal of Refrigeration,* 40**,** 317-327.

MOFFAT, R. J. 1982. Contributions to the Theory of Single-Sample Uncertainty Analysis. *Journal of Fluids Engineering,* 104**,** 250-258.

MWESIGYE, A., BELLO-OCHENDE, T. & MEYER, J. P. 2014. Minimum entropy generation due to heat transfer and fluid friction in a parabolic trough receiver with non-uniform heat flux at different rim angles and concentration ratios. *Energy,* 73**,** 606-617.

NREL, S. 2018. *Concentrating Solar Power Project Files* [Online]. Available: https://solarpaces.nrel.gov/ [Accessed 15 August 2018].

OKAFOR, I. F., DIRKER, J. & MEYER, J. P. 2014. Influence of circumferential solar heat flux distribution on the heat transfer coefficients of linear Fresnel collector absorber tubes. *Solar Energy,* 107**,** 381-397.

OKAFOR, I. F., DIRKER, J. & MEYER, J. P. 2017. Influence of non-uniform heat flux distributions on the secondary flow, convective heat transfer and friction factors for a parabolic trough solar collector type absorber tube. *Renewable Energy,* 108**,** 287-302.

OULD DIDI, M. B., KATTAN, N. & THOME, J. R. 2002. Prediction of two-phase pressure gradients of refrigerants in horizontal tubes. *International Journal of Refrigeration,* 25**,** 935-947.

REMLEY, T., ABDEL-KHALIK, S., JETER, S., GHIAASIAAN, S. & DOWLING, M. 2001. Effect of non-uniform heat flux on wall friction and convection heat transfer coefficient in a trapezoidal channel. *International journal of heat and mass Transfer,* 44**,** 2453-2459.

RYCROFT, M. 2016. *Organic Rankine cycle and waste heat recovery* [Online]. EE Publishers. Available: https://www.ee.co.za/article/organic-rankine-cycle-waste-heat-recovery.html [Accessed 02 April 2021].

SAISORN, S., KAEW-ON, J. & WONGWISES, S. 2013. An experimental investigation of flow boiling heat transfer of R-134a in horizontal and vertical mini-channels. *Experimental Thermal and Fluid Science,* 46**,** 232-244.

SALLABERRY, F., ZHIYONG, T., JAUREGI, O. G., FURBO, S., PERERS, B., ZOURELLIS, A. & ROTHMANN, J. H. 2018. Evaluation of the Tracking Accuracy of Parabolic-Trough Collectors in a Solar Plant for District Heating. *AIP Conference Proceedings,* 2033.

SARDESHPANDE, M. V. & RANADE, V. V. 2013. Two-phase flow boiling in small channels: A brief review. *Sadhana,* 38**,** 1083-1126.

SHIPPLANTS, A. I. 2018. *Solar Thermal Plants Database* [Online]. Available: http://ship-plants.info/solar-thermal-plants?collector_type=5 [Accessed 18 August 2019].

SHIRES, G. L. 2011. *Nusselt Number* [Online]. Thermopedia. [Accessed 10 October 2019].

SIEDER, E. N. & TATE, G. E. 1936. Heat Transfer and Pressure Drop of Liquids in Tubes. *Industrial and Engineering Chemistry,* 28**,** 1429–1435.

SPEDDING, P. L., COOPER, R. K. & MCBRIDE, W. J. 2003. A Universal Flow Regime Map for Horizontal Two-Phase Flow in Pipes. *Developments in Chemical Engineering and Mineral Processing,* 11**,** 95-106.

SYDNEY, U. O. 2005. *Classification of Flows, Laminar and Turbulent Flows* [Online]. Available: http://www-mdp.eng.cam.ac.uk/web/library/enginfo/aerothermal_dvd_only/aero/fprops/pipeflow/node8.html [Accessed October 2019].

TANG, Z., ZHAO, X. P., LI, Z. Y. & TAO, W. Q. 2017. Multi-scale numerical analysis of flow and heat transfer for a parabolic trough collector. *International Journal of Heat and Mass Transfer,* 106**,** 526-538.

VAN DEN BERGH, W. J., DIRKER, J., MARKIDES, C. N. & MEYER, J. P. Preliminary investigation into the effect of step changes in boiling heat flux on R134a in a horizontal macro tube. HEFAT Conference, 2019.

WANG, D., ZHAO, L., NIE, X., LU, Y. & DENG, S. 2019. Experimental study on flow boiling characteristics of R-245fa in circular tube under non-uniform heat flux. *International Journal of Heat and Mass Transfer,* 143.

WANG, Z., NI, J., ZHAO, L., DENG, S. & ZHAO, D. 2017. Simulation and optimization of parabolic trough receiver with non-uniform heat flux distribution: A review. *Energy Procedia,* 142**,** 700-707.

WEISE, S., DIETRICH, B. & WETZEL, T. 2020. Flow-pattern based prediction of flow boiling heat transfer in horizontal tubes with circumferentially varying heat flux. *International Journal of Heat and Mass Transfer,* 148.

WHITAKER, S. Forced convection heat transfer correlations for flow in pipes, past flat plates, single cylinders, single spheres, and for flow in packed beds and tube bundles. 1972.

ZARZA, E., VALENZUELA, L. & LEON, J. 2004. Solar Thermal Power Plants with Parabolic Trough Collectors.

Appendices

A. Thermal distribution in different tube materials

The investigation of a non-uniform heat flux boundary condition on the HTC of a fluid, requires the tube material through which the flow will be heated to have a low thermal conductivity. In solar fields, steel is used for the tube material.

Experimental investigations are often done on copper tubing (Jabardo *et al.*, 2000, Lin and Lin, 1996b). In the existing facility a copper test section was also utilized. A comparison of the heat transfer through copper and stainless steel has been done to determine qualitatively whether the imposed non-uniform heat flux will be transferred to the fluid. This calculation was done as an approximation of the thermal resistance each of the materials has to heat flow. The heat flow can be approximated by

$$Q = \frac{\Delta T}{R_{tot}} \tag{33}$$

The temperature difference ΔT can be set to 1°C to ease in the calculations: it is assumed to be of no consequence to the heat flux distribution alteration that occurs in the material. An equivalent thermal resistance network can be created to further simplify the problem. A schematic of the "path" follows by heat transfer is shown in Figure 59.

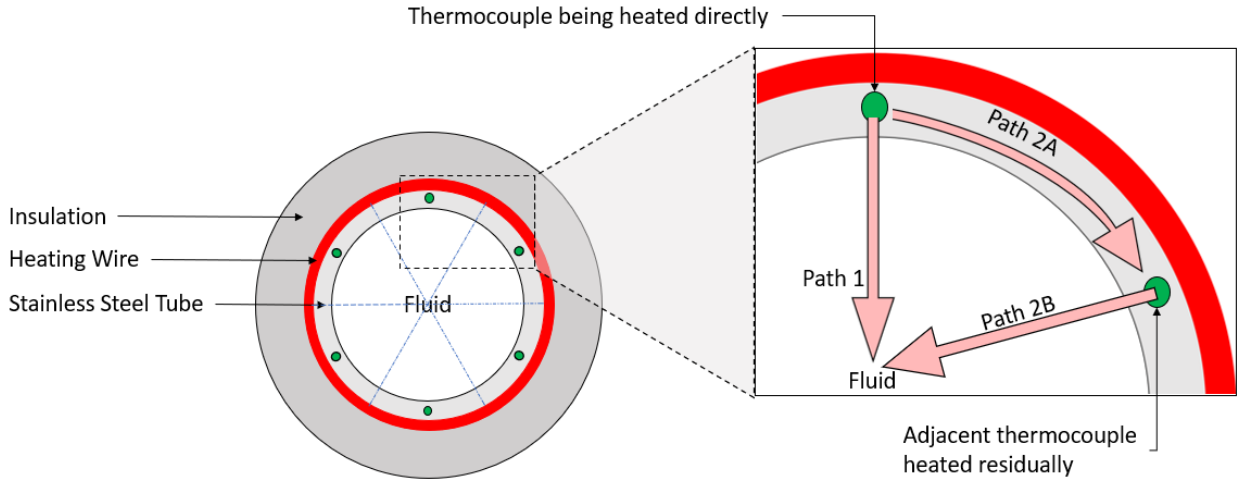

Figure 59: Thermal resistance network for material selection

The affinity for heat transfer in two specific directions are considered. The first is the heat flux through the tube wall and directly to the fluid, Path 1, and the second is the heat flux through the tube wall to the adjacent heating segment, and through that segment to the fluid, Path 2. The amount of heat flux through the two paths should give a rudimentary approximation of the heat flux distribution through the tube wall.

For both paths, the thermal resistance is determined:

$$R_1 = R_{2B} = R_{conv} = \frac{1}{\alpha A} \tag{34}$$

$$R_{2A} = R_{cond} = \frac{\frac{\pi D_{mid}}{6}}{kA} \tag{35}$$

$$R_{path\,2} = R_{2A} + R_{2B} \tag{36}$$

The parameters utilised in this investigation are summarised in Table 16. The middle diameter and thickness were chosen arbitrarily, and the heat transfer coefficient was chosen such that the convection term might be as small as possible, though not necessarily practically possible. Due to the nature of this investigation being comparative, these assumptions are not critical for the accurate determination of the qualitative nature of the heat transfer characteristics of the material.

Table 16: Parameters for conduction heat transfer comparison between stainless steel and copper

Quantity	Value
L	900 mm
D_{mid}	10.29 mm
k_{SS}	16.5 W/mK
k_{Cu}	386 W/mK
t	1.24 mm
α	100000 W/m²K

The properties of the materials are the only parameter that influences the distribution of heat in the material. It was found that in copper 67% of the heat applied to a specific station will pass directly to the fluid through path 1, while the remaining 33% passes through path 2 into the fluid. Stainless-steel on the other hand allows 83% of the heat applied to the station to pass directly to the fluid through path 1, and only 17% of the applied heat to pass through adjacent segments into the fluid (through path 2).

This difference is significant enough to establish a conclusion. Stainless steel holds an applied non-uniform heat distribution better than a copper material. The copper material will tend to disperse the non-uniformity applied. The results seen in stainless-steel are what is required for this study. Therefore, stainless steel was used in the experimental investigation.

B. Calibration

The calibration curves of all the thermocouples used on the facility are indicated here. The facility thermocouples were calibrated with reference to a Lauda Digical digital thermometer with an accuracy of 0.01 °C, and the test section thermocouples were calibrated with reference to the average temperature of two Pt100 thermocouples positioned at the inlet and outlet of the test section, with an accuracy of 0.1 °C.

Figure 60a indicates a typical thermocouple linear fit adjustment curve.

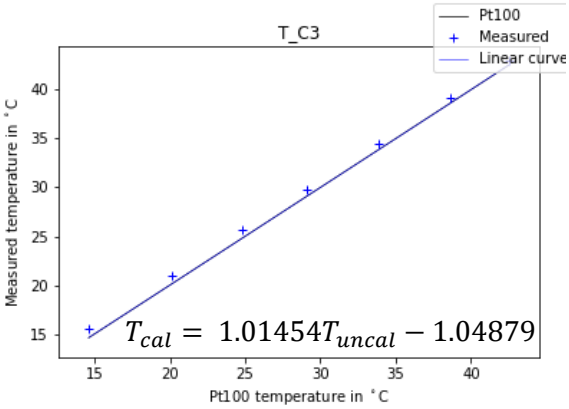

Figure 60 (a) Linear curve fit for uncalibrated thermocouple at temperature measuring station C, heating segment 3.

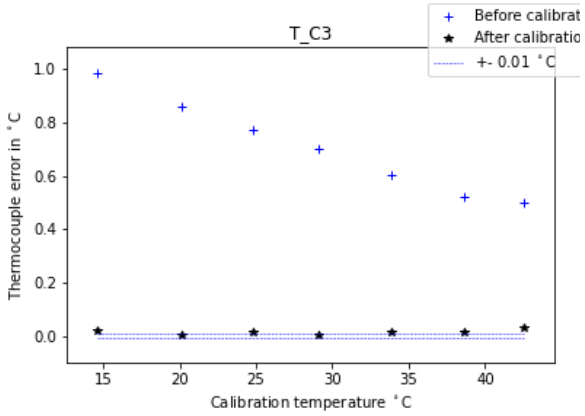

Figure 59 (b) Average difference of thermocouple reading and expected reading before and after calibration

The difference in expected and achieved readings were also plotted, to establish the level of accuracy achieved due to calibration of the thermocouples. The required level of accuracy was to have the thermocouples calibrated to within 0.02 °C of the average Pt100 reading. Figure 60b indicates for this specific thermocouple the change in temperature reading from before calibration, compared to after calibration.

There was a drastic increase in the accuracy of the temperature readings, seen on the test section thermocouples, whereas the thermocouples positioned on the facility had less of a variation in readings to begin with. This was due to the manufacturing process attaching the thermocouples to the test section. The inaccuracies introduced due to manufacturer error were adjusted for by this calibration.

The average difference graphs obtained for all calibrated thermocouples are displayed in the following sections.

1 Facility Thermocouples

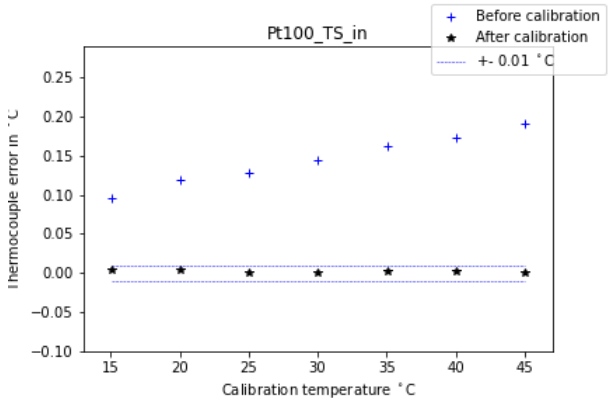

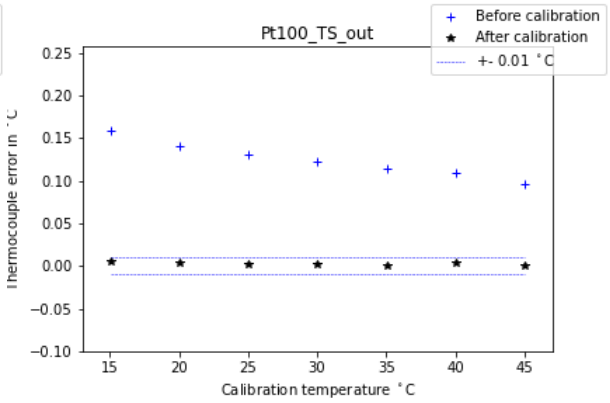

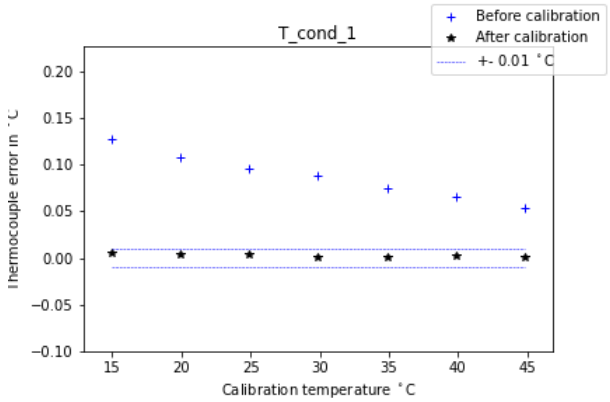

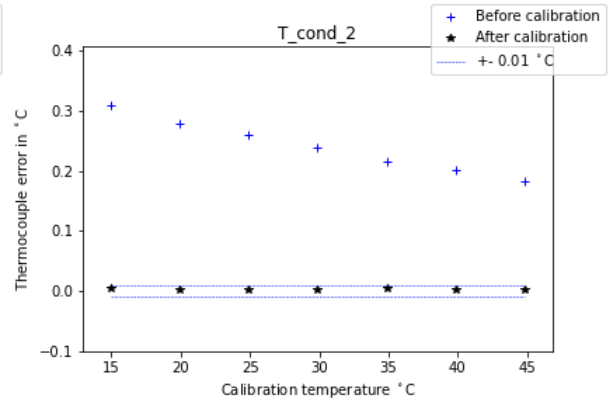

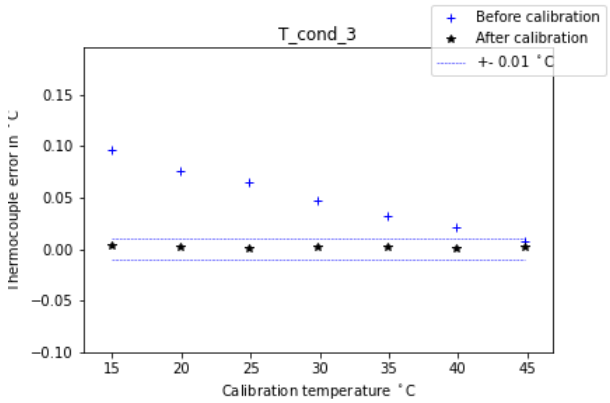

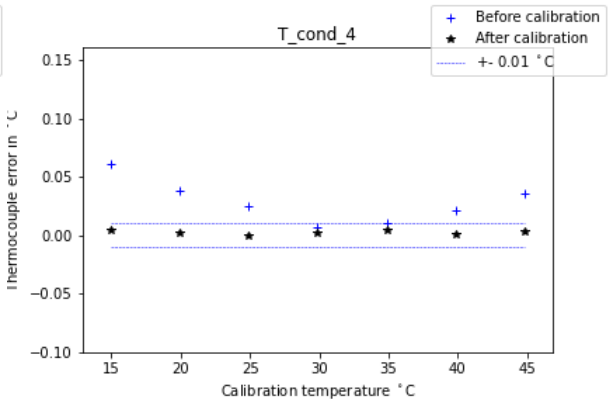

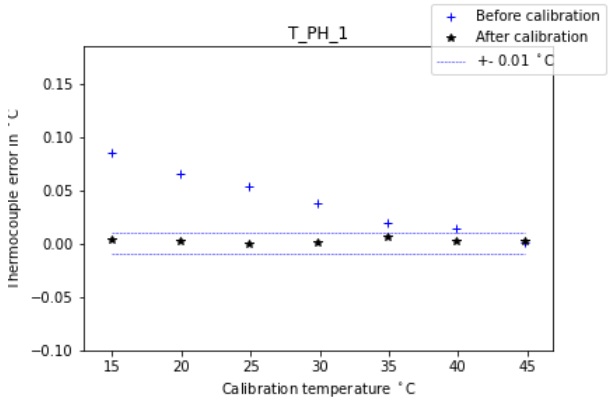
T_PH_1
Before calibration
After calibration
+- 0.01 °C
Thermocouple error in °C
Calibration temperature °C

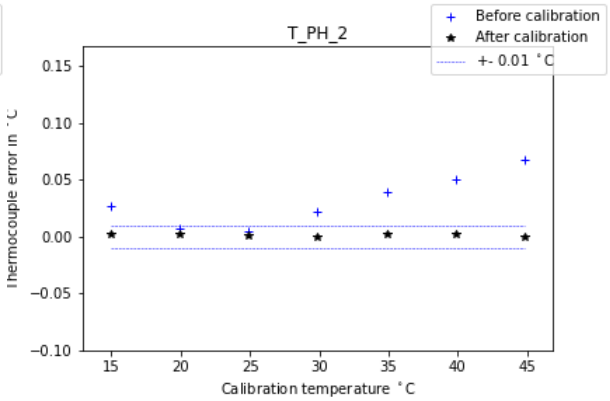
T_PH_2
Before calibration
After calibration
+- 0.01 °C
Thermocouple error in °C
Calibration temperature °C

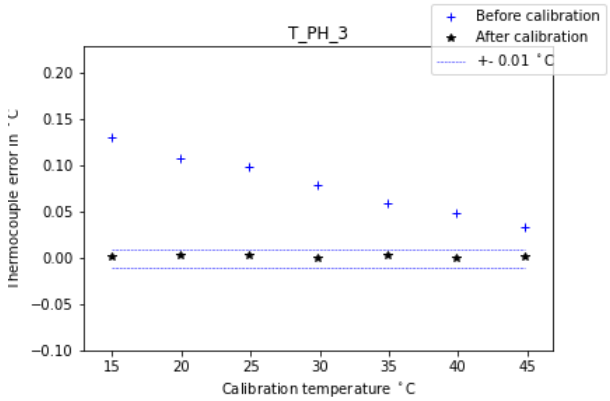
T_PH_3
Before calibration
After calibration
+- 0.01 °C
Thermocouple error in °C
Calibration temperature °C

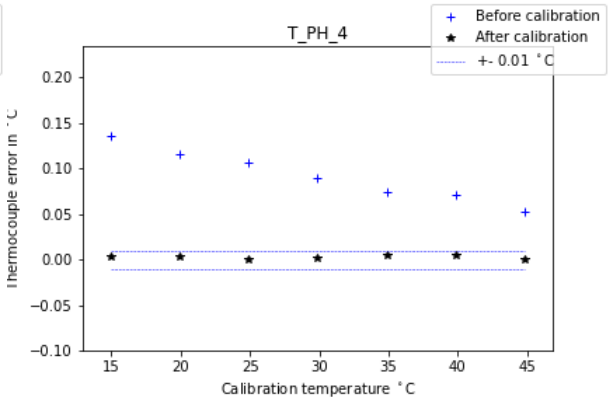
T_PH_4
Before calibration
After calibration
+- 0.01 °C
Thermocouple error in °C
Calibration temperature °C

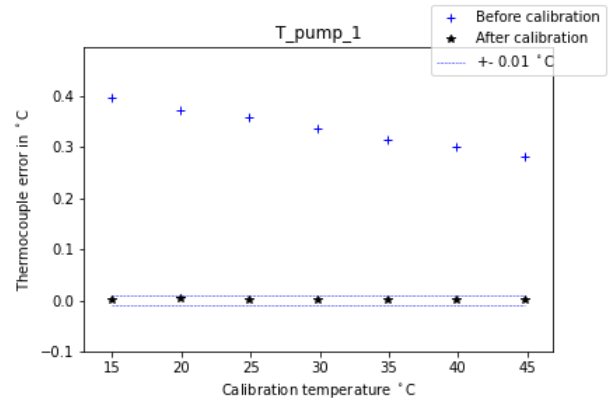
T_pump_1
Before calibration
After calibration
+- 0.01 °C
Thermocouple error in °C
Calibration temperature °C

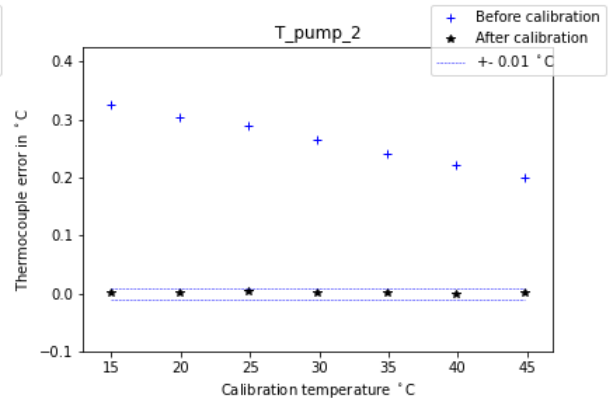
T_pump_2
Before calibration
After calibration
+- 0.01 °C
Thermocouple error in °C
Calibration temperature °C

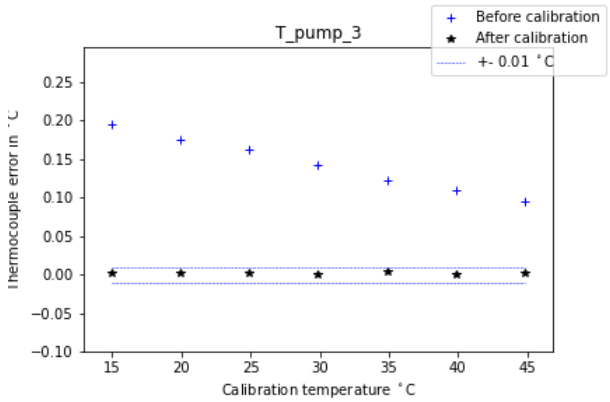
T_pump_3
Before calibration
After calibration
+- 0.01 °C
Thermocouple error in °C
Calibration temperature °C

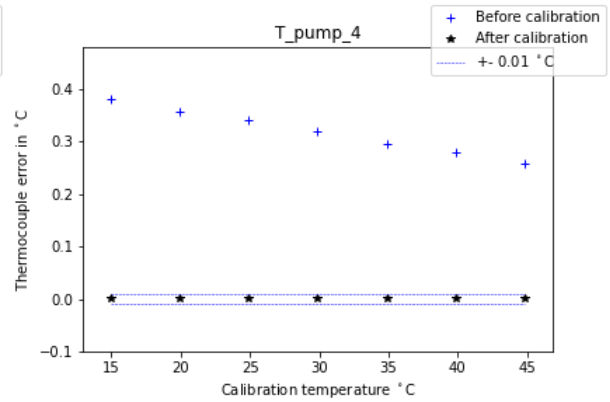
T_pump_4
Before calibration
After calibration
+- 0.01 °C
Thermocouple error in °C
Calibration temperature °C

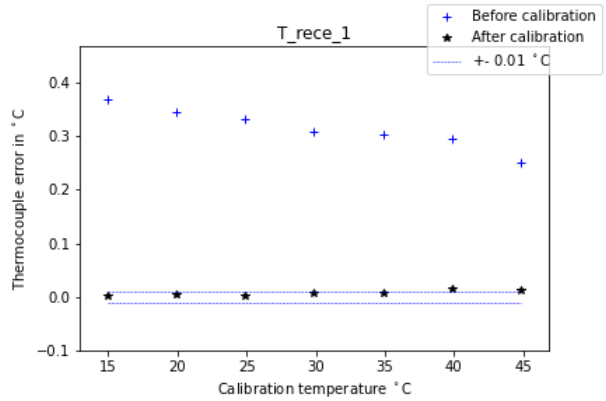
T_rece_1
Before calibration
After calibration
+- 0.01 °C
Thermocouple error in °C
Calibration temperature °C

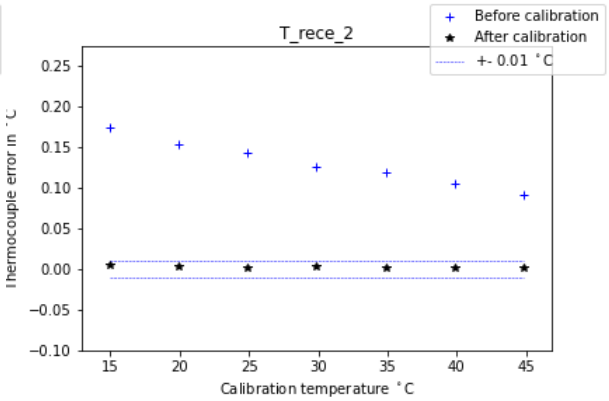
T_rece_2
Before calibration
After calibration
+- 0.01 °C
Thermocouple error in °C
Calibration temperature °C

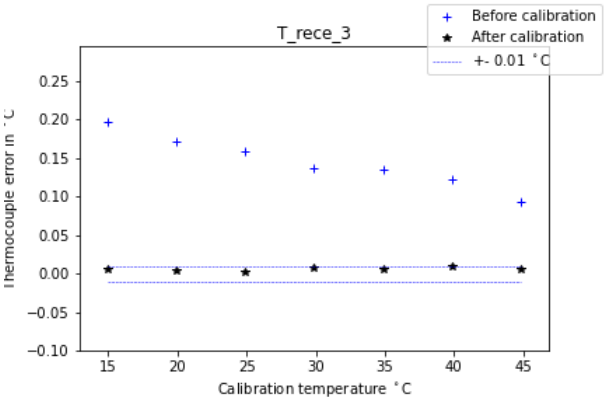
T_rece_3
Before calibration
After calibration
+- 0.01 °C
Thermocouple error in °C
Calibration temperature °C

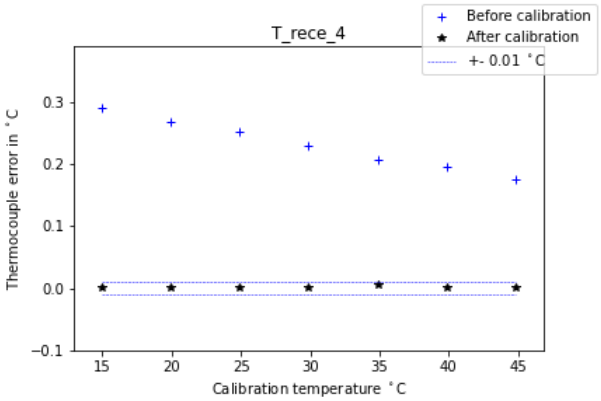
T_rece_4
Before calibration
After calibration
+- 0.01 °C
Thermocouple error in °C
Calibration temperature °C

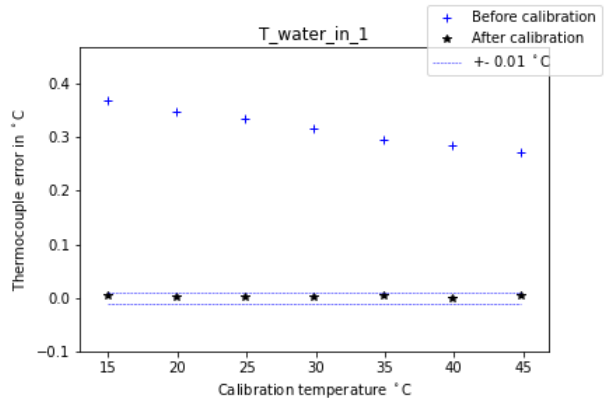
T_water_in_1
Before calibration
After calibration
+- 0.01 °C
Thermocouple error in °C
Calibration temperature °C

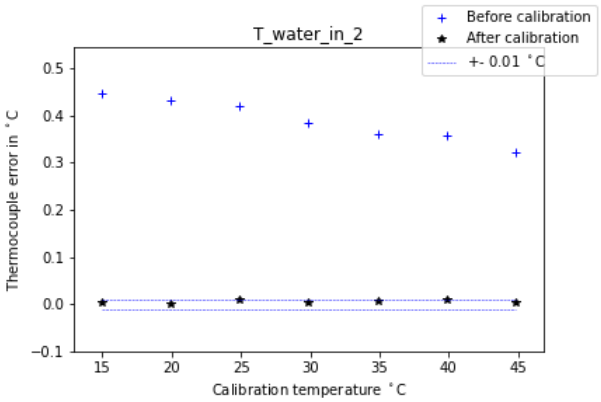
T_water_in_2
Before calibration
After calibration
+- 0.01 °C
Thermocouple error in °C
Calibration temperature °C

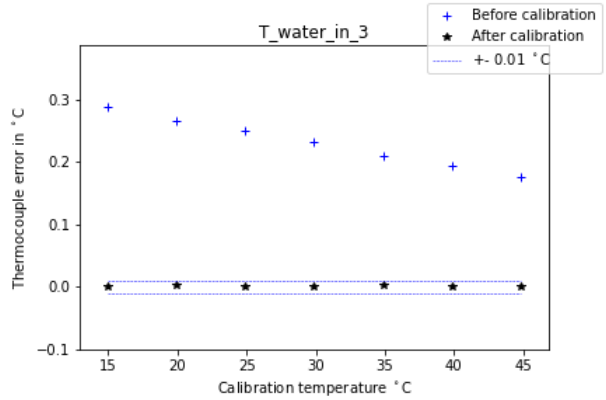
T_water_in_3
Before calibration
After calibration
+- 0.01 °C
Thermocouple error in °C
Calibration temperature °C

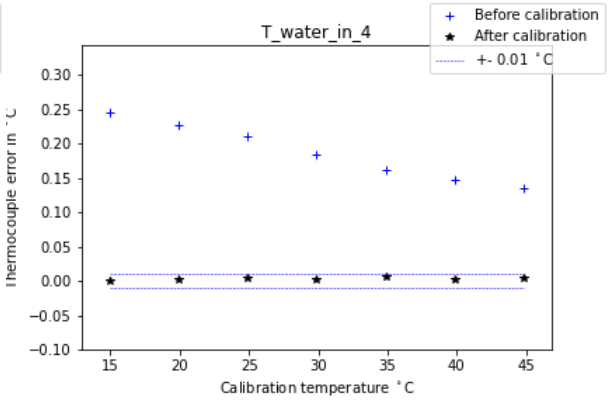
T_water_in_4
Before calibration
After calibration
+- 0.01 °C
Thermocouple error in °C
Calibration temperature °C

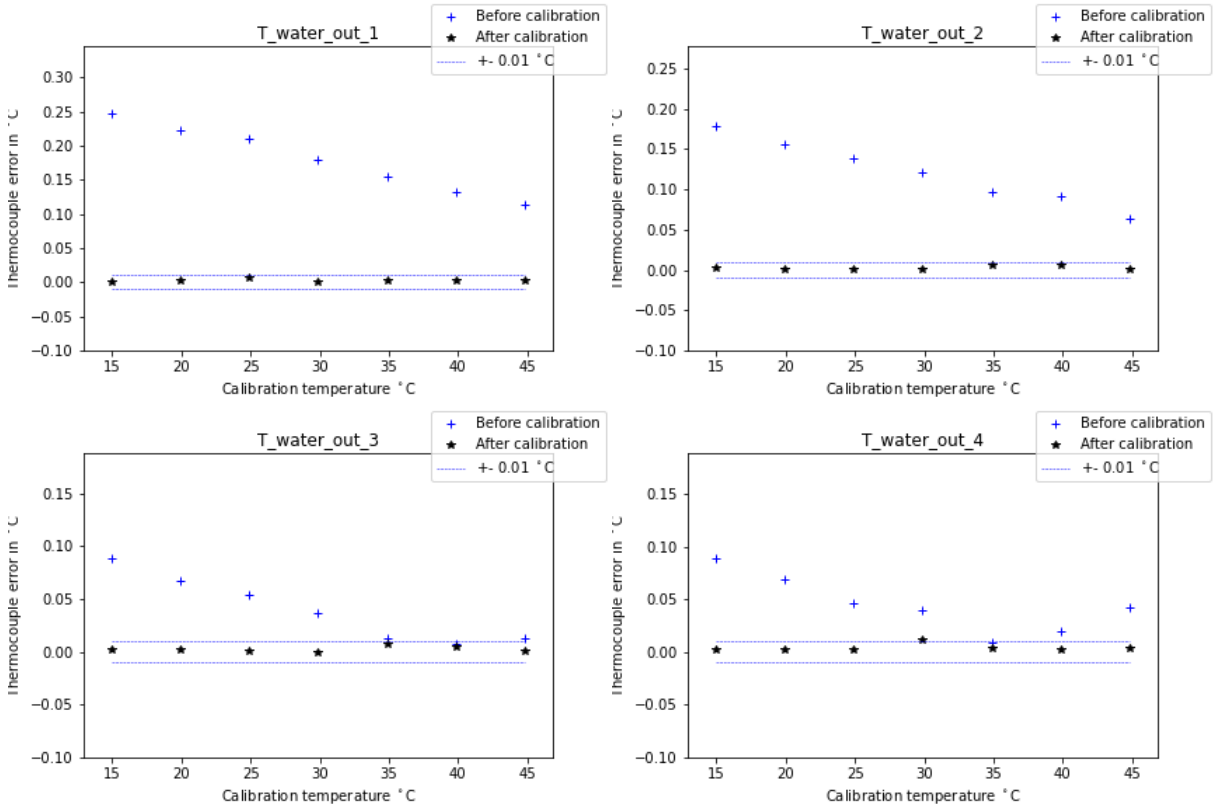
T_water_out_1
T_water_out_2
T_water_out_3
T_water_out_4
Before calibration
After calibration
+- 0.01 ˚C
Thermocouple error in ˚C
Calibration temperature ˚C

2 Test Section Thermocouples

2.1 Station A

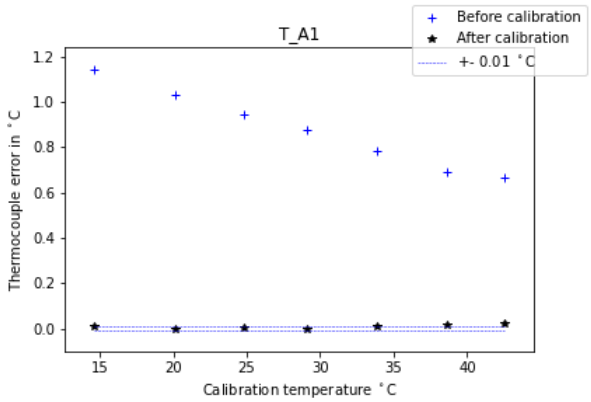

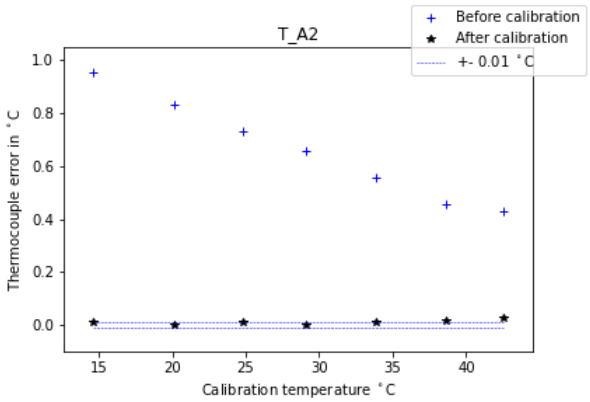

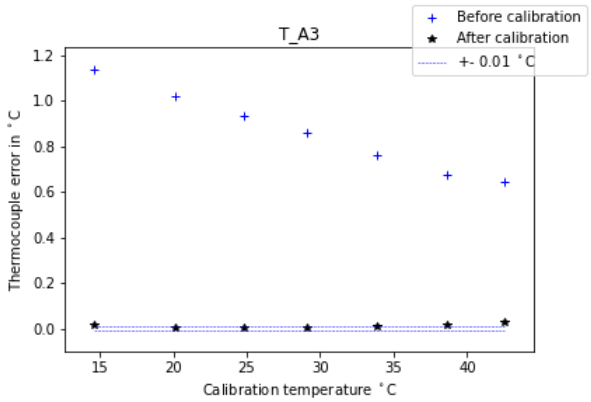

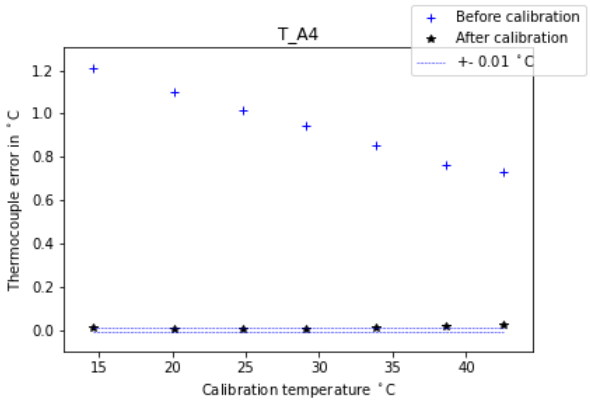

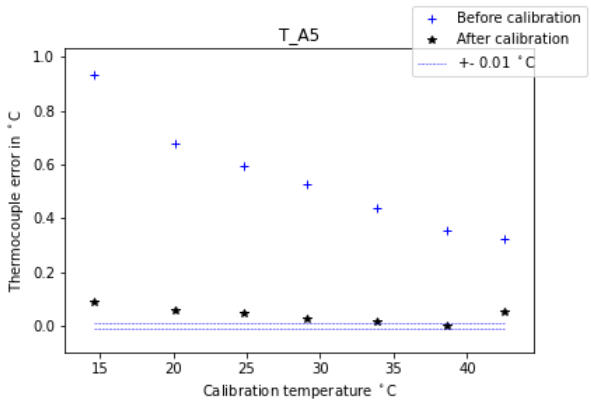

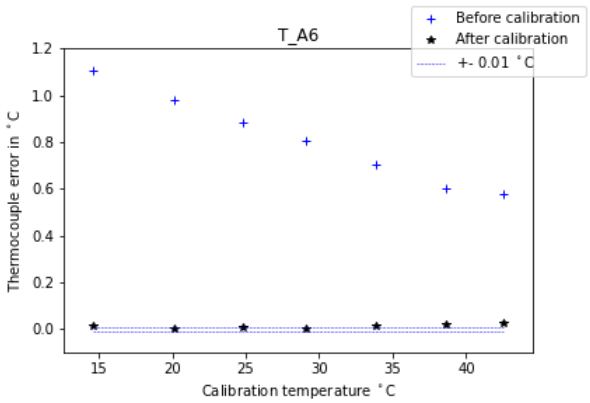

2.2 Station B

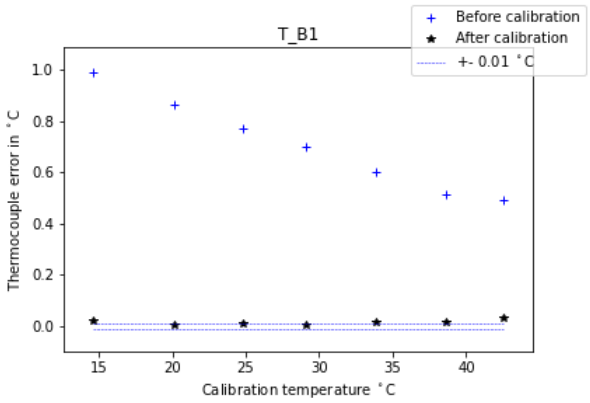
T_B1
Before calibration
After calibration
+- 0.01 °C
Thermocouple error in °C
Calibration temperature °C

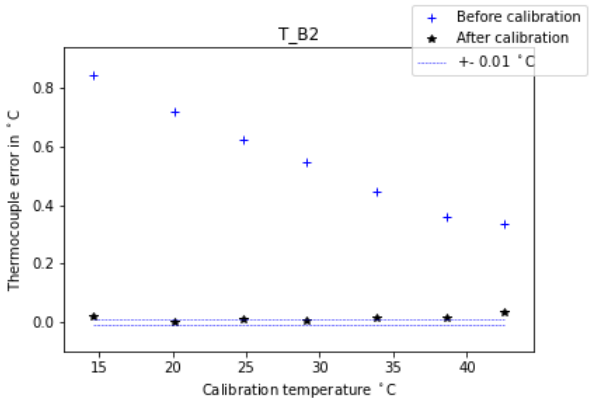
T_B2
Before calibration
After calibration
+- 0.01 °C
Thermocouple error in °C
Calibration temperature °C

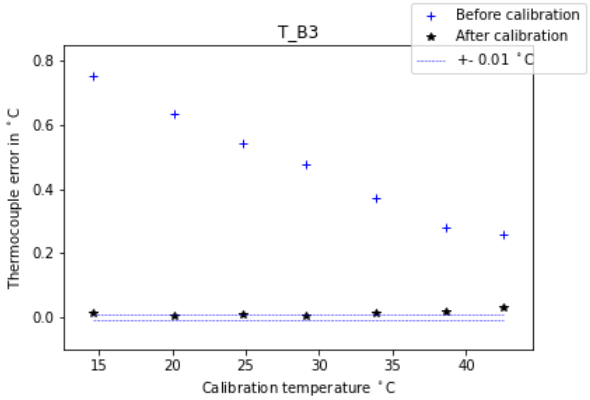
T_B3
Before calibration
After calibration
+- 0.01 °C
Thermocouple error in °C
Calibration temperature °C

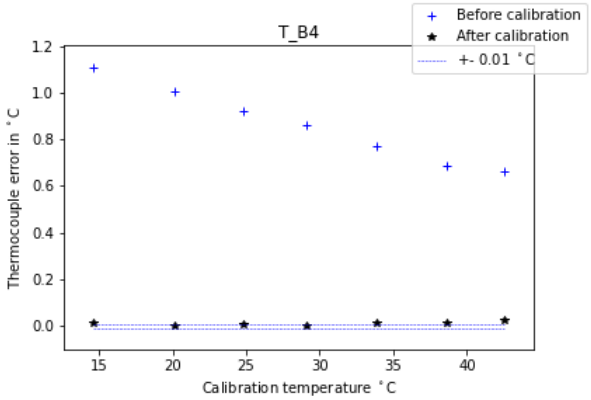
T_B4
Before calibration
After calibration
+- 0.01 °C
Thermocouple error in °C
Calibration temperature °C

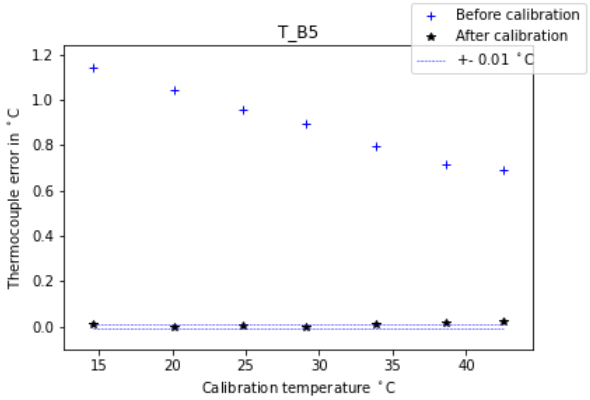
T_B5
Before calibration
After calibration
+- 0.01 °C
Thermocouple error in °C
Calibration temperature °C

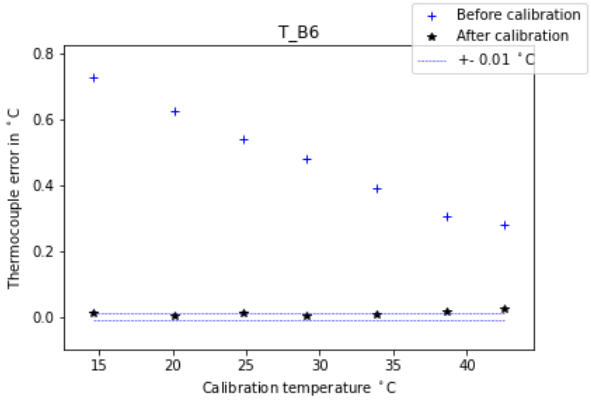
T_B6
Before calibration
After calibration
+- 0.01 °C
Thermocouple error in °C
Calibration temperature °C

2.3 Station C

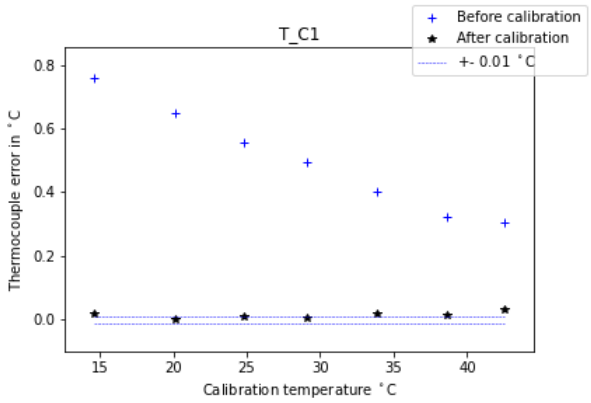
T_C1
Before calibration
After calibration
+- 0.01 °C
Thermocouple error in °C
Calibration temperature °C

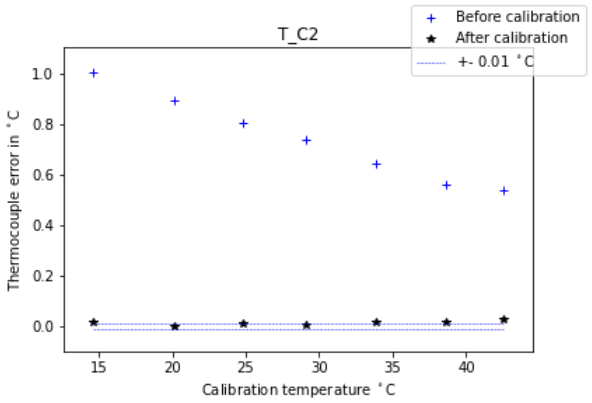
T_C2
Before calibration
After calibration
+- 0.01 °C
Thermocouple error in °C
Calibration temperature °C

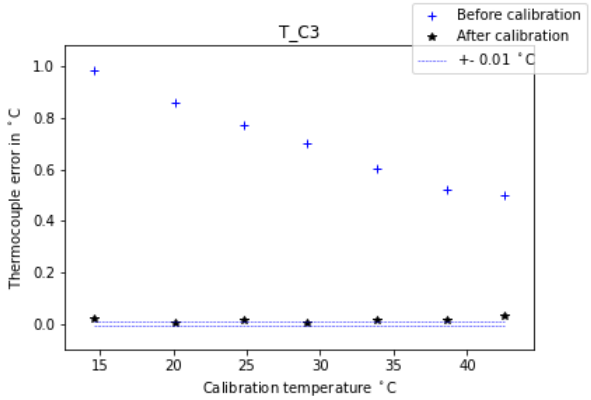
T_C3
Before calibration
After calibration
+- 0.01 °C
Thermocouple error in °C
Calibration temperature °C

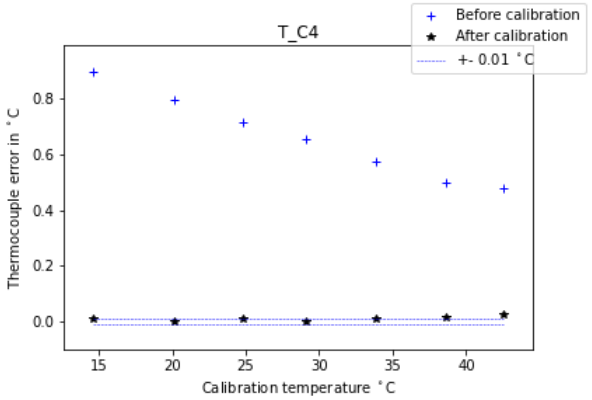
T_C4
Before calibration
After calibration
+- 0.01 °C
Thermocouple error in °C
Calibration temperature °C

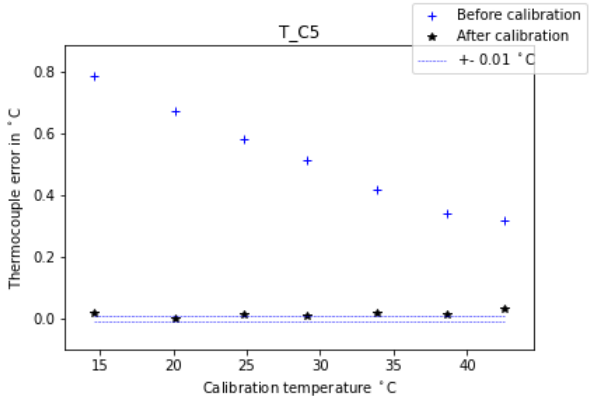
T_C5
Before calibration
After calibration
+- 0.01 °C
Thermocouple error in °C
Calibration temperature °C

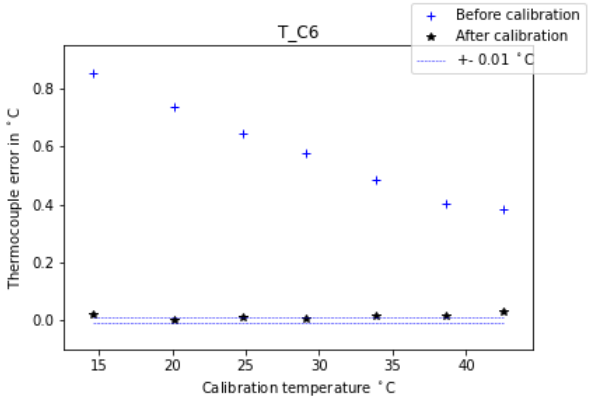
T_C6
Before calibration
After calibration
+- 0.01 °C
Thermocouple error in °C
Calibration temperature °C

2.4 Station D

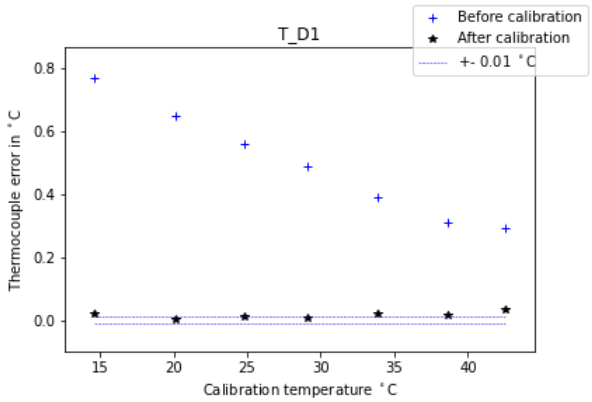
T_D1
Before calibration
After calibration
+- 0.01 °C
Thermocouple error in °C
Calibration temperature °C

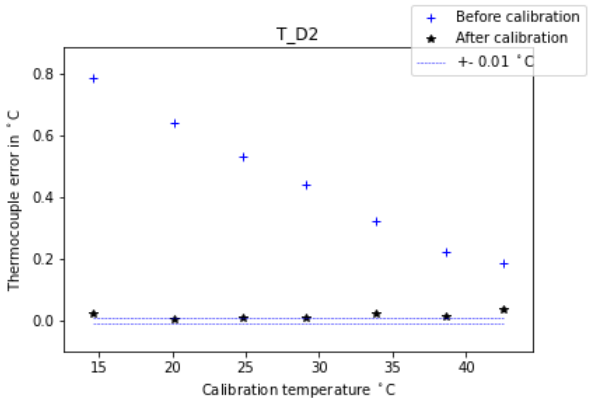
T_D2
Before calibration
After calibration
+- 0.01 °C
Thermocouple error in °C
Calibration temperature °C

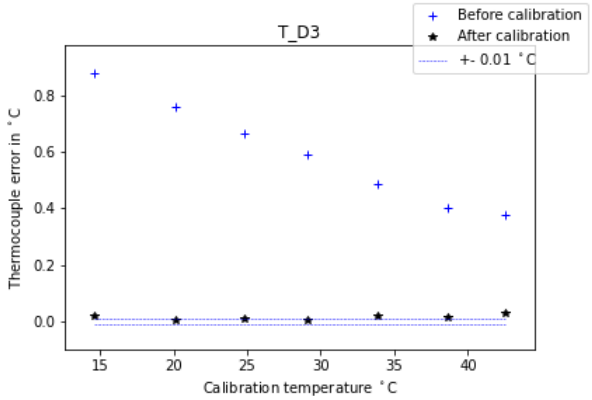
T_D3
Before calibration
After calibration
+- 0.01 °C
Thermocouple error in °C
Calibration temperature °C

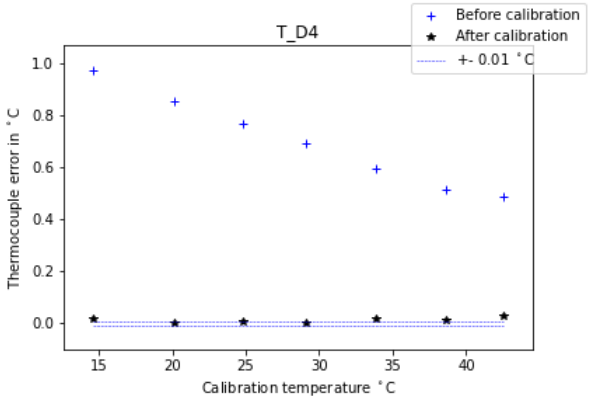
T_D4
Before calibration
After calibration
+- 0.01 °C
Thermocouple error in °C
Calibration temperature °C

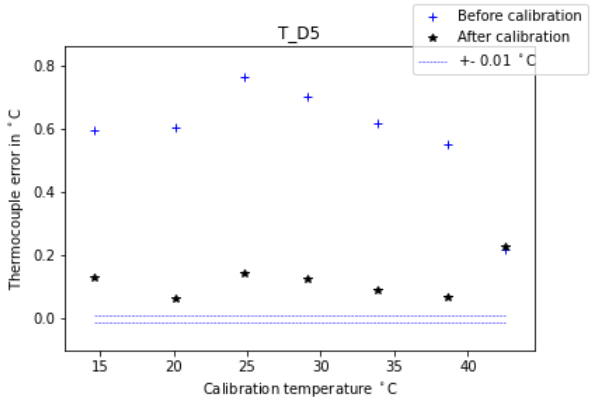
T_D5
Before calibration
After calibration
+- 0.01 °C
Thermocouple error in °C
Calibration temperature °C

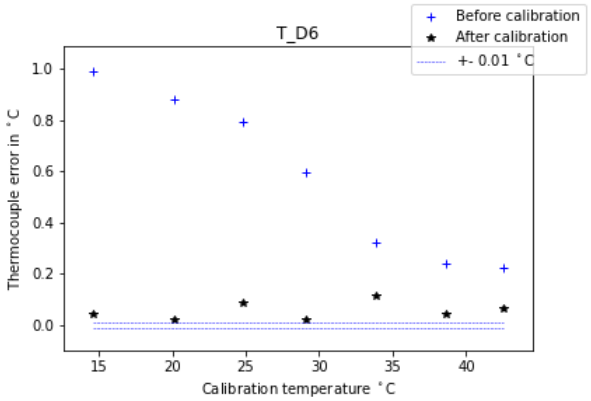
T_D6
Before calibration
After calibration
+- 0.01 °C
Thermocouple error in °C
Calibration temperature °C

2.5 Station E

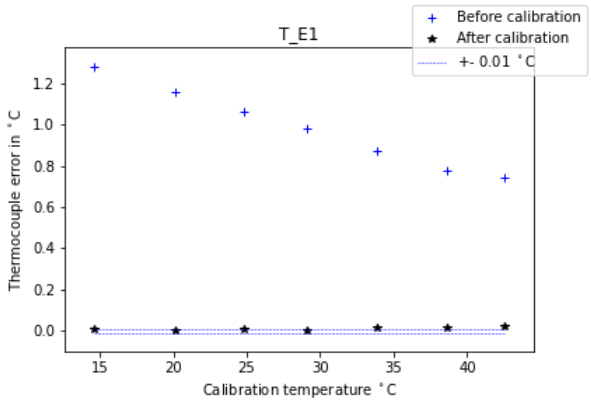
T_E1
Before calibration
After calibration
+- 0.01 °C
Thermocouple error in °C
Calibration temperature °C

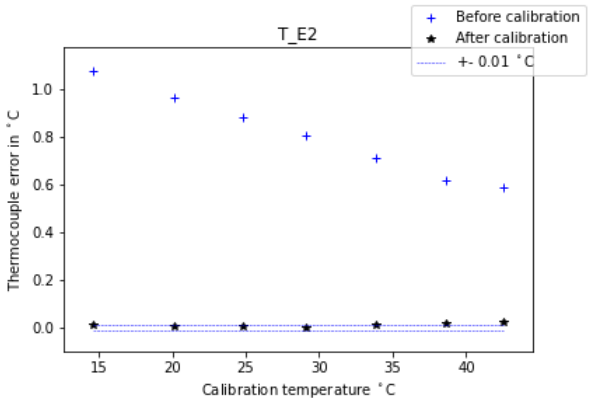
T_E2
Before calibration
After calibration
+- 0.01 °C
Thermocouple error in °C
Calibration temperature °C

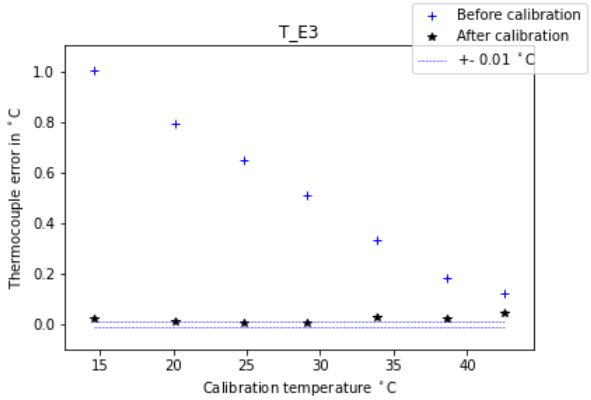
T_E3
Before calibration
After calibration
+- 0.01 °C
Thermocouple error in °C
Calibration temperature °C

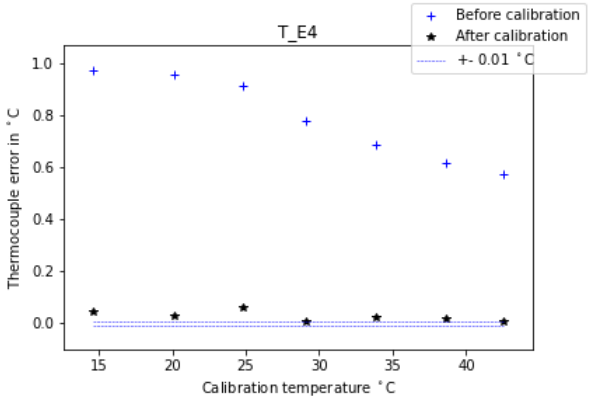
T_E4
Before calibration
After calibration
+- 0.01 °C
Thermocouple error in °C
Calibration temperature °C

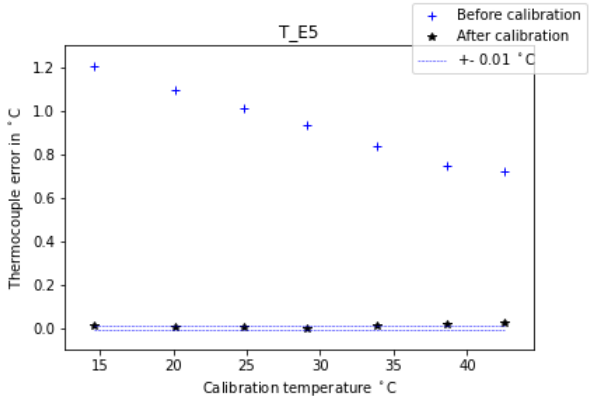
T_E5
Before calibration
After calibration
+- 0.01 °C
Thermocouple error in °C
Calibration temperature °C

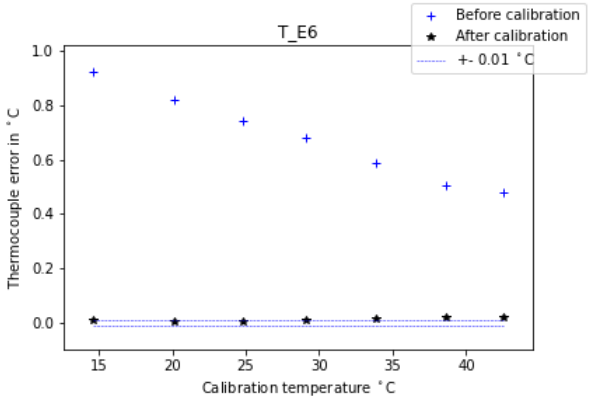
T_E6
Before calibration
After calibration
+- 0.01 °C
Thermocouple error in °C
Calibration temperature °C

2.6 Station F

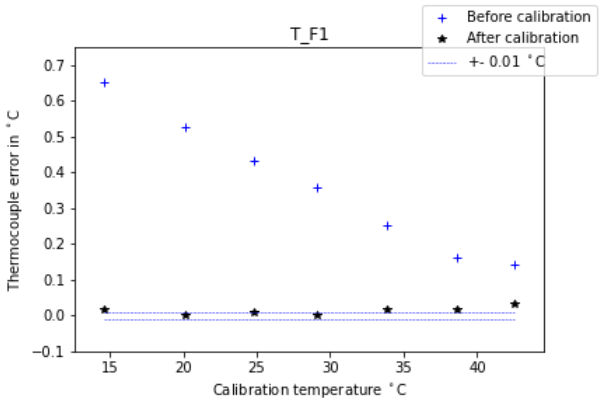
T_F1
Before calibration
After calibration
+- 0.01 °C
Thermocouple error in °C
Calibration temperature °C

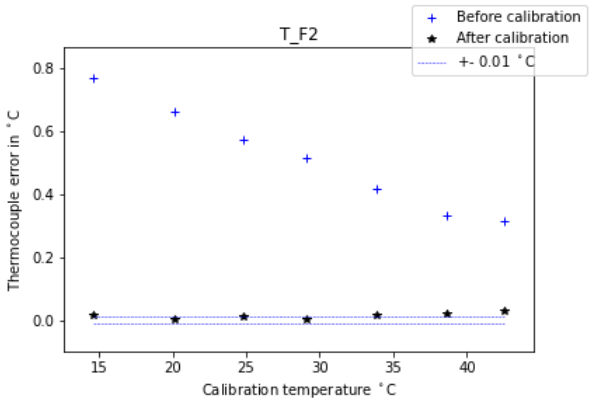
T_F2
Before calibration
After calibration
+- 0.01 °C
Thermocouple error in °C
Calibration temperature °C

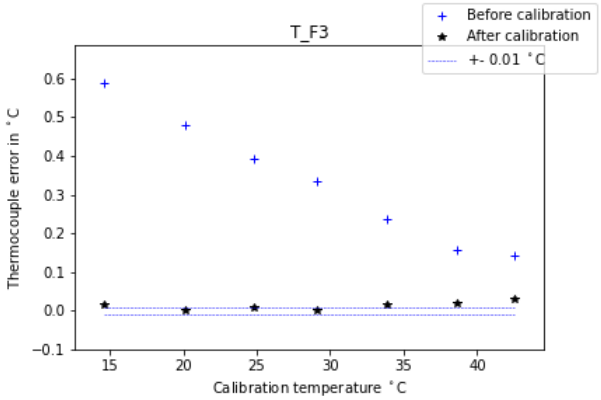
T_F3
Before calibration
After calibration
+- 0.01 °C
Thermocouple error in °C
Calibration temperature °C

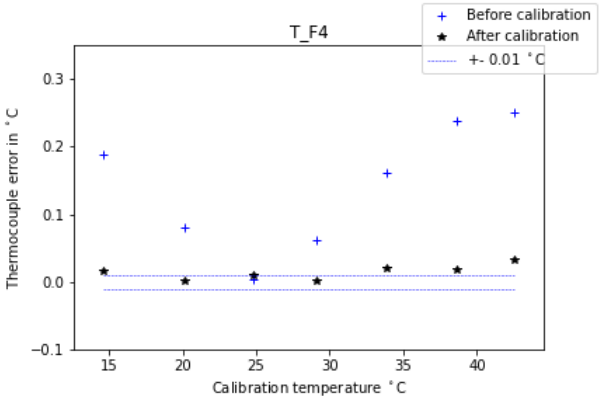
T_F4
Before calibration
After calibration
+- 0.01 °C
Thermocouple error in °C
Calibration temperature °C

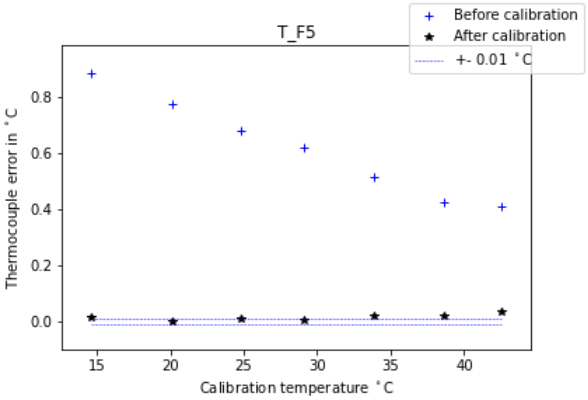
T_F5
Before calibration
After calibration
+- 0.01 °C
Thermocouple error in °C
Calibration temperature °C

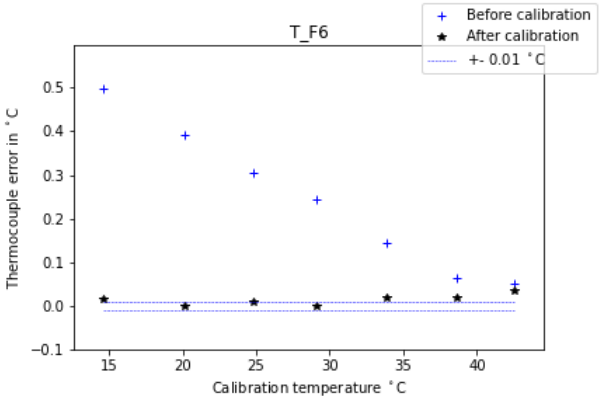
T_F6
Before calibration
After calibration
+- 0.01 °C
Thermocouple error in °C
Calibration temperature °C

2.7 Station G

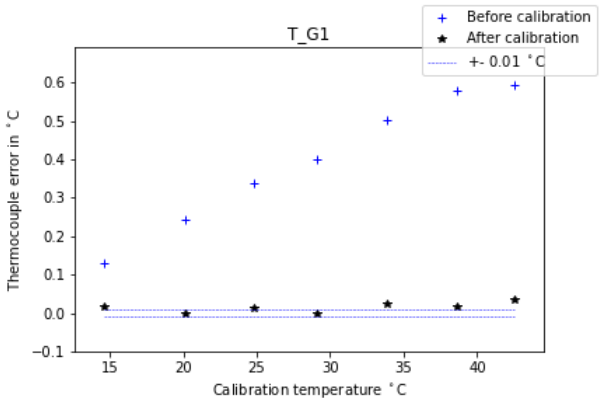
T_G1
Before calibration
After calibration
+- 0.01 °C
Thermocouple error in °C
Calibration temperature °C

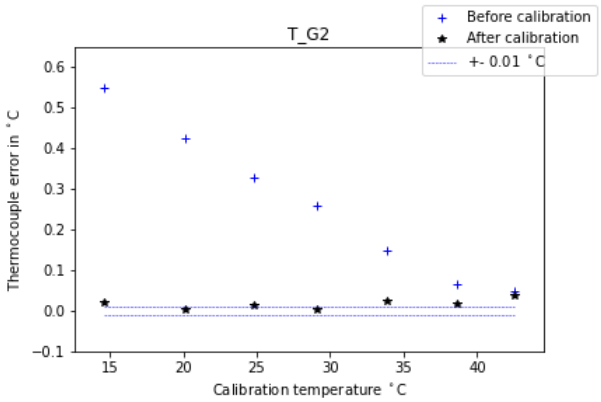
T_G2
Before calibration
After calibration
+- 0.01 °C
Thermocouple error in °C
Calibration temperature °C

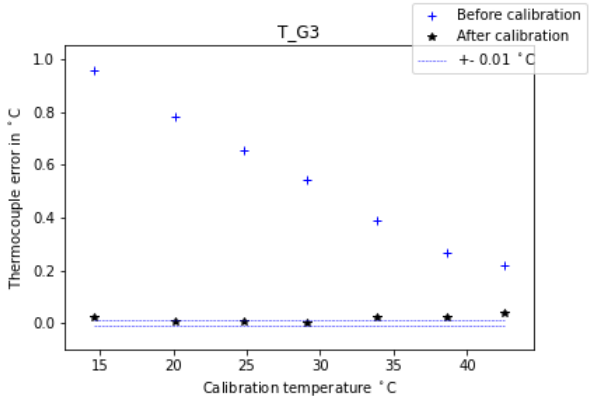
T_G3
Before calibration
After calibration
+- 0.01 °C
Thermocouple error in °C
Calibration temperature °C

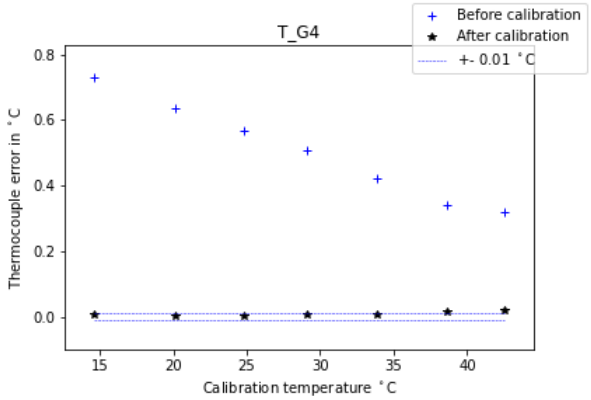
T_G4
Before calibration
After calibration
+- 0.01 °C
Thermocouple error in °C
Calibration temperature °C

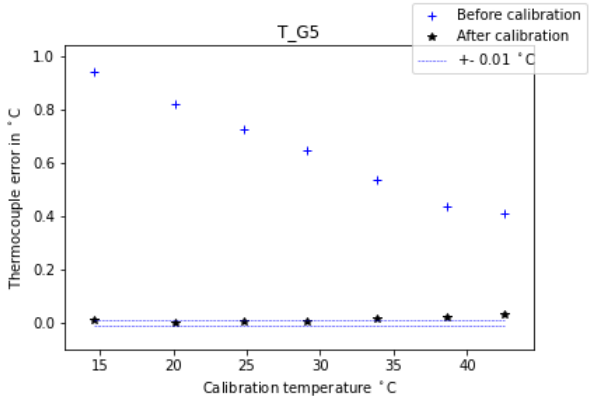
T_G5
Before calibration
After calibration
+- 0.01 °C
Thermocouple error in °C
Calibration temperature °C

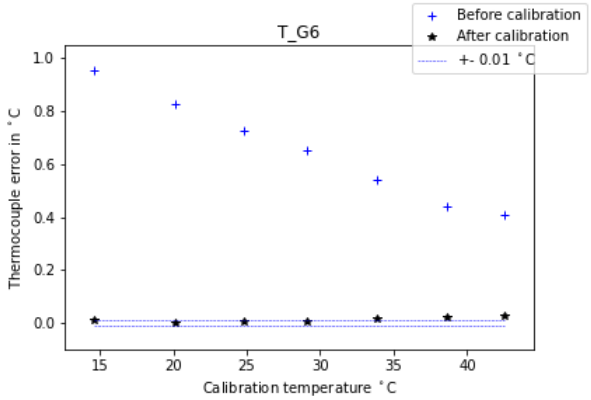
T_G6
Before calibration
After calibration
+- 0.01 °C
Thermocouple error in °C
Calibration temperature °C

2.8 Station H

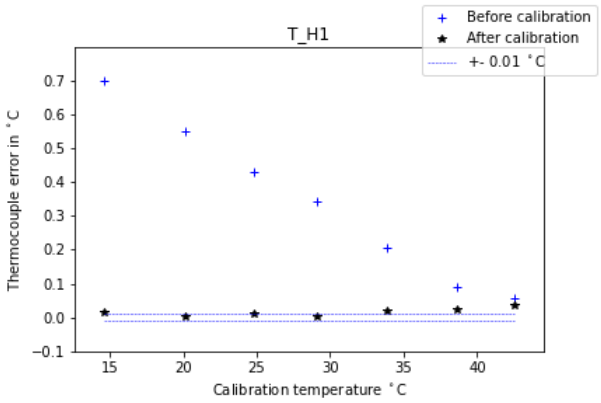
T_H1
Before calibration
After calibration
+- 0.01 °C
Thermocouple error in °C
Calibration temperature °C

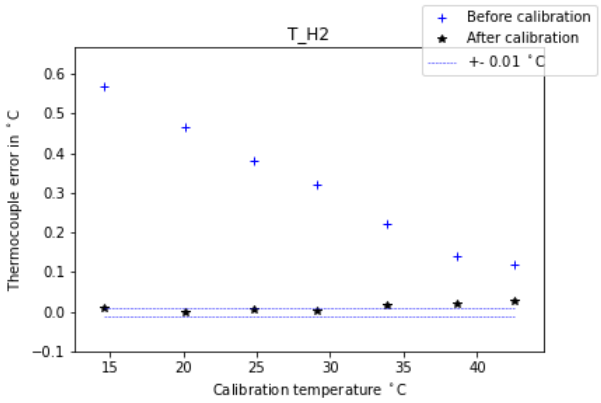
T_H2
Before calibration
After calibration
+- 0.01 °C
Thermocouple error in °C
Calibration temperature °C

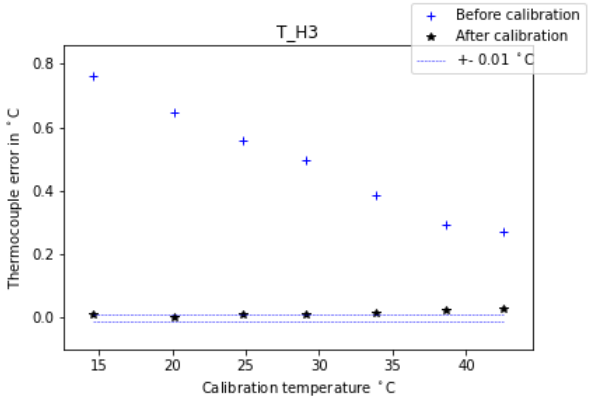
T_H3
Before calibration
After calibration
+- 0.01 °C
Thermocouple error in °C
Calibration temperature °C

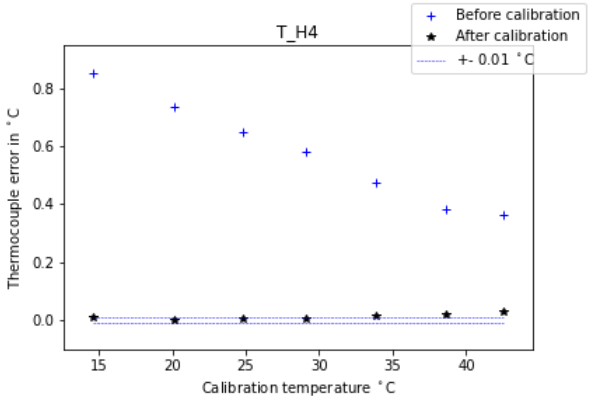
T_H4
Before calibration
After calibration
+- 0.01 °C
Thermocouple error in °C
Calibration temperature °C

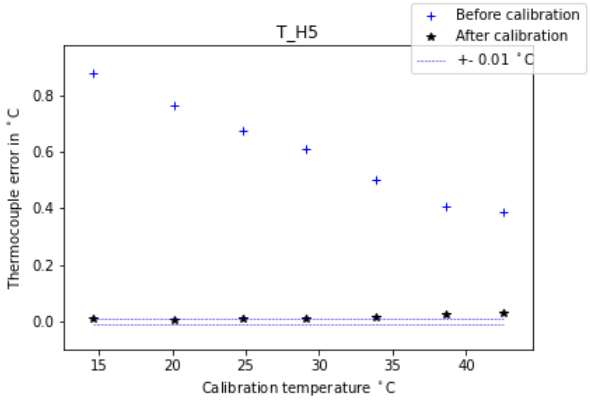
T_H5
Before calibration
After calibration
+- 0.01 °C
Thermocouple error in °C
Calibration temperature °C

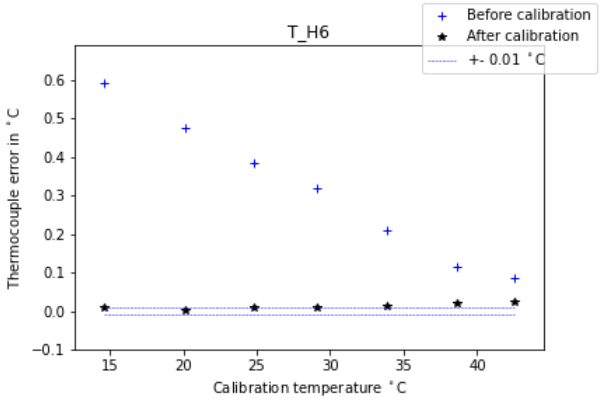
T_H6
Before calibration
After calibration
+- 0.01 °C
Thermocouple error in °C
Calibration temperature °C

2.9 Station I

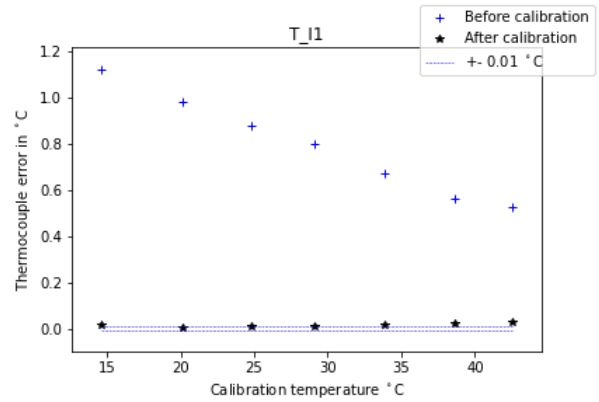
T_I1
Before calibration
After calibration
+- 0.01 °C
Thermocouple error in °C
Calibration temperature °C

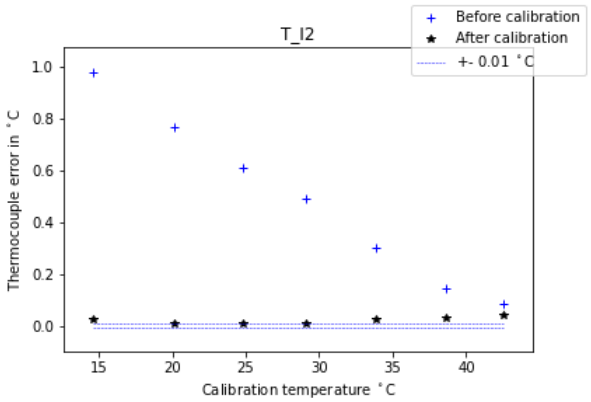
T_I2
Before calibration
After calibration
+- 0.01 °C
Thermocouple error in °C
Calibration temperature °C

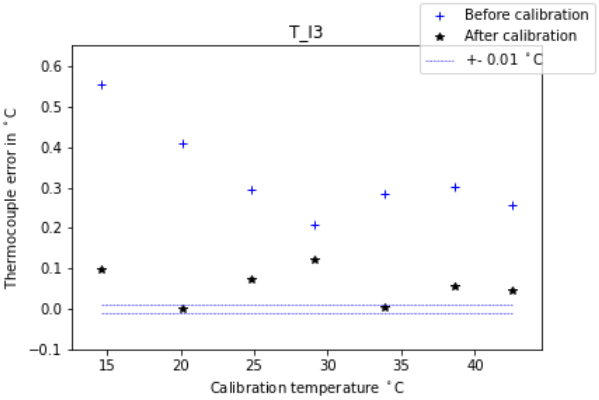
T_I3
Before calibration
After calibration
+- 0.01 °C
Thermocouple error in °C
Calibration temperature °C

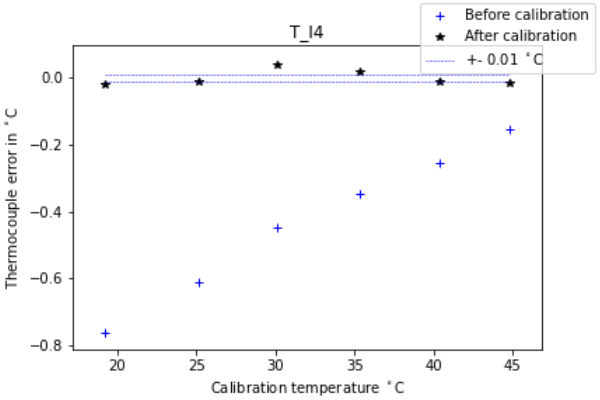
T_I4
Before calibration
After calibration
+- 0.01 °C
Thermocouple error in °C
Calibration temperature °C

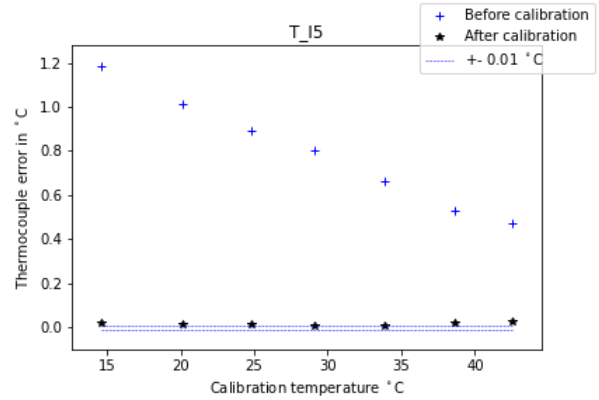
T_I5
Before calibration
After calibration
+- 0.01 °C
Thermocouple error in °C
Calibration temperature °C

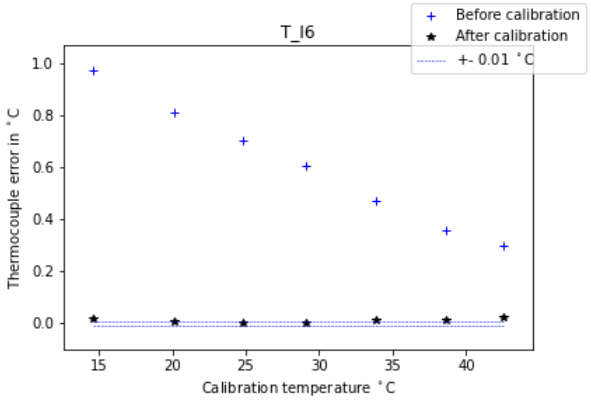
T_I6
Before calibration
After calibration
+- 0.01 °C
Thermocouple error in °C
Calibration temperature °C

C. Control circuit verification test matrix and results

The results for the verification of the control circuit are set out in this section. The tests were done by connecting a load with a set resistance onto the control circuit, setting the duty cycle with which the Darlington and power transistors will be switched and finally setting the DC power supply voltage, constituting the peak-to-peak voltage. The full range of duty cycles were tested on segment 6, while only a 30.98 % duty cycle was checked on all other segments. It was assumed that when a single duty cycle is seen as is expected, the circuit is functioning as it should, deeming the investigation successful.

The peak-to-peak voltage was not the maximum voltage that was switched over the load. The amount with which the resulting voltage differed from the supplied voltage was dependent on the transistor voltage drops expected during operation, and the effect that temperature has on the efficiency of the transistor. Finding the detailed losses and voltage drops are beyond the scope of this investigation.

1 Channel 1

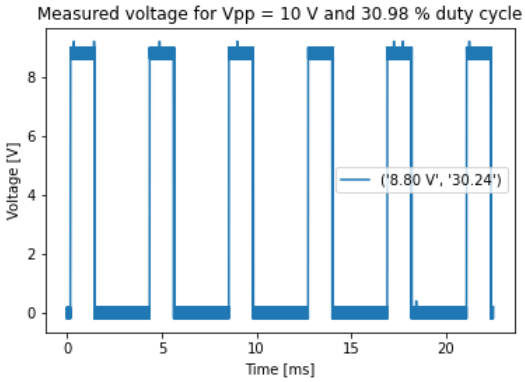

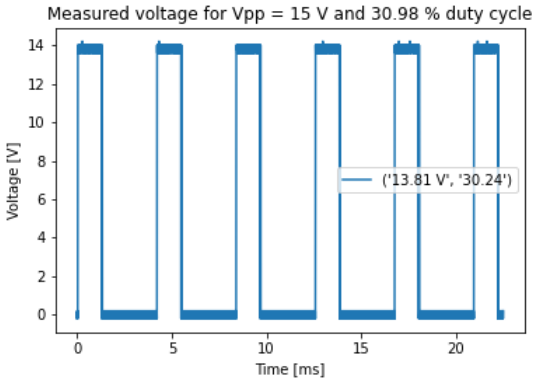

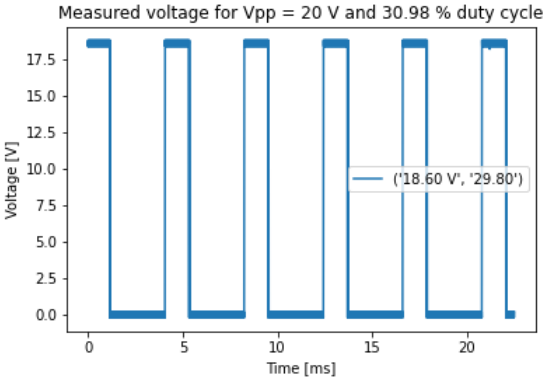

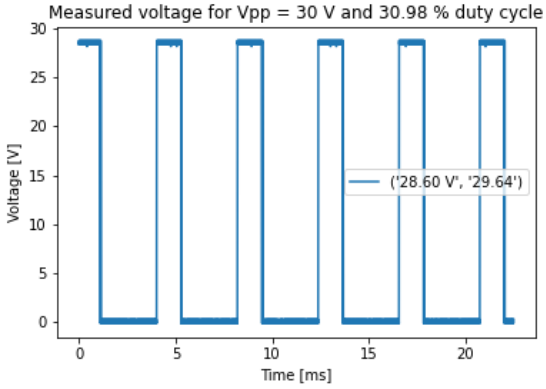

2 Channel 2

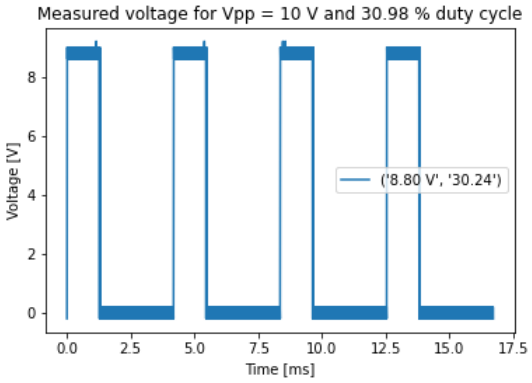

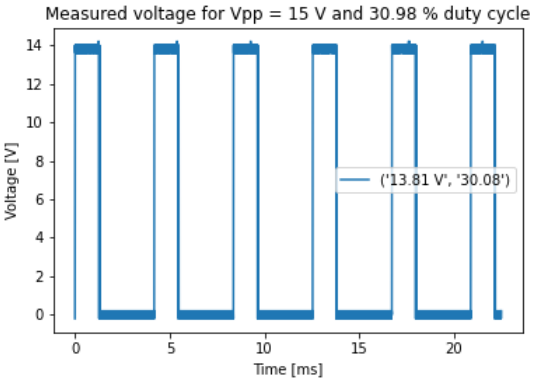

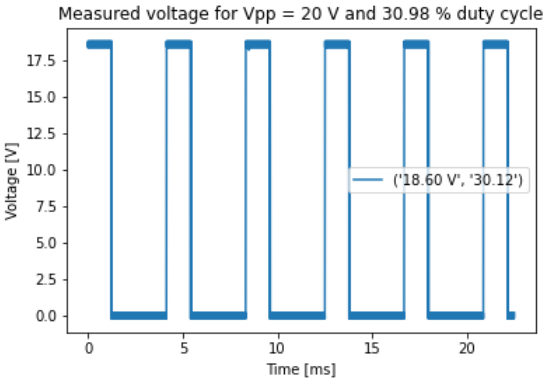

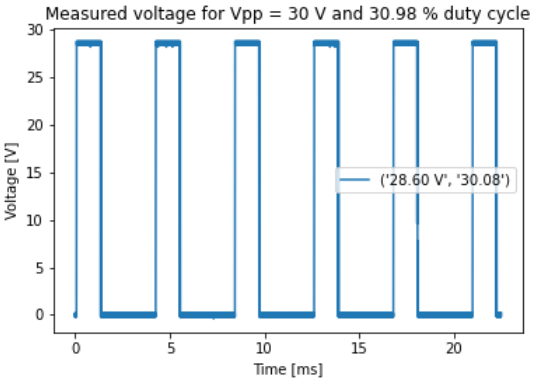

3 Channel 3

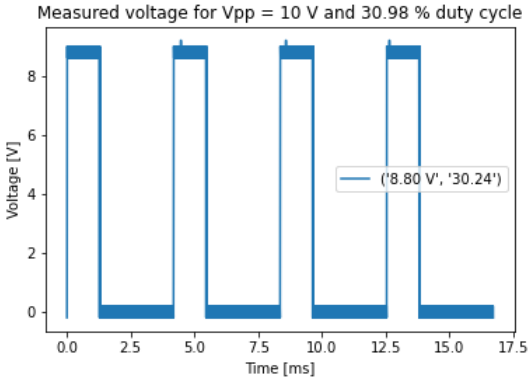

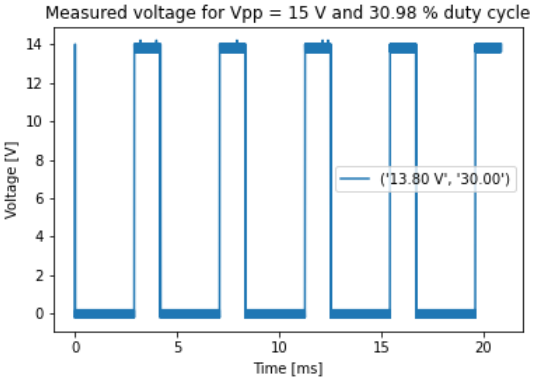

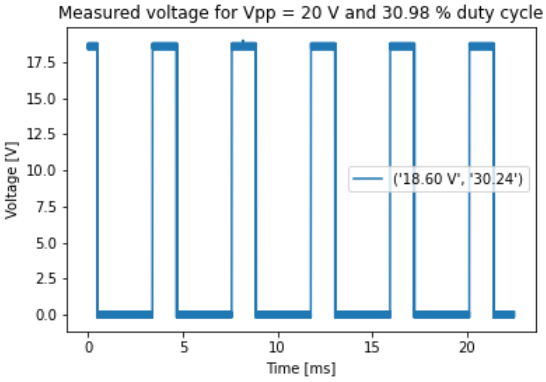

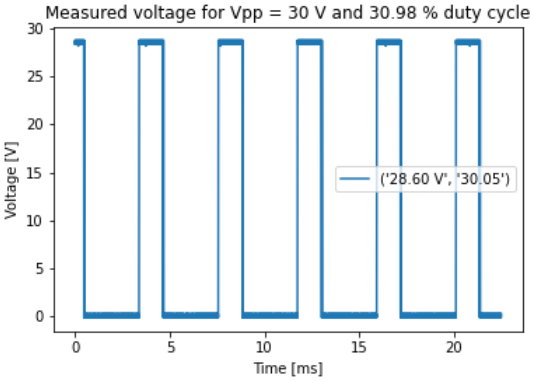

4 Channel 4

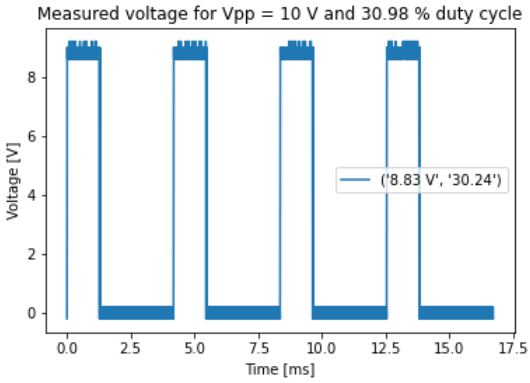

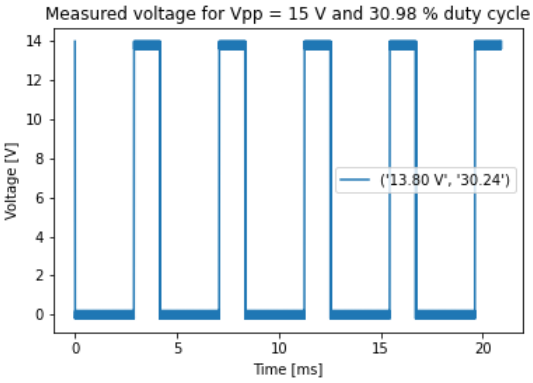

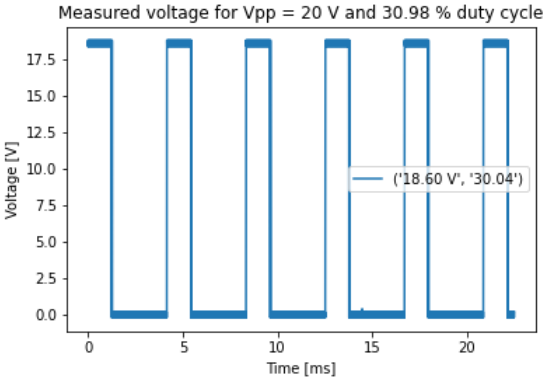

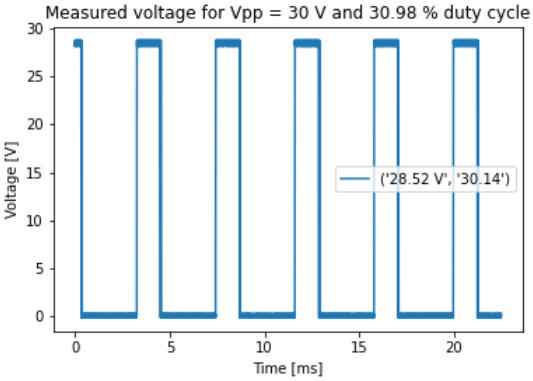

5 Channel 5

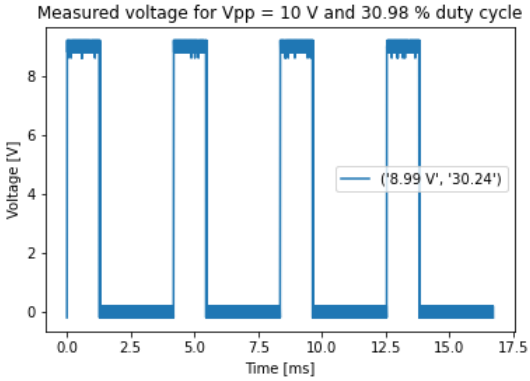

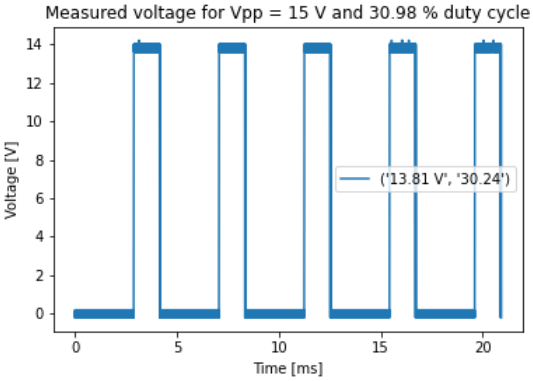

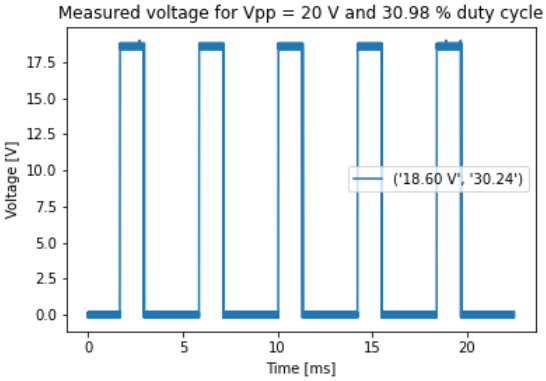

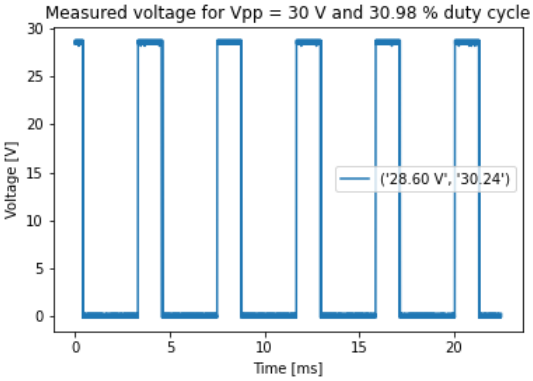

6 Channel 6 tests

6.1 10 V peak to peak voltage

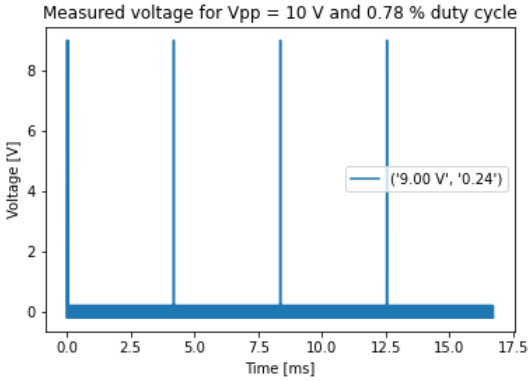

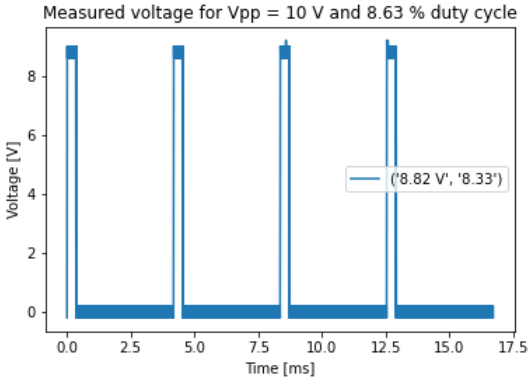

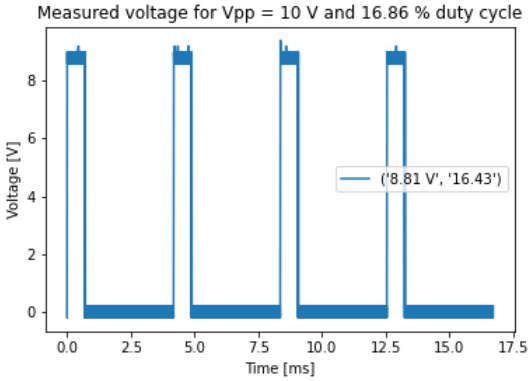

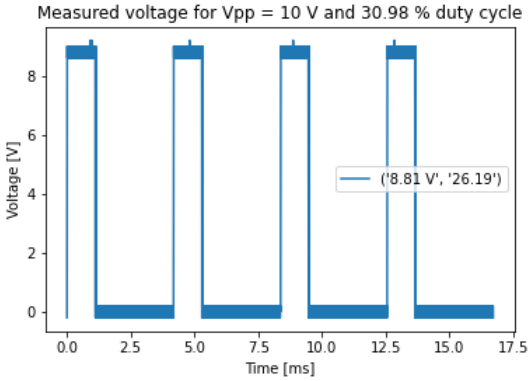

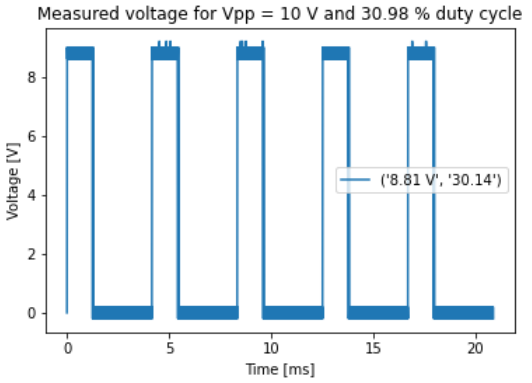

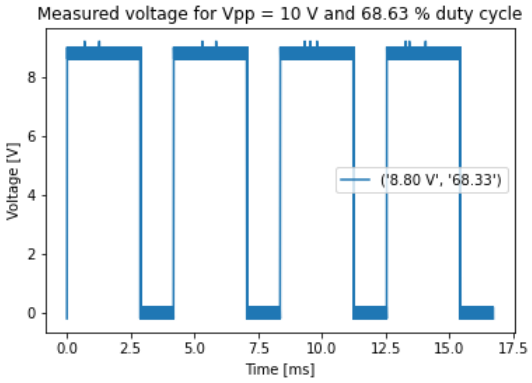

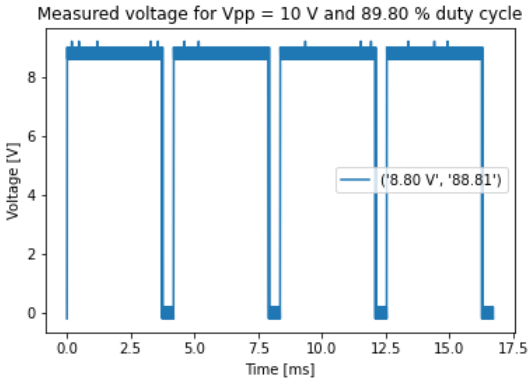
Measured voltage for Vpp = 10 V and 89.80 % duty cycle
Voltage [V]
Time [ms]
('8.80 V', '88.81')

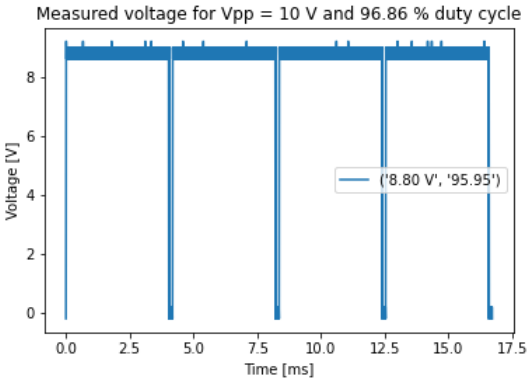
Measured voltage for Vpp = 10 V and 96.86 % duty cycle
Voltage [V]
Time [ms]
('8.80 V', '95.95')

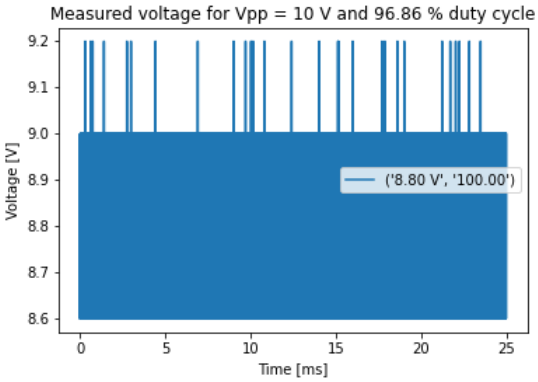
Measured voltage for Vpp = 10 V and 96.86 % duty cycle
Voltage [V]
Time [ms]
('8.80 V', '100.00')

6.2 15 V peak to peak voltage

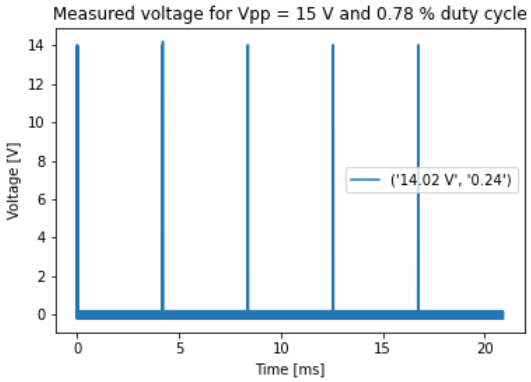

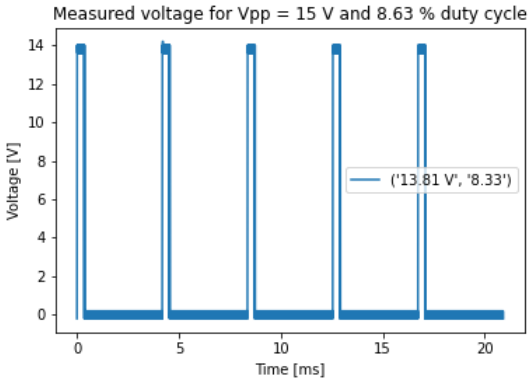

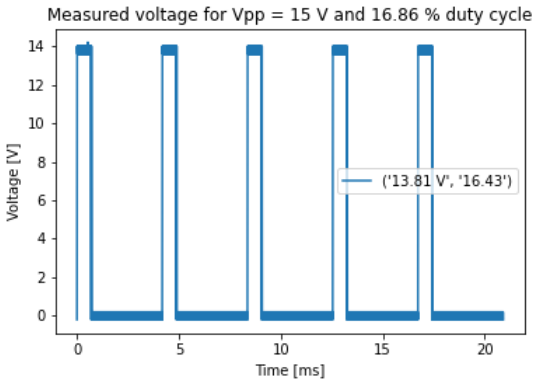

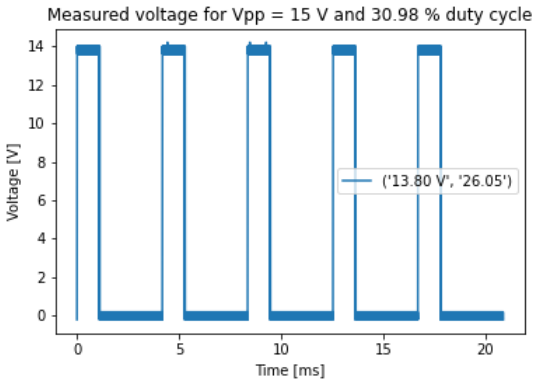

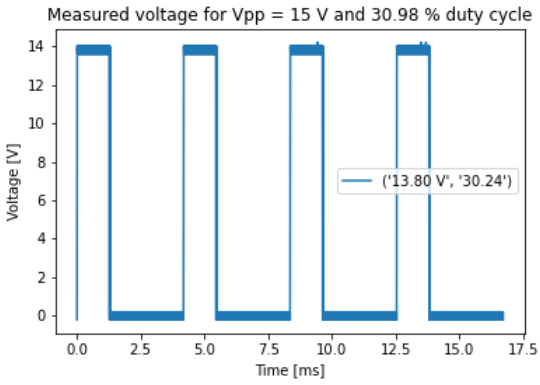

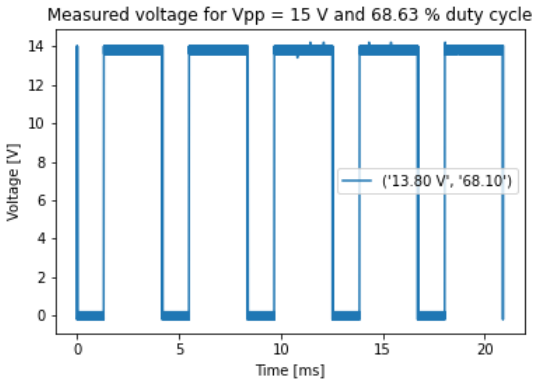

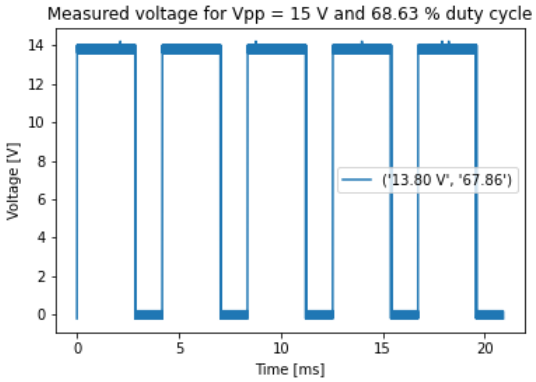

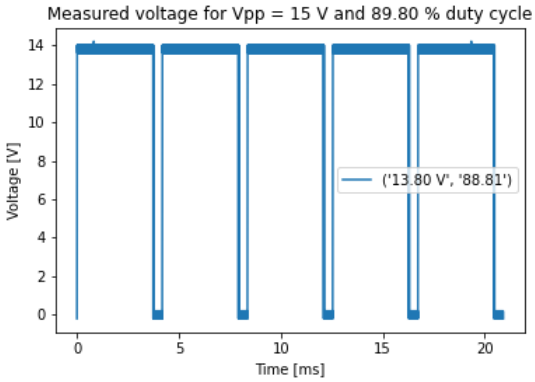

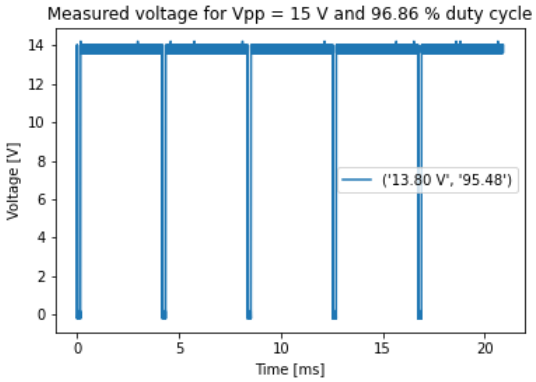

6.3 20 V peak to peak voltage

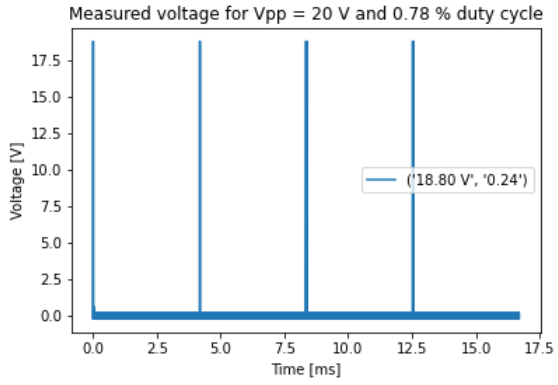

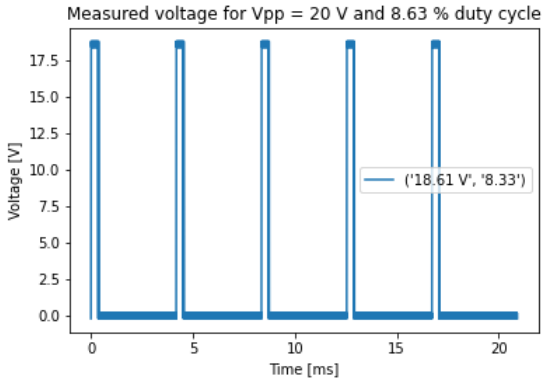

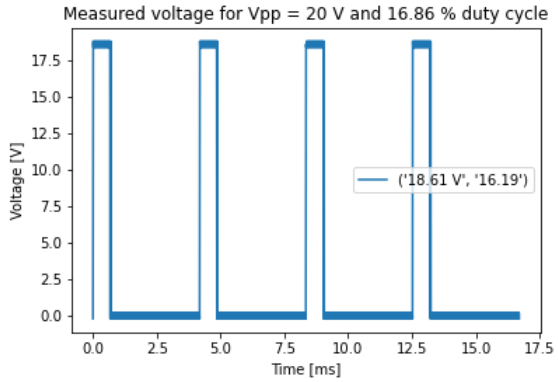

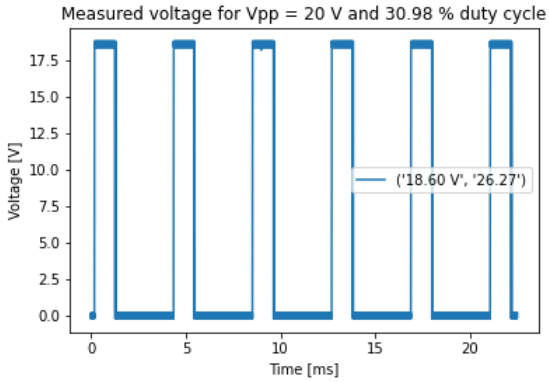

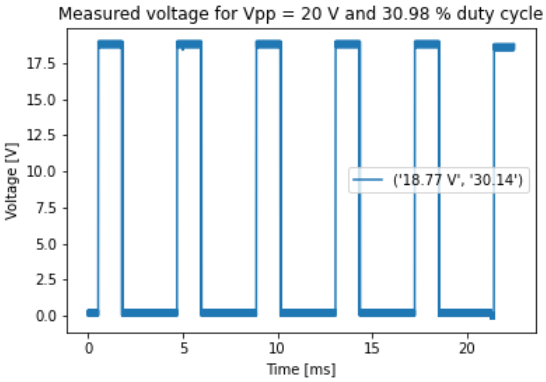

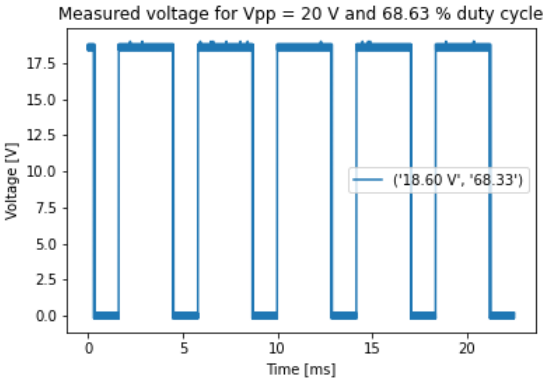

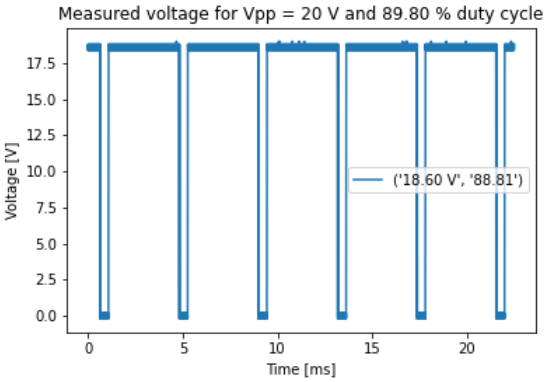

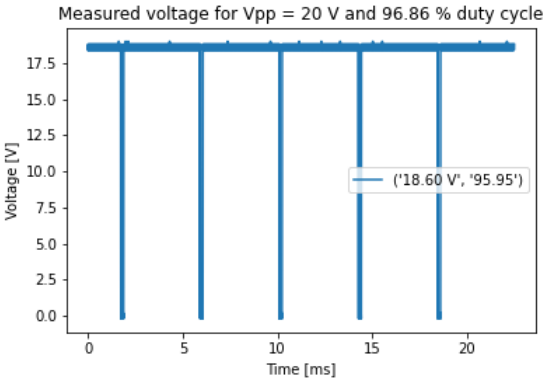

6.4 30 V peak to peak voltage

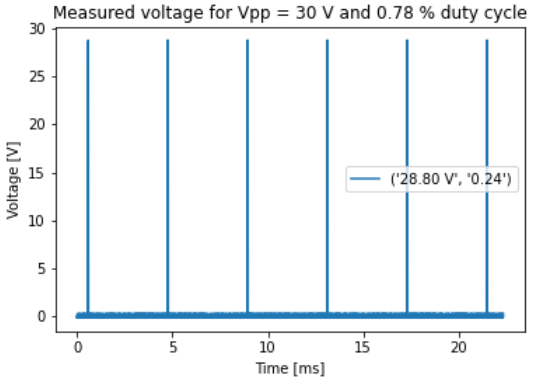

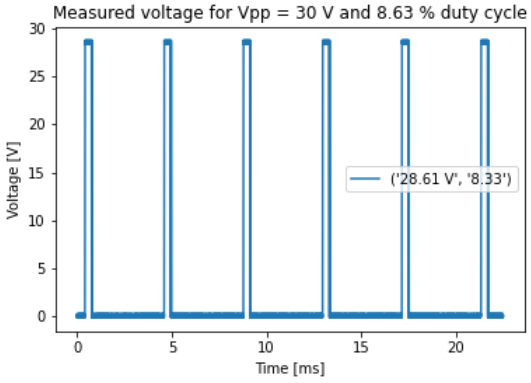

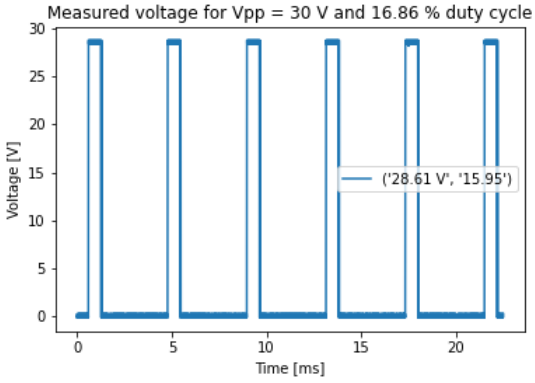

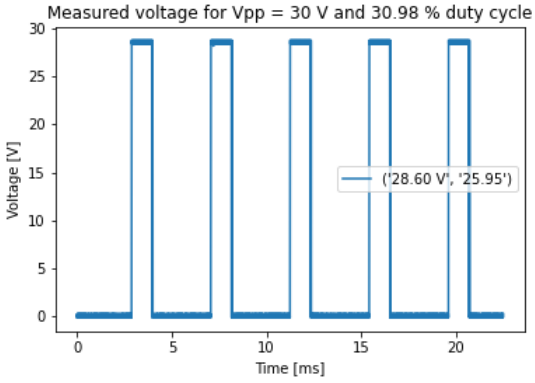

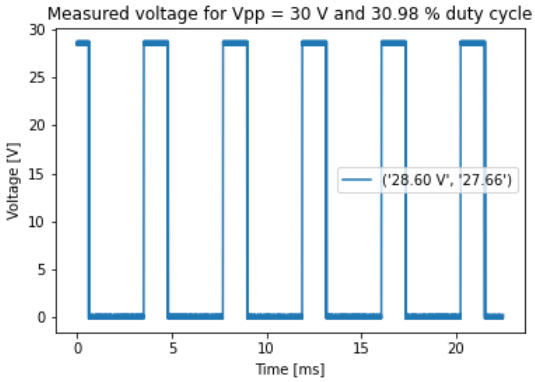
Measured voltage for Vpp = 30 V and 30.98 % duty cycle
Voltage [V]
Time [ms]
('28.60 V', '27.66')

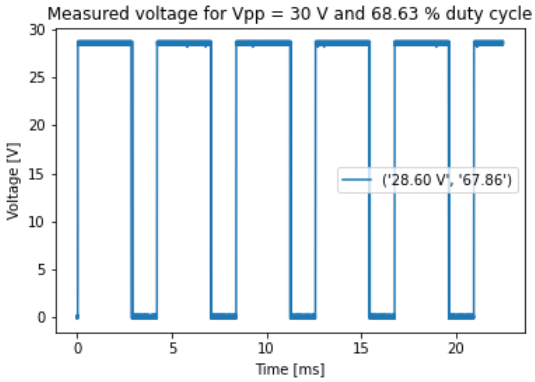
Measured voltage for Vpp = 30 V and 68.63 % duty cycle
Voltage [V]
Time [ms]
('28.60 V', '67.86')

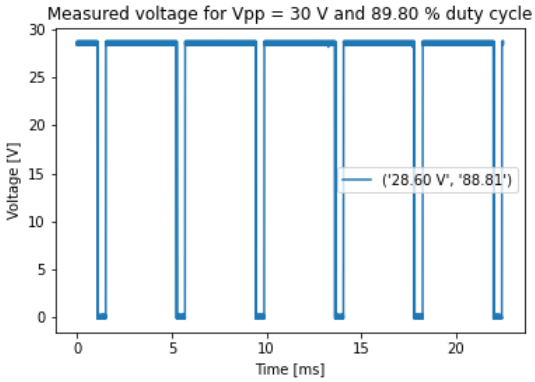
Measured voltage for Vpp = 30 V and 89.80 % duty cycle
Voltage [V]
Time [ms]
('28.60 V', '88.81')

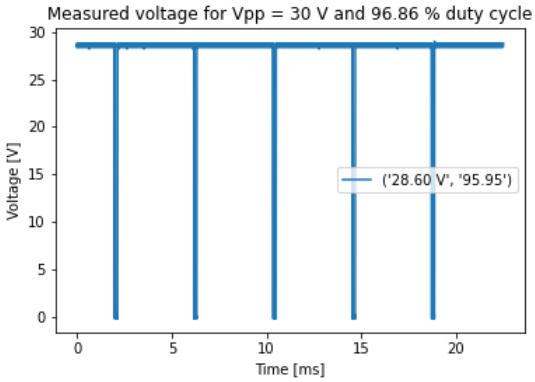
Measured voltage for Vpp = 30 V and 96.86 % duty cycle
Voltage [V]
Time [ms]
('28.60 V', '95.95')

D. Determining the equivalent thermal resistance of the thermocouples

An investigation into the influence of the applied heat flux to the equivalent thermal resistance of the thermocouples was done and is set out in this section. This investigation was done in a single-phase regime, with the flow fully turbulent (Re > 11 000).

The fluid was heated while in a subcooled single-phase state. Four uniform heating cases were run to establish the relation between the equivalent thermal resistance of a thermocouple and the applied heat flux.

The heating cases were for a uniform heat flux of 2 kW/m², 4 kW/m², 6.6 kW/m² and 7.6 kW/m². The ideal would have been to increase the applied heat flux to 20 kW/m^2, but these tests would render the flow in the two-phase region, regardless of the temperature of the fluid. This heat flux was applied to the outer diameter of the tube and assumed to the uniform to the point that it could be directly extrapolated onto the inner wall condition of the tube.

The data was reduced as set out in Section 5.1. The Gnielinski correlation was used to determine the Nusselt number, as it is applicable to the heat and flow conditions where the Reynolds number is between 3 000 and 5 000 000, with the Prandtl number between 0.5 and 2 000. The conditions of the flow were such that the Reynolds number was 11 300 and the Prandtl number 6.15.

The following graphs show the equivalent thermal resistances for the thermocouple at each station, determined at four different uniform heat flux conditions. From these results a linear regression was determined for each thermocouple such that the equivalent thermal resistance could be adjusted as the heat flux values at each segment changed during experimentation. In Figure 69, the uncertainty on the equivalent thermal resistance is larger than the value. This was due to a broken thermocouple. During testing, the temperature measurements from Station I was not included as the calibration in terms of temperature readings (Appendix B) and equivalent thermal resistance (Appendix D) failed.

Figures 61 to 69 capture a radial variation in the equivalent thermal resistance of the thermocouples at each station. This variation was due to the difference in radial position of the thermocouples introduced during manufacturing. The holes were drilled manually, the thermal paste varied in its thickness and the position of the thermocouple in the holes and thermal paste varied widely. The equivalent thermal resistance encapsulated all the possible uncertainties on these quantities accurately.

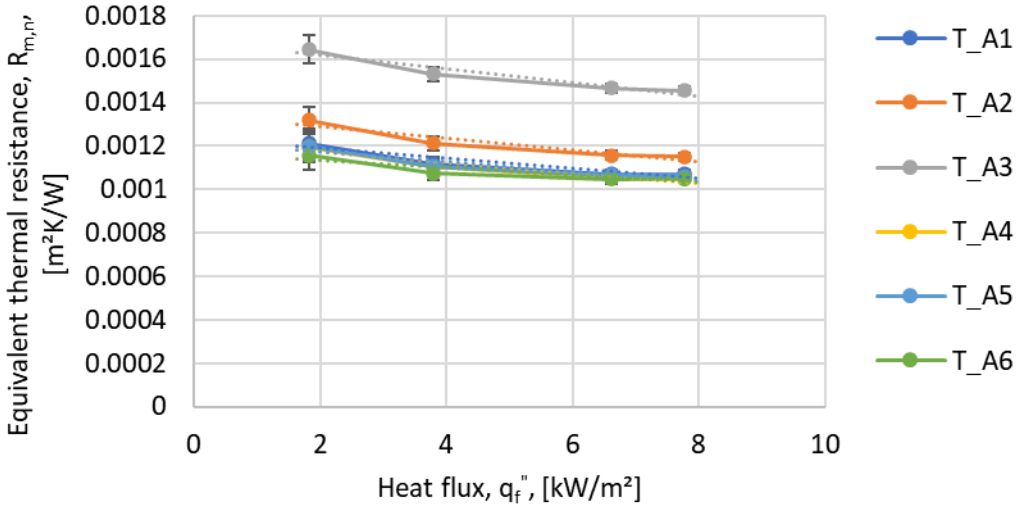

Figure 61: Equivalent thermal resistance change with heat flux for thermocouples at station A

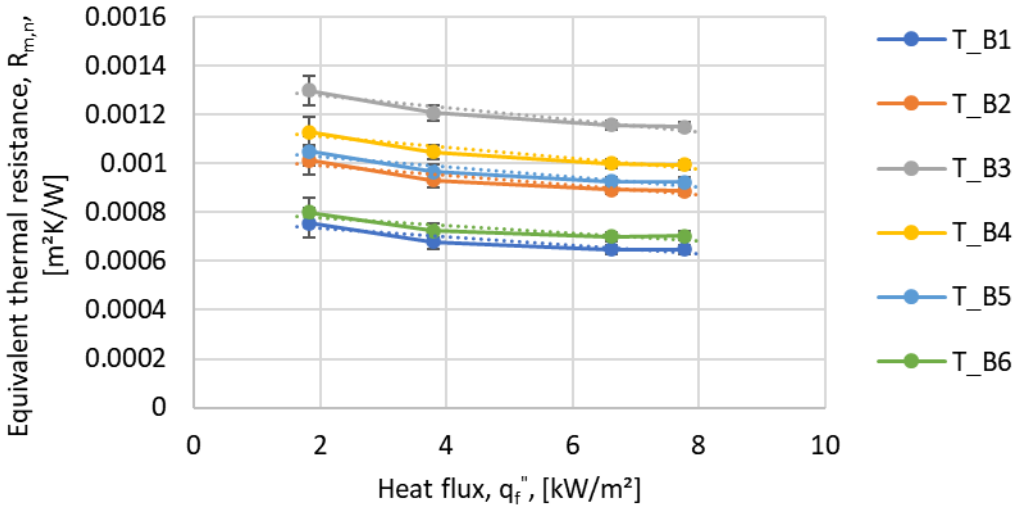

Figure 62: Equivalent thermal resistance change with heat flux for thermocouples at station B

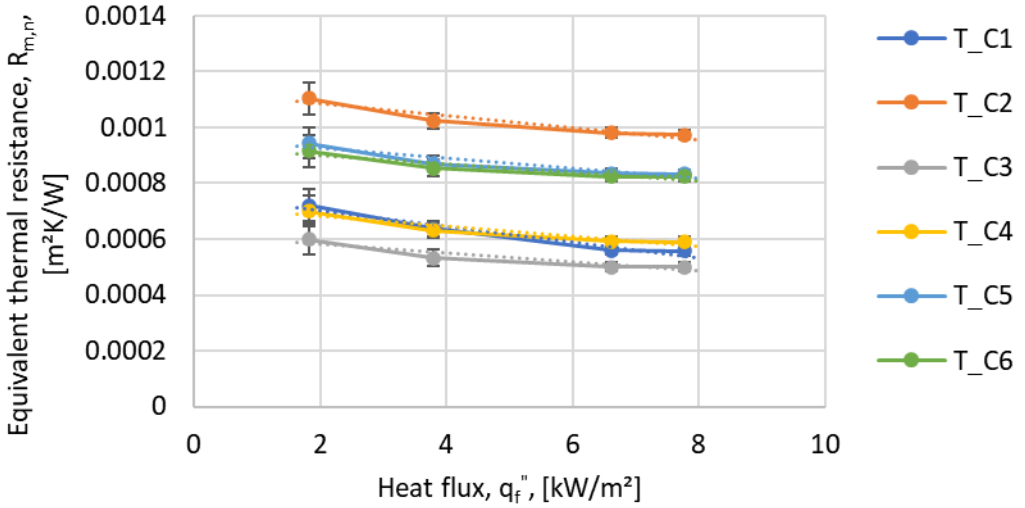

Figure 63: Equivalent thermal resistance change with heat flux for thermocouples at station C

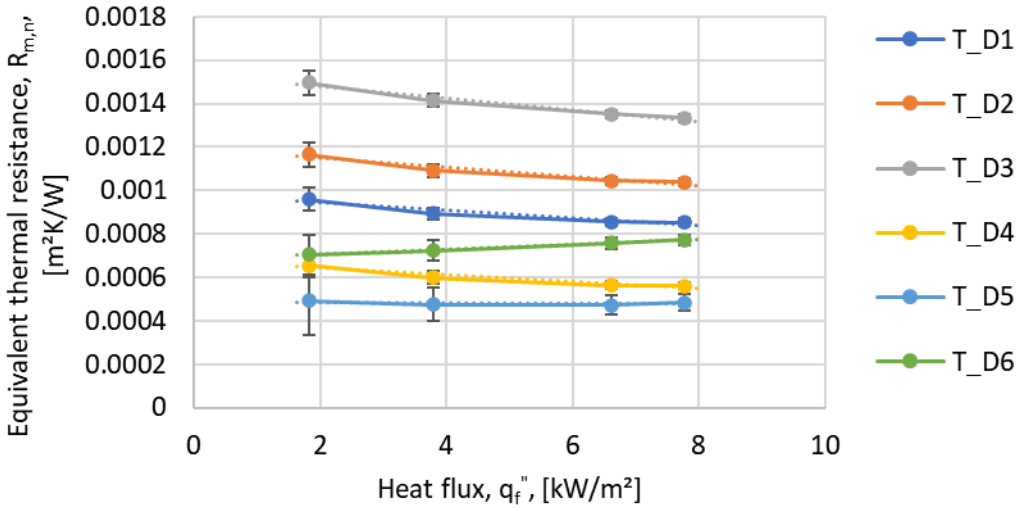

Figure 64: Equivalent thermal resistance change with heat flux for thermocouples at station D

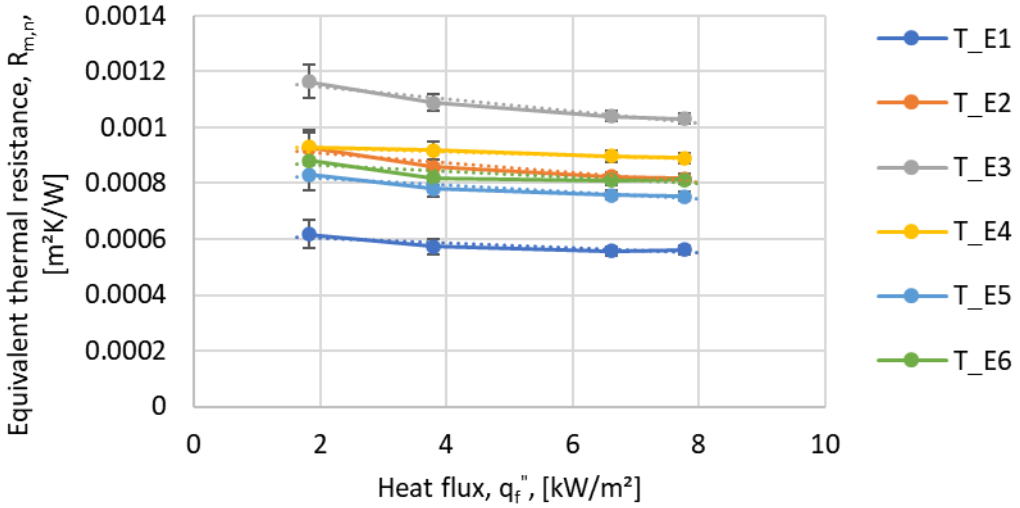

Figure 65: Equivalent thermal resistance change with heat flux for thermocouples at station E

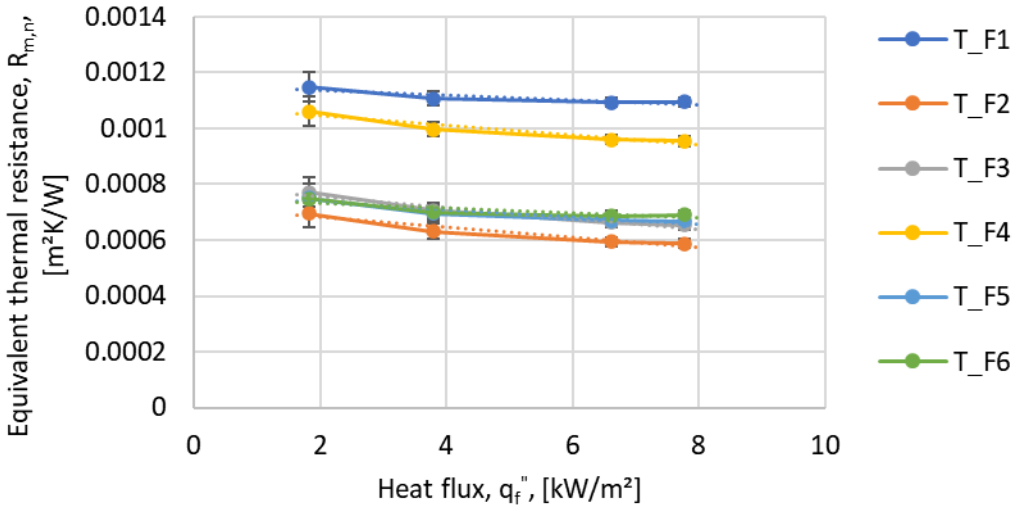

Figure 66: Equivalent thermal resistance change with heat flux for thermocouples at station F

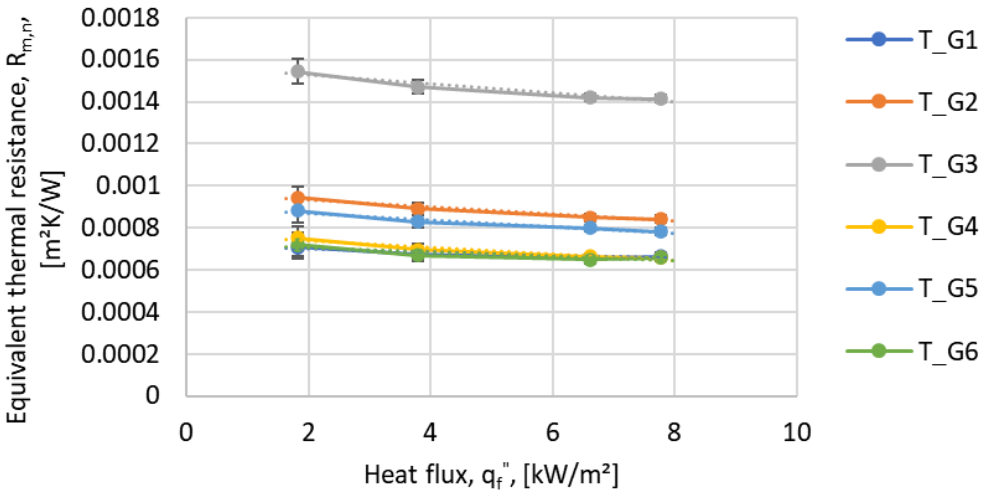

Figure 67: Equivalent thermal resistance change with heat flux for thermocouples at station G

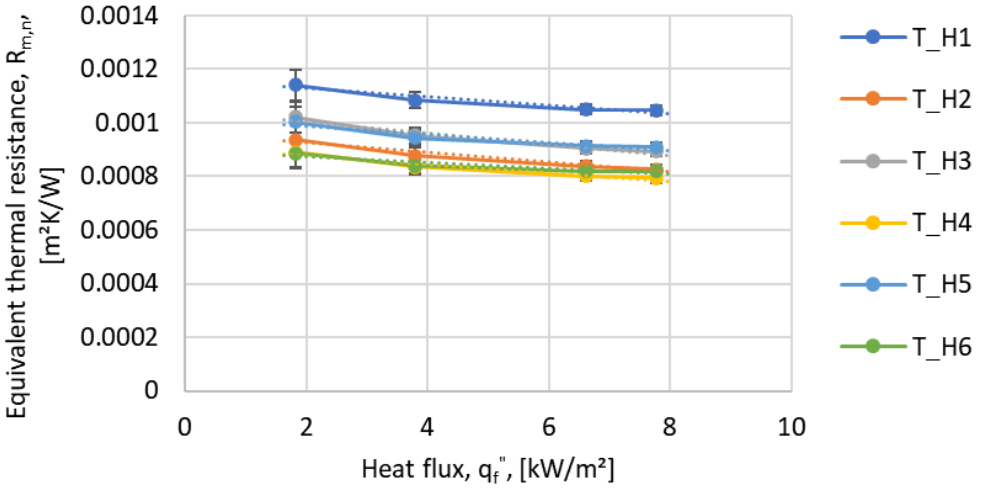

Figure 68: Equivalent thermal resistance change with heat flux for thermocouples at station H

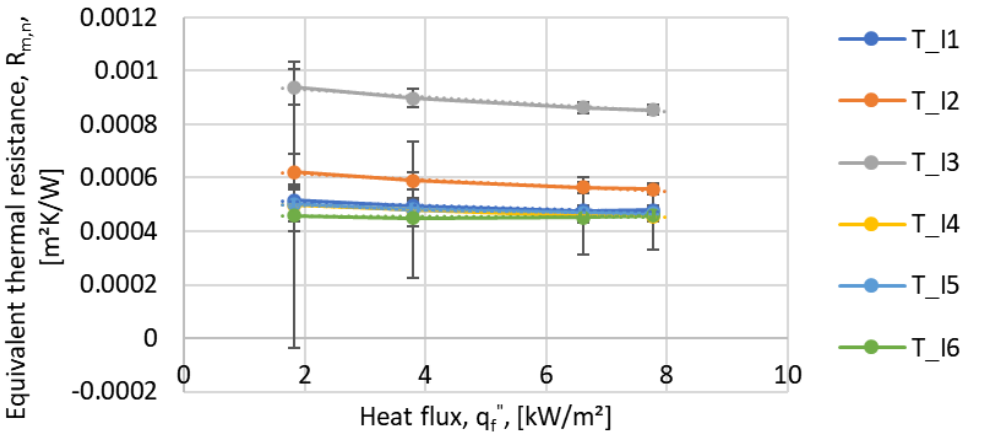

Figure 69: Equivalent thermal resistance change with heat flux for thermocouples at station I

E. Uncertainty analysis

In an experiment, the measurements taken are inherently flawed with errors introduced by noise and manufacturing inconsistencies. These errors propagate into the results that are achieved from the experiments and may have a significant effect on the validity of these results. It is therefore crucial that an uncertainty analysis be done on the system, taking each random and fixed error into account.

Uncertainty of a measurement

The error of an experimental result is the difference between the true value of result and the measured value. Since the true value of a result can never be exactly determined, the error can also only be estimated. This can be done through a statistical method known as an uncertainty analysis. The uncertainty of a result is the possible value that the error of that reported result might have.

The notation of a measurement should always include the uncertainty associated with that measurement. A convention for this has been established and is used in this investigation directly (Moffat, 1982). The measurements will be reported as follows:

$$X_{\mathrm{i}} = X_{\mathrm{i(measured)}} \pm \delta X_{\mathrm{i}}$$

The best estimate of X_{i} is $X_{\mathrm{i(measured)}}$. There is an uncertainty in X_{i} that may be as large as $\pm\delta X_{\mathrm{i}}$. The chances are 20 to 1 against the uncertainty of X_{i} being larger than δX_{i}.

In a single sample experiment, that will be the measured value directly. In a multi-sample experiment, $X_{\mathrm{i(measured)}}$ will be the mean of a set of N observations.

$$X_{\mathrm{i(measured)}} = \frac{\sum_{\mathrm{i}=1}^{\mathrm{N}} X_{\mathrm{i}}}{\mathrm{N}}$$

In a multi-sample experiment, the uncertainty δX_{i} can be a representation of the bias limit for fixed errors, and overall uncertainty in X_{i} with a confidence interval of 95%, or $\frac{tS_{\mathrm{N}}}{\sqrt{\mathrm{N}}}$ for random error components.

There are two errors that are captured within the uncertainty of a measured result. The fixed error (bias) and the random error (imprecision). The bias is specified by the manufacture. It is caused by imperfections in the instrumentation and determines the accuracy of the measurements being taken. Imprecision in measurements is caused by scatter in the data, or electrical noise. Through calibration this random error can be reduced, or the effect thereof eliminated. This is done by making use of a linear regression analysis.

According to the propagation of uncertainty, the bias and random errors need to be considered on the uncertainty of a measured result in the following way:

$$\delta X_{\mathrm{i}} = \sqrt{bias^2 + precision^2}$$

The uncertainty of any measured quantity has a set value. These values are propagated into the calculated results.

Uncertainty propagation

In an experiment where multiple variables are being measured to obtain a result, the result will be presented as:

$$R = R(X_1, X_2, X_3, \dots, X_N)$$

The uncertainty of a calculated result should have the same odds associated with it, as the uncertainty associated with each measurement.

Determining the uncertainty associated with a calculated result, the method of uncertainty propagation is utilized in this study. This method holds true if each measurement was made independently, repeated observations of each measurement would display a Gaussian distribution, and the uncertainty of each measurement was initially expressed at the same odds.

Where only one measurement is used to determine the result, the error would simply be:

$$\delta R_{X_\mathrm{i}} = \frac{\partial R}{\partial X_\mathrm{i}}(\delta X_\mathrm{i})$$

Where multiple measurements are required to determine the result, the error can be calculated as:

$$\delta R = \sqrt{\sum_{\mathrm{i}=1}^{\mathrm{N}} \left(\frac{\partial R}{\partial X_\mathrm{i}}(\delta X_\mathrm{i})\right)^2}$$

$\frac{\partial R}{\partial X_\mathrm{i}}$ is the partial derivative of the result with respect to each contributing measurement. This is a sensitivity coefficient: the larger the contribution of the measurement to the result, the larger the contribution of its error.

Sample Calculation

The uncertainty of the local HTC of a segment will be done to indicate the application of the method throughout the study. It should be noted that each individual measurement and calculated result has an associated uncertainty that can be determined in the instant the measurement is taken through mathematical codes scripted in the data acquisition setup. This sample calculation is written into such a mathematical code.

The physical set up of the test section

The test section is 900 mm (L_h) in heated length, with an outer diameter of 12,7 mm (D_i)and a wall thickness of 2 mm (t_SS). The stainless-steel tube has a conductive HTC of 16.5 W/mK (k_SS). The fluid flowing is R245FA. The uncertainty analysis is done on a case with a uniform heat flux boundary condition, with the fluid in the two-phase region.

Table 17: Measured quantities values and uncertainties for uncertainty propagation

Quantity	Value (X_i)	Uncertainty (δX_i)
L_h	900 mm	1 mm
D_o	12.7 mm	0.02 mm
t_{SS}	2 mm	0.02 mm
D_i	8.7 mm	0.02 mm
T_{in}, T_{out}	37.95 °C	0.06 °C
$T_{ins,o,n}, T_{ins,i,n}$	32.8 °C,35.6 °C	0.1 °C
$T_{TC,(m,n)}$	40.2 °C	0.1 °C
I_{tot}	6.75 A	0.1 A
R_n	20 Ω	0.1 Ω
C_{dc}	95 %	0.1 %
z_m	0.3 m	1 mm
t_{ins}	19.5 mm	0.5 mm
k_{SS}	16.5 W/mK	0.33 W/mK
k_{ins}	0.036 W/mK	0.00072 W/mK
k_f	0.095 W/mK	0.00190 W/mK
n	2	-

The uncertainty associated with the result of the HTC:

$$\alpha_n = \frac{q''_{f,n}}{T_{W,n} - T_B} = 2527\ \frac{W}{m^2K}$$

$$\delta\alpha_n = \sqrt{\left(\frac{\partial\alpha_n}{\partial q''_{f,n}}\left(\delta q''_{f,n}\right)\right)^2 + \left(\frac{\partial\alpha_n}{\partial T_{W,n}}\left(\delta T_{W,n}\right)\right)^2 + \left(\frac{\partial\alpha_n}{\partial \bar{T}_B}\left(\delta T_B\right)\right)^2}$$

$$\delta\alpha_n = \sqrt{\left(\frac{\left(\delta q''_{f,n}\right)}{\left(T_{W,n} - T_B\right)}\right)^2 + \left(\frac{-q''_{f,n}\left(\delta T_{w,n}\right)}{\left(T_{W,n} - T_B\right)^2}\right)^2 + \left(\frac{q''_{f,n}\left(\delta T_B\right)}{\left(T_{W,n} - T_B\right)^2}\right)^2}$$

$$\delta\alpha_n = 116\frac{W}{m^2K}$$

The wall temperature of the segment:

$$T_{W,n} = \frac{1}{9}\sum_{m=1}^{9} T_{W(m,n)} = 40.63\ °C$$

$$\delta T_{W,n} = \sqrt{\sum_{m=1}^{9}\frac{1}{9}\left(\frac{\partial T_{W,n}}{\partial T_{W(m,n)}}\left(\delta T_{W(m,n)}\right)\right)^2}$$

$$\delta T_{W,n} = \sqrt{\sum_{m=1}^{9}\frac{1}{9}\left(\delta T_{W(m,n)}\right)^2}$$

$$\delta T_{W,n} = 0.07\ °C$$

$$T_{\mathrm{W(m,n)}} = T_{\mathrm{TC(m,n)}} - q''_{\mathrm{o,n}} R_{\mathrm{m,n}} = 39.6\ °C$$

$$\delta T_{\mathrm{W(m,n)}} = \sqrt{\left(\frac{\partial T_{\mathrm{W(m,n)}}}{\partial T_{\mathrm{TC(m,n)}}}\left(\delta T_{\mathrm{TC(m,n)}}\right)\right)^2 + \left(\frac{\partial T_{\mathrm{W(m,n)}}}{\partial R_{\mathrm{m,n}}}\left(\delta R_{\mathrm{m,n}}\right)\right)^2 + \left(\frac{\partial T_{\mathrm{W(m,n)}}}{\partial q''_{\mathrm{o,n}}}\left(\delta q''_{\mathrm{o,n}}\right)\right)^2}$$

$$\delta T_{\mathrm{W(m,n)}} = \sqrt{\left(\delta T_{\mathrm{TC(m,n)}}\right)^2 + \left(-q''_{\mathrm{o,n}}\left(\delta R_{\mathrm{m,n}}\right)\right)^2 + \left(-R_{\mathrm{m,n}}\left(\delta q''_{\mathrm{o,n}}\right)\right)^2}$$

$$\delta T_{\mathrm{W(m,n)}} = 0.13\ °C$$

The heat flux on the segment:

$$q''_{\mathrm{o,n}} = \frac{\left(\dot{Q}_{\Omega,\mathrm{n}} + \dot{Q}_{\mathrm{ins,n}}\right)}{\frac{\pi D_{\mathrm{o}} L_{\mathrm{h}}}{6}} = 4503\ \frac{W}{m^2}$$

$$\delta q''_{\mathrm{o,n}} = \sqrt{\left(\frac{\partial q''_{\mathrm{o,n}}}{\partial \dot{Q}_{\Omega,\mathrm{n}}}\left(\delta \dot{Q}_{\Omega,\mathrm{n}}\right)\right)^2 + \left(\frac{\partial q''_{\mathrm{o,n}}}{\partial \dot{Q}_{\mathrm{ins,n}}}\left(\delta \dot{Q}_{\mathrm{ins,n}}\right)\right)^2 + \left(\frac{\partial q''_{\mathrm{o,n}}}{\partial D_{\mathrm{o}}}\left(\delta D_{\mathrm{o}}\right)\right)^2 + \left(\frac{\partial q''_{\mathrm{o,n}}}{\partial L_{\mathrm{h}}}\left(\delta L_{\mathrm{h}}\right)\right)^2}$$

$$\delta q''_{\mathrm{o,n}} = \sqrt{\left(\frac{\left(\delta \dot{Q}_{\Omega,\mathrm{n}}\right)}{\frac{\pi D_{\mathrm{o}} L_{\mathrm{h}}}{6}}\right)^2 + \left(\frac{\left(\delta \dot{Q}_{\mathrm{ins,n}}\right)}{\frac{\pi D_{\mathrm{o}} L_{\mathrm{h}}}{6}}\right)^2 + \left(-\frac{6\left(\dot{Q}_{\Omega,\mathrm{n}} + \dot{Q}_{\mathrm{ins,n}}\right)}{\pi D_{\mathrm{o}}^2 L_{\mathrm{h}}}\left(\delta D_{\mathrm{o}}\right)\right)^2 + \left(-\frac{6\left(\dot{Q}_{\Omega,\mathrm{n}} + \dot{Q}_{\mathrm{ins,n}}\right)}{\pi D_{\mathrm{o}} L_{\mathrm{h}}^2}\left(\delta L_{\mathrm{h}}\right)\right)^2}$$

$$\delta q''_{\mathrm{o,n}} = 154.2\ \frac{W}{m^2}$$

The bulk fluid temperature:

$$T_{\mathrm{B}} = \frac{1}{2}\left(T_{\mathrm{in}} + T_{\mathrm{out}}\right) = 37.95\ °C$$

$$\delta T_{\mathrm{B}} = \sqrt{\left(\frac{\partial T_{\mathrm{B}}}{\partial T_{\mathrm{in}}}\left(\delta T_{\mathrm{in}}\right)\right)^2 + \left(\frac{\partial T_{\mathrm{B}}}{\partial T_{f,o}}\left(\delta T_{\mathrm{out}}\right)\right)^2}$$

$$\delta T_{\mathrm{B}} = \sqrt{\left(\frac{1}{2}\left(\delta T_{\mathrm{in}}\right)\right)^2 + \left(\frac{1}{2}\left(\delta T_{\mathrm{out}}\right)\right)^2}$$

$$\delta T_{\mathrm{B}} = 0.04\ °C$$

Applied heating from the heating element:

$$\dot{Q}_{\Omega,\mathrm{n}} = I_{\mathrm{n}}^2 R_{\mathrm{n}} = 27.04\ W$$

$$\delta\dot{Q}_{\Omega,\mathrm{n}} = \sqrt{\left(\frac{\partial\dot{Q}_{\Omega,\mathrm{n}}}{\partial I_{\mathrm{n}}}(\delta I_{\mathrm{n}})\right)^2 + \left(\frac{\partial\dot{Q}_{\Omega,\mathrm{n}}}{\partial R_{\mathrm{n}}}(\delta R_{\mathrm{n}})\right)^2}$$

$$\delta\dot{Q}_{mn} = \sqrt{\left(2I_{\mathrm{n}}R_n(\delta I_{\mathrm{n}})\right)^2 + \left(I_{\mathrm{n}}^2(\delta R_{\mathrm{n}})\right)^2}$$

$$\delta\dot{Q}_{mn} = 0.921\ W$$

Root mean square (RMS) electric current through a particular element:

$$I_{\mathrm{n}} = I_{\mathrm{tot}}\frac{\frac{C_{\mathrm{dc,n}}}{R_{\mathrm{n}}}}{\sum_{n=1}^{6}\frac{C_{\mathrm{dc,n}}}{R_{\mathrm{n}}}} = 1.124\ A$$

$$R_{\mathrm{ns}} = \sum_{n=1}^{6}\frac{C_{\mathrm{dc,n}}}{R_{\mathrm{n}}} = 0.2717\ \Omega$$

$$\delta R_{\mathrm{ns}} = \sqrt{\sum_{m=1}^{6}\sqrt{\left(\frac{\partial R_{\mathrm{ns}}}{\partial C_{\mathrm{dc,n}}}\left(\delta C_{\mathrm{dc,n}}\right)\right)^2 + \left(\frac{\partial R_{\mathrm{ns}}}{\partial R_{\mathrm{n}}}(\delta R_{\mathrm{n}})\right)^2}}$$

$$\delta R_{\mathrm{ns}} = \sqrt{\sum_{m=1}^{6}\left(\frac{\left(\delta C_{\mathrm{dc,n}}\right)}{R_{\mathrm{n}}}\right)^2 + \left(\frac{-C_{\mathrm{dc,n}}}{R_{\mathrm{n}}^2}(\delta R_{\mathrm{n}})\right)^2}$$

$$\delta R_{\mathrm{ns}} = 0.000542\ \Omega$$

$$\delta I_{\mathrm{n}} = \sqrt{\left(\frac{\partial I_{\mathrm{n}}}{\partial I_{\mathrm{tot}}}(\delta I_{\mathrm{tot}})\right)^2 + \left(\frac{\partial I_{\mathrm{n}}}{\partial C_{\mathrm{dc,n}}}\left(\delta C_{\mathrm{dc,n}}\right)\right)^2 + \left(\frac{\partial I_{\mathrm{n}}}{\partial R_{\mathrm{n}}}(\delta R_{\mathrm{n}})\right)^2 + \left(\frac{\partial I_{\mathrm{n}}}{\partial R_{ns}}(\delta R_{ns})\right)^2}$$

$$\delta I_{\mathrm{n}} = \sqrt{\left(\frac{\frac{C_{\mathrm{dc,n}}}{R_{\mathrm{n}}}(\delta I_{\mathrm{tot}})}{R_{\mathrm{ns}}}\right)^2 + \left(\frac{\frac{I_{\mathrm{tot}}}{R_{\mathrm{n}}}\left(\delta C_{\mathrm{dc,n}}\right)}{R_{\mathrm{ns}}}\right)^2 + \left(\frac{-I_{\mathrm{tot}}\frac{C_{\mathrm{dc,n}}}{R_{\mathrm{n}}^2}(\delta R_{\mathrm{n}})}{R_{\mathrm{ns}}}\right)^2 + \left(\frac{-I_{\mathrm{tot}}\frac{C_{\mathrm{dc,n}}}{R_{\mathrm{n}}}(\delta R_{\mathrm{ns}})}{R_{\mathrm{ns}}^2}\right)^2}$$

$$\delta I_{RMS,n} = 0.0177\ A$$

Heat transfer through the insulation:

$$\dot{Q}_{\mathrm{ins,n}} = \frac{k_{\mathrm{ins}} A_{\mathrm{ins,n}} \left(T_{\mathrm{ins,o,n}} - T_{\mathrm{ins,i,n}}\right)}{t_{\mathrm{ins}}} = -0.0791\ W$$

$$\delta\dot{Q}_{\mathrm{ins,n}} = \sqrt{\left(\frac{\partial \dot{Q}_{\mathrm{ins,n}}}{\partial k_{\mathrm{ins}}}(\delta k_{\mathrm{ins}})\right)^2 + \left(\frac{\partial \dot{Q}_{\mathrm{ins,n}}}{\partial A_{\mathrm{ins,n}}}(\delta A_{\mathrm{ins,n}})\right)^2 + \left(\frac{\partial \dot{Q}_{\mathrm{ins,n}}}{\partial T_{\mathrm{ins,o,n}}}(\delta T_{\mathrm{ins,o,n}})\right)^2 + \left(\frac{\partial \dot{Q}_{\mathrm{ins,n}}}{\partial T_{\mathrm{ins,i,n}}}(\delta T_{\mathrm{ins,i,n}})\right)^2 + \left(\frac{\partial \dot{Q}_{\mathrm{ins,n}}}{\partial t_{\mathrm{ins}}}(\delta t_{\mathrm{ins}})\right)^2}$$

$$\delta\dot{Q}_{\mathrm{ins,n}} = \sqrt{\left(\frac{\dot{Q}_{\mathrm{ins,n}}}{k_{\mathrm{ins}}}(\delta k_{ins})\right)^2 + \left(\frac{\dot{Q}_{\mathrm{ins,n}}}{A_{\mathrm{ins,n}}}(\delta A_{\mathrm{ins,n}})\right)^2 + \left(\frac{k_{\mathrm{ins}} A_{\mathrm{ins,n}}}{t_{\mathrm{ins}}}(\delta T_{\mathrm{ins,o,n}})\right)^2 + \left(\frac{-k_{\mathrm{ins}} A_{\mathrm{ins,n}}}{t_{\mathrm{ins}}}(\delta T_{\mathrm{ins,i,n}})\right)^2 + \left(-\frac{\dot{Q}_{\mathrm{ins,n}}}{t_{\mathrm{ins}}}(\delta t_{\mathrm{ins}})\right)^2}$$

$$\delta\dot{Q}_{\mathrm{ins,n}} = 0.0047\ W$$

Conduction heat transfer area :

$$A_{\mathrm{ins,n}} = \frac{\pi D_{\mathrm{mid}} L_{\mathrm{h}}}{6} = 0.0153\ m^2$$

$$\delta A_{\mathrm{ins,n}} = \sqrt{\left(\frac{\partial A_{\mathrm{ins,n}}}{\partial D_{\mathrm{mid}}}(\delta D_{\mathrm{mid}})\right)^2 + \left(\frac{\partial A_{\mathrm{ins,n}}}{\partial L_{\mathrm{h}}}(\delta L_{\mathrm{h}})\right)^2}$$

$$\delta A_{\mathrm{ins,n}} = \sqrt{\left(\frac{\pi L}{6}(\delta D_{\mathrm{mid}})\right)^2 + \left(\frac{\pi D_{\mathrm{mid}}}{6}(\delta L_{\mathrm{h}})\right)^2}$$

$$\delta A_{\mathrm{ins,n}} = 0.0000295\ m^2$$

Mid insulation diameter:

$$D_{\mathrm{mid}} = D_{\mathrm{o}} + t_{\mathrm{ins}} = 0.0325\ m$$

$$\delta D_{\mathrm{mid}} = \sqrt{\left(\frac{\partial D_{\mathrm{mid}}}{\partial D_{\mathrm{o}}}(\delta D_{\mathrm{o}})\right)^2 + \left(\frac{\partial D_{\mathrm{mid}}}{\partial t_{\mathrm{ins}}}(\delta t_{\mathrm{ins}})\right)^2}$$

$$\delta D_{\mathrm{mid}} = \sqrt{(\delta D_{\mathrm{o}})^2 + (\delta t_{\mathrm{ins}})^2}$$

$$\delta D_{\mathrm{mid}} = 0.0005\ m$$

The uncertainty associated with the position of the thermocouples:

$$R_{\mathrm{m,n}} = \frac{\left(T_{\mathrm{TC,(m,n)}} - T_{\mathrm{W}}\right)}{q^{"}_{\mathrm{uniform}}} = 0.00051\ \frac{°C\,.m^2}{W}$$

$$\delta R_{\mathrm{m,n}} = \sqrt{\left(\frac{\partial R_{\mathrm{m,n}}}{\partial q^{"}_{\mathrm{uniform}}}\left(\delta q^{"}_{\mathrm{uniform}}\right)\right)^2 + \left(\frac{\partial R_{\mathrm{m,n}}}{\partial T_{mn}}\left(\delta T_{\mathrm{TC,(m,n)}}\right)\right)^2 + \left(\frac{\partial R_{\mathrm{m,n}}}{\partial T_{\mathrm{W}}}\left(\delta T_{\mathrm{W}}\right)\right)^2}$$

$$\delta R_{\mathrm{m,n}} = \sqrt{\left(\frac{-R_{\mathrm{m,n}}\delta q^{"}_{\mathrm{uniform}}}{q^{"}_{\mathrm{uniform}}}\right)^2 + \left(\frac{\delta T_{\mathrm{TC,(m,n)}}}{q^{"}_{\mathrm{uniform}}}\right)^2 + \left(\frac{\delta T_{\mathrm{W}}}{q^{"}_{\mathrm{uniform}}}\right)^2}$$

$$\delta R_{\mathrm{m,n}} = \ 0.00000851\ \frac{°C\,.m^2}{W}$$

Wetted wall temperature:

$$T_{\mathrm{W}} = T_{\mathrm{B}} + \frac{q^{"}}{\alpha_{\mathrm{liq}}} = \ 40.63\ °C$$

$$\delta T_{\mathrm{W}} = \sqrt{\left(\frac{\partial T_{\mathrm{W}}}{\partial T_{\mathrm{B}}}\left(\delta T_{\mathrm{B}}\right)\right)^2 + \left(\frac{\partial T_{\mathrm{W}}}{\partial q^{"}}\left(\delta q^{"}\right)\right)^2 + \left(\frac{\partial T_{\mathrm{W}}}{\partial \alpha_{\mathrm{liq}}}\left(\delta \alpha_{\mathrm{liq}}\right)\right)^2}$$

$$\delta T_{\mathrm{W}} = \sqrt{\left(\delta T_{\mathrm{B}}\right)^2 + \left(\frac{\delta q^{"}}{\alpha_{\mathrm{liq}}}\right)^2 + \left(\frac{q^{"}}{\alpha^2_{\mathrm{liq}}}\left(\delta \alpha_{\mathrm{liq}}\right)\right)^2}$$

$$\delta T_{\mathrm{W}} = 0.07\frac{W}{m^2K}$$

Single phase Gnielinski heat transfer coefficient:

$$\alpha_{\mathrm{liq}} = \frac{k_{\mathrm{f}}Nu}{D_{\mathrm{i}}} = 741\frac{W}{m^2K}$$

$$\delta \alpha_{\mathrm{liq}} = \sqrt{\left(\frac{\partial \alpha_{\mathrm{liq}}}{\partial Nu}\left(\delta Nu\right)\right)^2 + \left(\frac{\partial \alpha_{\mathrm{liq}}}{\partial k_{\mathrm{f}}}\left(\delta k_{\mathrm{f}}\right)\right)^2 + \left(\frac{\partial \alpha_{\mathrm{liq}}}{\partial D_{\mathrm{i}}}\left(\delta D_{\mathrm{i}}\right)\right)^2}$$

$$\delta \alpha_{\mathrm{liq}} = \sqrt{\left(\frac{\delta Nu\ k_{\mathrm{f}}}{D_{\mathrm{i}}}\right)^2 + \left(\frac{Nu\delta k_{\mathrm{f}}}{D_{\mathrm{i}}}\right)^2 + \left(\frac{Nu\ k_{\mathrm{f}}}{D^2_{\mathrm{i}}}\left(\delta D_{\mathrm{i}}\right)\right)^2}$$

$$\delta \alpha_{\mathrm{liq}} = 14.92\frac{W}{m^2K}$$

Outer wall uniform heat flux:

$$q''_{\text{uniform}} = \frac{\sum_{n=1}^{6}\left(\dot{Q}_{\Omega,n} + \dot{Q}_{\text{ins,n}}\right)}{\pi D_{\text{o}} L_{\text{h}}} = 4503\frac{W}{m^2}$$

$$\delta q''_{\text{uniform}} = \sqrt{\left(\frac{\partial q''_{\text{uniform}}}{\partial \dot{Q}_{\Omega,n}}\left(\delta \dot{Q}_{\Omega,n}\right)\right)^2 + \left(\frac{\partial q''_{\text{uniform}}}{\partial \dot{Q}_{\text{ins,n}}}\left(\delta \dot{Q}_{\text{ins,n}}\right)\right)^2 + \left(\frac{\partial q''_{\text{uniform}}}{\partial D_{\text{o}}}\left(\delta D_{\text{o}}\right)\right)^2 + \left(\frac{\partial q''_{\text{uniform}}}{\partial L_{\text{h}}}\left(\delta L_{\text{h}}\right)\right)^2}$$

$$\delta q''_{\text{uniform}} = \sqrt{\left(\frac{\partial q''_{\text{uniform}}}{\pi D_{\text{o}} L_{\text{h}}}\left(\delta \dot{Q}_{\Omega,n}\right)\right)^2 + \left(\frac{\partial q''_{\text{uniform}}}{\partial \dot{Q}_{\text{ins,n}}}\left(\delta \dot{Q}_{\text{ins,n}}\right)\right)^2 + \left(\frac{\partial q''_{\text{uniform}}}{\partial D_{\text{o}}}\left(\delta D_{\text{o}}\right)\right)^2 + \left(\frac{\partial q''_{\text{uniform}}}{\partial L_{\text{h}}}\left(\delta L_{\text{h}}\right)\right)^2}$$

$$\delta q''_{\text{uniform}} = 60.7\ \frac{W}{m^2}$$

F. Results for clusters

As discussed in Section 6.4, the contour plots for all the clusters tested are presented. The clusters are named according to the mass flux and saturation temperature combination that was investigated. For each mass flux and saturation temperature combination, nine (9) different heating cases were investigated, over a range of vapour qualities, ranging from 0.228 – 0.695. The cluster names are as set out in Table F-1.

Table F-1: Cluster name convention

		Mass flux, G, [kg/m²s]	
		200	**300**
Saturation temperature, T_{sat} [°C]	**35**	200_35	300_35
	40	200_40	300_40

200_40

Case I – Uniform heating — Mass flux = 200 kg/m²s; Saturation temperature = 40 °C

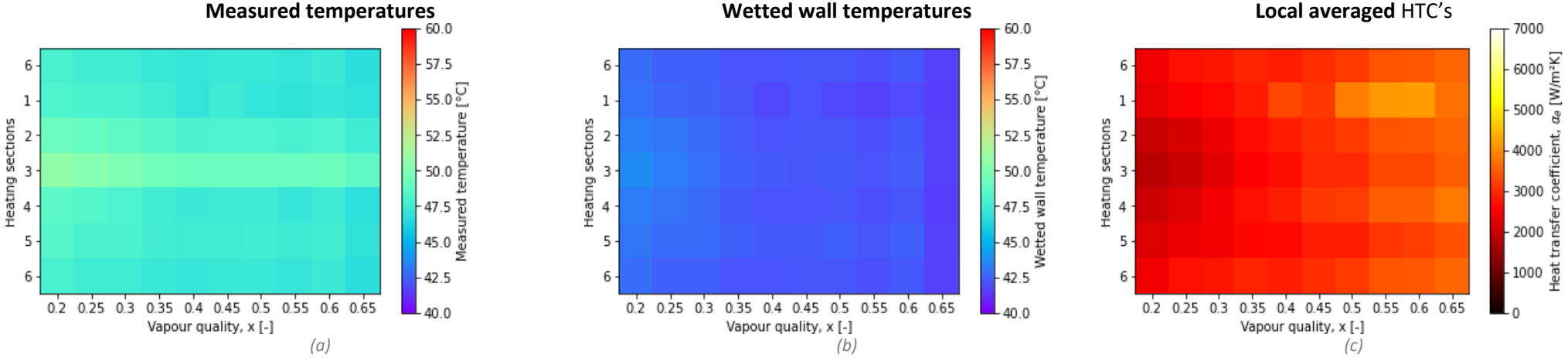

Figure 70: Results for case I - Uniform heating for G = 200 kg/m²s and T_B = 40 °C

Case II – Bottom heating

Mass flux = 200 kg/m²s; Saturation temperature = 40 °C

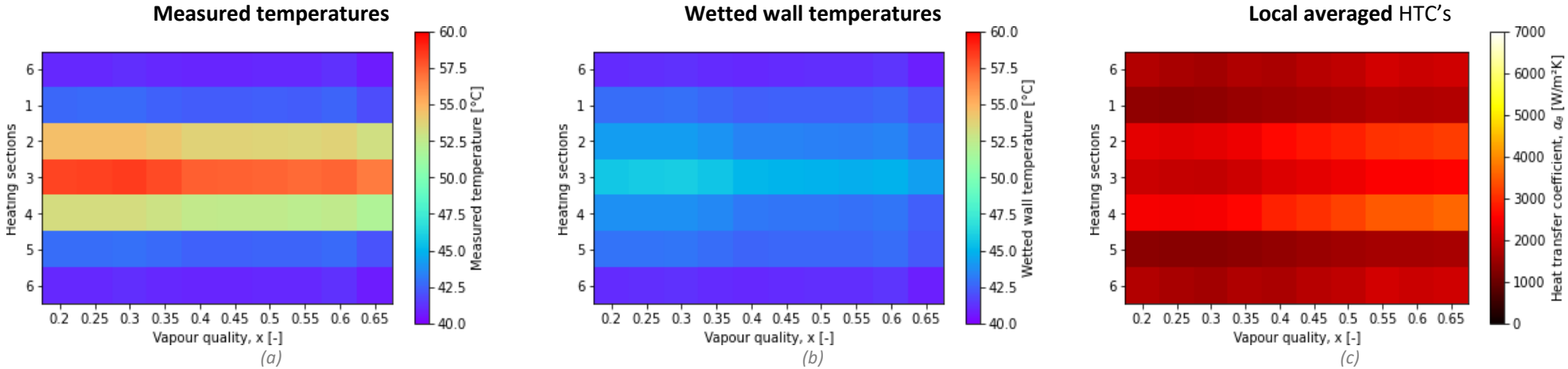

Figure 71: Results for case II - Bottom heating for G = 200 kg/m²s and T_B = 40 °C

Case III – Top heating

Mass flux = 200 kg/m²s; Saturation temperature = 40 °C

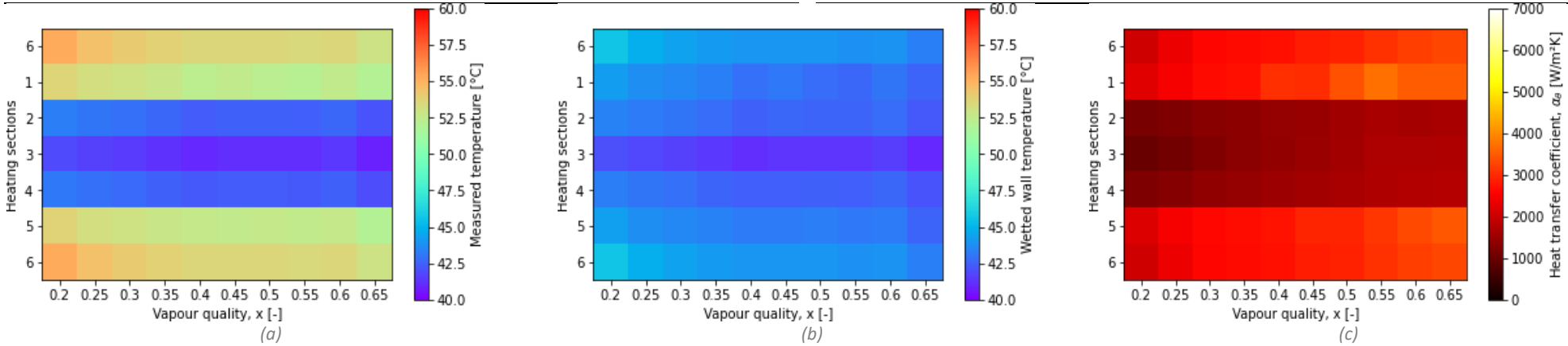

Figure 72: Results for case III - Top heating for G = 200 kg/m²s and T_B = 40 °C

Case IV – Left heating

Mass flux = 200 kg/m²s; Saturation temperature = 40 °C

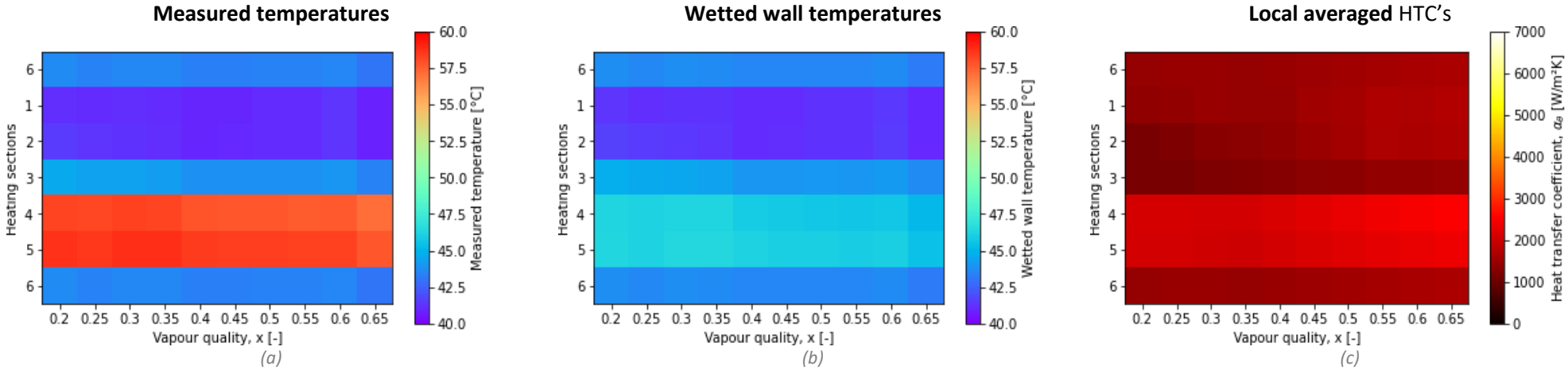

Figure 73: Results for case IV - Left heating for G = 200 kg/m²s and T_B = 40 °C

Case V – Right heating

Mass flux = 200 kg/m²s; Saturation temperature = 40 °C

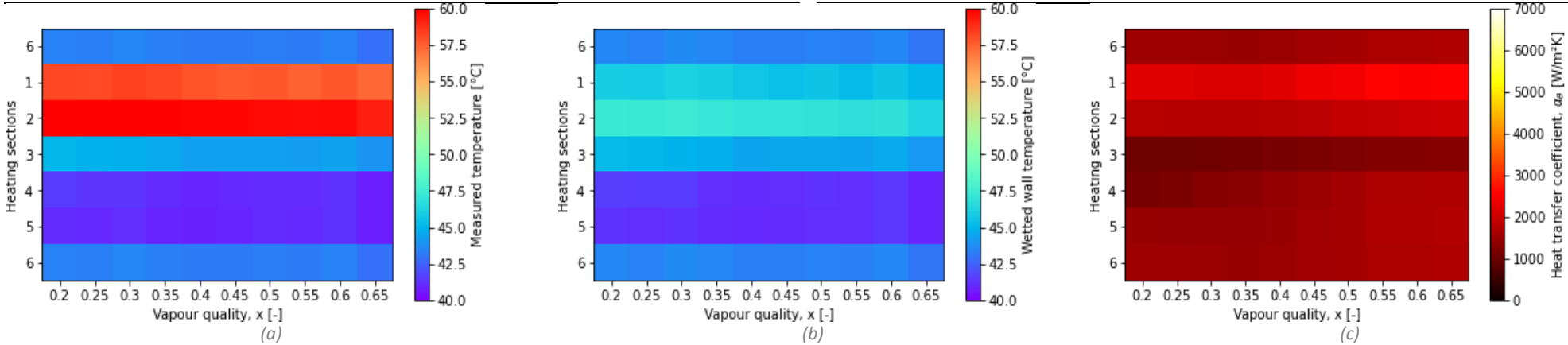

Figure 74: Results for case V - Right heating for G = 200 kg/m²s and T_B = 40 °C

Case VI – Segment 3 heating

Mass flux = 200 kg/m²s; Saturation temperature = 40 °C

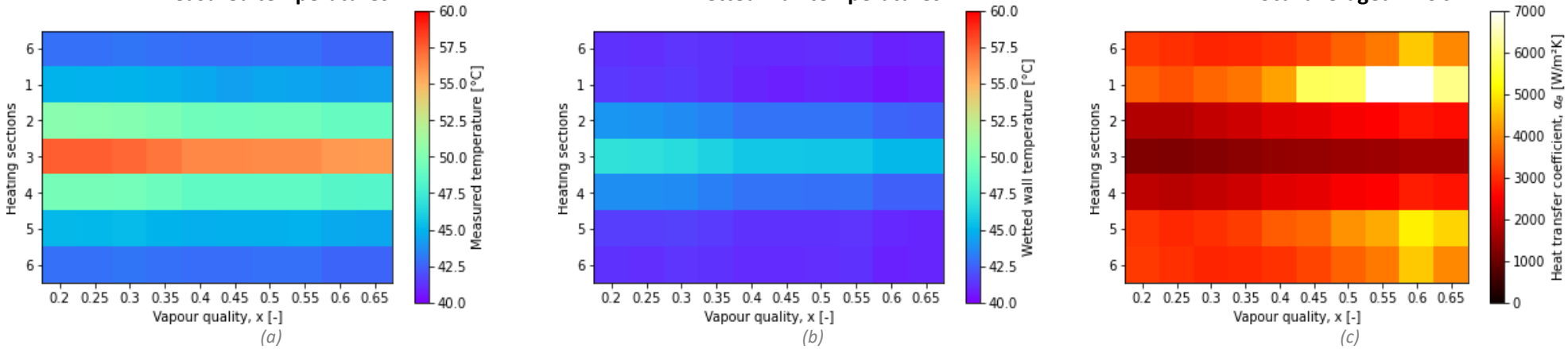

Figure 75: Results for case VI – Segment 3 heating for G = 200 kg/m²s and T_B = 40 °C

Case VII – Segment 6 heating

Mass flux = 200 kg/m²s; Saturation temperature = 40 °C

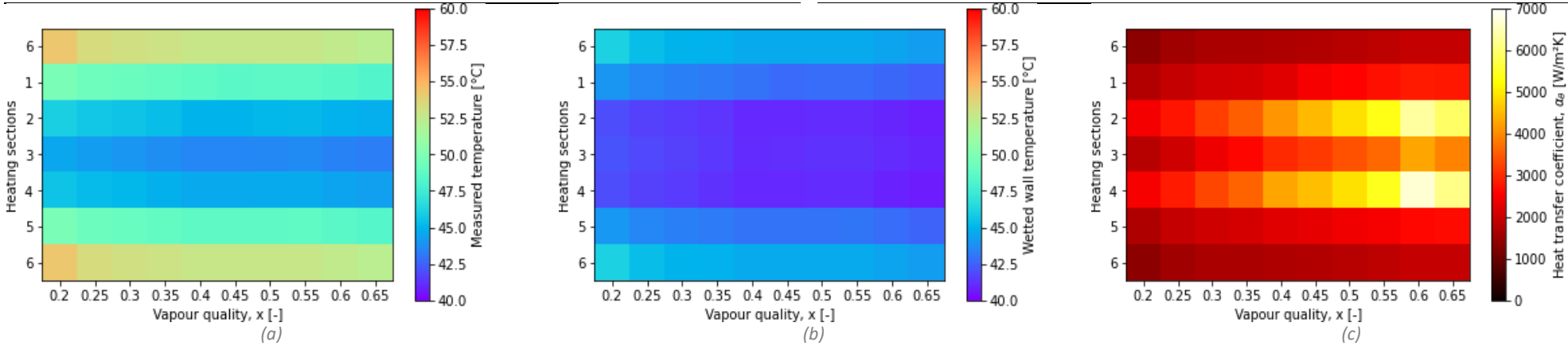

Figure 76: Results for case VII – Segment 6 heating for G = 200 kg/m²s and T_B = 40 °C

Case VIII – Segment 1 heating

Mass flux = 200 kg/m²s; Saturation temperature = 40 °C

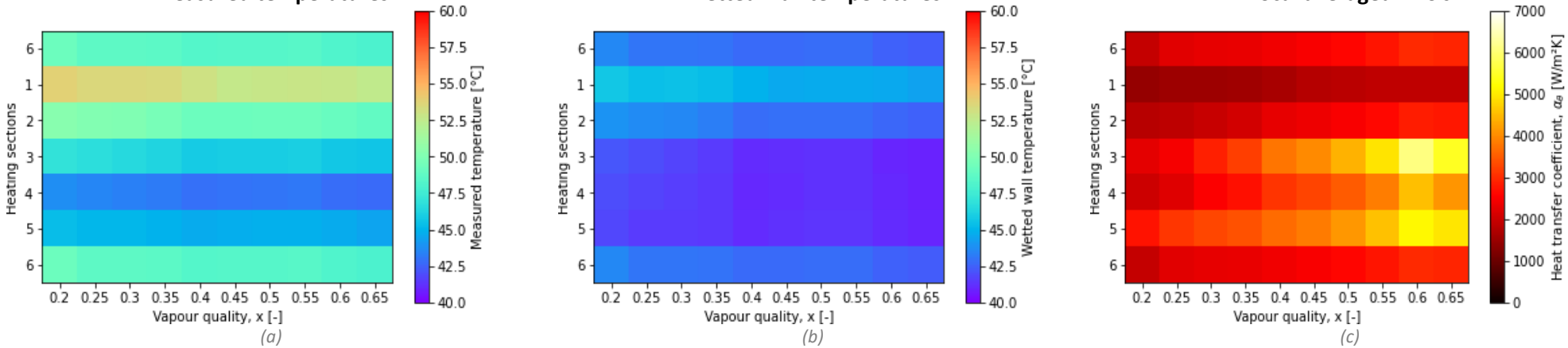

(a) *(b)* *(c)*

Figure 77: Results for case VIII – Segment 1 heating for G = 200 kg/m²s and T_B = 40 °C

Case IX – Segment 2 heating

Mass flux = 200 kg/m²s; Saturation temperature = 40 °C

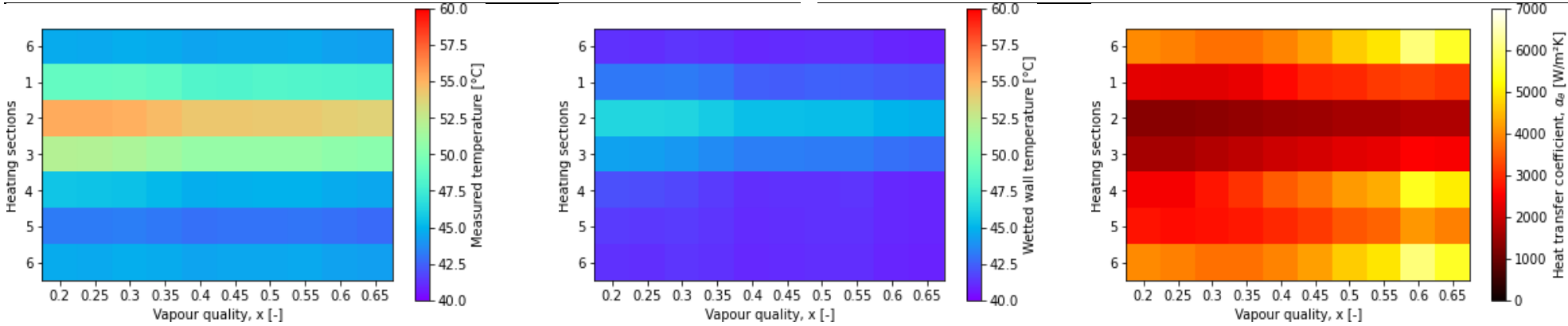

(a) *(b)* *(c)*

Figure 78: Results for case IX – Segment 2 heating for G = 200 kg/m²s and T_B = 40 °C

300_40

Case I – Uniform heating

Mass flux = 300 kg/m²s; Saturation temperature = 40 °C

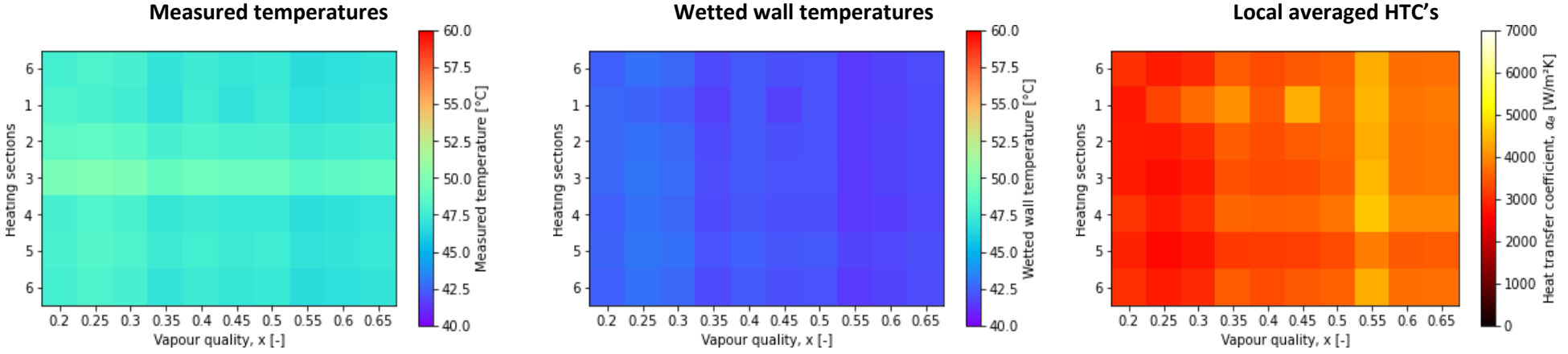

(a) *(b)* *(c)*

Figure 79: Results for case I - Uniform heating for G = 300 kg/m²s and T_B = 40 °C

Case II – Bottom heating

Mass flux = 300 kg/m²s; Saturation temperature = 40 °C

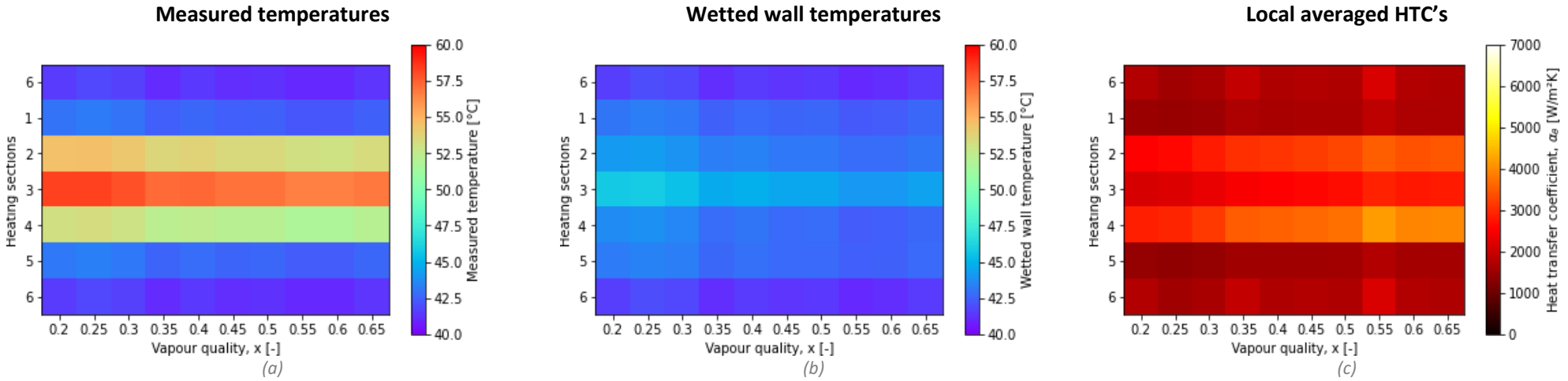

Figure 80: Results for case II - Bottom heating for G = 300 kg/m²s and T_B = 40 °C

Case III – Top heating

Mass flux = 300 kg/m²s; Saturation temperature = 40 °C

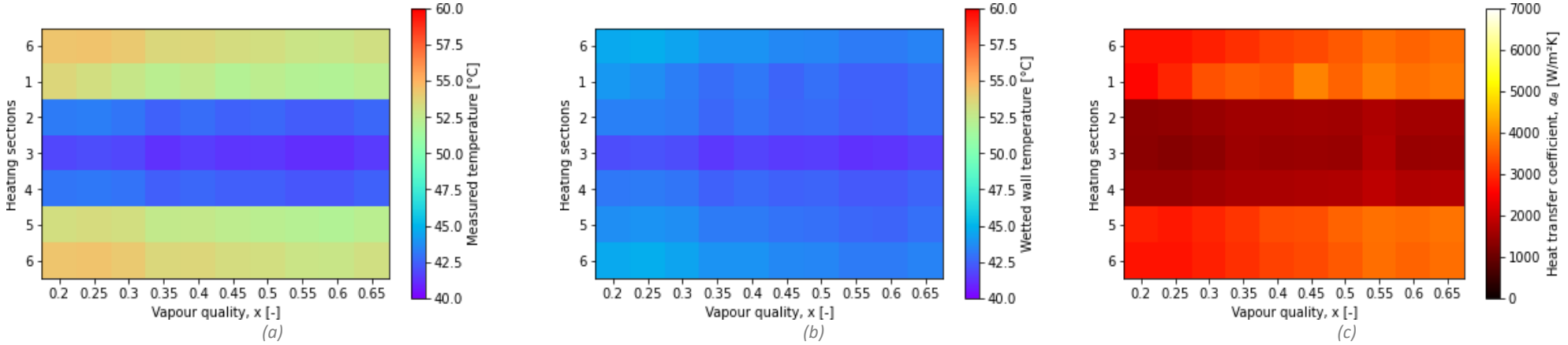

Figure 81: Results for case III - Top heating for G = 300 kg/m²s and T_B = 40 °C

Case IV – Left heating

Mass flux = 300 kg/m²s; Saturation temperature = 40 °C

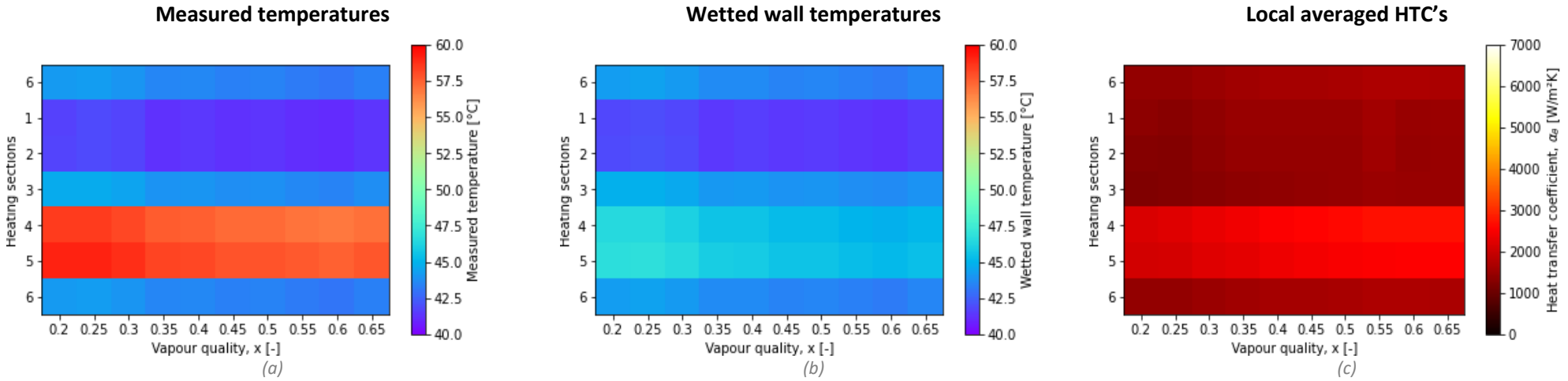

Figure 82: Results for case IV - Left heating for G = 300 kg/m²s and T_B = 40 °C

Case V – Right heating

Mass flux = 300 kg/m²s; Saturation temperature = 40 °C

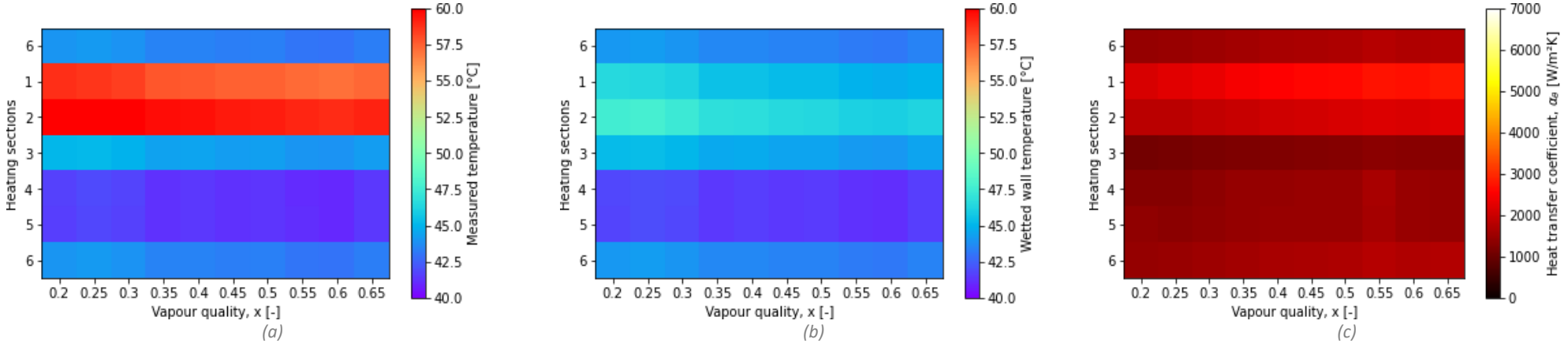

Figure 83: Results for case V - Right heating for G = 300 kg/m²s and T_B = 40 °C

Case VI – Segment 3 heating

Mass flux = 300 kg/m²s; Saturation temperature = 40 °C

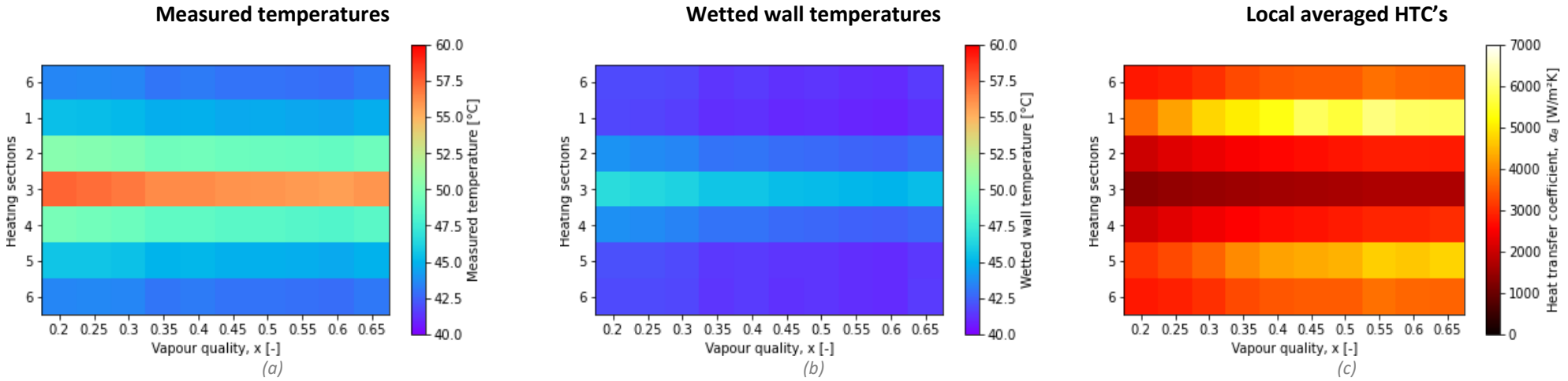

Figure 84: Results for case VI – Segment 3 heating for G = 300 kg/m²s and T_B = 40 °C

Case VII – Segment 6 heating

Mass flux = 300 kg/m²s; Saturation temperature = 40 °C

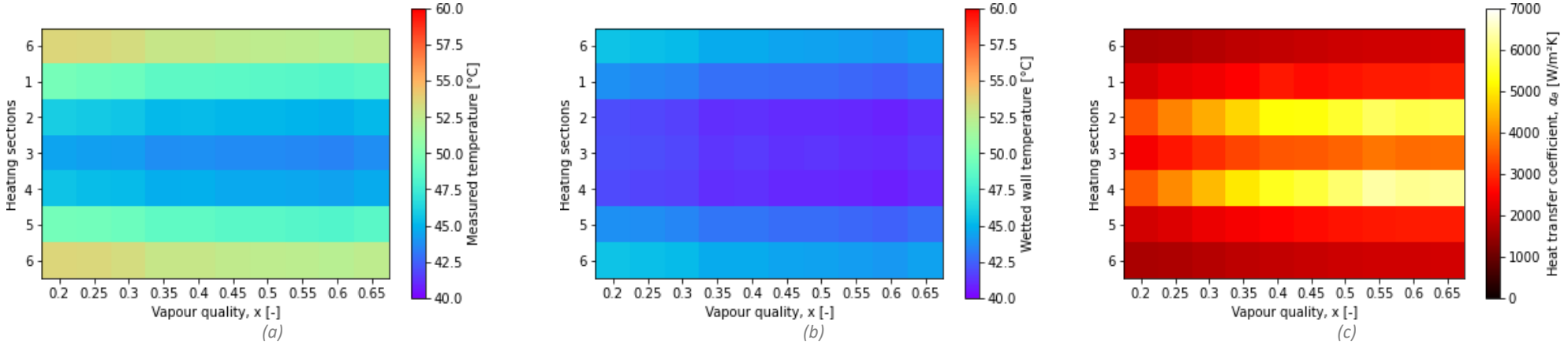

Figure 85: Results for case VII – Segment 6 heating for G = 300 kg/m²s and T_B = 40 °C

Case VIII – Segment 1 heating

Mass flux = 300 kg/m²s; Saturation temperature = 40 °C

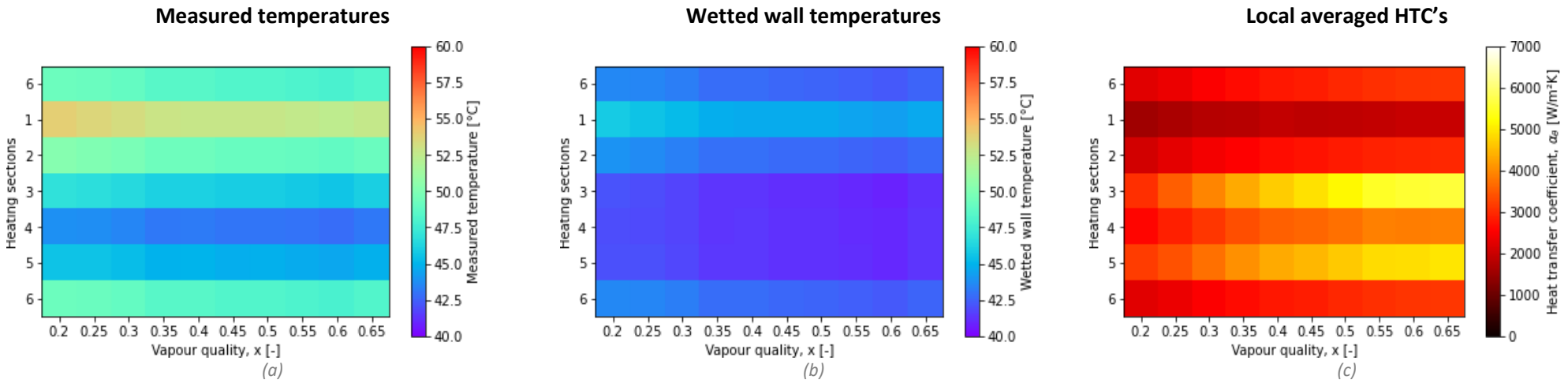

(a) (b) (c)

Figure 86: Results for case VIII – Segment 1 heating for G = 300 kg/m²s and T_B = 40 °C

Case IX – Segment 2 heating

Mass flux = 300 kg/m²s; Saturation temperature = 40 °C

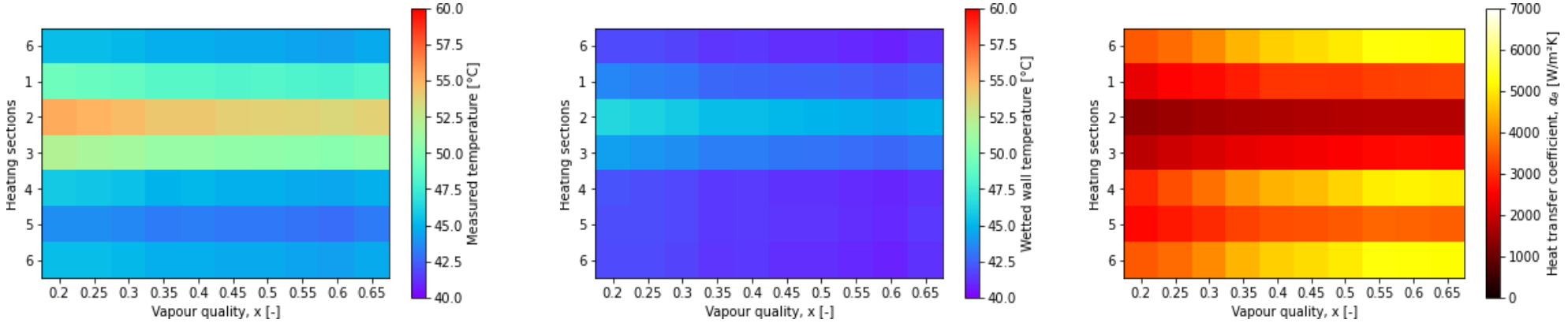

(a) (b) (c)

Figure 87: Results for case IX – Segment 2 heating for G = 300 kg/m²s and T_B = 40 °C

300_35

Case I – Uniform heating

Mass flux = 300 kg/m²s; Saturation temperature = 35 °C

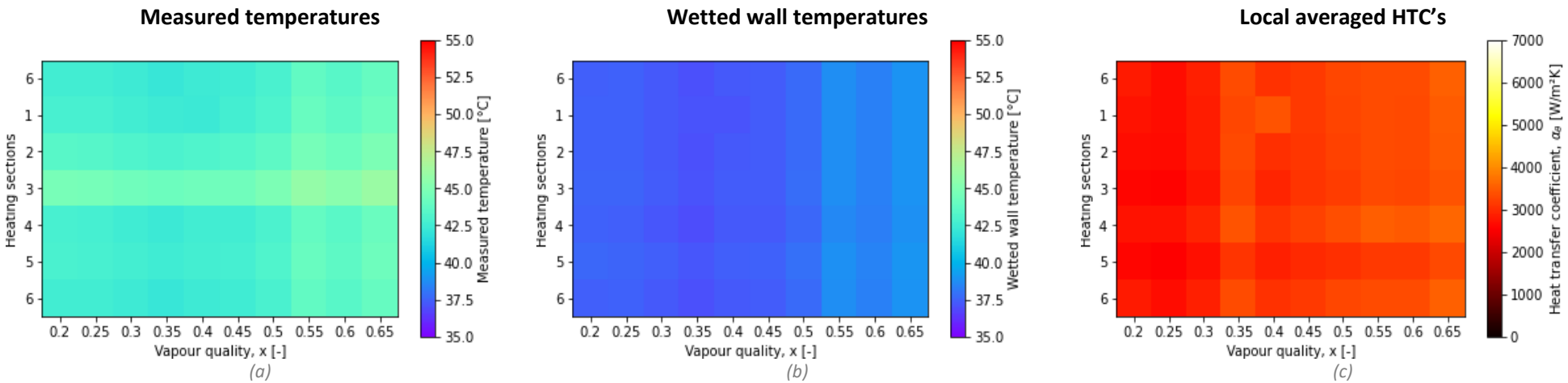

Figure 88: Results for case I - Uniform heating for G = 300 kg/m²s and T_B = 35 °C

Case II – Bottom heating

Mass flux = 300 kg/m²s; Saturation temperature = 35 °C

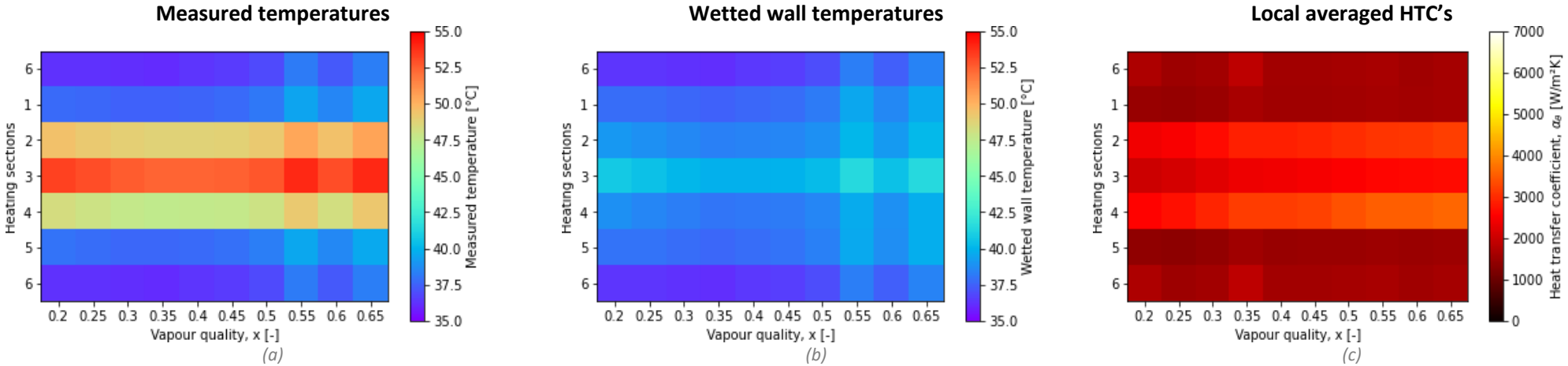

(a) (b) (c)

Figure 89: Results for case II - Bottom heating for G = 300 kg/m²s and T_B = 35 °C

Case III – Top heating

Mass flux = 300 kg/m²s; Saturation temperature = 35 °C

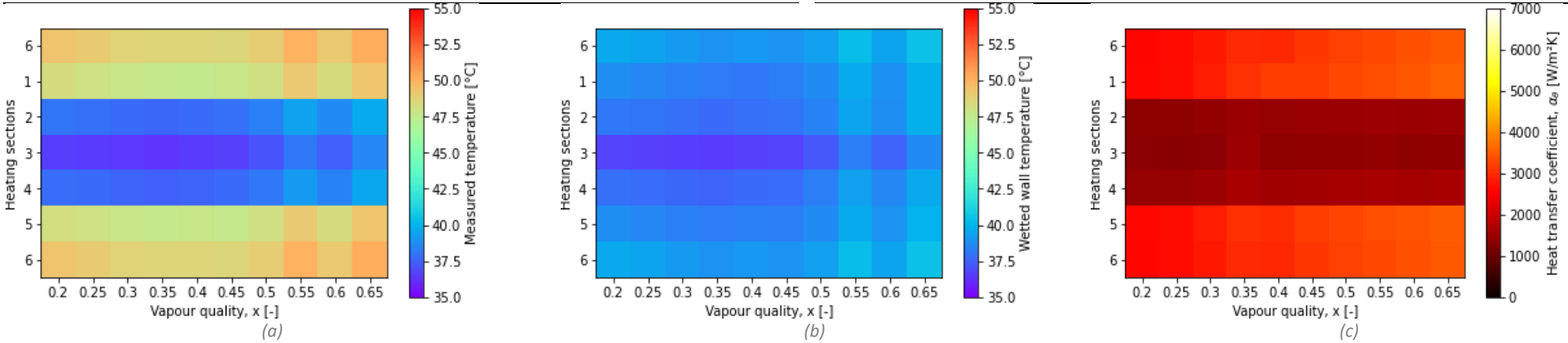

(a) (b) (c)

Figure 90: Results for case III - Top heating for G = 300 kg/m²s and T_B = 35 °C

Case IV – Left heating

Mass flux = 300 kg/m²s; Saturation temperature = 35 °C

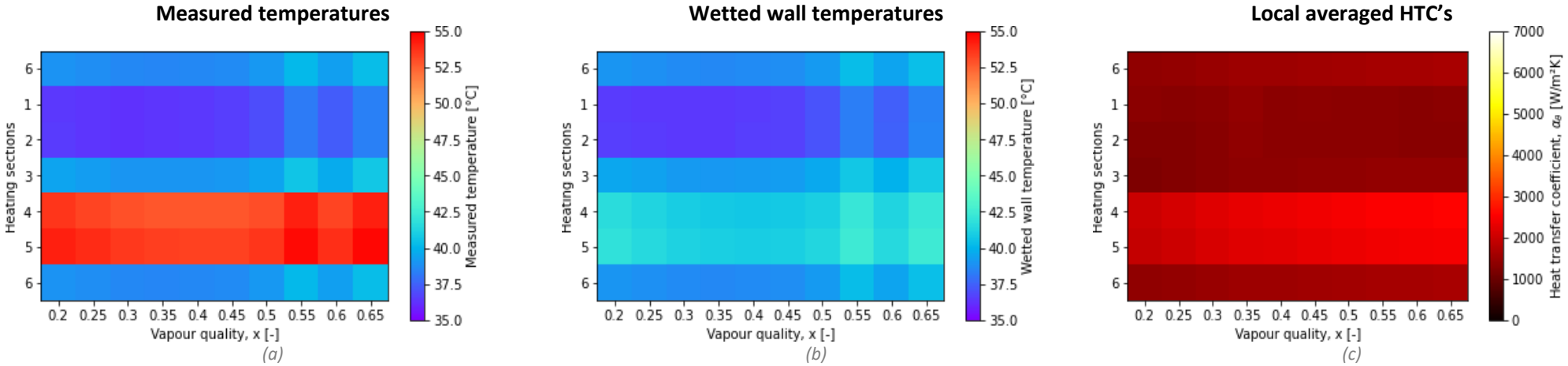

(a) (b) (c)

Figure 91: Results for case IV - Left heating for G = 300 kg/m²s and T_B = 35 °C

Case V – Right heating

Mass flux = 300 kg/m²s; Saturation temperature = 35 °C

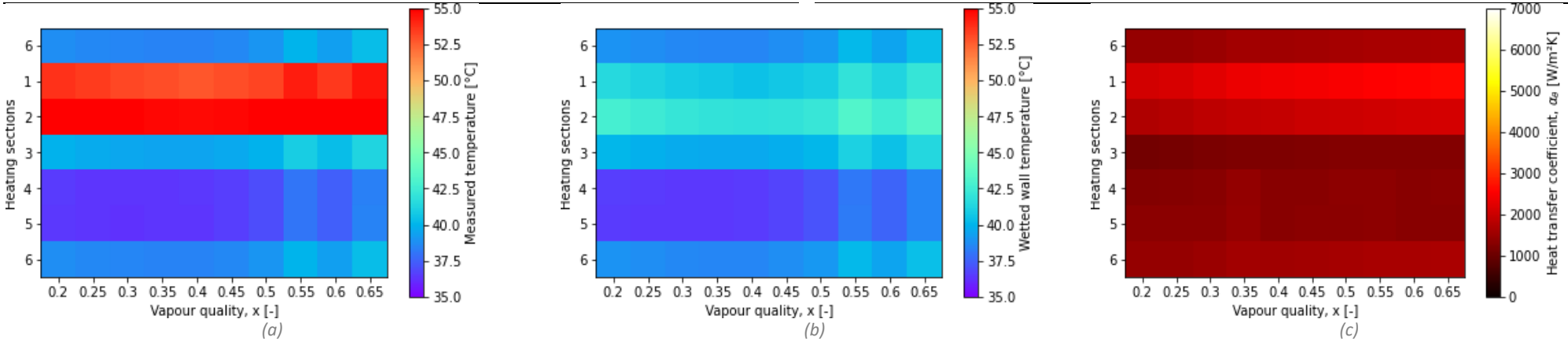

(a) (b) (c)

Figure 92: Results for case V - Right heating for G = 300 kg/m²s and T_B = 35 °C

Case VI – Segment 3 heating

Mass flux = 300 kg/m²s; Saturation temperature = 35 °C

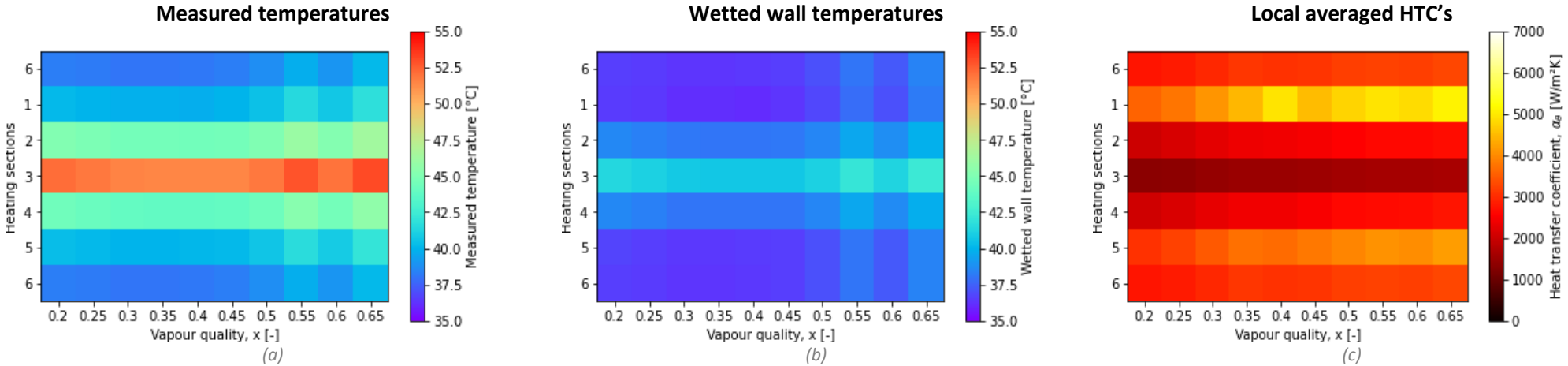

(a) (b) (c)

Figure 93: Results for case VI – Segment 3 heating for G = 300 kg/m²s and T_B = 35 °C

Case VII – Segment 6 heating

Mass flux = 300 kg/m²s; Saturation temperature = 35 °C

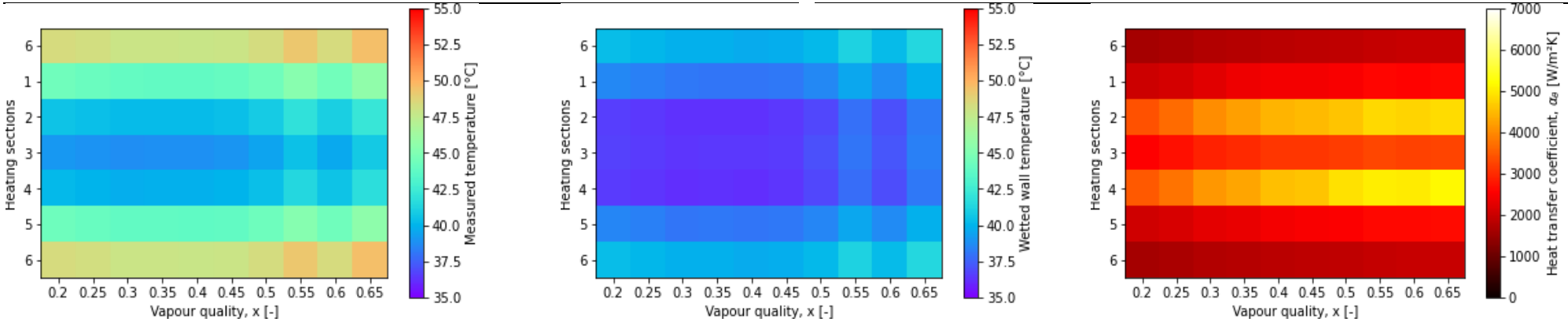

(a) (b) (c)

Figure 94: Results for case VII – Segment 6 heating for G = 300 kg/m²s and T_B = 35 °C

Case VIII – Segment 1 heating

Mass flux = 300 kg/m²s; Saturation temperature = 35 °C

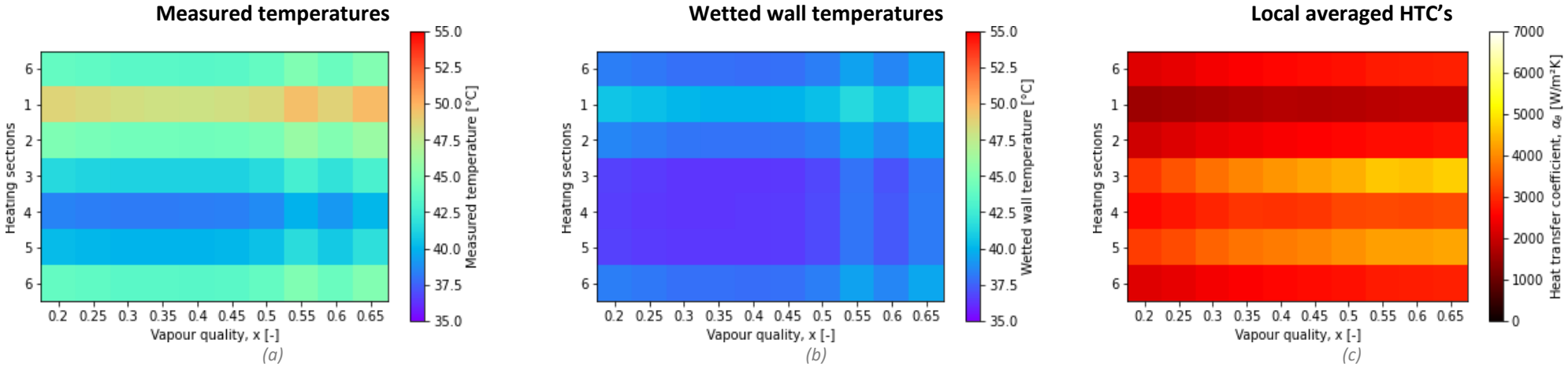

(a) (b) (c)

Figure 95: Results for case VIII – Segment 1 heating for G = 300 kg/m²s and T_B = 35 °C

Case IX – Segment 2 heating

Mass flux = 300 kg/m²s; Saturation temperature = 35 °C

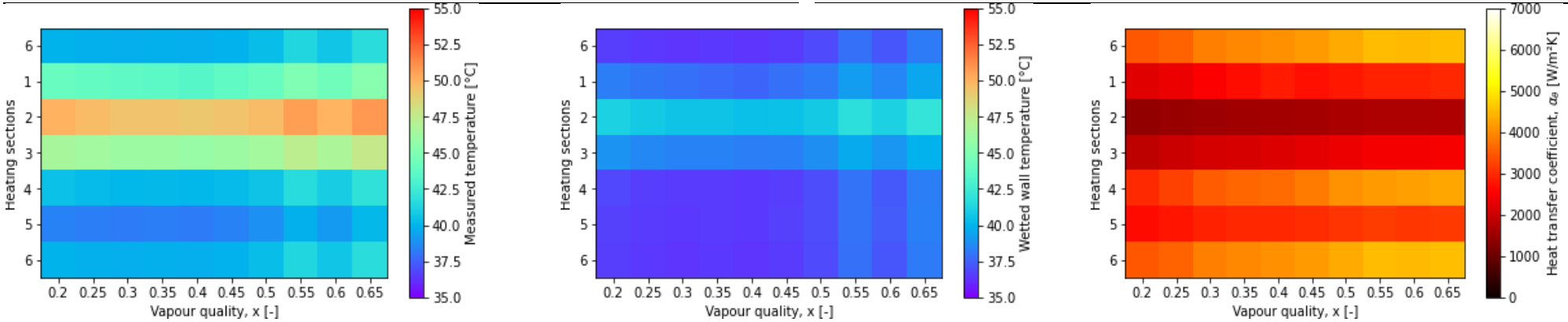

(a) (b) (c)

Figure 96: Results for case IX – Segment 2 heating for G = 300 kg/m²s and T_B = 35 °C

200_35

Case I – Uniform heating

Mass flux = 200 kg/m²s; Saturation temperature = 35 °C

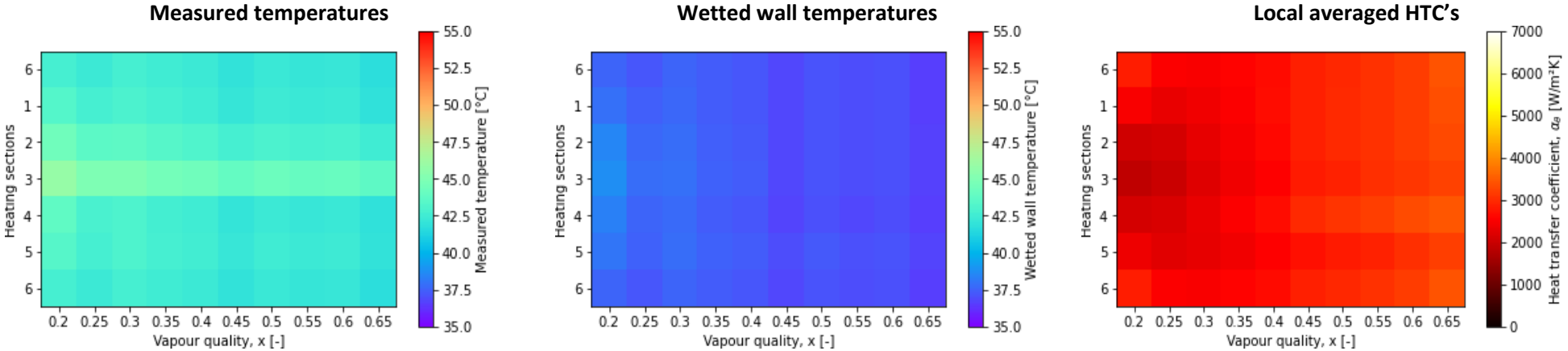

Figure 97: Results for case I - Uniform heating for G = 200 kg/m²s and T_B = 35 °C

Case II – Bottom heating

Mass flux = 200 kg/m²s; Saturation temperature = 35 °C

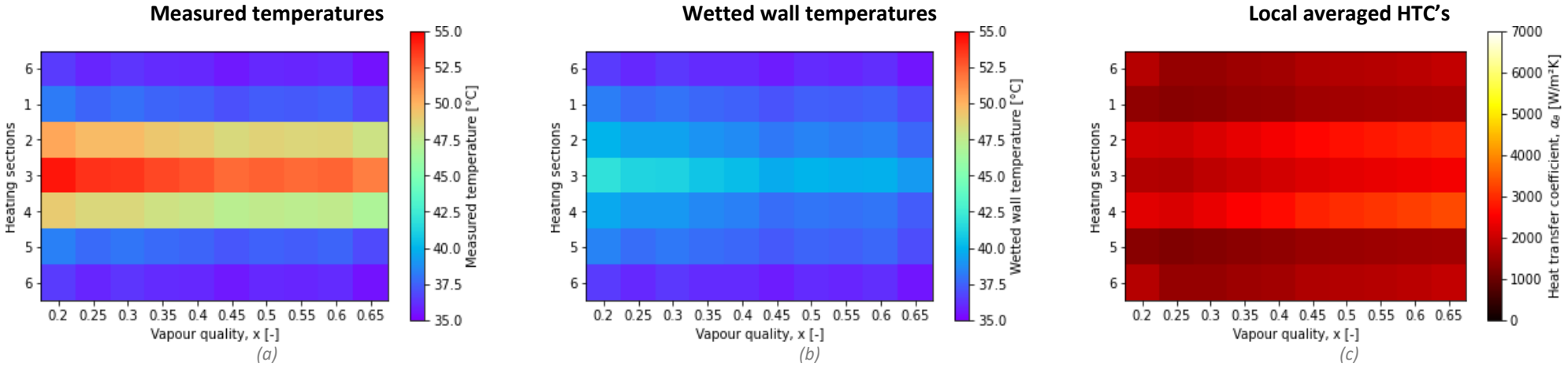

Figure 98: Results for case II - Bottom heating for G = 200 kg/m²s and T_B = 35 °C

Case III – Top heating

Mass flux = 200 kg/m²s; Saturation temperature = 35 °C

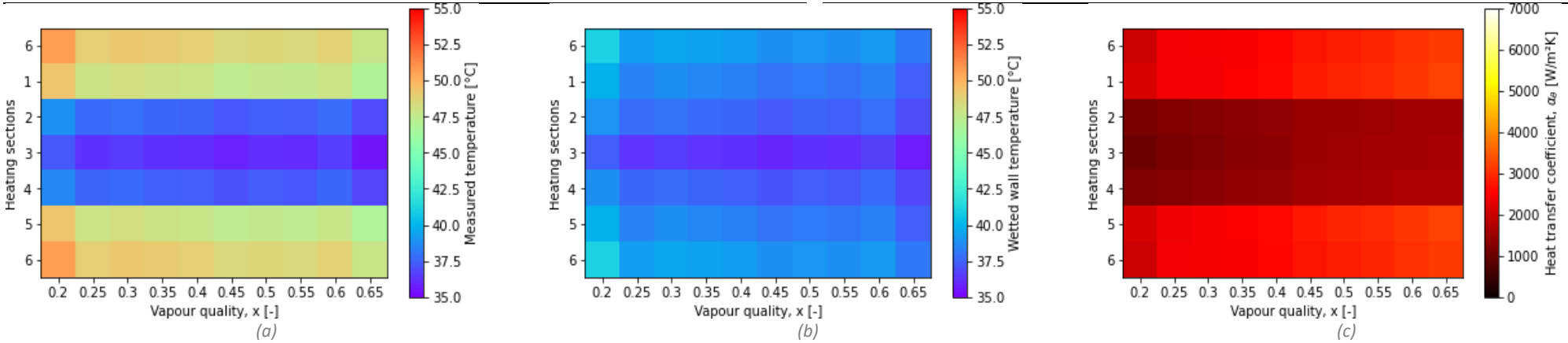

Figure 99: Results for case III - Top heating for G = 200 kg/m²s and T_B = 35 °C

Case IV – Left heating

Mass flux = 200 kg/m²s; Saturation temperature = 35 °C

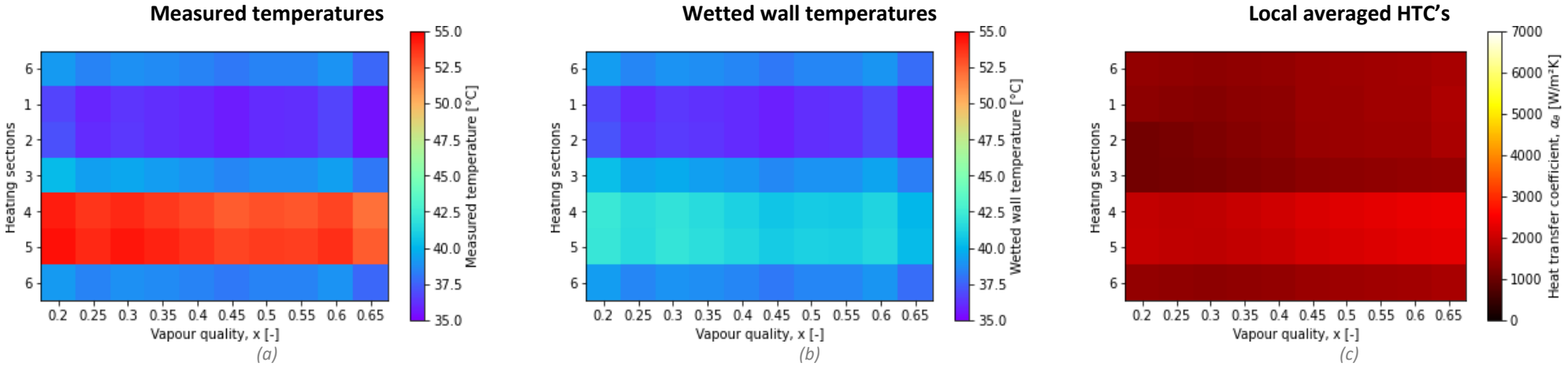

Figure 100: Results for case IV - Left heating for G = 200 kg/m²s and T_B = 35 °C

Case V – Right heating

Mass flux = 200 kg/m²s; Saturation temperature = 35 °C

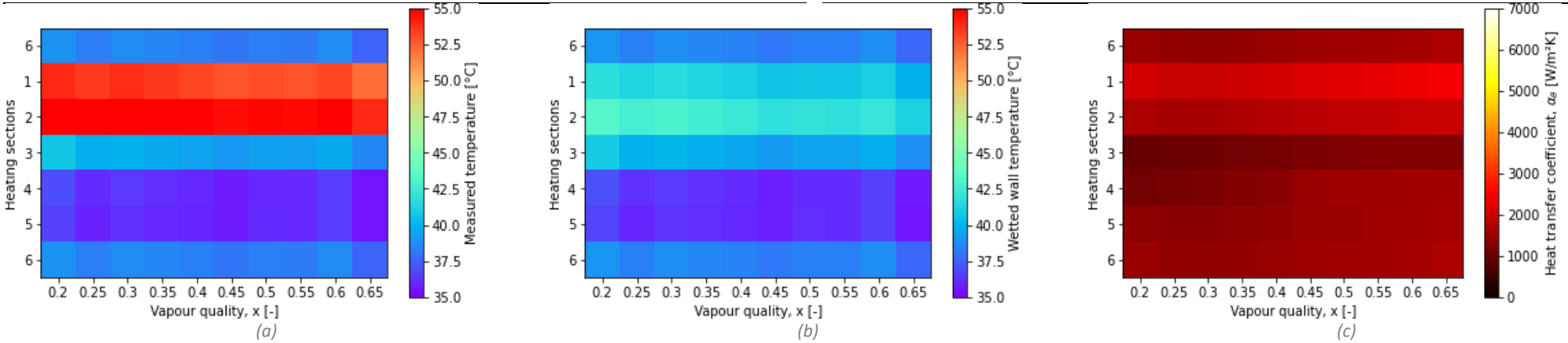

Figure 101: Results for case V - Right heating for G = 200 kg/m²s and T_B = 35 °C

Case VI – Segment 3 heating

Mass flux = 200 kg/m²s; Saturation temperature = 35 °C

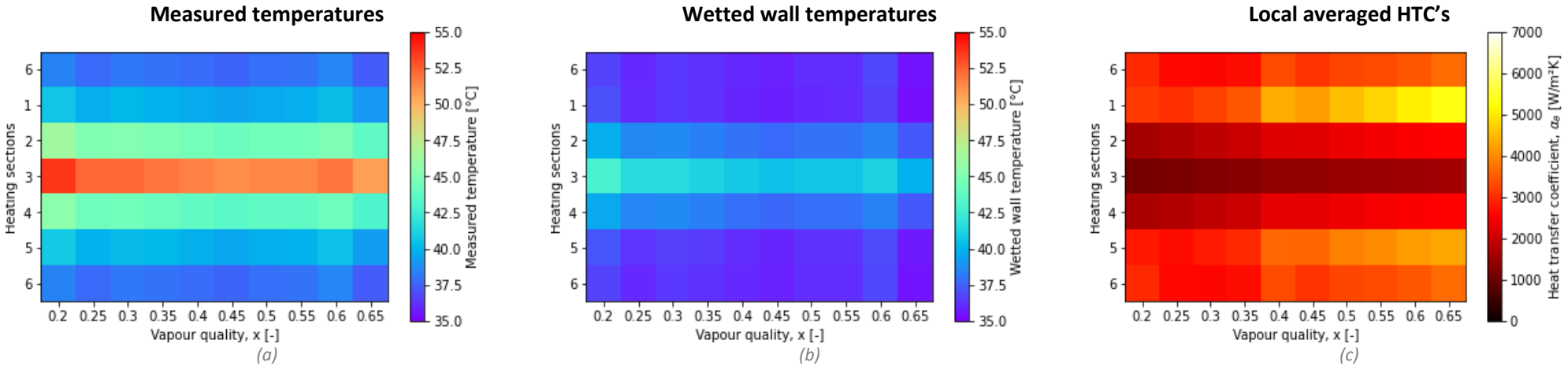

Figure 102: Results for case VI – Segment 3 heating for G = 200 kg/m²s and T_B = 35 °C

Case IX – Segment 6 heating

Mass flux = 200 kg/m²s; Saturation temperature = 35 °C

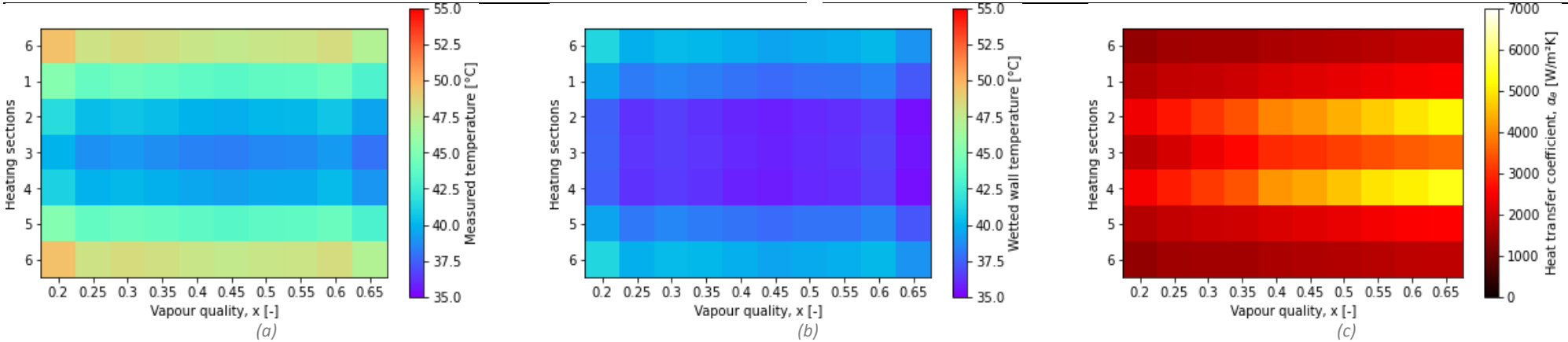

Figure 103: Results for case IX – Segment 6 heating for G = 200 kg/m²s and T_B = 35 °C

Case VIII – Segment 1 heating

Mass flux = 200 kg/m²s; Saturation temperature = 35 °C

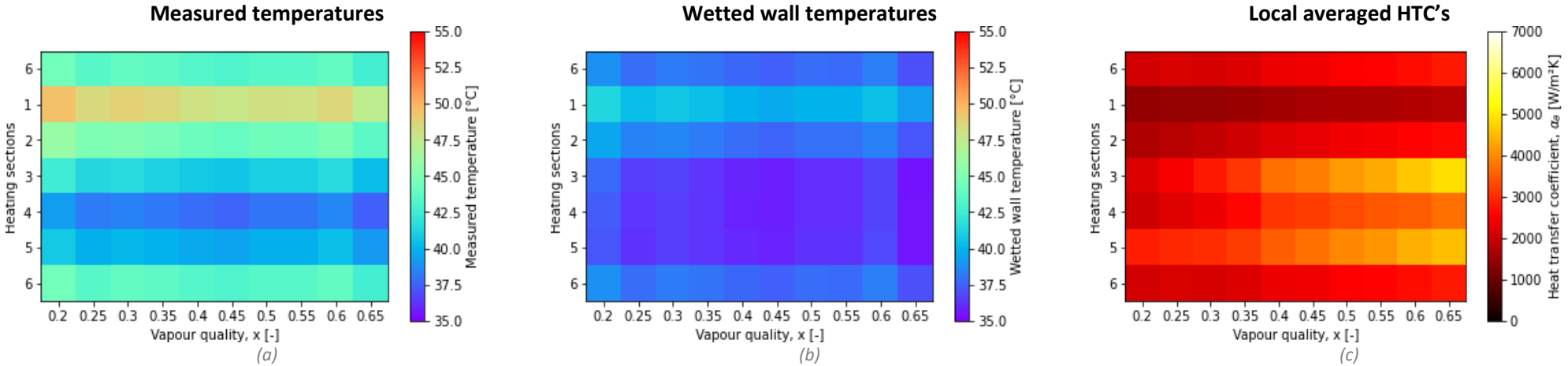

Figure 104: Results for case VIII – Segment 1 heating for G = 200 kg/m²s and T_B = 35 °C

Case IX – Segment 2 heating

Mass flux = 200 kg/m²s; Saturation temperature = 35 °C

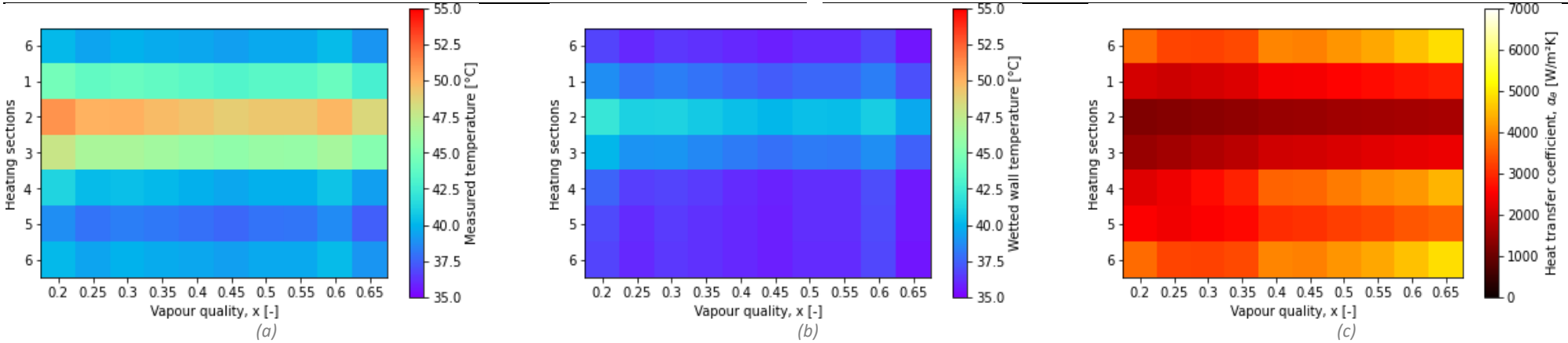

Figure 105: Results for case IX – Segment 2 heating for G = 200 kg/m²s and TB = 35 °C